Daniel Filipe Mestre Simão

Mestre em Genética Molecular e Biomedicina

Development of human central nervous system 3D *in vitro* models for preclinical research

Dissertação para obtenção do Grau de Doutor em Bioengenharia

Orientador: Prof. Doutora Paula M. Alves, ITQB-NOVA

Co-orientador: Doutora Catarina Brito, ITQB-NOVA

Júri

Presidente: Prof. Doutor Manuel Nunes da Ponte

Arguentes: Prof. Doutor Marcel Leist

Doutor Thierry Galli

Vogais: Prof. Doutor Luís Pereira de Almeida

Prof. Doutor Manuel J. T. Carrondo

FACULDADE DE CIÊNCIAS E TECNOLOGIA
UNIVERSIDADE NOVA DE LISBOA

Dezembro, 2015

Development of human central nervous system 3D *in vitro* models for preclinical research

À minha família

Acknowledgements

I would like to express my gratitude to all the people who have contributed directly or indirectly to this thesis.

To my supervisor, Prof. Paula Alves, for the opportunity to work in an inspiring and excellent scientific environment at the Animal Cell Technology Unit. Thank you for all the support, knowledge, confidence and also for all the opportunities and challenges that contributed for my development as scientist.

To my co-supervisor, Dr. Catarina Brito, for sharing this journey with me and for the constant support, guidance, confidence and motivation throughout these years. For constantly pushing me towards my goals and never letting me settle, allowing me to potentiate my skills and making me go further. Also for stimulating such a challenging and team spirit within the 3D team

To Prof. Manuel Carrondo for his always present leadership and inspiring example of excellence, rigor and hard work.

To Dr. Eric J Kremer, Dr. Giampietro Schiavo and Dr. Isabella Saggio for all the support provided during our collaboration.

To Dr. Ursula Sonnewald for such a warm welcoming in your laboratory at the NTNU in Trondheim and for all your enthusiasm and knowledge.

To Dr. Ana Teixeira for being always available and for the fruitfull discussions on cellular metabolism.

To Marcos Sousa for all the knowledge and support on the bioprocess field. Also for the constant enthusiasm, promptness to help and friendship during this journey.

To the MIT-Portugal program and all my professors for the intensive learning experience in the field of bioengineering systems. Also to my colleagues, especially to Sérgio, Jorge, Tomás, Ricardo, Sofia and Patrícia for the great moments during the first year and the "occasional" group dinners.

To my colleagues at the Animal Cell Technology Unit for creating such a great working environment, where we can continuosly learn so much from all the different fields. An especial thank you to my "partner" Catarina Pinto for sharing with me all the challenges and also the "wow" moments of working with such delicate cells. To Francisca A. for all the help and friendship during this last year and for trusting in my coaching skills. To all the 3D team, Ana Paula, Marta E., Marta, Sofia, Rita and Vítor for the strong team spirit, constant discussions, suggestions, enthusiasm and for sharing all the good and not so good moments. Also, to the rest of the people who made these

years in ACTU so especial, namely João Vidigal, Francisca, Paulo, Raquel, Tiago, Mafalda, João Sá, Ana Oliveira.

À Marta, pelo carinho, partilha e apoio constante. Por compreender melhor que ninguém todas as dificuldades e alegrias durante estes anos. Pela constante motivação e por acreditar sempre em mim.

À minha família, em especial à minha mãe, pai, irmão e avós, pelo apoio incondicional e por serem um exemplo a seguir. Obrigado por toda a confiança, por tudo o que me ensinaram e por terem contribuído para a pessoa que sou hoje.

Abstract

Neurological disorders are a major concern in modern societies, with increasing prevalence mainly related with the higher life expectancy. Most of the current available therapeutic options can only control and ameliorate the patients' symptoms, often becoming refractory over time. Therapeutic breakthroughs and advances have been hampered by the lack of accurate central nervous system (CNS) models. The development of these models allows the study of the disease onset/progression mechanisms and the preclinical evaluation of novel therapeutics. This has traditionally relied on genetically engineered animal models that often diverge considerably from the human phenotype (developmentally, anatomically and physiologically) and 2D *in vitro* cell models, which fail to recapitulate the characteristics of the target tissue (cell-cell and cell-matrix interactions, cell polarity).

The *in vitro* recapitulation of CNS phenotypic and functional features requires the implementation of advanced culture strategies that enable to mimic the *in vivo* structural and molecular complexity. Models based on differentiation of human neural stem cells (hNSC) in 3D cultures have great potential as complementary tools in preclinical research, bridging the gap between human clinical studies and animal models. This thesis aimed at the development of novel human 3D *in vitro* CNS models by integrating agitation-based culture systems and a wide array of characterization tools.

Neural differentiation of hNSC as 3D neurospheres was explored in **Chapter 2**. Here, it was demonstrated that human midbrain-derived neural progenitor cells from fetal origin (hmNPC) can generate complex tissue-like structures containing functional dopaminergic neurons, as well as astrocytes and oligodendrocytes. **Chapter 3** focused on the development of cellular characterization assays for cell aggregates based on light-sheet fluorescence imaging systems, which resulted in increased spatial resolution both for fixed samples or live imaging. The applicability of the developed human 3D cell model for preclinical research was explored in **Chapter 4**, evaluating the potential of a viral vector candidate for gene therapy. The efficacy and safety of helper-dependent CAV-2 (hd-CAV-2) for gene delivery in human neurons was evaluated, demonstrating increased neuronal tropism, efficient transgene expression and minimal toxicity. The potential of human 3D *in vitro* CNS models to mimic brain functions was further addressed in **Chapter 5**. Exploring the use of ^{13}C-labeled substrates and Nuclear Magnetic Resonance (NMR) spectroscopy tools, neural metabolic signatures were evaluated showing lineage-specific metabolic specialization and establishment of neuron-astrocytic shuttles upon differentiation. **Chapter 6** focused on transferring the knowledge and strategies described in the previous chapters for the implementation of

a scalable and robust process for the 3D differentiation of hNSC derived from human induced pluripotent stem cells (hiPSC). Here, software-controlled perfusion stirred-tank bioreactors were used as technological system to sustain cell aggregation and differentiation.

The work developed in this thesis provides practical and versatile new *in vitro* approaches to model the human brain. Furthermore, the culture strategies described herein can be further extended to other sources of neural phenotypes, including patient-derived hiPSC. The combination of this 3D culture strategy with the implemented characterization methods represents a powerful complementary tool applicable in the drug discovery, toxicology and disease modeling.

Keywords: Human neural stem cells; 3D cell culture; agitation-based culture systems; neural differentiation.

Resumo

As doenças neurológicas representam um crescente problema para as sociedades modernas, nomeadamente com o aumento na sua prevalência devido a uma maior esperança média de vida. As opções terapêuticas actualmente disponíveis, na sua maioria, apenas proporcionam uma melhoria dos sintomas, tornando-se muitas vezes refractárias com o tempo. Os avanços terapêuticos têm sido dificultados pela falta de modelos de sistema nervoso central (SNC) adequados. O desenvolvimento destes modelos permitem o estudo do mecanismos associados ao aparecimento e progressão de doença, assim como a caracterização pré-clínica de novas terapias. Esta investigação tem maioritariamente sido baseada no uso de modelos animais genéticamente modificados, que por norma divergem consideravelmente do fénotipo humano (desenvolvimento, anatómico e fisiológico), e modelos celulares *in vitro* 2D, que não permitem mimetizar as características do tecido de interesse (interacções célula-célula, polaridade, etc).

Para a recapitulação *in vitro* das características fénotipicas e funcionais do SNC é necessário a implementação de estratégias de cultura avançadas que permitam mimetizar a complexidade estrutural e molecular observada *in vivo*. Os modelos celulares baseados na diferenciação de células estaminais neurais (CEN) humanas em sistemas de cultura 3D apresentam um elevado potencial para a investigação pré-clínica, complementando a lacuna existente entre os ensaios clínicos em humanos e os modelos animais. O trabalho apresentado nesta tese teve como objectivo o desenvolvimento de um novo modelo humano *in vitro* 3D de SNC, com particular ênfase no fénotipo dopaminérgico, através da integração de sistemas de cultura agitados e uma vasta gama de ferramentas de caracterização.

A diferenciação neural de CEN humanas em culturas 3D como neurosferas foi explorada no **Capítulo 2**. Aqui, foi demonstrado que células progenitoras neurais humanas derivadas de mesencéfalo podem ser utilizadas para gerar estruturas complexas compostas por neurónios dopaminérgicos funcionais, assim como astrócitos e oligodendrócitos. O **Capítulo 3** focou-se na necessidade de desenvolvimento técnico de sistemas de imagiologia para agregados celulares, através da implementação da técnologia de microscopia de fluorescencia "*light-sheet*" para a análise da neurosferas de hmNPC. A aplicação do modelo celular desenvolvido para a investigação pré-clínica foi explorada no **Capítulo 4**, avaliando o potencial de um vector viral como candidato para terapia génica. A eficácia e segurança dos vectores CAV-2 "*helper-dependent*" (hd-CAV-2) para transferência de genes em neurónios humanos foi analisada, demonstrando um tropismo neuronal elevado, eficiente expressão do

transgene e toxicidade mínima. O potencial do modelos humanos *in vitro* 3D de SNC para mimetizar funções neurais foi ainda mais explorado no **Capítulo 5**. Através do uso de compostos marcados com ^{13}C e de ferramentas de espectroscopia por resonância magnética nuclear de ^{13}C (^{13}C-NMR), características metabolicas neurais foram analisadas demonstrando a existência de especialização metabólicas específicas para diferentes linhagens celulares neurais e o estabelecimento de tráfegos metabólicos entre neurónios e astrócitos. No **Capítulo 6** todo o conhecimento e estratégias desenvolvidas nos capítulos anteriores foram aplicadas na implementação de um sistema escalonável e robusto para a diferenciação 3D de CEN derivadas de células estaminais pluripotentes induzidas (iPSC) humanas. O uso de bioreactores de tanque agitado controlados por software e operados em modo de perfusão permitiu o desenvolvimento de um processo eficiente para a agregação e diferenciação celular.

O trabalho desenvolvido nesta tese apresenta abordagens práticas e versáteis para a modelação *in vitro* do cérebro humano. As estratégias de cultura celular desenvolvidas podem ainda ser transferida para outras fontes celulares, incluíndo iPSC derivadas de pacientes. A combinação destas estratégias de cultura 3D com o conjunto de métodos implementados para a sua caracterização, representa uma poderosa ferramenta complementar no desenvolvimento de novos fármacos, em toxicologia e para modelação *in vitro* de neuropatologias humanas.

Palavras-chave: cultura celular 3D; sistemas de cultura agitados; diferenciação neural; células estaminais neurais humanas

Thesis Publications

Brito C., **Simão D.**, Costa I., Malpique R., Pereira C.I., Fernandes P., Serra M., Schwarz S.C., Schwarz J., Kremer E.J., Alves P.M. (2012) 3D cultures of human neural progenitor cells: dopaminergic differentiation and genetic modification. *Methods* 56, 452–60.

Gualda E. J., **Simão D.**, Pinto C., Alves P.M., Brito C. (2014) Imaging of human differentiated 3D neural aggregates using light sheet fluorescence microscopy. *Front. Cell. Neurosci.* 8, 221.

Simão D., Pinto C., Piersanti S., Weston A., Peddie C.J., Bastos A.E.P., Licursi V., Schwarz S.C., Collinson L.M., Salinas S., Serra M., Teixeira A.P., Saggio I., Lima P.A., Kremer E.J., Schiavo G., Brito C., Alves P.M. (2015) Modeling human neural functionality *in vitro*: 3D culture for dopaminergic differentiation. *Tissue Eng. Part A* 21, 654–668.

Simão D., Pinto C., Fernandes P., Peddie C.J., Piersanti S., Collinson L.M., Salinas S., Saggio I., Schiavo G., Kremer E.J., Brito C., Alves P.M. (2016) Evaluation of helper-dependent canine adenovirus vectors in a 3D human CNS model. *Gene Therapy* 23(1): 86-94

Simão D., Terrasso A.P., Teixeira A.P., Brito C., Sonnewald U., Alves P.M. (2016) Functional metabolic interactions of neuron-astrocyte 3D networks derived from human stem cells. *Submitted*

Additional Publications

Silva A. C.*, **Simão D.***, Küppers C.*, Lucas T.*, Sousa M. F. Q., Cruz P., Carrondo M. J. T., Kochanek S., Alves P. M. (2015) Human amniocyte-derived cells are a promising cell host for adenoviral vector production under serum-free conditions. *Biotechnol. J.* 10, 760–771.

Fernandes P., **Simão D.**, Guerreiro M. R., Kremer E. J., Coroadinha a S., Alves P. M. (2015) Impact of adenovirus life cycle progression on the generation of canine helper-dependent vectors. *Gene Therapy.* 22, 40–49.

Piersanti S., Burla R., Licursi V., Brito C., Torre M. La, Alves P. M., **Simao D.**, Mottini C., Salinas S., Negri R., Tagliafico E., Kremer E.J., Saggio I. (2015) Transcriptional Response of Human Neurospheres to Helper-Dependent CAV-2 Vectors Involves the Modulation of DNA Damage Response, Microtubule and Centromere Gene Groups. *PLoS One* 10, e0133607.

Simão D., Costa I., Serra M., Schwarz J., Brito C., Alves P. M. (2011) Towards human central nervous system *in vitro* models for preclinical research: strategies for 3D neural cell culture. *BMC Proc.* 5 Suppl 8, P53.

Simão D., Pinto C., Teixeira A. P., Alves P.M., Brito C. (2013) 1H-NMR spectroscopy for human 3D neural stem cell cultures metabolic profiling. *BMC Proc.* 7, O8.

Simão D., Pinto C., Serra M., Brito C., Alves P.M. (2013) Sistemas de cultura 3D para diferenciação neural de células estaminais humanas. *Bol. Biotecnol.* 4, 17–20.

*These authors contributed equally to this work

Table of Contents

List of Figures

List of Tables

List of Abbreviations

2D	Two-dimensional
3D	Three-dimensional
AAV	Adeno-associated viruses
AdV	Adenoviruses
AM	Aggregation medium
ANOVA	Analysis of variance
BCAA	Branched-chain aminoacids
bFGF	Basic fibroblast growth factor
BSA	Bovine serum albumin
cAMP	Cyclic adenosine monophosphate
CAR	Coxsackievirus and adenovirus receptor
CNS	Central nervous system
CREB	cyclic AMP response element-binding protein
dbcAMP	dibutyryl cyclic adenosine monophosphate
DM	Differentiation medium
DMEM	Dulbecco's modified Eagle medium
dpt	days post-transduction
DRD2	Dopamine receptor D2
ECM	Extracellular matrix
EdU	5-ethynyl-2´-deoxyuridine
EGF	Epidermal growth factor
EM	Expansion medium
ESC	Embryonic stem cells
FBS	Fetal bovine serum
FDA	Fluorescein diacetate
FSG	Fish skin gelatin

GABA	γ-aminobutyric acid
GAD67/65	Glutamate decarboxylase 65/67
GEMM	Genetically engineered mouse models
GFAP	Glial fibrillary acidic protein
GLAST	Glutamate aspartate transporter
GS	Glutamine synthase
HAdV5	Human adenovirus type 5 vectors
hd-CAV-2	Helper-dependent canine adenovirus type 2 vectors
HIF	Hypoxia-inducible factor
hiPSC-NSC	human induced pluripotent stem cell-derived neural stem cells
hmNPC	Human midbrain-derived neural precursor cells
HTS	High-throughput screening
ip	Infectious particles
iPSC	Induced pluripotent stem cells
LSFM	Light-sheet fluorescence microscopy
MAPK	Mitogen-activated protein kinase
MEA	Micro-electrode arrays
MM	Maturation medium
MOI	Multiplicity of infection
MS	Mass spectrometry
MSO	Methionine sulfoximine
NMR	Nuclear Magnetic Resonance
NSC	Neural stem cells
NT2	Ntera-2 cell line
NURR1	Nuclear receptor related-1 protein
PC	Pyruvate carboxylase
PCNA	Proliferating cell nuclear antigen
PD	Parkinson's Disease

PDH	Pyruvate dehydrogenase
PFA	Paraformaldehyde
PI	Propidium iodide
PLOF	Poly-L-ornithine-fibronectin
PLOL	Poly-L-ornithine-laminin
pp	Physical particles
PSC	Pluripotent stem cells
RA	Retinoic acid
RPL22	Ribossomal protein L22
RT-qPCR	Reverse transcriptase quantitative polymerase chain reaction
SBF-SEM	Serial block face scanning electron microscopy
SEM	Scanning electron microscopy
SHH	Sonic hedgehog
SPIM	Selective plane illumination microscopy
STB	Stirred-tank bioreactor
SVZ	Subventricular zone
SYN2	Synapsin II
SYP	Synaptophysin
SYT1	Synaptogamin I
tBHP	Tert-butyl hydroperoxide
TCA	Tricarboxylic acid
TEM	Transmission electron microscopy
TH	Tyrosine hydroxylase
TX-100	Triton X-100
VEGF	Vascular endothelial growth factor
vGAT	Vesicular GABA transporter
vGluT1	Vesicular glutamate transporter
Vm	Cell membrane potential

1

Introduction

Table of Contents

1. Central nervous system (CNS) models for neuroscience research

1.1. Motivation for CNS modeling

The increase of life expectancy led to a dramatic increase in the prevalence of many age-related diseases over the last decades, as the case of most neurological disorders. In 2012, 8.4 million people aged 60 years or older were estimated to be afflicted with these disorders in Europe (OECD 2014). These numbers are estimated to increase over the next decades, possibly affecting up to 115 million people aged over 60 years worldwide in 2050 (Alzheimer's Disease International 2010).

Despite the increasing prevalence of neurodegenerative disorders no significant breakthroughs have been made in the available therapies. The few novel therapeutics reaching the market are only symptomatic treatments, which although ameliorating patients mental impairment do not address disease progression (Calcoen *et al.* 2015). Drug development pipelines have been registering high attrition rates over the last decades, with only around 10% of the compounds that enter phase I clinical trials reaching the market (Hay *et al.* 2014). This is even more critical for neurological disorders, as Alzheimer's disease for which there is an estimated overall success rate of 0.5%, significantly lower than the industry average of 4.1% (Calcoen *et al.* 2015). Therefore, the lack of effective treatments is expected to lead to overwhelming financial and sociological costs in a near future (Forman *et al.* 2004).

One of the greatest challenges for the improvement of clinical translation success rates is the use of more adequate and predictive preclinical models (Figure 1.1). This has been particularly emphasized for therapeutic fields as neurological disorders and oncology, where many of the available preclinical models based on animals or cell lines do not enable the accurate recapitulation of specific disease mechanisms (Jucker 2010; Begley and Ellis 2012; Mak *et al.* 2014). This is mainly due to differences at biochemical and genetic levels between species, which hamper the relevance of such preclinical studies and ultimately the success of its clinical translation towards human patients (Schüle *et al.* 2009; Ben-Nun and Benvenisty 2006).

Therefore, there has been an increasing demand for a paradigm shift towards more predictive preclinical CNS models, which can withstand the stringent and rigorous drug screening pipelines allowing for successful clinical translation.

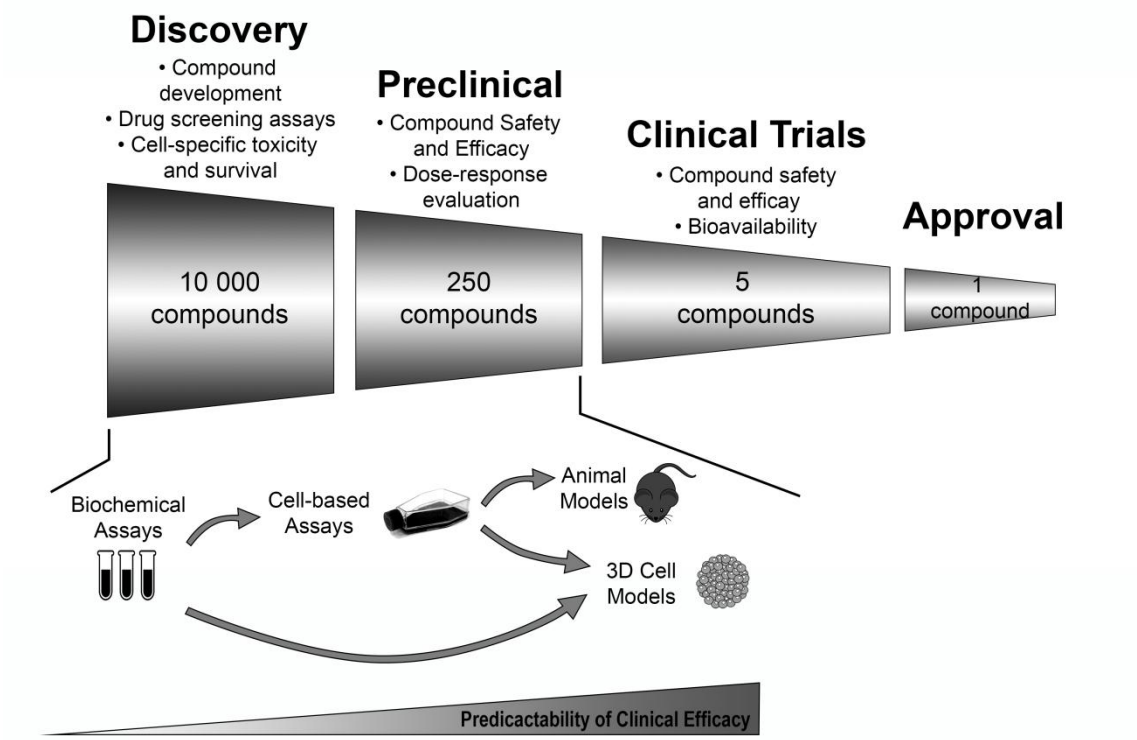

Figure 1.1 – Overview of drug discovery and development workflow in pharmaceutical industry. The different stages of the development process present specific goals and readouts that turns compound selection a very stringent process, typically with only 1 in 10 000 new compounds ending up being approved. During discovery and preclinical stages, 3D cell models can represent a complementary tool in the development operations, offering increased predictability of clinical efficacy from *in vitro* validation. The use of these models allows also to decrease the dependency on animal models, contributing for significant reductions in cost and time. Adapted from Kunz-Schughart *et al.* (2004) and Ebert and Svendsen (2010).

1.2. CNS cellular components

Central Nervous System (CNS), presents a highly complex architecture and cellular composition, which difficult the task of accurately modeling this system. The main cell types present in brain tissue are neurons, astrocytes, oligodendrocytes and microglia (Figure 1.2). Together these different cells generate a complex network of intercellular interactions that are crucial for the correct integration and interpretation of the information received from our body and the surrounding environment (Brodal 2010).

Neurons present very specific morphological features, with a cell body (soma), where the nucleus and most of the cellular machinery are located, dendrites, responsible for receiving the information from neighbor neurons, and a long axon, which transmits the information (Brodal 2010; Byrne *et al.* 2009). The nerve impulse is transmitted along the axon until it reaches the site of contact with the downstream neuron,

or synapse. In this highly specialized cellular region, neurotransmitters are released into the synaptic cleft, conveying a chemical signal to the post-synaptic neuron (Brodal 2010). In this context, neurons can be classified according to the molecules used as neurotransmitters. The most abundant and ubiquitous neurotransmitters in the CNS are glutamate, released by the excitatory glutamatergic neurons, and GABA (γ-aminobutyric acid), released by the inhibitory GABAergic neurons. Other important neurotransmitters include monoamines, such as dopamine, serotonin or norepinephrine, which are typically restricted to specialized regions within CNS (Byrne *et al.* 2009).

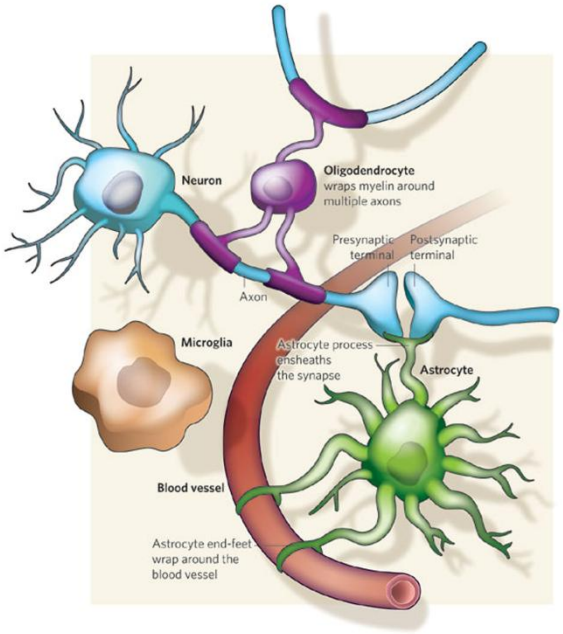

Figure 1.2 – Cellular composition and structure in the brain. The different cell types present in brain tissue establish multiple interactions developing complex cell-cell networks. Astrocytes extend processes that ensheath blood vessels and neuronal synapses. Oligodendrocytes wrap neuronal axons with myelin, speeding up signal transmission. Microglia cells are responsible for the surveillance of the microenvironment for damage or infection signs. Reproduced form Allen and Barres (2009).

Astrocytes are the most abundant glial cells in the adult brain, which represent an average of 50% of human brain cells, even though its abundance can differ across different brain regions (Azevedo *et al.* 2009). Astrocytes are interspersed with neurons throughout brain tissue, extending many fine processes that have multiple contact sites with neurons (Allen 2014). These contacts can be established between one astrocyte and several different neurons. Moreover, astrocytes express receptors for many different neurotransmitters, eliciting a nonelectric activation with intracellular calcium elevation in response to synaptic stimuli (Agulhon *et al.* 2008). These cells play an essen-

tial role in supporting neuronal activity and maintaining tissue homeostasis, such as water, ion and glutamate buffering (Phatnani and Maniatis 2015). Moreover, they are active players in the formation, maintenance and elimination of synapses (Chung and Barres 2012). In addition to contacts with neuronal synapses, astrocytes also establish contact sites with the CNS vasculature, enabling the uptake of important nutrients which can be further metabolized and delivered to neurons (Foo *et al.* 2011). Together, these astrocytic functions play a central role in neuronal survival, which in case of dysfunction contribute to the onset and progression of neurodegeneration processes (Wagner *et al.* 2006; Brenner *et al.* 2001).

Oligodendrocytes play a fundamental role in neuronal electrical signal transmission, producing a lipid-rich membrane termed myelin sheath that enwraps the axons. This acts as an electrical insulator by decreasing the capacitance and increasing the electrical resistance, enabling an efficient and rapid long distance signal transmission along axonal membrane (Allen and Barres 2009). Oligodendrocytes have been gaining more relevance during the last years with the discovery of other important roles in metabolic homeostasis and their interactions with astrocytes and neurons (Amaral *et al.* 2013). Deficiencies in these supportive metabolic functions and in axonal myelinization have been demonstrated to be related with axonal degeneration, resulting in disabilititating disorders as multiple sclerosis and sensorimotor neuropathies (Lee *et al.* 2012).

Microglia cells are the CNS resident immune cells, acting as the macrophages of the brain by targeting pathogens and removing cellular debris from cell turnover and injury sites (Allen and Barres 2009). These are also able to produce and secrete neurotrophic factors upon the activation of inflammatory processes or in case of injury, modulating neuronal growth and survival (Gomes *et al.* 2013; Nakajima *et al.* 2001). Also, several evidences place microglia cells as players contributing for the onset and progression of pathological conditions, such as Parkinson's and Alzheimer's diseases (Dheen *et al.* 2007; Kim and De Vellis 2005).

1.3. Available CNS Models

As abovementioned, neurological research has traditionally relied on animal models, with rodents being the most popular. These animals can be genetically engineered to either overexpress or silence a disease-related gene, being able to recapitulate features of human neurodegenerative disorders, such as Parkinson's and Alzheimer's diseases. Other non-genetic strategies consist in the administration of toxins that will induce brain lesions that can mimic to some extent the human disease phenotype. These models present the advantage of recapitulating a systemic tissue setting, however due

to its complexity accurate studies on cell-specific changes are often precluded. Moreover, most age-related neurological disorders are largely human-specific diseases, with most genetically engineered animal models being only able to partially recapitulate the complex features of these pathologies (Jucker 2010). Additionally, these models are not amenable for high throughput screening platforms, precluding its use in early stage drug development.

In vitro models allow for simpler and more efficient protocols for gene delivery and drug screening. One of the firstly established models for neuroscience research was achieved through the use of organotypic brain slices. This culture method preserves the *in situ* cellular organization and architecture, showing to be an interesting platform for the study of synaptic transmission and plasticity mechanisms (Gähwiler *et al.* 1997; Cho *et al.* 2007). Studies have been performed using both human and animal brain tissue, although the use of post-mortem human tissue poses serious limitations due to its scarce availability. These cultures present additional challenges, being technically highly demanding and variable. This arises in the difficulty of obtaining viable tissue slices in sterile conditions and transferring it to a culture vessel without compromising the tissue structure, which is the main advantage of these models (Walsh *et al.* 2005). These tissue slices are typically between 100 to 400 µm thick, being transferred into membrane inserts for *ex vivo* culture. Tissue thickness greatly affects cellular viability, due to nutrients and gases diffusion issues in thicker slices (Humpel 2015). Typically, brain slices obtained from postnatal donors at day 3-12 result in increased cell survival, being possible to maintain stable cultures up to several months (Marksteiner and Humpel 2008). However, these tissues often present immature neuronal phenotypes, since mature synapses are only established during week 2-3 *in vivo* (Cho *et al.* 2007). Adult donors could provide more mature biological material, however brain slices obtained from adult tissue are difficult to maintain longer than one week in culture, being unsuitable for long-term studies (Wilhelmi *et al.* 2002).

The *in vitro* culture of isolated cells or cell lines, although loosing the *in situ* tissue architecture information, can overcome the technical difficulties of organotypic cultures and the high complexity of *in vivo* models. Moreover, the available cell isolation and *in vitro* culture technologies allow to explore the use of human cell sources. Thus, these models can complement data from animal models bridging the gap between animal testing and human clinical trials (Crook and Kobayashi 2008; Imaizumi and Okano 2014). Furthermore, these can offer a renewable source of human neurons and glia to study human healthy or diseased central nervous system, providing new insights into the mechanisms underlying neurological pathogenesis. Different strategies have been explored for modeling disease phenotypes, namely through the exposure to

toxins, by genetic engineering or exploring patient-derived cell lines (Jakel *et al.* 2004; Imaizumi and Okano 2014).

1.3.1. Human Cell Sources for CNS *in vitro* models

The available human cell sources for *in vitro* cultures can be globally divided into three categories (Figure 1.3 and Table 1.1): (i) immortalized cell lines, which include cells from tumoral origin or by *in vitro* immortalization through transfection with oncogenes; (ii) primary cultures of neural stem cells (NSC), isolated from specific niches in fetal or adult brain tissue; (iii) pluripotent stem cells, including both embryonic and induced pluripotent stem cells (ESC and iPSC).

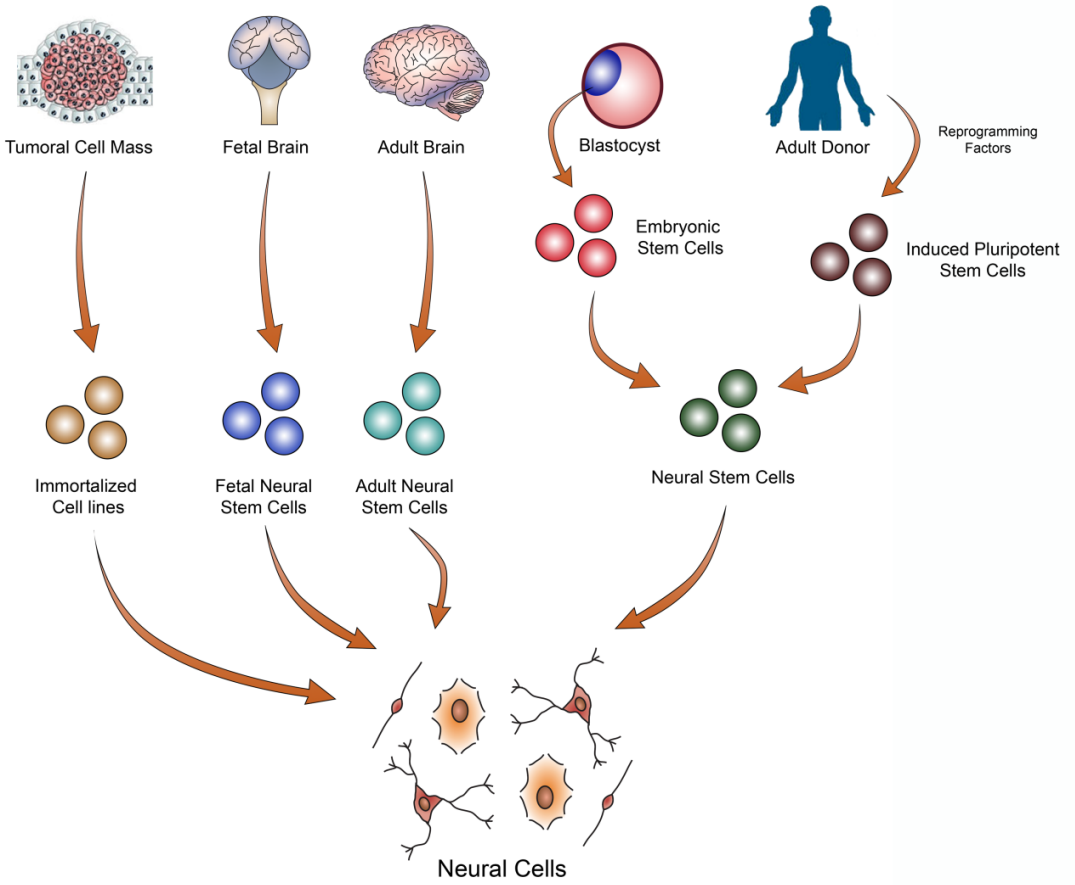

Figure 1.3 – Different stem cell sources available for the derivation of human neural cells. Immortalized cell lines are usually obtained from tumor cell masses presenting multipotent phenotypes, being responsive to neurogenic morphogens as retinoic acid. Neural stem cells can be isolated from fetal or adult brain tissue, retaining their self-renewal and multipotency abilities. Pluripotent stem cells, including embryonic stem cells and induced pluripotent stem cells, can be committed towards the neural lineage through neural induction protocols, giving rise to neural stem cell populations. Adapted from Jakel *et al.* (2004).

1.3.1.1. Immortalized Cell Lines

Immortalized cell lines have been one of the most common cell sources for modeling specific features of human brain, as well as neurodegeneration or neurotoxicity processes. Most of these cell lines present a tumoral origin, including the largely studied NTera-2 (NT2) cell line. This cell line was derived from a malignant embryonic carcinoma, conferring NT2 cells with many phenotypic characteristics of ESC and NSC (Pleasure and Lee 1993). These cells can be differentiated into neurons and astrocytes upon exposure to retinoic acid (RA). The differentiation protocols include prolonged and repeated RA treatments, which binds to different cell receptors, the RA receptor (RAR) and the retinoid X receptor (RXR). The RA signal transduction pathway modulates the transcriptional activity and contributes to cell growth arrestment by decreasing cyclin D1 levels (Spinella *et al.* 1999; Aranda *et al.* 2001). Downstream effects include the activation of neural developmental pathways, namely inducing the expression of transcription factors typically observed for dorsal/ventral forebrain, hindbrain and spinal cord regions development (Coyle *et al.* 2011). The resulting neurons express several mature markers, mostly comprising glutamatergic and GABAergic lineages, and display electrophysiological excitability. Also, astrocytic differentiation results in cells expressing phenotypic and functional markers, as the expression of glutamine synthase enzyme (Coyle *et al.* 2011; Hill *et al.* 2012; Podrygajlo *et al.* 2009). The high degree of differentiation and maturation attained with NT2-derived neural cells makes this a very interesting human cell source for modeling specific neural functions (Woehrling *et al.* 2015; Goodfellow *et al.* 2011) or neurotoxicity studies (Stern *et al.* 2014; Hill *et al.* 2008; Terrasso *et al.* 2015).

1.3.1.2. Primary Cultures of Neural Stem Cells

Neural stem cells can be isolated from adult and fetal brain tissue, retaining their inherent self-renewal ability and multipotency, being able to differentiate into the three neural lineages: neurons, astrocytes and oligodendrocytes (Conti and Cattaneo 2010). After tissue isolation, fetal and adult NSC can be selectively expanded *in vitro* using serum-free culture media supplemented with basic fibroblast growth factor (bFGF) and epidermal growth factor (EGF) (Reynolds and Weiss 1996; Reynolds *et al.* 1992; Storch *et al.* 2001). These growth factors are extracellular ligands of receptors that belong to the tyrosine kinase receptor family, namely EGFR and FGFR. Upon EGF/FGF receptor binding, a signal transduction pathway cascade is activated resulting in the activation of mitogen-activated protein kinase (MAPK). Activated MAPK is then translocated into the nucleus where it will phosphorylate and activate transcription factors responsible for triggering self-renewal pathways (Yamada *et al.* 2004; Annenkov 2014). Still,

these cells do not express high levels of telomerase, which is a requirement to maintain telomere length and continuous proliferation, leading therefore to senescence after some passages in culture (Ostenfeld *et al.* 2000). This is more evident for the case of NSC from adult origin, which despite overcoming the ethical concerns related with the use of fetal tissue, are typically harder to expand *in vitro* for long periods of time (Jakel *et al.* 2004). Additionally, the presence of NSC in adults is restricted to specific areas, such as the subventricular zone (SVZ), which makes this a scarcer cell source (Jakel *et al.* 2004; Zhao *et al.* 2008; Alvarez-Buylla *et al.* 2001). Together, these imply greater limitations for the use of NSC from adult origin in CNS *in vitro* modeling when compared with fetal-derived NSC. Immortalization of hNSC have also been explored to overcome the issue of long-term maintenance. This is the case of LUHMES cell line, which was transformed with the oncogene v-myc under the control of a tetracycline-controlled transactivator that activates the transcription from a minimal cytomegalovirus promoter (Lotharius *et al.* 2002).

NSC express several neural progenitor markers, such as the intermediate filament nestin and the transcription factors Pax6 and Sox2. NSC from fetal origin often express additional markers indicating its radial glia origin, such as GFAP or Glast (Solozobova *et al.* 2012). NSC isolated from fetal brain tissue can also differ in their phenotypic identity according to the time and region of isolation, following the developmental regionalization occurring during neurogenesis. As an example of NSC spatiotemporal identity, midbrain-derived precursor cells have been shown to present region-dependent commitment by preferentially generating dopaminergic neurons after *in vitro* differentiation (Storch *et al.* 2001).

1.3.1.3. Pluripotent Stem Cells

Human pluripotent stem cells (hPSC) include hESC derived from the inner cell mass of the blastocyst and hiPSC that are reprogrammed from somatic cells through the introduction of a set of pluripotency factors. hPSC can virtually be maintained in culture for indefinite periods of time without losing their intrinsic characteristics. This is considered to be one of the most important advantages in using these cells, since it can allow the establishment of industrial production platforms and standardization methods for generating human neural cells (Jiang *et al.* 2012). These cells enable the *in vitro* recapitulation of early developmental processes by differentiating into all three embryonic germ layers – exoderm, mesoderm and endoderm. Given this, hPSC have attracted great interest for *in vitro* modeling of healthy and disease-affected human tissues.

Multiple hESC lines have been established, which although presenting similar phenotypic features in their undifferentiated state, upon differentiation can reveal different propensity towards specific lineages. This can be traced to the fact that these cell lines have been generated under diverse culture conditions and from embryos with different genetic backgrounds. Examples of these include HSF1 line that preferentially generates forebrain neurons while HSF6 give rise to midbrain and hindbrain neurons (Wu *et al.* 2007). The somatic cell reprogramming into hiPSC was achieved by the induction of exogenous expression of four reprogramming factors: Oct4, Sox2, Klf4 and c-Myc (Takahashi *et al.* 2007). Much of the knowledge gathered for hESC research was applied in hiPSC culture and differentiation, accelerating its widespread implementation (Imaizumi and Okano 2014). The advent of hiPSC generation brought a number of advantages over the use of hESC, circumventing the ethical concerns of research based on tissue from embryonic origin (Jiang *et al.* 2012). Importantly, reprogramming methodologies enable the possibility of generating a renewable cell source of human neural cells carrying the genetic information of specific individuals. This is an interesting feature for *in vitro* modeling of human neurological diseases, through the use of patient-derived hiPSC. These cells can contribute for basic research on disease mechanisms as well as for development of new therapies (Telias and Ben-Yosef 2014; Srikanth and Young-Pearse 2014; Ooi *et al.* 2013; Kunkanjanawan *et al.* 2011).

Conventional differentiation protocols for hPSC include a first step of neural induction by promoting the differentiation in suspension cultures, through the formation of cellular aggregates termed embryoid bodies. A following period in stringent serum-free culture conditions allows the expansion of the neural progenitor cells. These cells will form characteristic rosette-like structures (Broccoli *et al.* 2014; Jiang *et al.* 2012; Cai and Grabel 2007; Wilson and Stice 2006). This recapitulates early neurogenesis architecture of cellular organization in the neural tube. Further exposure of these progenitors to specific morphogens, such as RA and Sonic Hedgehog (SHH), allows the directed differentiation towards the neural lineages of interest (Srikanth and Young-Pearse 2014). However, these approaches rely on poorly defined culture conditions and heterogeneous embryoid body formation, which typically results in low cell yields (Yap *et al.* 2015). Significant progress has been made in developing protocols for efficient hPSC neural differentiation under chemically defined conditions. The dual-SMAD inhibition protocol is an example of this trend, where two small molecules noggin and SB431542 are used as SMAD signaling pathways inhibitors. Noggin inhibits bone morphogenic protein (BMP) pathway, while SB431542 acts by blocking Lefty/activin/TGFβ signaling. This protocol bypasses the need for embryoid body formation, achieving efficiencies of neural differentiation above 80% (Chambers *et al.* 2009).

Table 1.1. Available human cell sources for development of CNS cell models and their advantages and disadvantages. Based on Hunsberger *et al.* (2015) and Jakel *et al.* (2004).

Cell Source	*Advantages*	*Disadvantages*
Immortalized cell lines	• Availability • Unlimited proliferation • Easy maintenance and manipulation • Reproducibility	• Low physiological relevance for disease modeling
Primary cultures of neural stem cells	• Already committed towards neural lineages • Physiological relevance	• Limited availability • Limited proliferation ability • Ethical concerns (fetal origin)
Pluripotent stem cells	• Availability • Unlimited proliferation • Not committed to specific lineages • Patient-derived cell source	• Complex and cumbersome differentiation protocols • Not specified as neural precursors • Ethical concerns (embryonic origin)

1.3.2. Culture Systems for development of Advanced CNS models

Conventional strategies for *in vitro* cultures of neural cells for drug screening and toxicology applications typically rely on monolayer systems (2D). These culture systems, despite their ease of implementation and utilization, preclude the establishment of more complex and physiologically-relevant cell-cell and cell-extracellular matrix (ECM) interactions that occur in the target tissues, essential to mimic important cellular functions (Breslin and O'Driscoll 2013; Hopkins *et al.* 2015) Advanced three-dimensional (3D) culture systems have shown to greatly differ from their 2D counterparts in several features, such as cell morphology, cell polarity and gene expression (Pampaloni *et al.* 2007). Engineered 3D constructs, in contrast with equivalent 2D cultures, have shown to sustain features of axonal branching reflecting morphological patterns observed *in vivo*, such as the development of unipolar neurons (Ribeiro *et al.* 2012). These morphological differences between 3D and 2D systems were demonstrated to be mediated by β1-integrin signaling via focal adhesion kinase (FAK), which have lower expression levels in neurons cultured in 3D (Ribeiro *et al.* 2013). Electrophysiological properties of *in vitro* neurons were also shown to differ when these are cultured as 3D or 2D networks, with 3D cultures demonstrating more complex and

heterogenous responses closer to what is observed for *in vivo* recordings (Frega *et al.* 2014). Importantly, differentiation of hNSC overexpressing disease-related mutated genes in a 3D setting have been shown to recapitulate key features of Alzheimer's disease, which have not been previously observed in mouse models (Choi *et al.* 2014). Given this, 3D systems can potentially improve the physiological relevance of cell-based assays, contributing to increase the predictive power of drug screening and toxicology platforms in preclinical research.

Multiple methods have been developed and implemented for 3D cell culture, although several challenges have still to be addressed in order to maximize the full potential of 3D cell models. These methods can be included in two main categories: (i) methods based on development of artificial scaffolds, exploring synthetic or natural biomaterials for matrix design; (ii) scaffold-free methods or cell spheroids.

The first category is based on the design and construction of artificial scaffolds to act as support for cell attachment and proliferation in a 3D architecture. These scaffolds can be constituted both by synthetic or biologically-derived materials, which present their own individual advantages and disadvantages according to the target application. Although some materials or scaffold architecture may present itself some passive differentiation stimuli towards the desired cell fate, biological active cues can also be incorporated in these scaffolds, in order to enhance the tissue formation (Drury and Mooney 2003). Two main approaches have been explored in the fabrication of tissue engineering applicable scaffolds, which include the encapsulation of the cells in the material during its processing or seeding the cells in a pre-formed porous scaffold. In the first strategy, the fabrication process must be cytocompatible and under mild conditions, which limits the available materials and formulations that can be applied in these approaches. The use of prefabricated scaffolds allows more harsh fabrication methods, as long as the final product is cytocompatible (Nicodemus and Bryant 2008). Both approaches have been applied for the generation of 3D neural constructs, being able to sustain neuronal differentiation and maturation into functional networks (Schmidt and Leach 2003; Willerth and Sakiyama-Elbert 2007; Irons *et al.* 2008). Moreover, more recent 3D bioprinting technologies have been explored to create complex and layered scaffolds that are able to sustain cell survival, proliferation and neural differentiation (Lozano *et al.* 2015; Hsieh *et al.* 2015). Nevertheless, these methods are often based on low cell densities and laborious scaffold fabrication, which can difficult the analysis of important biological readouts and decrease its applicability in high throughput screenings (Hopkins *et al.* 2015).

Cellular spheroids, taking advantage of the potential of some cell types to self-assemble into aggregates, do not require the design and fabrication of a artificial scaf-

folds to support cell growth and differentiation (Breslin and O'Driscoll 2013; Pampaloni *et al.* 2007; Hopkins *et al.* 2015). These spheroids can be generated using different methods (Figure 1.4), including static culture systems, such as low adherence culture surfaces and hanging-drop technologies, or dynamic culture systems, including shake flasks, spinner flasks, rotating wall vessels and stirred-tank bioreactors. The first option offers a simple and relatively inexpensive process, although presenting low mass transfer properties and low degree of control over culture variables. Low adherence surface cultures allow forcing cell aggregation even in cell types typically difficult to aggregate. This system does not allow a high degree of control over spheroid size, resulting in some cases in heterogeneous spheroids (Valamehr *et al.* 2008; Zhang *et al.* 2012; Ng *et al.* 2005). Still, this can be attenuated through the optimization of initial cell number and using multi-well plates for single spheroid generation per well. These strategies have shown to be able to sustain efficient neural differentiation of hPSC lines recapitulating phenotypic and transcriptional events of cortical development. These include polarization of neural progenitors and development of different layer-specific cortical neurons with transcriptional signatures typical of telencephalon brain region (Eiraku *et al.* 2008; Mariani *et al.* 2012). Hanging-drop techniques, despite being labor intensive and difficult to handle due to the small working volume, are amenable for automated platforms and high-throughput testing (Kelm *et al.* 2003; Timmins *et al.* 2004; Tung *et al.* 2011; Yoon *et al.* 2006). This system proved to be very effective for the generation of cell spheroids, still the inherent difficulty to maintain long-term cultures, precludes many applications. Therefore, most studies exploring hanging-drop methodology have used this mainly for initial neural induction of hPSC as spheroids over a period of 2-3 days, with posterior transfer to other culture systems (Baharvand *et al.* 2004; Ohnuki and Kurosawa 2013).

Agitation-based culture systems allow the generation of homogenous cultures, presenting improved mass transfer properties over static culture systems. These systems have been largely use for development of scalable expansion strategies of human stem cells, aiming at clinical cell therapy applications (Sen *et al.* 2002; Baghbaderani *et al.* 2008; Olmer *et al.* 2012). Agitation-based systems have proved to be also able to sustain efficient neuronal differentiation of stem cell spheroids, attaining increased neuronal differentiation efficiencies under shorter periods of time as compared to static 2D cultures (Serra *et al.* 2007). This system have been showed also to generate mature neurons, expressing typical neuronal-specific markers and synaptic activity, and astrocytes able to clear extracellular glutamate and converting it to glutamine (Terrasso *et al.* 2015). The scalable properties of this system allow the generation of large numbers of spheroids, which can be used to feed neurotoxicity testing platforms. However, on the

down side, agitation-based systems equipped with a stirrer (e.g. spinner-flasks, stirred-tank bioreactors) expose cells to shear forces that can adversely affect cell physiology. Also, specialized equipment is often required for these cultures, which in combination with higher working volumes as compared to static systems increases the overall costs (Breslin and O'Driscoll 2013).

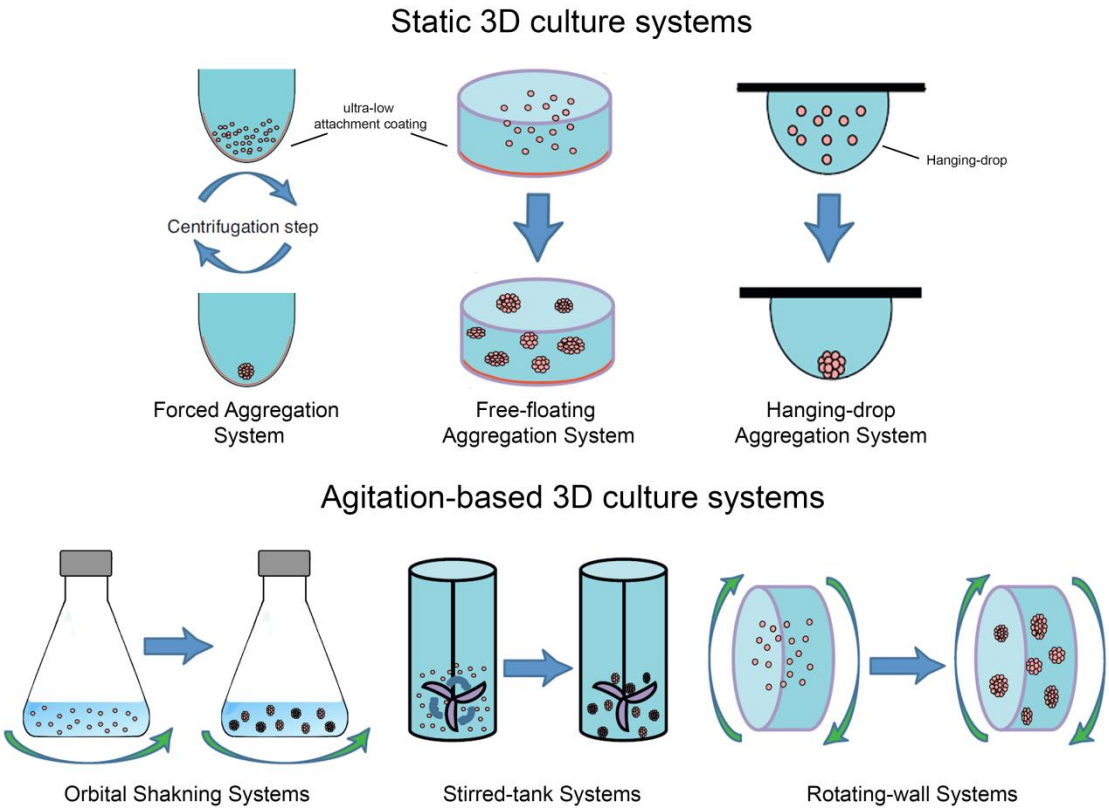

Figure 1.4 – Schematic representation of the different 3D culture systems available. Static culture systems include allow to induce cell aggregation based on centrifugal forces (forced aggregation system), gravity forces (hanging-drop aggregation system) or by preventing cell adhesion (free-floating aggregation system). Agitation-based culture systems maintain cells in suspension by orbital shaking, stirring systems or rotating-wall systems, which induces cell aggregation. Adapted from Breslin and O'Driscoll (2013).

Table 1.2. Available CNS models for neuroscience research and their advantages and disadvantages. Adapted from Breslin and O'Driscoll 2013; Hopkins *et al.* 2015.

	Advantages	*Disadvantages*
Animal Models	• Systemic context • Cellular organization and tissue architecture • Presence of immune system	• Interspecies differences • High variation between individuals • Low control over variables • Ethical concerns and limitations on animal usage
Organotypic Cultures	• Maintenance of cellular organization and tissue architecture • Possible to use human tissue • Contains all cell types of the tissue	• Scarcity of human tissue • Technically demanding • Difficult to maintain long-term viability and functionality • Low throughput
Monolayer cultures	• Inexpensive • Relatively simple • Suitable for high-throughput screening	• Low physiological relevance • Can require labor intensive plate-coating • Short-term cultures
Matrices and Scaffolds	• Provide 3D support for cell growth and differentiation • Tailor-made scaffolds • Incorporation of growth factors or morphogens	• Can be expensive for large-scale production • Can be difficult to retrieve cells from matrices • Difficult to monitor/sampling
Scaffold-free cell spheroids	• Provide 3D support for cell growth and differentiation • Do not require scaffold manufacturing • Cells secrete own ECM • Large-scale production (dynamic systems) • Agitation-based systems assist nutrient transport • Accessible and non-destructive sampling	• Cells exposed to shear stress • Dependent on cell ability to aggregate • Specialized equipment required (for agitation-based systems)

2. Stem Cell Bioprocessing and Cell Fate Determinants

Human stem cells offer unique challenges for successful implementation of robust bioprocesses, aiming at efficient cell expansion and differentiation towards the lineages of interest. The main hurdles in stem cell bioprocessing include the complex kinetics of typically heterogeneous starting cell populations, the transient state of subpopulations of interest and the interactions between different culture parameters, as the concentration of growth factors and other media components, dissolved oxygen, cell-cell interactions and mechanical cues (Serra *et al.* 2012; Rodrigues *et al.* 2011). Approaches to surpass and better understand these challenges include the implementation of integrated on-line measurements, which allow monitoring the culture state in terms of biomass, metabolic state and differentiation stage. Therefore, successful and efficient cultures are highly dependent on the development of well-defined and fully controlled bioprocess towards a specific culture outcome. In this context, agitation-based culture systems display significant advantages over static conditions, since these allow for a more homogeneous setting. Namely, culture performance can be optimized by the ability to implement systems to monitor and control important physical and chemical culture parameters, such as hydrodynamics (*e.g.* impeller type, agitation rate), pH, oxygen tensions or media composition (*e.g.* perfusion or fed-batch modes) (King and Miller 2007).

In culture, stem cells can either retain their identity by symmetric cell division, giving rise to two identical cells, or asymmetric division, which will give rise to one cell committed to differentiate towards a specific lineage. This is tightly associated with cell-cycle progression as well as with the integration of multiple external cues, ranging from mechanical signals to the presence of soluble factors that will trigger the activation of the genetic developmental programs (Figure 1.5) (Pauklin and Vallier 2013; Serra *et al.* 2012).

2.1. Soluble Factors

The presence of specific molecules in culture media, including growth factors and other morphogens, can switch on or off genetic circuits involved in cell survival, proliferation or differentiation. These can either be added externally or secreted by the cells. As mentioned above (section 1.3.1.2), for NSC proliferation the requirement of EGF and bFGF presence is well established (Reynolds and Weiss 1996; Reynolds *et al.* 1992; Storch *et al.* 2001). The increasing knowledge on the differentiation switches led to the development of improved protocols, mainly based on culture media supplementation with cocktails of several small molecules. These small molecules act on regulato-

ry pathways, such as Notch, SHH, RA, Wnt/β-catenin and TGFβ/BMP signaling, which will modulate cell fate decisions (Figure 1.6).

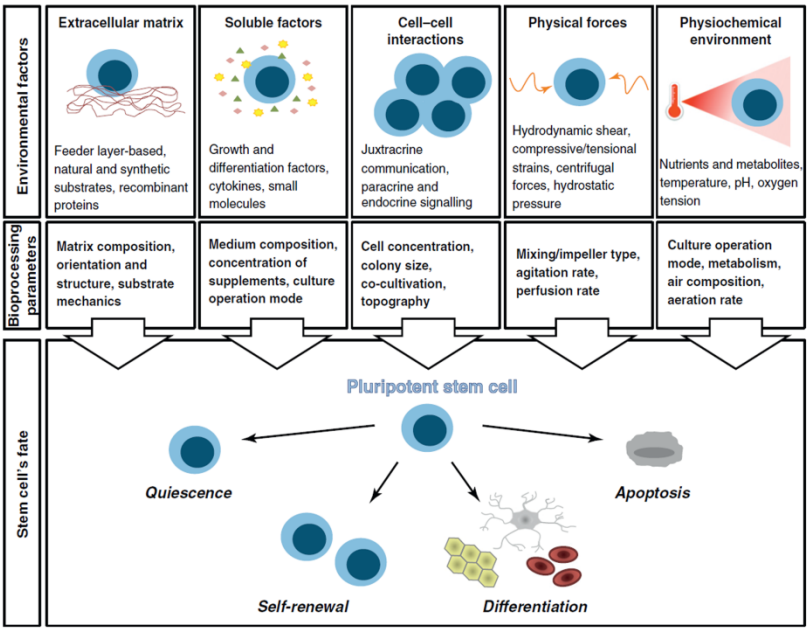

Figure 1.5 – Stem cell bioprocessing and cell fate determinants. Cell fate decisions are highly dependent on the integration and combination of different external parameters, including chemical, biologic and environmental factors that can be modulated during bioengineering processes. Adapted from Serra *et al.* (2012).

The activation of Notch signaling regulates the maintenance of neural progenitors, repressing progression of differentiation pathways. This acts through the binding of Delta or Jagged ligands to the Notch receptors, activating the expression of hairy/enhancer of split (Hes) genes. Hes genes in turn lead to the transcriptional repression of proneural genes, such as *Ngn* and *Ascl*, maintaining cells in a proliferative state (Shimojo *et al.* 2008). SHH signaling is activated by the binding of ligands, including SHH and purmorphamine, to the Patched receptors. This induces the activation of Gli transcription factors promoting symmetric proliferative divisions of progenitors. Still, SHH signaling is highly dependent on the concentration of SHH agonists, being able also to differentially modulate neuronal specification during differentiation (Paridaen and Huttner 2014; Mobassarah *et al.* 2014). RA promotes the activation of cyclic AMP response element-binding protein (CREB), by increasing the activity of c-Jun N-terminal kinase (JNK). Also it promotes the increase of Src kinase levels and phosphorylation of extracellular signal related kinase 1/2 (p-Erk 1/2), which in combination with CREB induce the transcription of proneural genes (Chuang 2015). Wnt/β-catenin signal transduction acts after binding of Wnt ligands to their Frizzled/LRP5/6

receptors. This stabilizes cytoplasmic β-catenin, which would be otherwise degraded by the proteasome system, enabling its translocation into the nucleus. Association of β-catenin in the nucleus with the LEF/TCF transcription factors will then exert its downstream effects on transcriptional activity. This pathway can also play dual roles in neurogenesis, by promoting progenitor self-renewal in early stages and inducing neuronal differentiation in later stages, through the upregulation of N-myc (Paridaen and Huttner 2014). TGFβ/BMP signaling activates SMAD proteins that are translocated to the nucleus, acting as transcription factors (Yun *et al.* 2008). Repression of these signaling pathways, as in the dual-SMAD protocol referred in section 1.3.1.3, can activate the neurogenic developmental pathways. The fact that these pathways can induce opposite effects, either promoting or inhibiting neural differentiation, is related with the complexity of the signaling networks and the cross-talk between the different pathways that will lead to different responses (Guo and Wang 2009).

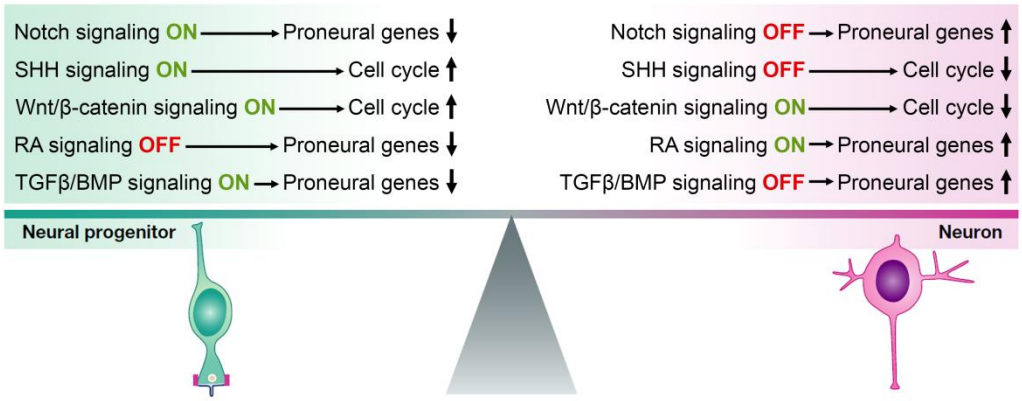

Figure 1.6 – Major signaling pathways regulating cell fate decisions. These pathways establish complex interplay connections that mediate the balance between progenitors self-renewal or neural differentiation. Adapted from Paridaen and Huttner (2014).

Media composition can be tailored for optimization and direct stem cell differentiation towards the lineages of interest. Examples of this include the derivation of dopaminergic neurons from hPSC through the dual-SMAD inhibition with noggin and SB431542 (Chambers *et al.* 2009), combining the Wnt activator CHIR99021 and SHH agonist purmorphamine (Kriks *et al.* 2011), or thorugh the sequential exposure to dual-SMAD inhibitors dorsomorphin and SB431542 followed by maturation with purmorphamine (Mak *et al.* 2012). Other lineages can be also targeted, as cholinergic motor neurons by combining RA treatments with purmorphamine (Hu and Zhang 2010; Li *et al.* 2008).

Nevertheless, further improvements in efficiency and control of the differentiation can be achieved by continuous characterization of small molecules and their down-

stream targets. The main challenge in optimizing media composition for stem cell differentiation lies on the presence of multiple cell types, which compete differently for the several cytokines. This has often relied on empirical experimentation, highlighting the need for more rational-oriented methods. The development of computational models of relevant cell fate signaling pathways can provide ligand delivery regimen predictions for directing stem cell fate, based on knowledge of intracellular signaling pathway kinetics (Mahdavi *et al.* 2007). Also, approaches enabling the high-throughput testing of different combinations of differentiation factors have been explored, contributing to accelerate and optimize the development of directed hPSC differentiation protocols (Nazareth *et al.* 2013).

2.2. Extracellular matrix (ECM) Composition

The composition of ECM has been shown to regulate proliferation, survival, proliferation, migration and neurite outgrowth in NSC. This is regulated at integrin-signaling level, mainly by interaction of integrin α6β1 that binds to laminin. Laminin-rich substrates have been shown to promote greater hESC-derived NSC neuronal differentiation and neurite outgrowth, as compared with other ECM components as fibronectin, poly-D-lysine and collagen I (Ma *et al.* 2008). Moreover, enrichment of poly-D-lysine or collagen I/IV substrates with laminin or heparin sulfate was found to promote neuronal differentiation, while poly-D-lysine alone mostly supported glial differentiation (Raghavan *et al.* 2013). Different scaffolds of biomaterials from synthetic or natural origin have also been studied for driving neural cell fate, including hydrogels, microfibrous and nanofibrous matrices. Small diameter poly-ε-caprolactone (PCL) loop mesh scaffolds functionalized with RA, were shown to promote and increase neural commitment of hiPSC into neural progenitors, as compared with other PCL scaffold topographies (Mohtaram *et al.* 2014). Natural biopolymers as chitosan can be further engineered to improve its properties, as the fabrication of fluorinated methacrylamide chitosan (MACF) hydrogels, which have shown higher oxygen diffusion properties than non fluorinated versions. These improved MACF hydrogels showed to be able to increase the neuronal differentiation efficiency of NSC, as compared with non fluorinated scaffolds (Li *et al.* 2014).

2.3. Physical Forces

Mechanical properties of ECM, such as geometry, stiffness or elasticity affect cell shape and morphology by altering the cell adhesion interactions. The transduction of these mechanical factors results in signal transduction events, which will regulate cell differentiation (Guilak *et al.* 2009). These interactions are proposed to be sensed at

membrane integrins level after cell contraction, following signal transduction through cytoskeletal actin and myosin filaments contractility, resulting in an accumulation of additional molecules at the contraction sites. These include mainly an increase in Rho GTPase and MAP kinase activity, which will modulate gene expression and consequently cell fate (Vogel and Sheetz 2006; Paszek *et al.* 2005; Ingber 2006). Artificial biomaterials can be custom-engineered to mimic the natural ECM mechanical properties, favoring cell differentiation towards the tissue of interest. This was shown for mesenchymal stem cell differentiation, where soft matrices that mimic the elasticity and compliance of brain tissue could direct cell fate towards the neuronal phenotype, while intermediate stiffness resulted in myoblast differentiation and high stiffness in osteoblasts (Engler *et al.* 2006). These scaffolds can be further tailored by the inclusion of cell adhesion domains (e.g. RGD domains), which will result in a synergistic effect further potentiating cell differentiation towards the lineage of interest (Even-Ram *et al.* 2006; Guilak *et al.* 2009; Lutolf *et al.* 2009). The functionalization of 3D networks of nanofibers formed by self-assembly of peptide amphiphilic molecules with laminin epitope IKVAV showed to sustain rapid differentiation of NSC towards neuronal lineages, discouraging the differentiation to other cell lineages (Silva *et al.* 2004). The combinatorial effect of polyethylene glycol (PEG) hydrogel functionalized with RGD domains and tenascin C has shown to be able to promote and enhance NSC survival and differentiation, as in comparison with PEG-RGD hydrogel alone (Hadjizadeh and Doillon 2010).

2.4. Physicochemical Environment

In addition to the molecular composition and mechanical properties of the cellular microenvironment, physicochemical parameters as pH, dissolved oxygen and temperature can greatly affect the outcome of the differentiation processes. Metabolic activity results in the accumulation of by-products that lead to acidification of the culture media. Low pH has been associated with cell growth arrest and loss of cellular viability in NSC cultures, demonstrating the importance of monitoring and controlling this parameter (Kallos and Behie 1999). Dissolved oxygen has also been shown to have significant influence on determining cell fate. Culture conditions with physiological levels of oxygen (2-5%), versus 21% of atmospheric oxygen, have shown to greatly contribute to improve NSC self-renewal, differentiation and neuronal maturation (Shin *et al.* 2012; Studer *et al.* 2000; Sun *et al.* 2015; Milosevic *et al.* 2005). The influence of low oxygen tensions appears to play a particularly important role in promoting dopaminergic differentiation. Although the underlying mechanisms are not completely understood, this has been shown to be related with the stabilization/activation of hypoxia-inducible

factor 1 (HIF-1), which leads to the upregulation of erythropoietin (EPO), vascular endothelial growth factor (VEGF) and the cell cycle regulator p21, while decreasing the expression of cyclin D1 (Vieira *et al.* 2011).

Additional factors are also proposed to play an important role in regulating NSC self-renewal and differentiation, namely energy metabolism (Rafalski and Brunet 2011) and epigenetic mechanisms (Lunyak and Rosenfeld 2008; Hsieh and Gage 2004).

3. Cellular Characterization Toolbox for 3D Cell Models

3D *in vitro* models can unarguably provide a setting of increased physiological relevance for cell-based assays, relatively do 2D culture systems. Still, these models have to be validated not only in terms of phenotypic features but also in functionality, demonstrating its ability to mimic key properties of the target tissue. Therefore, for maximizing the potential of such models and to be able to extract relevant data, robust and sensitive characterization methods and assays have to be implemented for these cultures. Many of these methodologies have been adapted from configurations optimized for 2D cultures. Due to the higher biological complexity of 3D tissue-like structures, this translation offers several technical and biological challenges that differ according to the readout in analysis. Due to the importance of the 3D structure for cell functionality, development of analytical methodologies that can provide and preserve spatial resolution data of intact cell aggregates are preferable. Alternatively, protocols for spheroid dissociation have been developed, allowing following assays to be performed on 2D settings. These protocols have been applied for a wide range of spheroids of different cell types, including neural stem cells and tumoral cells (Lin *et al.* 2013; Qiu *et al.* 2015; Sen *et al.* 2004; Ho *et al.* 2012); however differentiated neurospheres present highly complex neurite networks, which compromise the recovery of high cell yields with high viability after dissociation. Moreover, comparisons between mechanical dissociation strategies and approaches where intact neurospheres are plated, allowing cells to migrate along the culture surface, have shown that the later attains significantly higher neuronal survival (Caldwell *et al.* 2001).

3.1. Image-based Phenotypic Assays

As the traditional wide-field fluorescence microscopes do not allow accurate imaging of spheroids, mainly due to the thickness and low transparency of these structures, several imaging modalities have been developed in order to allow the analysis of intact cell aggregates. Confocal imaging has been the most widely used modality for spheroid imaging, allowing good signal-to-noise ratio, optical sectioning capability and good spatial resolution. Still, confocal imaging also offers limited sample penetration

depth, which precludes its use for *in toto* studies of thick 3D samples. Further shortcomings of confocal imaging, despite being eased on spinning disk confocal technologies, include photobleaching/phototoxic effects and low image recording rate, posing significant challenges for implementation of live assays (Pampaloni *et al.* 2013).

Multiphoton imaging offers an attractive alternative mainly due to a significant increase in penetration depth, in comparison with confocal microscopy (Masters *et al.* 1997; Centonze and White 1998; Gilbert *et al.* 2000). This is related to the use of near-infrared excitation light sources that have lower tissue absortion and scattering coefficients, allowing the collection of data from deep sites with minimal phototoxicity and low signal-to-noise ratio. Given this, multi-photon has been largely implemented as imaging modality of choice for spheroid analyses (Andresen *et al.* 2009). Other attractive feature of multiphoton microscopy is the ability to perform marker-free imaging based on molecules autofluorescence, including the analysis of NAD(P)H, flavoproteins or collagen content that can be correlated with stem cell differentiation (König *et al.* 2011; Uchugonova and König 2013).

More recently, light-sheet-based fluorescence microscopy (LSFM) has emerged as state-of-the art imaging modality for large 3D samples (Pampaloni *et al.* 2007; Pampaloni *et al.* 2013; Bruns 2012; Stelzer 2015). This technology illuminates the sample only in one plane through a thin light-sheet and collects the emitted light at a perpendicular axis, allowing a good penetration depth. This lowers the energy required for illuminating the sample in comparison with confocal microscopy, significantly decreasing phototoxicity and bleaching issues. Moreover, depending on the setting it is possible to rotate the sample, acquiring data from different angles that can be later processed in a multi-view fusion increasing the in-depth resolution of the final projection. Given these properties and high speed recording, LSFM has been widely used to follow embryonic development and to record whole-brain activity of animal models, such as *Drosophila* or zebra fish. For cell spheroid imaging, LSFM has also been explored for long-term live assays, including monitoring cell division in tumor spheroids (Lorenzo *et al.* 2011).

Electron microscopy has been also largely employed for the characterization of 3D cell models, largely surpassing optical imaging in terms of resolution (Ma *et al.* 2012; Hess *et al.* 2010; No *et al.* 2012; Bez *et al.* 2003). Transmission electron microscopy (TEM), although involving laborious sample preparation, enables a high subcellular imaging resolution. Therefore, TEM data can provide important morphological insights, for instance when analyzing neurodegeneration signs in neurodegenerative disease cell models (Choi *et al.* 2013). Scanning electron microscopy (SEM) allows for topographical imaging of the spheroids, providing data on cellular organiza-

tion/architecture and on the development of specific structures, such as synaptic sites (Irons *et al.* 2008; LaPlaca *et al.* 2010).

Simple readouts as morphological analysis can be extracted from imaging data, aiding the characterization of 3D neural models and the analyses of the effects of specific drugs or other biopharmaceuticals. These morphological analyses have been used for instance to understand the influence of the microenvironment on cell growth, neurite extension and cell branching. Reported data revealed significant differences on neurite extension in 2D and 3D substrates, with neurons responding differently to specific cell adhesion cues (Blewitt and Willits 2007; Kofron *et al.* 2009). Several studies focused on the influence of scaffold mechanical properties on neuronal growth (Flanagan *et al.* 2002; Willits and Skornia 2004; Balgude *et al.* 2001). Neurite extension analysis have also been used for the development and characterization of 3D *in vitro* models of peripheral nerves, which are based on scaffold design to sustain cell alignment (Daud *et al.* 2012; East *et al.* 2010). Morphological features as number of neuritis per neuron and total neurite length can also provide relevant readouts in toxicology, as neurite degeneration is one of the most visible symptoms of neurotoxicity (Robinette *et al.* 2011).

3.2. Cell Functional Assays

In addition to morphological and phenotypic characterizations, evaluation of neuronal functionality is imperative to confirm the presence of mature neurons in culture. Neuronal functionality is most accurately measured through electrophysiological methodologies, which can be complemented with other assays such as fluorescence-based probes. Neurons typically present polarized cell membranes with a resting potential between -80 and -55 mV. This membrane potential is mainly modulated by the open and close of ionic potassium and sodium channels, which are gated by voltage, neurotransmitters and second messengers. Upon a depolarizing stimulus, an action potential can be elicited through a brief sodium influx followed by activation of voltage-dependent potassium efflux (Rutecki 1992). These changes in membrane currents can be recorded using methodologies such as voltage-clamp or patch clamp, which provides increased resolution in single channel or whole-cell recordings (Halliwell and Adams 1982; Hamill *et al.* 1981).

These are laborious methods that require the use of invasive microelectrodes, which are limited to individual neurons. Also, voltage or patch clamp techniques are dependent on sample optical clarity for the correct electrode placement, which can be problematic for 3D cell cultures. Nevertheless, these methodologies have been successfully implemented for the characterization of neuronal excitability in 3D neural con-

structs (Xu *et al.* 2009; Irons *et al.* 2008). Other tools have also became available for electrophysiological analysis as the micro-electrode arrays (MEA) that can non-invasively analyze multiple cells along culture time without compromising neuronal membrane integrity (Spira and Hai 2013). This methodology have also been explored for evaluation of neuronal functionality in 3D *in vitro* structures, for recordings of spontaneous activity, response to neurotoxins and to model mechanical injuries (Tang-Schomer *et al.* 2014; Dubois-Dauphin *et al.* 2010; Frega *et al.* 2014).

Alternative methods for analyzing neural functionality include image-based assays through the use of fluorescence dyes. Synaptic activity can be analyzed by the use of the FM family of fluorescent dyes. These dyes can be loaded into synaptic vesicles, which will be released through neuronal excitation following depolarizing stimuli. The release of fluorescently labeled synaptic vesicles can be then imaged in time-lapse setting, allowing the quantification of the vesicle release rate (Gaffield and Betz 2006). Calcium signaling also plays a major role in neuronal functionality, with fast calcium influx being observed following membrane depolarization, triggering synaptic vesicle exocitosys. These calcium transients can be imaged using also fluorescent calcium indicators, such as Fluo-4 or Fura-2 that increase its fluorescent signal in presence of calcium ions, providing indirect measurements of neuronal functionality (Grienberger and Konnerth 2012). All these image-based assays can be potentiated in 3D settings by exploring more advanced imaging modalities, such as multi-photon imaging and LSFM that were previously discussed.

3.3. Gene Expression and Protein Analysis

Other methodologies, namely transcriptomic and proteomic technologies, have been applied to the characterization of 3D cell cultures. These methodologies involve the complete cell dissociation and lysis to harvest the intracellular compartment. Although loosing the 3D spatial information, these methodologies provide sensitive and quantitative platforms, for instance to quantify the expression and content in specific cell markers.

Global gene expression analyses have been performed to study the influence of specific parameters on gene expression profile. This provides important insights on cell processes, as proliferation, survival and differentiation. Such analyses have been used to study the impact of a 3D setting on gene expression profile and identity of stem cells, tumoral cells and epithelial cells, highlighting the specific pathways specifically modulated on 3D culture systems (Bartosh *et al.* 2010; Kim *et al.* 2012; Lawrenson *et al.* 2013; Cody *et al.* 2008). NSC cultured as neurospheres or in 3D scaffolds have also demonstrated upregulation of specific cytokines involved in processes as angiogenesis

and terminal neural differentiation, as compared with monolayer cultures (Lai *et al.* 2011). Proteomic tools can also aid these analyses in 3D systems, as it has been demonstrated for tumor spheroids that further stressed the physiological differences between 2D and 3D cultures, namely the enrichment of the later in proteins related with tumor cell proliferation, survival and chemoresistance (He *et al.* 2014; Kumar *et al.* 2008; Gaedtke *et al.* 2007).

Aiming to overcome the lack of spatial information, further efforts are ongoing to push these technologies towards spatially resolved omics tools (Crosetto *et al.* 2014), which include novel technologies such as the single-molecule RNA fluorescence *in situ* hybridization (smFISH) for gene expression analysis (Lubeck and Cai 2012; Hansen and van Oudenaarden 2013) or imaging mass spectrometry (Ahlf *et al.* 2014) and imaging mass cytometry (Giesen *et al.* 2014; Angelo *et al.* 2014) for proteomic interrogation.

3.4. Cell Metabolism Analysis

Cell metabolism has been for long applied as readout for cell-based assays or to study and understand fundamental cellular mechanisms. Study of neural metabolism is particularly relevant, since differences in the diverse neural cell types include specialized metabolic features and establishment of intercellular metabolic shuttles that in case of deregulation often result in pathological conditions (Bélanger *et al.* 2011).

Strategies for metabolic analyses may focus only on one compartment or both extra- and intracellular compartments. Methods for metabolite quantification include targeted methodologies, mostly based on enzymatic assays, or non-targeted methologies, namely nuclear magnetic resonance (NMR) spectroscopy and mass spectrometry (MS). The later are powerful technologies that allow to obtain a snapshot of cell metabolome, enabling the identification of most highly active pathways. NMR spectroscopy is a non-destructive methodology, with few sample preparation requirements. Moreover it can be combined with the use ^{13}C-labeled compounds since it has a highly chemical specificity, due to its ability to distinguish isotope incorporation in different molecules and also in specific positions in the same molecule (isotopomers). This enables to study the metabolic pathways followed by the ^{13}C-labeled substrates, providing important insights on the cell metabolic activity. Nevertheless, NMR presents as main disadvantage its low sensitivity in comparison with other technologies, such as MS (Rodrigues *et al.* 2009).

NMR has been widely used for metabolic profiling of mammalian cell cultures (Carinhas *et al.* 2013; Goudar *et al.* 2010; Wagstaff *et al.* 2013). Also, it has provided important data on the characterization of neural cell metabolism in 3D cultures (Sá Santos

et al. 2011; Santos *et al.* 2007). MS techniques have been also employed for neural metabolism due to its high sensitivity, although it cannot distinguish which ^{13}C-labeling between the different carbon positions in the same molecule, providing only the number of labeled atoms per molecule (Ando and Tanaka 2005). Since for MS analysis samples have to be derivatized, this confers a destructive character to these methodologies, since the samples are disintegrated during analysis (Halket *et al.* 2005). NMR spectroscopy and MS methodologies can also be combined providing data that can be used to estimate the metabolic fluxes, which can then be further processed to generate metabolic models of the different neural cell types (Amaral *et al.* 2010; Amaral *et al.* 2011).

4. Aims and Scope of Thesis

The use of advanced human cell models, being able to sustain more predictive preclinical cell based assays, are interesting platforms for the development and preclinical evaluation of novel therapeutics. The main goal of this thesis was the development of a novel human *in vitro* CNS model, which could recapitulate key phenotypic and functional features of human brain tissue. This was pursued by the integration of agitation-based culture systems, to promote cellular aggregation, and the use of human NSC as cell source. The strategy of NSC differentiation as spheroids was developed aiming at the establishment of complex 3D networks of cell-cell and cell-ECM interactions, mimicking the cellular organization of brain tissue. In parallel, a wide range of characterization methods, including imaging, transcriptomic, metabolic and functional tools were implemented, enabling to understand the changes during differentiation at different levels in 3D cultures.

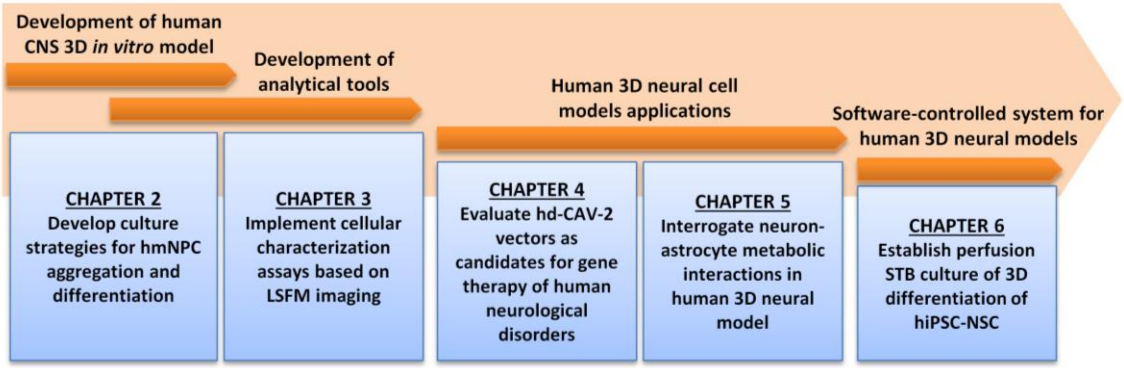

Figure 1.7 – Schematic representation of the major aims of this thesis and its discrimination according to the different chapters. CNS – central nervous system; hmNPC – human midbrain-derived neural precursor cells; LSFM – light-sheet fluorescence microscopy; hd-CAV-2 – helper-dependent canine adenovirus vectors type 2; STB – stirred-tank bioreactors; hiPSC-NSC – neural stem cells derived from human induced pluripotent stem cells.

The development of a culture system able to sustain the aggregation and 3D differentiation of human midbrain-derived neural progenitor cells from fetal origin (hmNPC) is described in **chapter 2**. Differentiation efficiency was evaluated at different levels, exploring a wide range of phenotypic and functional characterization methods. The results showed the correct activation of midbrain developmental programs, with increased expression of mature neuronal markers and functional properties (synaptic and electrophysiological functions).

Given the need for technical development of cellular characterization tools and assays with high spatial resolution for 3D cell aggregates, **chapter 3** focused on the implementation of LSFM technology for image-based characterization of hmNPC differentiated neurospheres. The potential of the LSFM setting was evaluate both for fixed samples, in immunostained neurospheres, and live samples, for functional analysis, such as calcium imaging or viability assays.

The human 3D *in vitro* CNS model developed was explored in **chapter 4** for the evaluation of a novel viral vector as candidate for gene therapy strategies. Here, the efficacy and safety of third generation or helper-dependent canine adenovirus type 2 vectors (hd-CAV-2) for neuronal gene delivery was evaluated in a 3D human context. The obtained results demonstrated efficient transgene expression following hd-CAV-2 transduction, with minimal toxic effects. Additionally, hd-CAV-2 demonstrated to be able to preferentially transduce human neurons and low glia transduction, while vectors derived from human adenovirus type 5 (HAdV5) showed increased glia transduction.

In **chapter 5**, the potential of human CNS cell models to mimic human brain tissue functions and cell-cell interactions was further assessed. Here, a previously established 3D cell model based on neural differentiation of NT2 cells (Terrasso 2015) was used to analyze specific neural metabolic pathways. For this, strategies based on the use of ^{13}C-labeled metabolic substrates were explored, allowing the detection of typical metabolic features and neuron-glia shuttles described for murine neural cells. Furthermore, as proof-of-concept this approach was used for toxicological analysis on the effects of two well-described compounds. This highlights the potential of metabolic analysis in toxicology field to uncover the specific pathways or cell types affected by the molecules of interest.

Chapter 6 focused on transferring the knowledge and strategies described in the previous chapters for the implementation of a scalable and robust platform for the 3D differentiation of human NSC derived from hiPSC. For this, software-controlled perfusion stirred-tank bioreactors were explored, which provide a high degree of control

over the culture physico-chemical environment, increasing the process reproducibility. Neuronal and glia differentiation was assessed and confirmed both phenotipically and functionally. This provides the basis for studies with patient-derived cells for the development of more accurate *in vitro* human disease models in a scalable system, which can feed high throughput screening platforms in preclinical research.

The results obtained in this thesis were discussed in **chapter 7**, contextualizing the findings with the available literature and state-of-the-art for the fields addressed throughout the previous chapters.

5. References

Agulhon C., Petravicz J., McMullen A. B., Sweger E. J., Minton S. K., Taves S. R., Casper K. B., Fiacco T. a., McCarthy K. D. (2008) What Is the Role of Astrocyte Calcium in Neurophysiology? *Neuron* **59**, 932–946.

Ahlf D. R., Masyuko R. N., Hummon A. B., Bohn P. W. (2014) Correlated mass spectrometry imaging and confocal Raman microscopy for studies of three-dimensional cell culture sections. *Analyst* **139**, 4578–85.

Allen N. J. (2014) Astrocyte Regulation of Synaptic Behavior. *Annu. Rev. Cell Dev. Biol.* **30**, 439–463.

Allen N. J., Barres B. a (2009) Neuroscience: Glia - more than just brain glue. *Nature* **457**, 675–677.

Alvarez-Buylla a, García-Verdugo J. M., Tramontin a D. (2001) A unified hypothesis on the lineage of neural stem cells. *Nat. Rev. Neurosci.* **2**, 287–293.

Alzheimer's Disease International (2010) World Alzheimer Report 2010. *Alzheimer's Dis. Int. (ADI).*

Amaral A. I., Meisingset T. W., Kotter M. R., Sonnewald U. (2013) Metabolic aspects of neuron-oligodendrocyte-astrocyte interactions. *Front. Endocrinol. (Lausanne).* **4**, 54.

Amaral A. I., Teixeira A. P., Håkonsen B. I., Sonnewald U., Alves P. M. (2011) A comprehensive metabolic profile of cultured astrocytes using isotopic transient metabolic flux analysis and C-labeled glucose. *Front. Neuroenergetics* **3**, 5.

Amaral A. I., Teixeira A. P., Martens S., Bernal V., Sousa M. F. Q., Alves P. M. (2010) Metabolic alterations induced by ischemia in primary cultures of astrocytes: Merging 13C NMR spectroscopy and metabolic flux analysis. *J. Neurochem.* **113**, 735–748.

Ando S., Tanaka Y. (2005) Mass spectrometric studies on brain metabolism, using stable isotopes. *Mass Spectrom. Rev.* **24**, 865–886.

Andresen V., Alexander S., Heupel W. M., Hirschberg M., Hoffman R. M., Friedl P. (2009) Infrared multiphoton microscopy: subcellular-resolved deep tissue imaging. *Curr. Opin. Biotechnol.* **20**, 54–62.

Angelo M., Bendall S. C., Finck R., Hale M. B., Hitzman C., Borowsky A. D., Levenson R. M., *et al.* (2014) Multiplexed ion beam imaging of human breast tumors. *Nat. Med.* **20**, 436–42.

Annenkov A. (2014) Receptor tyrosine kinase (RTK) signalling in the control of neural stem and progenitor cell (NSPC) development. *Mol. Neurobiol.* **49**, 440–471.

Aranda a, Aranda a, Pascual a, Pascual a (2001) Nuclear hormone receptors and gene expression. *Physiol. Rev.* **81**, 1269–304.

Azevedo F. a C., Carvalho L. R. B., Grinberg L. T., Farfel J. M., Ferretti R. E. L., Leite R. E. P., Filho W. J., Lent R., Herculano-Houzel S. (2009) Equal numbers of neuronal and nonneuronal cells make the human brain an isometrically scaled-up primate brain. *J. Comp. Neurol.* **513**, 532–541.

Baghbaderani B. A., Behie L. A., Sen A., Tn C., Mukhida K., Hong M., Mendez I. (2008) Expansion of Human Neural Precursor Cells in Large-Scale Bioreactors for the Treatment of Neurodegenerative Disorders. *Biotechnol. Prog.* **24**, 859–870.

Baharvand H., Power J. M., Ozsarac N., Matthaei K. I. (2004) Differentiation of embryonic stem cells into functional neurons *in vitro*. *Neurosci. Res. Commun.* **35**, 130–138.

Balgude a. P., Yu X., Szymanski a., Bellamkonda R. V. (2001) Agarose gel stiffness determines rate of DRG neurite extension in 3D cultures. *Biomaterials* **22**, 1077–1084.

Bartosh T. J., Ylöstalo J. H., Mohammadipoor A., Bazhanov N., Coble K., Claypool K., Lee R. H., Choi H., Prockop D. J. (2010) Aggregation of human mesenchymal stromal cells (MSCs) into 3D spheroids enhances their antiin fl ammatory properties. *Proc. Natl. Acad. Sci. U. S. A.* **107**, 13724–13729.

Begley C. G., Ellis L. M. (2012) Drug development: Raise standards for preclinical cancer research. *Nature* **483**, 531–533.

Bélanger M., Allaman I., Magistretti P. J. (2011) Brain energy metabolism: Focus on Astrocyte-neuron metabolic cooperation. *Cell Metab.* **14**, 724–738.

Ben-Nun I. F., Benvenisty N. (2006) Human embryonic stem cells as a cellular model for human disorders. *Mol Cell Endocrinol* **252**, 154–159.

Bez A., Corsini E., Curti D., Biggiogera M., Colombo A., Nicosia R. F., Pagano S. F., Parati E. A. (2003) Neurosphere and neurosphere-forming cells: Morphological and ultrastructural characterization. *Brain Res.* **993**, 18–29.

Blewitt M. J., Willits R. K. (2007) The effect of soluble peptide sequences on neurite extension on 2D collagen substrates and within 3D collagen gels. *Ann. Biomed. Eng.* **35**, 2159–2167.

Brenner M., Johnson a B., Boespflug-Tanguy O., Rodriguez D., Goldman J. E., Messing a (2001) Mutations in GFAP, encoding glial fibrillary acidic protein, are associated with Alexander disease. *Nat. Genet.* **27**, 117–120.

Breslin S., O'Driscoll L. (2013) Three-dimensional cell culture: The missing link in drug discovery. *Drug Discov. Today* **18**, 240–249.

Broccoli V., Giannelli S. G., Mazzara P. G. (2014) Modeling physiological and pathological human neurogenesis in the dish. *Front. Neurosci.* **8**, 183.

Brodal P. (2010) *The Central Nervous System: Structure and Function*. Oxford University Press.

Bruns T. (2012) Preparation strategy and illumination of three-dimensional cell cultures in light sheet–based fluorescence microscopy. *J. Biomed. Opt.* **17**, 101518.

Byrne J., Byrne J. H., Roberts J. L. (2009) *From Molecules to Networks: An Introduction to Cellular and Molecular Neuroscience*. Academic Press.

Cai C., Grabel L. (2007) Directing the differentiation of embryonic stem cells to neural stem cells. *Dev. Dyn.* **236**, 3255–3266.

Calcoen D., Elias L., Yu X. (2015) What does it take to produce a breakthrough drug? *Nat. Rev. Drug Discov.* **14**, 161–162.

Caldwell M. a, He X., Wilkie N., Pollack S., Marshall G., Wafford K. a, Svendsen C. N. (2001) Growth factors regulate the survival and fate of cells derived from human neurospheres. *Nat. Biotechnol.* **19**, 475–479.

Carinhas N., Duarte T. M., Barreiro L. C., Carrondo M. J. T., Alves P. M., Teixeira A. P. (2013) Metabolic signatures of GS-CHO cell clones associated with butyrate treatment and culture phase transition. *Biotechnol. Bioeng.* **110**, 3244–3257.

Centonze V. E., White J. G. (1998) Multiphoton excitation provides optical sections from deeper within scattering specimens than confocal imaging. *Biophys. J.* **75**, 2015–2024.

Chambers S. M., Fasano C. a, Papapetrou E. P., Tomishima M., Sadelain M., Studer L. (2009) Highly efficient neural conversion of human ES and iPS cells by dual inhibition of SMAD signaling. *Nat. Biotechnol.* **27**, 275–280.

Cho S., Wood A., Bowlby M. R. (2007) Brain slices as models for neurodegenerative disease and screening platforms to identify novel therapeutics. *Curr. Neuropharmacol.* **5**, 19–33.

Choi S., Kim Y., Hebisch M., Sliwinski C., Lee S., D'Avanzo C., Chen H., *et al.* (2014) A three-dimensional human neural cell culture model of Alzheimer's disease. *Nature* **515**, 274–278.

Choi Y. J., Park J., Lee S. H. (2013) Size-controllable networked neurospheres as a 3D neuronal tissue model for Alzheimer's disease studies. *Biomaterials* **34**, 2938–2946.

Chuang J.-H. (2015) Neural differentiation from embryonic stem cells *in vitro* : An overview of the signaling pathways. *World J. Stem Cells* **7**, 437.

Chung W. S., Barres B. a. (2012) The role of glial cells in synapse elimination. *Curr. Opin. Neurobiol.* **22**, 438–445.

Cody N. Al, Zietarska M., Filali-Mouhim A., Provencher D. M., Mes-Masson A.-M., Tonin P. N. (2008) Influence of monolayer, spheroid, and tumor growth conditions on chromosome 3 gene expression in tumorigenic epithelial ovarian cancer cell lines. *BMC Med. Genomics* **1**, 34.

Conti L., Cattaneo E. (2010) Neural stem cell systems: physiological players or *in vitro* entities? *Nat. Rev. Neurosci.* **11**, 176–87.

Coyle D. E., Li J., Baccei M. (2011) Regional differentiation of retinoic acid-induced human pluripotent embryonic carcinoma stem cell neurons. *PLoS One* **6**.

Crook J. M., Kobayashi N. R. (2008) Human stem cells for modeling neurological disorders: accelerating the drug discovery pipeline. *J. Cell. Biochem.* **105**, 1361–1366.

Crosetto N., Bienko M., Oudenaarden A. Van (2014) Spatially resolved transcriptomics and beyond. *Nat. Rev. Genet.* **16**, 57–66.

Daud M. F. B., Pawar K. C., Claeyssens F., Ryan A. J., Haycock J. W. (2012) An aligned 3D neuronal-glial co-culture model for peripheral nerve studies. *Biomaterials* **33**, 5901–5913.

Dheen S. T., Kaur C., Ling E.-A. (2007) Microglial activation and its implications in the brain diseases. *Curr. Med. Chem.* **14**, 1189–1197.

Drury J. L., Mooney D. J. (2003) Hydrogels for tissue engineering: scaffold design variables and applications. *Biomaterials* **24**, 4337–4351.

Duarte I. F., Lamego I., Rocha C., Gil A. M. (2009) NMR metabonomics for mammalian cell metabolism studies. *Bioanalysis* **1**, 1597–1614.

Dubois-Dauphin M. L., Toni N., Julien S. D., Charvet I., Sundstrom L. E., Stoppini L. (2010) The long-term survival of *in vitro* engineered nervous tissue derived from the specific neural differentiation of mouse embryonic stem cells. *Biomaterials* **31**, 7032–7042.

East E., Oliveira D. B. de, Golding J. P., Phillips J. B. (2010) Alignment of astrocytes increases neuronal growth in three-dimensional collagen gels and is maintained following plastic compression to form a spinal cord repair conduit. *Tissue Eng. Part A* **16**, 3173–3184.

Ebert A. D., Svendsen C. N. (2010) Human stem cells and drug screening: opportunities and challenges. *Nat. Rev. Drug Discov.* **9**, 367–72.

Eiraku M., Watanabe K., Matsuo-Takasaki M., Kawada M., Yonemura S., Matsumura M., Wataya T., Nishiyama A., Muguruma K., Sasai Y. (2008) Self-Organized Formation of Polarized Cortical Tissues from ESCs and Its Active Manipulation by Extrinsic Signals. *Cell Stem Cell* **3**, 519–532.

Engler A. J., Sen S., Sweeney H. L., Discher D. E. (2006) Matrix Elasticity Directs Stem Cell Lineage Specification. *Cell* **126**, 677–689.

Even-Ram S., Artym V., Yamada K. M. (2006) Matrix Control of Stem Cell Fate. *Cell* **126**, 645–647.

Flanagan L. a, Ju Y.-E., Marg B., Osterfield M., Janmey P. a (2002) Neurite branching on deformable substrates. *Neuroreport* **13**, 2411–2415.

Foo L. C., Allen N. J., Bushong E. A., Ventura P. B., Chung W. S., Zhou L., Cahoy J. D., *et al.* (2011) Development of a method for the purification and culture of rodent astrocytes. *Neuron* **71**, 799–811.

Forman M. S., Trojanowski J. Q., Lee V. M. (2004) Neurodegenerative diseases: a decade of discoveries paves the way for therapeutic breakthroughs. *Nat. Med.* **10**, 1055–63.

Frega M., Tedesco M., Massobrio P., Pesce M., Martinoia S. (2014) Network dynamics of 3D engineered neuronal cultures: a new experimental model for in-vitro electrophysiology. *Sci. Rep.* **4**, 5489.

Fünfschilling U., Supplie L. M., Mahad D., Boretius S., Saab A. S., Edgar J., Brinkmann B. G., et al. (2012) Glycolytic oligodendrocytes maintain myelin and long-term axonal integrity. *Nature* **485**, 517–21.

Gaedtke L., Thoenes L., Culmsee C., Mayer B., Wagner E. (2007) Proteomic Analysis Reveals Differences in Protein Expression in Spheroid versus Monolayer Cultures of Low-Passage Colon Carcinoma Cells research articles. *J. Proteome Res.*, 4111–4118.

Gaffield M. a, Betz W. J. (2006) Imaging synaptic vesicle exocytosis and endocytosis with FM dyes. *Nat. Protoc.* **1**, 2916–2921.

Gähwiler B. H., Capogna M., Debanne D., McKinney R. a., Thompson S. M. (1997) Organotypic slice sultures: a technique has come of age. 471–477.

Giesen C., Wang H. a O., Schapiro D., Zivanovic N., Jacobs A., Hattendorf B., Schüffler P. J., *et al.* (2014) Highly multiplexed imaging of tumor tissues with subcellular resolution by mass cytometry. *Nat. Methods* **11**, 417–22.

Gilbert R. J., Hoffman M., Capitano A., So P. T. C. (2000) Imaging of three-dimensional epithelial architecture and function in cultured CaCO2A monolayers with two-photon excitation microscopy. *Microsc. Res. Tech.* **51**, 204–210.

Gomes C., Ferreira R., George J., Sanches R., Rodrigues D. I., Gonçalves N., Cunha R. a (2013) Activation of microglial cells triggers a release of brain-derived neurotrophic factor (BDNF) inducing their proliferation in an adenosine A2A receptor-dependent manner: A2A receptor blockade prevents BDNF release and proliferation of microglia. *J. Neuroinflammation* **10**, 16.

Goodfellow C. E., Graham S. E., Dragunow M., Glass M. (2011) Characterization of NTera2/D1 cells as a model system for the investigation of cannabinoid function in human neurons and astrocytes. *J. Neurosci. Res.* **89**, 1685–1697.

Goudar C., Biener R., Boisart C., Heidemann R., Piret J., Graaf A. de, Konstantinov K. (2010) Metabolic flux analysis of CHO cells in perfusion culture by metabolite balancing and 2D [13C, 1H] COSY NMR spectroscopy. *Metab. Eng.* **12**, 138–49.

Grienberger C., Konnerth A. (2012) Imaging Calcium in Neurons. *Neuron* **73**, 862–885.

Guilak F., Cohen D. M., Estes B. T., Gimble J. M., Liedtke W., Chen C. S. (2009) Control of Stem Cell Fate by Physical Interactions with the Extracellular Matrix. *Cell Stem Cell* **5**, 17–26.

Guo X., Wang X.-F. (2009) Signaling cross-talk between TGF-beta/BMP and other pathways. *Cell Res.* **19**, 71–88.

Hadjizadeh A., Doillon C. J. (2010) Directional migration of endothelial cells towards angiogenesis using polymer fibres in a 3D co-culture system. *J. Tissue Eng. Regen. Med.* **4**, 524–531.

Halket J. M., Waterman D., Przyborowska A. M., Patel R. K. P., Fraser P. D., Bramley P. M. (2005) Chemical derivatization and mass spectral libraries in metabolic profiling by GC/MS and LC/MS/MS. *J. Exp. Bot.* **56**, 219–243.

Halliwell J. V., Adams P. R. (1982) Voltage-clamp analysis of muscarinic excitation in hippocampal neurons. *Brain Res.* **250**, 71–92.

Hamill O. P., Marty a., Neher E., Sakmann B., Sigworth F. J. (1981) Improved patch-clamp techniques for high-resolution current recording from cells and cell-free membrane patches. *Pflügers Arch. Eur. J. Physiol.* **391**, 85–100.

Hansen C. H., Oudenaarden A. van (2013) Allele-specific detection of single mRNA molecules *in situ*. *Nat. Methods* **10**, 869–71.

Hay M., Thomas D. W., Craighead J. L., Economides C., Rosenthal J. (2014) Clinical development success rates for investigational drugs. *Nat. Biotechnol.* **32**, 40–51.

He W., He W., Kuang Y., Xing X., Simpson R. J., Huang H., Yang T., *et al.* (2014) Proteomic comparison of 3D and 2D glioma models reveals increased HLA-E expression in 3D models is associated with resistance to NK cell-mediated cytotoxicity. *J. Proteome Res.* **13**, 2272–2281.

Hess M. W., Pfaller K., Ebner H. L., Beer B., Hekl D., Seppi T. (2010) *3D versus 2D cell culture. Implications for electron microscopy*. Elsevier Inc.

Hill E. J., Jiménez-González C., Tarczyluk M., Nagel D. a., Coleman M. D., Parri H. R. (2012) NT2 derived neuronal and astrocytic network signalling. *PLoS One* **7**, 1–10.

Hill E. J., Woehrling E. K., Prince M., Coleman M. D. (2008) Differentiating human NT2/D1 neurospheres as a versatile *in vitro* 3D model system for developmental neurotoxicity testing. *Toxicology* **249**, 243–250.

Ho W. Y., Yeap S. K., Ho C. L., Rahim R. A., Alitheen N. B. (2012) Development of Multicellular Tumor Spheroid (MCTS) Culture from Breast Cancer Cell and a High Throughput Screening Method Using the MTT Assay. *PLoS One* **7**.

Hopkins A. M., DeSimone E., Chwalek K., Kaplan D. L. (2015) 3D *in vitro* modeling of the central nervous system. *Prog. Neurobiol.* **125**, 1–25.

Hsieh F.-Y., Lin H.-H., Hsu S. (2015) 3D bioprinting of neural stem cell-laden thermoresponsive biodegradable polyurethane hydrogel and potential in central nervous system repair. *Biomaterials* **71**, 48–57.

Hsieh J., Gage F. H. (2004) Epigenetic control of neural stem cell fate. *Curr. Opin. Genet. Dev.* **14**, 461–469.

Hu B.-Y., Zhang S.-C. (2010) Directed Differentiation of Neural-stem cells and Subtype-Specific Neurons from hESCs, in *Cell. Program. Reprogramming,* (Ding S., ed), Vol. 636, pp. 123–137. Humana Press.

Humpel C. (2015) Organotypic brain slice cultures: A review. *Neuroscience* **305**, 86–98.

Hunsberger J. G., Efthymiou A. G., Malik N., Behl M., Mead I. L., Zeng X., Simeonov A., Rao M. (2015) Induced Pluripotent Stem Cell Models to Enable *In vitro* Models for Screening in the Central Nervous System. *Stem Cells Dev.* **24**, 1852–1864.

Imaizumi Y., Okano H. (2014) Modeling human neurological disorders with induced pluripotent stem cells. *J. Neurochem.* **129**, 388–99.

Ingber D. E. (2006) Mechanical control of tissue morphogenesis during embryological development. *Int. J. Dev. Biol.* **50**, 255–266.

Irons H. R., Cullen D. K., Shapiro N. P., Lambert N. a, Lee R. H., Laplaca M. C. (2008) Three-dimensional neural constructs: a novel platform for neurophysiological investigation. *J. Neural Eng.* **5**, 333–341.

Jakel R. J., Schneider B. L., Svendsen C. N. (2004) Using human neural stem cells to model neurological disease. *Nat. Rev. Genet.* **5**, 136–144.

Jiang Y., Zhang M.-J., Hu B.-Y. (2012) Specification of functional neurons and glia from human pluripotent stem cells. *Protein Cell* **3**, 818–25.

Jucker M. (2010) The benefits and limitations of animal models for translational research in neurodegenerative diseases. *Nat. Med.* **16**, 1210–1214.

Kallos M. S., Behie L. a. (1999) Inoculation and growth conditions for high-cell-density expansion of mammalian neural stem cells in suspension bioreactors. *Biotechnol. Bioeng.* **63**, 473–483.

Kelm J. M., Timmins N. E., Brown C. J., Fussenegger M., Nielsen L. K. (2003) Method for generation of homogeneous multicellular tumor spheroids applicable to a wide variety of cell types. *Biotechnol. Bioeng.* **83**, 173–180.

Kim H., Phung Y., Ho M. (2012) Changes in global gene expression associated with 3D structure of tumors: An *ex vivo* matrix-free mesothelioma spheroid model. *PLoS One* **7**.

Kim S. U., Vellis J. De (2005) Microglia in health and disease. *J. Neurosci. Res.* **81**, 302–313.

King J. A., Miller W. M. (2007) Bioreactor development for stem cell expansion and controlled differentiation. *Curr. Opin. Chem. Biol.* **11**, 394–398.

Kofron C. M., Fong V. J., Hoffman-Kim D. (2009) Neurite outgrowth at the interface of 2D and 3D growth environments. *J. Neural Eng.* **6**, 016002.

König K., Uchugonova A., Gorjup E. (2011) Multiphoton fluorescence lifetime imaging of 3D-stem cell spheroids during differentiation. *Microsc. Res. Tech.* **74**, 9–17.

Kriks S., Shim J.-W., Piao J., Ganat Y. M., Wakeman D. R., Xie Z., Carrillo-Reid L., *et al.* (2011) Dopamine neurons derived from human ES cells efficiently engraft in animal models of Parkinson's disease. *Nature* **480**, 547–551.

Kumar H. R., Zhong X., Hoelz D. J., Rescorla F. J., Hickey R. J., Malkas L. H., Sandoval J. a (2008) Three-dimensional neuroblastoma cell culture: proteomic analysis between monolayer and multicellular tumor spheroids. *Pediatr. Surg. Int.* **24**, 1229–1234.

Kunkanjanawan T., Noisa P., Parnpai R. (2011) Modeling neurological disorders by human induced pluripotent stem cells. *J. Biomed. Biotechnol.* **2011**.

Kunz-Schughart L. a, Freyer J. P., Hofstaedter F., Ebner R. (2004) The use of 3-D cultures for high-throughput screening: the multicellular spheroid model. *J. Biomol. Screen.* **9**, 273–85.

Lai Y., Asthana A., Cheng K., Kisaalita W. S. (2011) Neural cell 3d microtissue formation is marked by cytokines' up-regulation. *PLoS One* **6**.

LaPlaca M. C., Vernekar V. N., Shoemaker J. T., Cullen D. K. (2010) Three-Dimensional Neuronal Cultures. *Methods Bioeng. 3d Tissue Eng.*, 187–204.

Lawrenson K., Notaridou M., Lee N., Benjamin E., Jacobs I. J., Jones C., Gayther S. a (2013) *In vitro* three-dimensional modeling of fallopian tube secretory epithelial cells. *BMC Cell Biol.* **14**, 43.

Lee Y., Morrison B. M., Li Y., Lengacher S., Farah M. H., Hoffman P. N., Liu Y., *et al.* (2012) Oligodendroglia metabolically support axons and contribute to neurodegeneration. *Nature* **487**, 443–448.

Li H., Wijekoon A., Leipzig N. D. (2014) Encapsulated neural stem cell neuronal differentiation in fluorinated methacrylamide chitosan hydrogels. *Ann. Biomed. Eng.* **42**, 1456–1469.

Li X. J., Hu B. Y., Jones S. a., Zhang Y. S., LaVaute T., Du Z. W., Zhang S. C. (2008) Directed differentiation of ventral spinal progenitors and motor neurons from human embryonic stem cells by small molecules. *Stem Cells* **26**, 886–893.

Lin C. H., Lee D. C., Chang H. C., Chiu I. M., Hsu C. H. (2013) Single-cell enzyme-free dissociation of neurospheres using a microfluidic chip. *Anal. Chem.* **85**, 11920–11928.

Lorenzo C., Frongia C., Jorand R., Fehrenbach J., Weiss P., Maandhui A., Gay G., Ducommun B., Lobjois V. (2011) Live cell division dynamics monitoring in 3D large spheroid tumor models using light sheet microscopy. *Cell Div.* **6**, 22.

Lotharius J., Barg S., Wiekop P., Lundberg C., Raymon H. K., Brundin P. (2002) Effect of mutant α-synuclein on dopamine homeostasis in a new human mesencephalic cell line. *J. Biol. Chem.* **277**, 38884–38894.

Lozano R., Stevens L., Thompson B. C., Gilmore K. J., Gorkin R., Stewart E. M., Panhuis M. in het, Romero-Ortega M., Wallace G. G. (2015) 3D printing of layered brain-like structures using peptide modified gellan gum substrates. *Biomaterials* **67**, 264–273.

Lubeck E., Cai L. (2012) Single-cell systems biology by super-resolution imaging and combinatorial labeling. *Nat. Methods* **9**, 743–748.

Lunyak V. V., Rosenfeld M. G. (2008) Epigenetic regulation of stem cell fate. *Hum. Mol. Genet.* **17**, 28–36.

Lutolf M. P., Gilbert P. M., Blau H. M. (2009) Designing materials to direct stem-cell fate. *Nature* **462**, 433–441.

Ma H. L., Jiang Q., Han S., Wu Y., Tomshine J. C., Wang D., Gan Y., Zou G., Liang X. J. (2012) Multicellular tumor spheroids as an *in vivo*-like tumor model for three-dimensional imaging of chemotherapeutic and nano material cellular penetration. *Mol. Imaging* **11**, 487–498.

Ma W., Tavakoli T., Derby E., Serebryakova Y., Rao M. S., Mattson M. P. (2008) Cell-extracellular matrix interactions regulate neural differentiation of human embryonic stem cells. *BMC Dev. Biol.* **8**, 90.

Mahdavi A., Davey R. E., Bhola P., Yin T., Zandstra P. W. (2007) Sensitivity analysis of intracellular signaling pathway kinetics predicts targets for stem cell fate control. *PLoS Comput. Biol.* **3**, 1257–1267.

Mak I. W., Evaniew N., Ghert M. (2014) Lost in translation: animal models and clinical trials in cancer treatment. *Am. J. Transl. Res.* **6**, 114–8.

Mak S. K., Huang Y. A., Iranmanesh S., Vangipuram M., Sundararajan R., Nguyen L., Langston J. W., Schüle B. (2012) Small molecules greatly improve conversion of human-induced pluripotent stem cells to the neuronal lineage. *Stem Cells Int.* **2012**.

Mariani J., Simonini M. V., Palejev D., Tomasini L., Coppola G., Szekely A. M., Horvath T. L., Vaccarino F. M. (2012) Modeling human cortical development *in vitro* using induced pluripotent stem cells. *Proc. Natl. Acad. Sci.* **109**, 12770–12775.

Marksteiner J., Humpel C. (2008) Beta-amyloid expression, release and extracellular deposition in aged rat brain slices. *Mol. Psychiatry* **13**, 939–952.

Masters B. R., So P. T., Gratton E. (1997) Multiphoton excitation fluorescence microscopy and spectroscopy of *in vivo* human skin. *Biophys. J.* **72**, 2405–2412.

Milosevic J., Schwarz S. C., Krohn K., Poppe M., Storch A., Schwarz J. (2005) Low atmospheric oxygen avoids maturation, senescence and cell death of murine mesencephalic neural precursors. *J. Neurochem.* **92**, 718–729.

Mobassarah N. J., Choudhry Z., Rikani A. a, Choudhry A. M., Tariq S., Zakaria F., Asghar M. W., Sarfraz M. K., Haider K., Shafiq A. a (2014) Sonic Hedgehog Signalling Pathway: A Complex Network. *Ann. Neurosci.* **21**, 19–22.

Mohtaram N. K., Ko J., King C., Sun L., Muller N., Jun M. B.-G., Willerth S. M. (2014) Electrospun biomaterial scaffolds with varied topographies for neuronal differentiation of human-induced pluripotent stem cells. *J. Biomed. Mater. Res. Part A*, n/a–n/a.

Nakajima K., Honda S., Tohyama Y., Imai Y., Kohsaka S., Kurihara T. (2001) Neurotrophin secretion from cultured microglia. *J. Neurosci. Res.* **65**, 322–331.

Nazareth E. J. P., Ostblom J. E. E., Lücker P. B., Shukla S., Alvarez M. M., Oh S. K. W., Yin T., Zandstra P. W. (2013) High-throughput fingerprinting of human pluripotent stem cell fate responses and lineage bias. *Nat. Methods* **10**, 1225–31.

Ng E. S., Davis R. P., Azzola L., Stanley E. G., Elefanty A. G. (2005) Forced aggregation of defined numbers of human embryonic stem cells into embryoid bodies fosters robust, reproducible hematopoietic differentiation. *Blood* **106**, 1601–1603.

Nicodemus G. D., Bryant S. J. (2008) Cell encapsulation in biodegradable hydrogels for tissue engineering applications. *Tissue Eng. Part B. Rev.* **14**, 149–65.

No D. Y., Lee S. a., Choi Y. Y., Park D., Jang J. Y., Kim D. S., Lee S. H., Johnson R. (2012) Functional 3D Human Primary Hepatocyte Spheroids Made by Co-Culturing Hepatocytes from Partial Hepatectomy Specimens and Human Adipose-Derived Stem Cells. *PLoS One* **7**.

OECD (2014) *Health at a Glance: Europe 2014*, (Publishing O., ed).

Ohnuki Y., Kurosawa H. (2013) Effects of hanging drop culture conditions on embryoid body formation and neuronal cell differentiation using mouse embryonic stem cells: Optimization of culture conditions for the formation of well-controlled embryoid bodies. *J. Biosci. Bioeng.* **115**, 571–574.

Olmer R., Lange A., Selzer S., Ing D., Kasper C., Haverich A., Martin U., Zweigerdt R. (2012) Suspension Culture of Human Pluripotent Stem Cells in Controlled, Stirred Bioreactors. *Tissue Eng Part C Methods* **18**, 772–784.

Ooi L., Sidhu K., Poljak A., Sutherland G., O'Connor M. D., Sachdev P., Münch G. (2013) Induced pluripotent stem cells as tools for disease modelling and drug discovery in Alzheimer's disease. *J. Neural Transm.* **120**, 103–111.

Ostenfeld T., Caldwell M. a, Prowse K. R., Linskens M. H., Jauniaux E., Svendsen C. N. (2000) Human neural precursor cells express low levels of telomerase *in vitro* and show diminishing cell proliferation with extensive axonal outgrowth following transplantation. *Exp. Neurol.* **164**, 215–226.

Pampaloni F., Ansari N., Stelzer E. H. K. (2013) High-resolution deep imaging of live cellular spheroids with light-sheet-based fluorescence microscopy. *Cell Tissue Res.*, 161–177.

Pampaloni F., Reynaud E. G., Stelzer E. H. K. (2007) The third dimension bridges the gap between cell culture and live tissue. *Nat. Rev. Mol. Cell Biol.* **8**, 839–845.

Paridaen J. T., Huttner W. B. (2014) Neurogenesis during development of the vertebrate central nervous system. *EMBO Rep.* **15**, 351–364.

Paszek M. J., Zahir N., Johnson K. R., Lakins J. N., Rozenberg G. I., Gefen A., Reinhart-King C. a., *et al.* (2005) Tensional homeostasis and the malignant phenotype. *Cancer Cell* **8**, 241–254.

Pauklin S., Vallier L. (2013) The Cell-Cycle State of Stem Cells Determines Cell Fate Propensity. *Cell* **155**, 135–147.

Phatnani H., Maniatis T. (2015) Astrocytes in Neurodegenerative Disease. *Cold Spring Harb. Perspect. Biol.* **7**, a020628.

Pleasure S. J., Lee V. M. (1993) NTera 2 cells: a human cell line which displays characteristics expected of a human committed neuronal progenitor cell. *J. Neurosci. Res.* **35**, 585–602.

Podrygajlo G., Tegenge M. a., Gierse A., Paquet-Durand F., Tan S., Bicker G., Stern M. (2009) Cellular phenotypes of human model neurons (NT2) after differentiation in aggregate culture. *Cell Tissue Res.* **336**, 439–452.

Qiu X., Jesus J. De, Pennell M., Troiani M., Haun J. B. (2015) Microfluidic device for mechanical dissociation of cancer cell aggregates into single cells. *Lab Chip* **15**, 339–350.

Rafalski V. a, Brunet A. (2011) Energy metabolism in adult neural stem cell fate. *Prog. Neurobiol.* **93**, 182–203.

Raghavan S., Gilmont R. R., Bitar K. N. (2013) Neuroglial differentiation of adult enteric neuronal progenitor cells as a function of extracellular matrix composition. *Biomaterials* **34**, 6649–6658.

Reynolds B. a, Tetzlaff W., Weiss S. (1992) A multipotent EGF-responsive striatal embryonic progenitor cell produces neurons and astrocytes. *J. Neurosci.* **12**, 4565–4574.

Reynolds B. a, Weiss S. (1996) Clonal and population analyses demonstrate that an EGF-responsive mammalian embryonic CNS precursor is a stem cell. *Dev. Biol.* **175**, 1–13.

Ribeiro a., Balasubramanian S., Hughes D., Vargo S., Powell E. M., Leach J. B. (2013) β1-Integrin cytoskeletal signaling regulates sensory neuron response to matrix dimensionality. *Neuroscience* **248**, 67–78.

Ribeiro A., Vargo S., Powell E. M., Leach J. B. (2012) Substrate Three-Dimensionality Induces Elemental Morphological Transformation of Sensory Neurons on a Physiologic Timescale. *Tissue Eng. Part A* **18**, 93–102.

Robinette B. L., Harrill J. a, Mundy W. R., Shafer T. J. (2011) *In vitro* Assessment of Developmental Neurotoxicity: Use of Microelectrode Arrays to Measure Functional Changes in Neuronal Network Ontogeny1. *Front. Neuroeng.* **4**, 1.

Rodrigues C. a V, Fernandes T. G., Diogo M. M., Silva C. L. da, Cabral J. M. S. (2011) Stem cell cultivation in bioreactors. *Biotechnol. Adv.* **29**, 815–829.

Rodrigues T. B., Fonseca C. P., Castro M. M. C. A., Cerdán S., Geraldes C. F. G. C. (2009) *13C NMR tracers in neurochemistry: Implications for molecular imaging*.

Rutecki P. a. (1992) Neuronal Excitability. *J. Clin. Neurophysiol.* **9**, 195–211.

Sá Santos S., Sonnewald U., Carrondo M. J. T., Alves P. M. (2011) The role of glia in neuronal recovery following anoxia: *In vitro* evidence of neuronal adaptation. *Neurochem. Int.* **58**, 665–675.

Santos S. S., Leite S. B., Sonnewald U., Carrondo M. J. T., Alves P. M. (2007) Stirred vessel cultures of rat brain cells aggregates: characterization of major metabolic pathways and cell population dynamics. *J. Neurosci. Res.* **85**, 3386–3397.

Schmidt C. E., Leach J. B. (2003) Neural tissue engineering: strategies for repair and regeneration. *Annu. Rev. Biomed. Eng.* **5**, 293–347.

Schüle B., Pera R. a R., Langston J. W. (2009) *Can cellular models revolutionize drug discovery in Parkinson's disease?* Elsevier B.V.

Sen A., Kallos M. S., Behie L. a (2004) New tissue dissociation protocol for scaled-up production of neural stem cells in suspension bioreactors. *Tissue Eng.* **10**, 904–913.

Sen A., Kallos M. S., Behie L. a. (2002) Passaging protocols for mammalian neural stem cells in suspension bioreactors. *Biotechnol. Prog.* **18**, 337–345.

Serra M., Brito C., Correia C., Alves P. M. (2012) *Process engineering of human pluripotent stem cells for clinical application*.

Serra M., Leite S. B., Brito C., Costa J., Carrondo M. J. T., Alves P. M. (2007) Novel culture strategy for human stem cell proliferation and neuronal differentiation. *J. Neurosci. Res.* **85**, 3557–3566.

Shimojo H., Ohtsuka T., Kageyama R. (2008) Oscillations in Notch Signaling Regulate Maintenance of Neural Progenitors. *Neuron* **58**, 52–64.

Shin E., Forsyth N. R., Fricker R. a. (2012) The effect of physiological oxygen levels on GABAergic neuronal differentiation from mouse embryonic stem cells. *Stem Cell Stud.* **2**, 13–20.

Silva G. a, Czeisler C., Niece K. L., Beniash E., Harrington D. a, Kessler J. a, Stupp S. I. (2004) Selective differentiation of neural progenitor cells by high-epitope density nanofibers. *Science (80-.).* **303**, 1352–1355.

Solozobova V., Wyvekens N., Pruszak J. (2012) Lessons from the Embryonic Neural Stem Cell Niche for Neural Lineage Differentiation of Pluripotent Stem Cells. *Stem Cell Rev. Reports* **8**, 813–829.

Spinella M. J., Freemantle S. J., Sekula D., Chang J. H., Christie A. J., Dmitrovsky E. (1999) Retinoic acid promotes ubiquitination and proteolysis of cyclin D1 during induced tumor cell differentiation. *J. Biol. Chem.* **274**, 22013–22018.

Spira M. E., Hai A. (2013) Multi-electrode array technologies for neuroscience and cardiology. *Nat. Nanotechnol.* **8**, 83–94.

Srikanth P., Young-Pearse T. L. (2014) Stem cells on the brain: modeling neurodevelopmental and neurodegenerative diseases using human induced pluripotent stem cells. *J. Neurogenet.* **28**, 5–29.

Stelzer E. H. K. (2015) Light-sheet fluorescence microscopy for quantitative biology. *Nat. Publ. Gr.* **12**, 23–26.

Stern M., Gierse A., Tan S., Bicker G. (2014) Human Ntera2 cells as a predictive *in vitro* test system for developmental neurotoxicity. *Arch. Toxicol.* **88**, 127–136.

Storch A., Paul G., Csete M., Boehm B. O., Carvey P. M., Kupsch A., Schwarz J. (2001) Long-term proliferation and dopaminergic differentiation of human mesencephalic neural precursor cells. *Exp Neurol* **170**, 317–325.

Studer L., Csete M., Lee S. H., Kabbani N., Walikonis J., Wold B., McKay R. (2000) Enhanced proliferation, survival, and dopaminergic differentiation of CNS precursors in lowered oxygen. *J. Neurosci.* **20**, 7377–7383.

Sun X., Volobouеva L. a., Stary C. M., Giffard R. G. (2015) Physiologically normal 5% O_2 supports neuronal differentiation and resistance to inflammatory injury in neural stem cell cultures. *J. Neurosci. Res.* **00**, n/a–n/a.

Takahashi K., Tanabe K., Ohnuki M., Narita M., Ichisaka T., Tomoda K., Yamanaka S. (2007) Induction of Pluripotent Stem Cells from Adult Human Fibroblasts by Defined Factors. *Cell* **131**, 861–872.

Tang-Schomer M. D., White J. D., Tien L. W., Schmitt L. I., Valentin T. M., Graziano D. J., Hopkins a. M., Omenetto F. G., Haydon P. G., Kaplan D. L. (2014) Bioengineered functional brain-like cortical tissue. *Proc. Natl. Acad. Sci.*, 1–6.

Telias M., Ben-Yosef D. (2014) Modeling neurodevelopmental disorders using human pluripotent stem cells. *Stem Cell Rev.* **10**, 494–511.

Terrasso A. P., Pinto C., Serra M., Filipe A., Almeida S., Ferreira A. L., Pedroso P., Brito C., Alves P. M. (2015) Novel scalable 3D cell based model for *in vitro* neurotoxicity testing: Combining human differentiated neurospheres with gene expression and functional endpoints. *J. Biotechnol.*

Timmins N., Dietmair S., Nielsen L. (2004) Hanging-drop multicellular spheroids as a model of tumour angiogenesis. *Angiogenesis* **7**, 97–103.

Tung Y.-C., Hsiao A. Y., Allen S. G., Torisawa Y., Ho M., Takayama S. (2011) High-throughput 3D spheroid culture and drug testing using a 384 hanging drop array. *Analyst* **136**, 473–478.

Uchugonova A., König K. (2013) Two-photon autofluorescence and second-harmonic imaging of adult stem cells. *J. Biomed. Opt.* **13**, 054068.

Valamehr B., Jonas S. J., Polleux J., Qiao R., Guo S., Gschweng E. H., Stiles B., *et al.* (2008) Hydrophobic surfaces for enhanced differentiation of embryonic stem cell-derived embryoid bodies Results. *Pnas* **105**, 14459–14464.

Vieira H. L. a, Alves P. M., Vercelli A. (2011) Modulation of neuronal stem cell differentiation by hypoxia and reactive oxygen species. *Prog. Neurobiol.* **93**, 444–455.

Vogel V., Sheetz M. (2006) Local force and geometry sensing regulate cell functions. *Nat. Rev. Mol. Cell Biol.* **7**, 265–275.

Wagner B., Natarajan A., Grünaug S., Kroismayr R., Wagner E. F., Sibilia M. (2006) Neuronal survival depends on EGFR signaling in cortical but not midbrain astrocytes. *EMBO J.* **25**, 752–762.

Wagstaff J. L., Masterton R. J., Povey J. F., Smales C. M., Howard M. J. (2013) 1H NMR Spectroscopy Profiling of Metabolic Reprogramming of Chinese Hamster Ovary Cells upon a Temperature Shift during Culture. *PLoS One* **8**, e77195.

Walsh K., Megyesi J., Hammond R. (2005) Human central nervous system tissue culture: A historical review and examination of recent advances. *Neurobiol. Dis.* **18**, 2–18.

Wilhelmi E., Schöder U. H., Benabdallah A., Sieg F., Breder J., Reymann K. G. (2002) Organotypic brain-slice cultures from adult rats: Approaches for a prolonged culture time. *ATLA Altern. to Lab. Anim.* **30**, 275–283.

Willerth S. M., Sakiyama-Elbert S. E. (2007) Approaches to neural tissue engineering using scaffolds for drug delivery. *Adv. Drug Deliv. Rev.* **59**, 325–338.

Willits R. K., Skornia S. L. (2004) Effect of collagen gel stiffness on neurite extension. *J. Biomater. Sci. Polym. Ed.* **15**, 1521–1531.

Wilson P. G., Stice S. S. (2006) Development and differentiation of neural rosettes derived from human embryonic stem cells. *Stem Cell Rev.* **2**, 67–77.

Woehrling E. K., Parri H. R., Tse E. H. Y., Hill E. J., Maidment I. D., Fox G. C., Coleman M. D. (2015) A Predictive *In vitro* Model of the Impact of Drugs with Anticholinergic Properties on Human Neuronal and Astrocytic Systems. *PLoS One* **10**, e0118786.

Wu H., Xu J., Pang Z. P., Ge W., Kim K. J., Blanchi B., Chen C., Südhof T. C., Sun Y. E. (2007) Integrative genomic and functional analyses reveal neuronal subtype differentiation bias in human embryonic stem cell lines. *Proc. Natl. Acad. Sci. U. S. A.* **104**, 13821–13826.

Xu T., Molnar P., Gregory C., Das M., Boland T., Hickman J. J. (2009) Electrophysiological characterization of embryonic hippocampal neurons cultured in a 3D collagen hydrogel. *Biomaterials* **30**, 4377–4383.

Yamada S., Taketomi T., Yoshimura A. (2004) Model analysis of difference between EGF pathway and FGF pathway. *Biochem. Biophys. Res. Commun.* **314**, 1113–1120.

Yap M. S., Nathan K. R., Yeo Y., Lim L. W., Poh C. L., Richards M., Lim W. L., Othman I., Heng B. C. (2015) Neural Differentiation of Human Pluripotent Stem Cells for Nontherapeutic Applications: Toxicology, Pharmacology, and *In vitro* Disease Modeling. *Stem Cells Int.* **2015**, 105172.

Yoon B. S., Yoo S. J., Lee J. E., You S., Lee H. T., Yoon H. S. (2006) Enhanced differentiation of human embryonic stem cells into cardiomyocytes by combining hanging drop culture and 5-azacytidine treatment. *Differentiation* **74**, 149–159.

Yun C., Mendelson J., Blake T., Mishra L., Mishra B. (2008) TGF-beta signaling in neuronal stem cells. *Dis. Markers* **24**, 251–255.

Zhang Q., Nguyen A. L., Shi S., Hill C., Wilder-Smith P., Krasieva T. B., Le A. D. (2012) Three-Dimensional Spheroid Culture of Human Gingiva-Derived Mesenchymal Stem Cells Enhances Mitigation of Chemotherapy-Induced Oral Mucositis. *Stem Cells Dev.* **21**, 937–947.

Zhao C., Deng W., Gage F. H. (2008) Mechanisms and Functional Implications of Adult Neurogenesis. *Cell* **132**, 645–660.

2

Modeling human neural functionality *in vitro*: 3D culture for dopaminergic differentiation

This chapter was adapted from:

Brito C, Simão D, Costa I, Malpique R, Pereira CI, Fernandes P, Serra M, Schwarz SC, Schwarz J, Kremer EJ, Alves PM (2012) 3D cultures of human neural progenitor cells: dopaminergic differentiation and genetic modification. *Methods* 56(3): 452-60

Simão D, Pinto C, Piersanti S, Weston A, Peddie CJ, Bastos AEP, Licursi V, Schwarz SC, Collinson LM, Salinas S, Serra M, Teixeira AP, Saggio I, Lima PA, Kremer EJ, Schiavo G, Brito C, Alves PM (2015) Modeling human neural functionality *in vitro*: 3D culture for dopaminergic differentiation. *Tissue Engineering Part A* 21(3-4): 654-68

Table of Contents

Abstract

Advances in mechanistic knowledge of human neurological disorders have been hindered by the lack of adequate human *in vitro* models. 3D cellular models displaying higher biological relevance are gaining momentum, however, their lack of robustness and scarcity of analytical tools adapted to 3D hampers their widespread implementation. This chapter shows that human midbrain-derived neural progenitor cells (hmNPC), cultured as 3D neurospheres in agitation-based culture systems, reproducibly differentiate into complex tissue-like structures containing functional dopaminergic neurons, as well as astrocytes and oligodendrocytes. Moreover, an extensive toolbox of analytical methodologies has been adapted to 3D neural cell models, allowing molecular and phenotypic profiling and interrogation. The generated neurons underwent synaptogenesis and elicit spontaneous Ca^{2+} transients. Synaptic vesicle trafficking and release of dopamine in response to depolarizing stimuli was also observed. Under whole-cell current-and-voltage-clamp, recordings showed polarized neurons ($V_m \approx$ -70 mV) and voltage-dependent potassium currents, which included A-type-like currents. Glutamate-induced currents sensitive to AMPA and NMDA antagonists revealed the existence of functional glutamate receptors. Molecular and phenotypic profiling showed recapitulation of midbrain patterning events, and remodeling towards increased similarity to human brain features such as ECM composition and metabolic signature. This work describes the development of a robust and reproducible human 3D neural cell model, which may be extended to patient-derived iPSC, broadening the applicability of this model.

1. Introduction

The demand for robust and predictable human *in vitro* models that can bridge the gap between human clinical studies and animal models is steadily increasing. Advances in our understanding of human diseases as well as drug development have been hindered by the lack of reliable model systems (Lin *et al.* 2008; Griffith and Swartz 2006). The study of central nervous system (CNS) disorders, such as Parkinson´s disease (PD), would particularly benefit from the development of more accurate cellular models, since only about 8% of new drugs that enter clinical trials are approved and reach the market (Miller 2010). In the case of PD, the available chemical or genetically-induced animal models poorly mimic most pathological features, due to fundamental biochemical, metabolic and genetic differences between species (Schüle *et al.* 2009). Recently, important advances have been made towards the development of human cellular models using immortalized cell lines, embryonic or adult neural stem cells and more recently induced pluripotent stem cells (iPSC) (Schüle *et al.* 2009).

Cell fate is determined by processes that integrate a wide range of external cues, such as nutritional status, growth factors, mechanical cues, cell-cell and cell-extracellular matrix (ECM) interactions (Fennema *et al.* 2013; Griffith and Swartz 2006). Thus, when aiming at mimicking the main features of tissues, it is imperative to establish 3D cellular networks, which play critical roles in cell fate, tissue specificity and homeostasis (Pampaloni *et al.* 2007). Therefore, *in vitro* cellular models with a higher spatial degree of complexity are necessary. With the growing set of platforms amenable to high-throughput screening (HTS), as well as the increasing power of methodologies that allow more comprehensive readouts, human 3D *ex vivo* models can contribute to generate accurate and predictive cell-based drug and toxicity screenings. Several cellular systems have been established, namely organotypic cultures, which fail to maintain long-term viability, and 3D *in vitro* cell cultures, either within matrices, highly dependent on time-consuming scaffold engineering and preparation (Potter *et al.* 2008), or as free floating aggregates (Pampaloni *et al.* 2007).

By taking advantage of the potential of many cell types to self-organize into 3D structures, with secretion of ECM (Breslin and O'Driscoll 2013; Fennema *et al.* 2013), one may culture isolated cells as 3D spheroids (Fennema *et al.* 2013; Pampaloni *et al.* 2007), which in case of neural cultures are referred to as neurospheres and have been reported to mimic basic processes of brain development (Moors *et al.* 2009). Different methods for aggregation have been explored, including spontaneous aggregation under static conditions and in rotating wall vessels or induced aggregation in agitation-based culture systems (Fennema *et al.* 2013).

In this work, an agitation-based culture system was explored in order to attain efficient dopaminergic differentiation and neuronal maturation, along with a comprehensive set of characterization methods adapted for a 3D setting. By extending culture time in the presence of cAMP, a reliable 3D differentiation process was established in which dopaminergic and synaptic markers were upregulated, recapitulating key events of midbrain development. Moreover, the expression of synaptic markers and their assembly in synaptic-like microvesicles resulted in increased neuronal functionality, as suggested by the ability to spontaneously elicit Ca^{2+}-firing and respond to depolarizing stimuli, analyzed by 3D live imaging. The functionality of the generated neurons was further confirmed by the appearance of hyperpolarized resting potentials, voltage-activated currents and glutamate evoked currents. Therefore, this 3D human neural model is biologically relevant, and it can be exploited in different applications ranging from mechanistic studies on disease pathogenesis to drug screening.

2. Materials and Methods

2.1. 2D cell expansion

hmNPC derived from aborted fetal brain tissue 12 to 14 weeks post-fertilization (Storch *et al.* 2001) were kindly provided by Dr. Johannes Schwarz (Technical University of Munich, Germany). Tissue was obtained with mother's consent and in accordance with the Ethics Committee of the University of Leipzig and the German state and federal laws. Expansion of hmNPC was performed on poly-L-ornithine-fibronectin (PLOF)-coated surfaces and serum-free medium, as described previously (Storch *et al.* 2001). Expansion medium (EM) was composed of Dulbecco's modified Eagle medium (DMEM) and Ham's F12 Nutrient Mix (both from Invitrogen) in a 1:1 ratio, 2% B27 supplement (Invitrogen) 20 ng/mL recombinant human (rhu)-bFGF and rhu-EGF (both from PrepoTech), 1 µg/mL tocopherol (Fluka), 1 µg/mL tocopherol acetate (Sigma) and 10 µg/mL gentamycin (Invitrogen). Cells were maintained in a multi-gas cell incubator (Sanyo) at 37°C, in a humidified atmosphere of 5% CO_2 and 3% O_2 in air. A 100% media exchange was performed every 3-4 days. Splitting was typically performed every 14 days, at 90-100% confluence, dislodging cells through incubation with Accutase (Sigma). The cell suspension was used to inoculate PLOF-coated T-flasks, at a cell density of 3×10^4 cell/cm^2.

2.2. 3D neurosphere differentiation

hmNPC were cultured in agitation-based culture systems, using shake flasks (Corning) under constant orbital shaking (stirring rate: 100 rpm) at 37°C in a multi-gas cell incubator (Sanyo), with a humidified atmosphere of 5% CO_2 and 3% O_2 in air. Typ-

ically, flasks were inoculated at 2 x 10^5 cell/mL (single cell suspension) in Aggregation medium (AM; EM with lower mitogen concentration 5 ng/mL of bFGF and EGF) and maintained in AM for 7 days with a 50% medium exchange performed at day 3-4. At day 7 of aggregation (7Diff), differentiation of neurospheres was induced by exchanging AM to Differentiation Medium (DM; Neurobasal medium (Invitrogen) supplemented with 2% of B27, 2 mM of Glutamax (Invitrogen), 100 µM dibutyryl cAMP (Sigma-Aldrich), 10 µM forskolin (Sigma-Aldrich), 100 µM fusaric acid (Sigma-Aldrich) and 10 µg/mL gentamycin (Invitrogen) (Wegner *et al.* 2012)). After 14 days in DM (21Diff), neurospheres were further cultured in Maturation Medium (MM; Same composition of DM, except for removal of forskolin and fusaric acid) for 18 days (18Mat). A 75% medium exchange was performed every 2-3 days.

2.3. Viability assay

For cell viability assessment, neurospheres were incubated with 20 µg/mL fluorescein diacetate (FDA), which stains viable cells, and with 10 µg/mL propidium iodide (PI), a membrane-impermeable DNA-dye that stains non-viable cells, in PBS for 5 minutes, washed with PBS and observed using fluorescence microscopy (DMI6000, Leica).

2.4. Fluorescence microscopy

Neurospheres were plated on PLOF-coated glass coverslips and allowed to attach for 3 days, fixed in 4% paraformaldehyde (PFA) + 4% sucrose in PBS for 40 min and processed for immunostaining as described (Serra *et al.* 2011). Primary and secondary antibodies were used as follows: mouse anti-βIII-tubulin (1:200; Millipore); rabbit anti-GFAP (1:200; Millipore); rabbit anti-TH (1:100; Santa Cruz Biotechnology); rabbit anti-Pitx3 (1:100; Abcam); mouse anti-synaptophysin (1:200; Millipore); mouse anti-O4 (1:100; Millipore); AlexaFluor® 488 goat anti-mouse IgG; AlexaFluor® 488 goat anti-mouse IgM; AlexaFluor® 594 goat anti-rabbit IgG and AlexaFluor® 488 goat anti-rabbit IgG (1:500; all from Invitrogen). Cell nuclei were counterstained with TO-PRO-3 (Invitrogen). Samples were visualized using fluorescence (DMI6000, Leica) and point scan confocal (SP5, Leica) microscopy. Merge between channels and maximum z-projections, as well as linear brightness and contrast adjustments of the images, were performed using the open source ImageJ software.

2.5. Electron microscopy

Neurospheres were fixed in 2.5% glutaraldehyde and 4% formaldehyde in 0.1 M phosphate buffer (pH 7.4) and then processed for scanning electron microscopy (SEM),

transmission electron microscopy (TEM) or serial block face SEM (SBF-SEM). For SEM, samples were dehydrated, critical point dried, mounted on stubs, coated with a thin layer of gold and imaged with a 6700F field emission SEM (JEOL Ltd., Japan). Secondary electron images were collected at 5 keV with a probe current of 10 µA and a probe distance of 7.8 – 7.9 mm. For TEM and SBF-SEM, samples were prepared using the NCMIR method (Deerinck *et al.* 2010). For TEM, 70 nm sections were collected from neurospheres embedded in Durcupan resin using a UCT ultramicrotome (Leica Microsystems, Vienna). No post-staining was required due to the density of metal deposited using the NCMIR protocol. Images were acquired using a Tecnai G2 Spirit Biotwin TEM (FEI, Eindhoven) and an Orius CCD camera (Gatan, Pleasanton). For SBF-SEM, neurospheres embedded in Durcupan resin were mounted on a pin and trimmed to a blockface of less than 1 mm^2. Imaging was performed in a Sigma variable pressure SEM (Carl Zeiss, Cambridge) equipped with a 3View ultramicrotome (Gatan) for automated serial imaging within the SEM chamber. Images were collected at 4 keV with a pixel dwell time of 3 µs at 40 Pa. One thousand serial images were collected overnight for each dataset with 7.2 nm^2 pixels and a slice thickness of 75 nm. The resulting image stack was aligned using Amira (Visage Imaging Inc.) and individual cells were manually segmented and rendered using the same software.

2.6. Metabolic Profiling

Metabolic profile of neurospheres was assessed at 7Diff and 18Mat and was performed using MM for both cultures, in order to discard the influence of different media composition. Neurospheres were plated on PLOF-coated plates and allowed to attach to the surface. A washing step with PBS was performed before adding fresh MM to the culture. Samples of supernatant were then collected at 6, 12, 24 and 48 hours after media exchange and stored at -20°C. Neurospheres were harvested and total protein was quantified with Micro BCA Protein Assay Kit (Pierce), according to manufacturer's instructions. Prior to NMR analysis, samples were thawed and filtered using Vivaspin 500 columns (Sigma-Aldrich) at 14,000x*g*. To minimize variations in pH, 400 µL of filtered samples were mixed with 200 µL of phosphate buffer (50 mM, pH 7.4) with 5 mM DSS-d_6 and centrifuged at 1,000x*g* for 1 min. For NMR analysis, 500 µL of the resulting supernatants were placed into 5 mm NMR tubes. All ^{1}H-NMR spectra were recorded at 25°C on a Bruker Avance II+ 500 MHz NMR spectrometer. One-dimensional (1D) spectra were recorded using a NOESY-based pulse sequence (4 s acquisition time, 1 s relaxation time and 100 ms mixing time). Typically, 256 scans were collected for each spectrum. All spectra were phase and baseline corrected automatically, with fine adjustments performed manually. Spectra analysis was performed using Chenomx NMR

Suite 7.1, using DSS-d_6 as internal standard for quantification of metabolites (Duarte *et al.* 2014).

2.7. RT-qPCR

Total RNA was extracted with High Pure RNA Isolation Kit (Roche) or RNeasy Mini Kit (Qiagen, Valencia, CA, USA), according to the manufacturer instructions. RNA was quantified in a NanoDrop 2000c (Thermo Scientific) and used for cDNA synthesis. Reverse transcription was performed with High Fidelity cDNA Synthesis Kit (Roche), using Anchored-oligo(dT)18 Primer (Roche) or with the Super Script III First Strand synthesis system (Invitrogen), using random hexamers (Invitrogen). qPCRs were performed in triplicates using LightCycler 480 SYBR Green I Master Kit (Roche) with the following primers: Nuclear receptor related-1 protein (*NURR1* fwd 5′-cgaccaagacctgctttttg-3′ and *NURR1* rev 5′-attgcaacctgtgcaagacc-3′), proliferating cell nuclear antigen (*PCNA* fwd 5′-cggagtgaaattttctgcaag-3′ and *PCNA* rev 5′-ttcaggtacctcagtgcaaaag-3′), synapsin II (*SYN2* fwd 5′-tggaacaggcagaattttca-3′ and *SYN2* rev 5′-ggacaacctttgtgccattc-3′) and ribosomal protein L22 (*RPL22* fwd 5′-cacgaaggaggagtgactgg-3′ and *RPL22* rev 5′-tgtggcacaccactgacatt-3′). As alternative, TaqMan Universal PCR Master Mix (Life Technologies) and the following TaqMan® Gene Expression Assays (Life Technologies) were used: *TRKA* (ID: Hs01021011_m1); *TRKB* (ID: Hs00178811_m1); *TH* (ID: Hs00165941_m1); *DRD2* (ID: Hs00241436_m1); *SYT1* (ID: Hs00194572_m1); *SYP* (ID: Hs00300531_m1); *PSD95* (ID: Hs00176354_m1); *vGAT* (ID: Dm01823909_g1); RPL22 (ID: Hs01865331_s1). The reactions were performed with Applied Biosystems 7300 Real Time PCR system or LightCycler 480 Instrument II 96-well block (Roche). Quantification cycle values (Cq's) and melting curves were determined using LightCycler 480 Software version 1.5 (Roche). All data were analyzed using the $2^{-\Delta\Delta Ct}$ method for relative gene expression analysis (Livak and Schmittgen 2001). Changes in gene expression were normalized using the housekeeping gene *RPL22* (ribosomal protein L22) as internal control. Statistical analysis was carried out using GraphPad Prism 5 software.

2.8. Microarray analysis

Three independent biological replicates of both undifferentiated and differentiated samples were analyzed by using the Affymetrix HG U133 plus2 gene chips, interrogating more than 47000 transcripts. Microarray data were normalized by the log scale robust multi-array analysis (RMA) procedure using R (Bioconductor) and differentially expressed genes were obtained with limma package (Smyth 2005). A moderated t-test was performed between differentiated and undifferentiated groups selecting genes

with a False Discovery Rate (FDR) -value ≤ 0.01 and with ≥ 2-fold change for upregulated genes and ≤ -2 fold change for downregulated genes.

The identified genes were categorized in generic GO functional clusters using Cytoscape_v 2.8.3 and its plug-in BINGO 2.44 (Biological Networks Gene Ontology tool) (Maere *et al.* 2005). The significance of overrepresented GO categories was assessed with a hypergeometric test and the Benjamini and Hochberg FDR correction. A corrected p value < 0.05 was considered significant and only significantly overrepresented GO categories are presented (Benjamini and Hochberg 1995).

2.9. Western blot

Cells were lysed in Lysis Buffer (50 mM Tris, 5 mM EDTA, 150 mM NaCl, 1% Triton X-100, pH 7.4) for 30 min at 4˚C. Extracts were clarified by centrifugation at 15,000x*g* for 10 min, followed by protein precipitation by overnight incubation in 80% ethanol. Precipitated proteins were collected at 15,000x*g* for 15 min and solubilized in reducing NuPAGE sample buffer (Invitrogen). Total protein was quantified with Micro BCA Protein Assay Kit (Pierce). Protein extracts were resolved on a 1 mm NuPAGE® Novex BisTris gel (Invitrogen) under reducing conditions and transferred with iBlot system (Invitrogen), according to the manufacturer's instructions. Membranes were blocked by incubation for 1 h with blocking solution (0.1% Tween 20 and 5% dry milk in PBS), and incubated overnight with primary antibodies, described in section 2.4 and mouse anti-alfa tubulin (Sigma) as loading control, diluted in blocking solution. Blots were developed using the enhanced chemiluminescence (ECL) detection system after incubation for 1 h at room temperature with horseradish peroxidase-labeled anti-mouse IgG or anti-rabbit antibodies (GE Healthcare) at 1:5,000 dilution. Chemiluminescence detection was performed by incubating the membranes with Amersham ECL Prime western blotting detection reagent (GE Healthcare) and analyzed under ChemiDoc XRS System (Bio-Rad).

2.10. Synaptic vesicles trafficking

Neurospheres plated on PLOF-coated glass coverslips were washed with PBS and exposed to a high potassium depolarizing solution (100mM KCl buffer; 5 mM Hepes-NaOH, 10 mM Glucose, 2.5 mM CaCl2, 1 mM MgCl2, 100 mM KCl, 37 mM NaCl), for 5 min. Afterwards, neurospheres were incubated with 10 µM FM 1-43 dye (Invitrogen) dissolved in normal saline (5mM KCl buffer: 5 mM Hepes-NaOH, 10 mM Glucose, 2.2 mM CaCl2, 1 mM MgCl2, 5 mM KCl, 137 mM NaCl) for 15 min and washed with ADVASEP-7 (Sigma) dissolved in 5 mM KCl buffer for 1 min. This was followed by 3 washes of 1 min with 5 mM KCl buffer prior to imaging. Exocytosis was stimulated

with 100 mM KCl buffer and samples imaged live in a fluorescence microscope (DMI6000, Leica) to monitor synaptic vesicle release. Fluorescence intensity was measured using ImageJ.

2.11. Calcium assay

Neurospheres were incubated with 1x Fluo4 Direct calcium reagent (Invitrogen) for 30 min at 37˚C, 5% CO_2 and 3% O_2 and for 15 min at RT. Samples were then imaged live using spinning disk microscopy (Nikon Eclipse Ti-E, confocal scanner: Yokogawa CSU-x1). Fluorescence change over time is defined as $\Delta F/F_0 = (F-F_0)/F_0$, where F is the fluorescence at any time point, and F_0 the baseline fluorescence determined by baseline fitting across the whole movie for each cell using PeakFit Software (v4.12).

2.12. Neurotransmitter release and quantification

Neurotransmitter synthesis and release was assessed at 18Mat. Neurospheres plated on PLOF-coated glass coverslips were washed with PBS and exposed to a high potassium depolarizing solution (100 mM KCl buffer, as described in section 2.10) for 15 min. The obtained supernatant was then collected and stored at -20°C prior to HPLC analysis. Dopamine in cell supernatants was quantified by HPLC after sample precipitation with 10% perchloric acid (PCA) (8:1). The separated monoamines were detected by fluorescence (Lakshmana and Raju 1997) and quantified by comparison to a calibration curve of dopamine. GABA was quantified by HPLC after supernatant freeze drying, using a pre-column derivatization method (Waters AccQ.Tag Amino Acid Analysis) previously described (Carinhas *et al.* 2010).

2.13. Electrophysiology Recording

Neurospheres were visualized in an inverted phase contrast microscope. Whole-cell voltage-clamp recordings were made from neurons within differentiated neurospheres at room temperature using an Axopatch 200B (Axon Instruments, Inc). Microelectrode contact to individual cells was made visually (cells on the neurosphere surface) or in deeper layers, using the blind approach common in brain slice recordings (Lima and Marrion 2007). Microelectrodes (1.2-3.0 MΩ) were pulled from borosilicate glass (Science Products GmbH). Two sets of solutions were used: one to record voltage activated K^+ conductances and to estimate membrane potential (Vm, under current clamp)(set 1), and a second to record excitatory ligand-activated currents (set 2). For set 1, electrodes were filled with solution containing (in mM): $KMeSO_4$ (140), $MgCl_2$ (1), HEPES (10), EGTA (10) $CaCl_2$ (1) Na_2ATP (2), Na-GTP(0.4), pH 7.2-7.3 titrated with KOH; (calculated free $[Ca^{2+}]$ = 60 nM by Webmaxclite v1.15, MaxChelator); external

solution to record outward K^+ currents contained (in mM): NaCl (135), KCl (5.4), $CaCl_2$ (2), $MgCl_2$ (1.5), HEPES (10), D-Glucose (25), pH 7.4 titrated with NaOH. In set 2, the pipette solution contained (in mM): CsF (140), NaCl (10), HEPES (10), EGTA (5), pH 7.3 titrated with CsOH; external solution (in mM): NaCI (100), KCl (5), HEPES (10), $CaCl_2$ (1.8), $MgCl_2$ (1), TEA-Cl (30), 4-amino-pyridine (3), D-Glucose (25), pH 7.4 titrated with NaOH. External bathing solution was constantly superfused (≈2-3 mL/min).

The estimated junction potentials (JPCalc, v2) for the external solution for set 1 of solutions was -8.8 mV and -8.5 mV for set 2 of solutions; data were not corrected for the junction potential. Currents were measured with cell capacitance compensation and series resistance compensation (80%), filtered at 2 kHz, sampled at 5 kHz, using a Digidata 1200 ADC converter (Axon Instruments) and pClamp software (v6). Time was allowed for the stabilization of the recording before experiments were conducted.

Different voltage-clamp protocols were applied according to the experimental needs, as follows: a) to study outward currents: a single command pulse to a fixed voltage was used and to isolate the fast current component such command pulse was preceded by a pulse to -120mV or to -30mV. Sets of incremental depolarizing commands were used for the characterization of the voltage dependence of activation. In this protocol, leakage current was compensated *a posteriori* from the current-voltage relation generated by a set of twelve pre-pulses in increments of 2 mV from -75 mV. To study steady-state inactivation, a single command step was preceded by incremental pre-pulses (Vicente *et al.* 2010). L-Glutamate induced currents were obtained by continuous recording under variable resting potentials. Glutamate was administered with a handmade adaptation of the perfusion system using gravity. Details of all the voltage protocols are given in the results section.

Whole-cell data were analyzed using Clampfit (v9) (Axon Instruments, Inc.), Pulsefit (v8.67) and Origin (v5) (Microcal Origin). Outward currents were measured as illustrated previously (Vicente *et al.* 2010). Peak current was taken for current amplitude of the faster current component; for each experiment, current decay was best fit with a sum of two exponentials (Eq. 3). For each current sweep, the amplitude of the slower component was taken at a time equal to $5x\ \tau_{fast}$ from the start of the command pulse. For steady-state inactivation and activation profiles, current values were fit with the following Boltzmann equation:

$$I= A_1-A_2/\{1+\exp[(V_{1/2}-V)/V_s]\} + A_2 \quad \text{(Eq.1)},$$

where I is the current amplitude at the test potential V, $V_{1/2}$ is the half-activation potential, V_s is the slope constant, A_1 and A_2 are coefficients.

In the case of voltage dependence of activation data were converted to conductance using the relationship $G=I/(V-E_{K+})$, where I is current amplitude, V is the step command potential and E_{K+} the estimated equilibrium potential for K^+. Results were plotted against the step command potential and fit with the following equation:

$$G= A_1-A_2/\{1+\exp [(V-V_{1/2})/V_s]\}+ A_2 \text{ (Eq.2)},$$

In the vast majority of the cases, current relaxations required the sum of two exponentials, using the following equation:

$$F(t) = A_f \exp (-t/ \tau_{fast}) + A_s \exp (-t/ \tau_{slow}) + C \text{ (Eq.3)},$$

Where τ_{fast} and τ_{slow} are the time constants of the fast and slow inactivating components respectively; A_{fast} and A_{slow} are the respective coefficients; C is a constant.

2.14. Statistical analysis

Data are expressed as the mean ± standard error of the mean. Data were analyzed using GraphPad Prism (version 5.01) by an analysis of variance (ANOVA), followed by Tukey's post-hoc multiple comparison test, and for metabolic profiling data using a two-tailed *t*-test. The α value was set at 0.05 with a 95% confidence interval and statistical significance was defined based on *p*-value (***p<0.001; **p<0.01; *p<0.05).

3. Results

3.1. hmNPC 3D differentiation induces molecular, metabolic and morphological remodeling

To determine the potential of hmNPC to generate innovative cellular models for CNS diseases, the cellular changes induced by 3D culture conditions were assessed. For multipotent hmNPC differentiation, cells expanded in 2D cultures were kept in an agitation-based culture system with constant orbital shaking (Fig. 2.1A). Following inoculation, hmNPC efficiently organized into neurospheres, resulting in a homogenous culture in terms of neurosphere size, ranging between 300 and 400 μm, as well as high cell viability (Fig. 2.1 B and B).

The onset of differentiation led to a significant downregulation (up to 4-fold) in the expression of the DNA polymerase co-factor *PCNA* (Fig. 2.2A), which was maintained during 32 days of differentiation, suggesting a decrease in cell proliferation. Concomitantly, the neurotrophic receptors *TrkA* and *TrkB* were positively modulated upon differentiation with a 2- and 28-fold increase at 18Mat, respectively (Fig. 2.2A). The expression of these tyrosine kinase receptors, activated by different neurotrophic factors, have been correlated with midbrain dopaminergic neurons during pre- and post-natal

development (Nishio *et al.* 1998; Numan *et al.* 2005), with reports suggesting an increased dependence on TrkB/BDNF signaling with differentiation (Zaman *et al.* 2004).

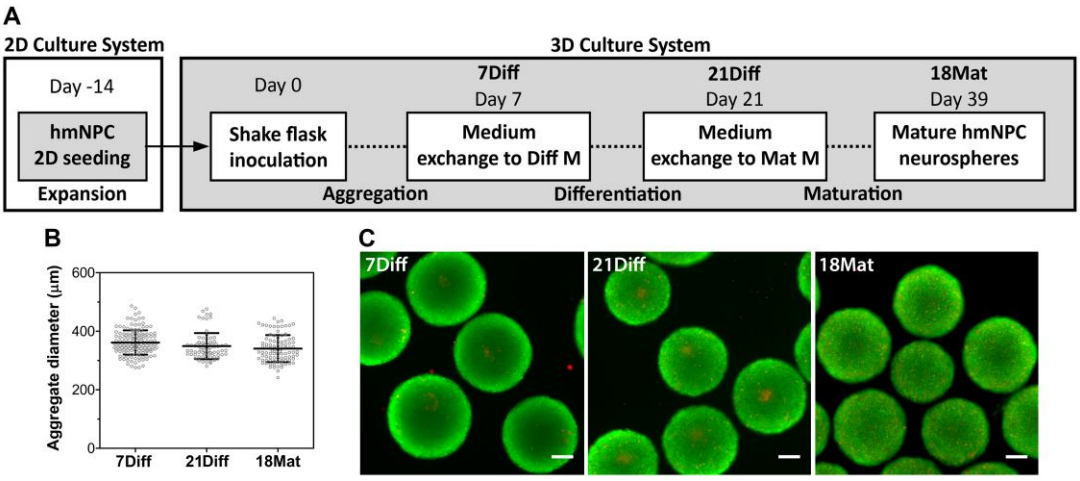

Figure 2.1 – Cell population dynamics of hmNPC as 3D neurospheres. (A) Workflow of expansion and 3D differentiation of hmNPC cultures (Diff M – Differentiation Medium; Mat M – Maturation Medium). **(B)** Neurosphere diameter as a function of time in culture. Data are from 3 independent experiments. **(C)** hmNPC neurosphere viability assay (fluorescein diacetate (FDA) - green; propidium iodide (PI) – red) along culture time. Scale bars, 100 µm. 7Diff – 7 days in aggregation medium; 21Diff – 14 days in differentiation medium; 18Mat – 18 days in maturation medium.

In contrast to 7Diff, when cells presented predominantly a progenitor phenotype, expressing the early neuroepithelial marker nestin (Fig. 2.2B), by 18Mat, a dense neurite network of βIII-tubulin positive neurons was observed both at the surface and inside the neurospheres (Fig. 2.2C). Moreover, differentiation into the three neural lineages was observed, as cells positive for the astrocytic-lineage marker glial fibrillary acidic protein (GFAP) and oligodendrocytic-lineage O4 were also detected (Fig. 2.2 D and E).

Morphological changes, including membrane rearrangements and cytoplasmic volume reduction, were observed during the differentiation process (Fig. 2.3), with a transition from lamellipodia, which were abundant in early differentiation stages (Fig. 2.3 A and C), towards filopodia (Fig. 2.3 B and D). In parallel, the complexity of cell processes and arborization of the network increased (Fig. 2.3 E and F), with thin filopodia (0.2-0.5 µm) protruding from the cell processes (Fig. 2.3H), which may indicate the ability of differentiating neurons to undergo synaptogenesis and form dendritic spines (Jontes and Smith 2000; Lendvai *et al.* 2000). Putative synaptic precursor sites were already visible in 7Diff neurospheres (Fig. 2.3L), suggesting that the synaptic machinery might be activated at early differentiation stages. Ultrastructural examination

revealed intact mitochondria, Golgi apparatus and endoplasmic reticulum both in undifferentiated (7Diff, Fig. 2.3K) and differentiated cultures (21Diff and 18Mat, Fig. 2.3 O and S respectively), consistent with the cells within the neurospheres being healthy and metabolically active. These features were observed throughout the neurospheres (for 7Diff, 21Diff and 18Mat, Fig. 2.3 I-J, M-N and Q-R respectively), which lacked any obvious sign of a necrotic center. Interestingly, in differentiated cultures (21Diff) it was also possible to identify cells with morphological features typical of oligodendrocytes, enfolding neighboring cells with membrane protrusions (Fig. 2.3P). By 18Mat putative synaptic sites enriched in synaptic vesicles and contacting adjacent cells were identified (Fig. 2.3T).

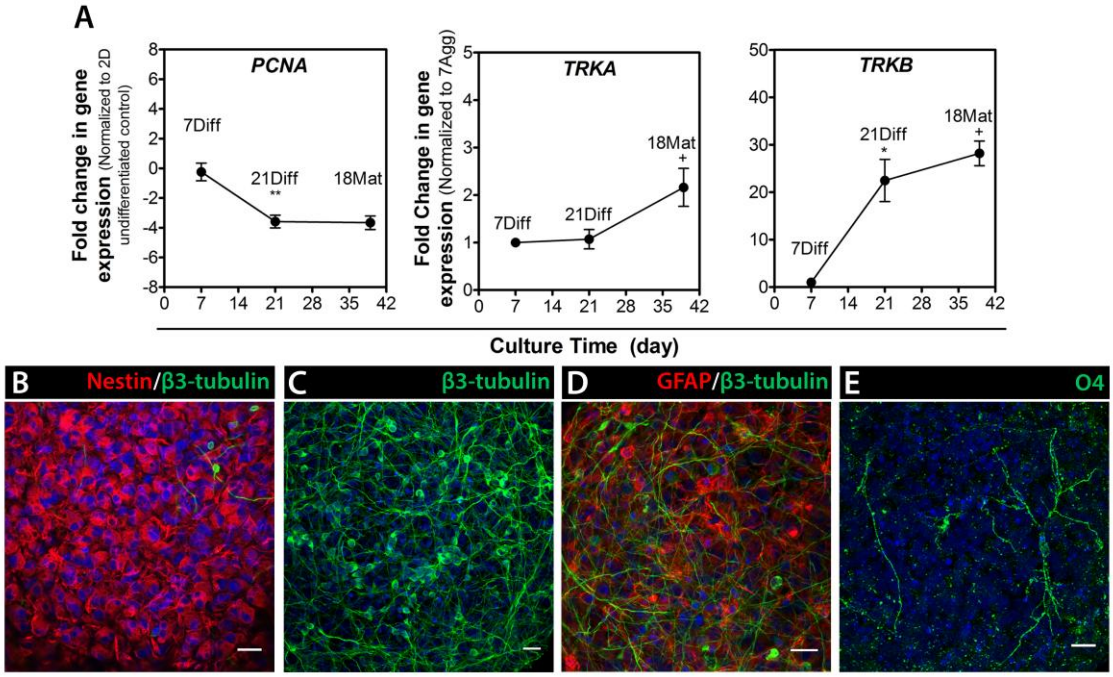

Figure 2.2 – Differentiation of hmNPC as 3D neurospheres. (A) RT-qPCR analysis of PCNA, TRKA and TRKB gene expression. Fold changes in gene expression normalized to undifferentiated hmNPC expanded in 2D culture systems (PCNA) or to 7Diff (TRKA and TRKB). Data are mean ± SEM of 3 independent cultures, asterisks indicate significant difference (*P < 0.05; **P < 0.01 vs 7Diff; +P < 0.05 vs 21Diff) by a one-way ANOVA analysis with a Tukey's post-hoc multiple comparison test. **(B-E)** Confocal immunofluorescence microscopy of whole neurospheres from 7Diff **(B)** and 18Mat **(C-E)**. Maximum intensity z-projections of 22 **(B)**, 7 **(C)**, 5 **(D)**, 25 **(E)** optical sections of 0.5 µm. Scale bars, 20 µm. Detection of nestin, β3-tubulin, GFAP and O4; nuclei were labeled with TO-PRO-3. 7Diff – 7 days in aggregation medium; 21Diff – 14 days in differentiation medium; 18Mat – 18 days in maturation medium.

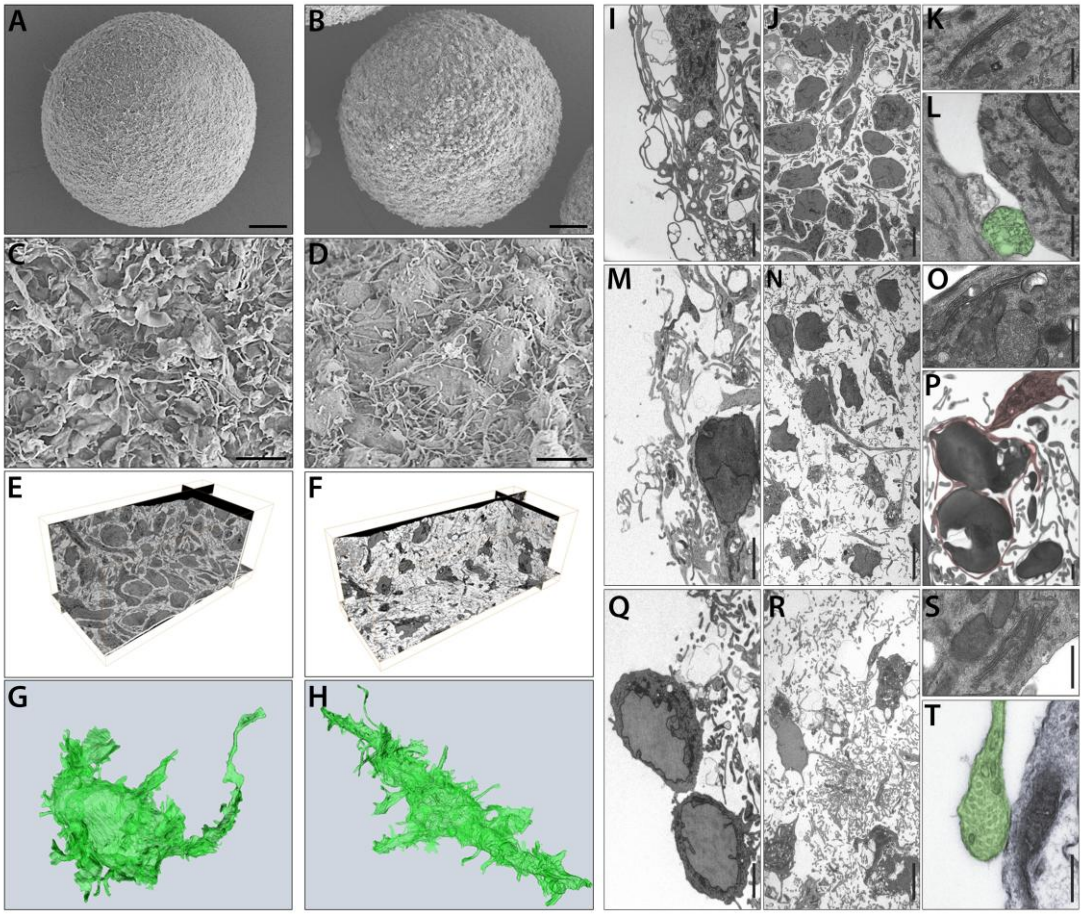

Figure 2. 3 – Morphological characterization of hmNPC neurospheres along differentiation. (A-D) Scanning electron microscopy (SEM) of neurospheres from 7Diff **(A, C)** and 21Diff **(B, D). (E, F)** Serial block-face scanning electron microscopy (SBF-SEM) of neurospheres from 7Diff **(E)** and 21Diff **(F)**. **(G, H)** Single cell reconstruction obtained from SBF-SEM data from 7Diff **(G)** and 21Diff **(H)**. Scale bars - 50 µm **(A, B)**; 5 µm **(C, D)**. Transmission electron microscopy of external **(I, M, Q)** and inner layers **(J, N, R)** of hmNPC neurospheres at day 7Diff **(I, J)**, 21Diff **(M, N)** and 18Mat **(Q, R)**. Inset of a cell depicting Golgi apparatus at 7Diff **(K)**, 21Diff **(O)** and 18Mat **(S)**. **(L)** Putative site of synaptogenesis at 7Diff (highlighted in green). **(P)** Oligodendrocyte-like cell at 21Diff (highlighted in red). **(T)** Putative synaptic site at 18Mat (highlighted in green). Scale bars - 2 µm **(I, M, Q)**; 5 µm **(J, N, R)**; 0.5 µm **(K, L, O, P, S, T)**; 0.2 µm **(P)**. 7Diff – 7 days in aggregation medium; 21Diff – 14 days in differentiation medium; 18Mat – 18 days in maturation medium.

Aiming at assessing metabolic alterations along differentiation, ^{1}H-NMR metabolic profiling of cell supernatants along 48 hours of culture was determined for undifferentiated and differentiated hmNPC neurospheres (Fig. 2.4). 7Diff neurospheres presented high glucose consumption to lactate production ratio ($Y_{Lac/Glc}$ = 1.68 ± 0.22), indicating anaerobic glucose utilization in progenitor cells. Despite taking up glucose at lower rates (Fig. 2.4B), differentiated hmNPC neurospheres maintained the reliance on glyco-

lytic metabolism ($Y_{Lac/Glc}$= 1.91 ± 0.12). As for pyruvate uptake and alanine accumulation rates, a four-fold increase and decrease, respectively, was observed (Fig. 2.4B), suggesting changes during differentiation in the alanine-lactate shuttle. Although glutamate was not detected in hmNPC cultures, its cyclized form pyroglutamate was released at higher rates in differentiated cultures (Fig. 2.4 A and B). Conversely, the accumulation rates of 2-oxoisocaproate and methylsuccinate, metabolites that result from the metabolism of branched-chain amino acids (BCAAs), were maintained in undifferentiated and differentiated cultures.

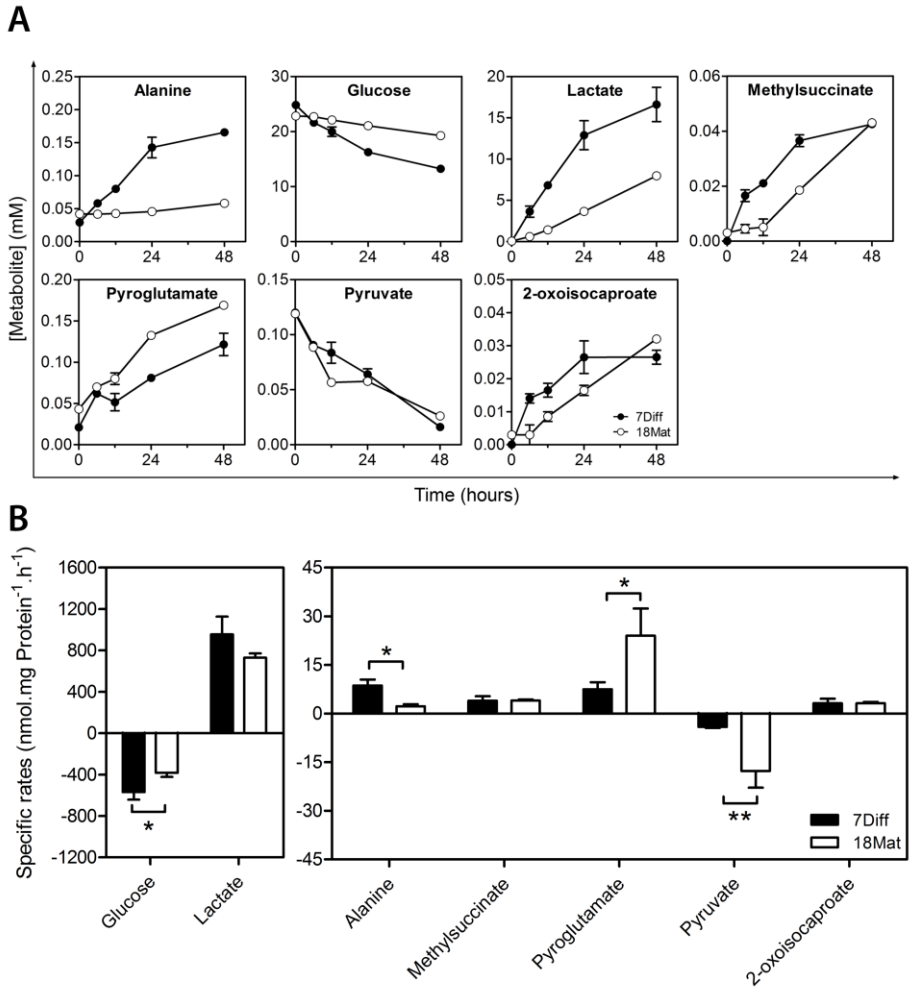

Figure 2.4 – Metabolic profiling of hmNPC neurospheres along differentiation. (A) Concentration profiles of the main metabolites quantified in the exometabolome of hmNPC cultures at 7Diff (black circles) and 18Mat (white circles) that have significantly changed during 48h. Data from one representative experiment of 2 independent experiments. **(B)** Specific rates (nmol.mg Protein-1.h-1) determined at 7Diff and 18Mat. Data are mean ± SEM of regression analysis performed with all time points from 2 independent experiments, with 2 replicates each. Asterisks indicate significant difference (*P < 0.05; **P < 0.01) by a two-tailed t-test. 7Diff – 7 days in aggregation medium; 18Mat – 18 days in maturation medium.

3.2. 3D differentiation activates neurogenesis developmental pathways

A coordinated change in gene expression is a hallmark of cellular differentiation. Therefore, a study on the transcriptomic programs that were modulated during hmNPC neurosphere differentiation was pursued. Global transcriptional analysis was performed in differentiated neurospheres (21Diff) and compared with undifferentiated hmNPC (Fig. 2.5A). The gene expression profile showed that 807 probes, which corresponded to 664 unique genes, were differently modulated upon neurosphere differentiation. As), were maintained in undifferentiated and differentiated cultures.

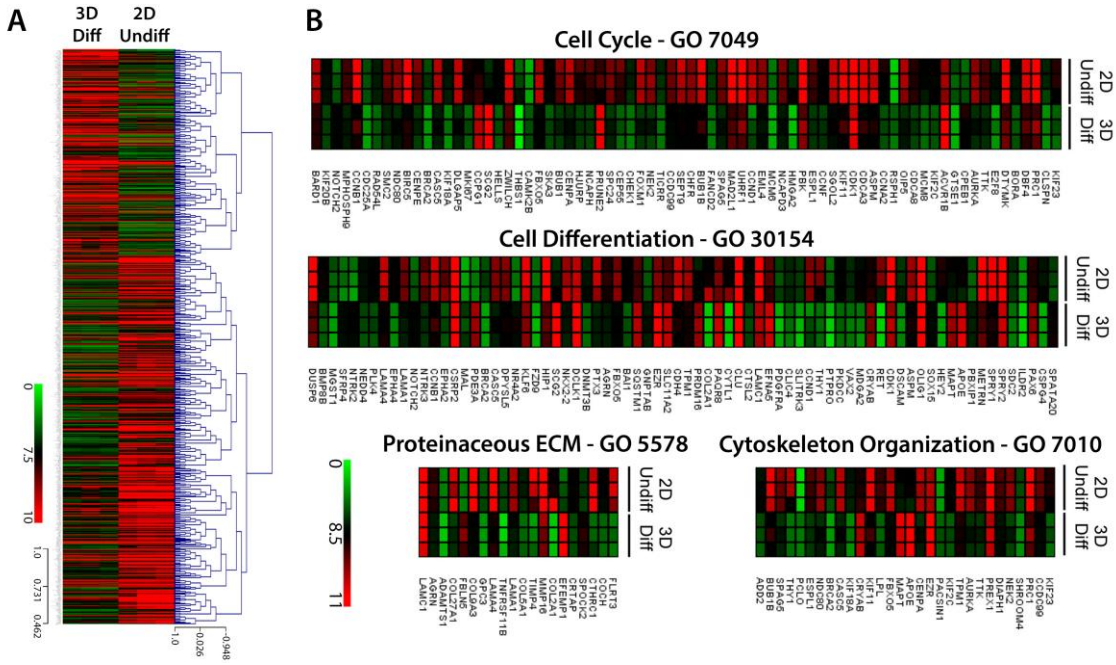

Figure 2.5 – Global gene expression analysis of differentiated hmNPC neurospheres. (A) Hierarchical clustering of the levels of modulation of 807 probes, corresponding to 664 unique genes, significantly altered (FDR ≤0.005, 2-fold change in upregulated and downregulated) compared to undifferentiated cells (data of 3 independent cultures; each column represents an independent sample). Color bar represents the scale of RMA-normalized log2-transformed expression value of each transcript of the replicates. **(B)** Heat maps of the expression patterns (RMA normalized values) of genes altered in each replicate of four significantly GO categories (corrected p-value≤ 0.01) according to a color scale ranging from green to red. Enriched biological clusters consist in Cell cycle (FDR 4.2x10-18), Cell differentiation (3.2x10-4), Proteinaceous extracellular matrix (6.9x10-3), Cytoskeleton organization (2.58x10-3).

Gene Ontology (GO) analysis showed that the 3D differentiation process led to a significant enrichment in genes involved in cell cycle, cell differentiation, cytoskeleton organization and proteinaceous extracellular matrix (Fig 2.5B). Genes involved in the cell cycle progression such as *MKI67*, *cyclin A2*, *cyclin B1*, *cyclin D1* and mitotic genes

like *BUB1B*, *BUB1*, *CCNB1*, *CDC25A*, *CDK1*, *AURKA*, *KIF23*, *MAD2L1*, *BIRC5* were significantly downregulated after 3D differentiation, suggesting an increase in cells exiting the cell cycle. Additionally, markers of neural stem cells, such as *SPRY1*, *SPRY2*, *FBXO5*, were also downregulated, whereas genes involved in neurogenesis and neuronal metabolism, namely *NOTCH2*, *PAX6*, *PRDM16*, *NR4A2*, *PDE3A*, *DCLK1*, *SCG2*, *PAQRB*, *EFNA5*, *MAPT*, *APOE* and *MAL*, were increased. The activation of TGFβ1 signaling associated genes, such as *ACVR1B* or *PRUNE2*, which are involved in the maintenance of mature CNS (Iwama *et al.* 2011), suggests maturation of the neuronal population. Several extracellular matrix-associated genes were downregulated after differentiation, such as genes involved in collagen synthesis and binding (*COL2A1*, *COL5A1*, *COL9A3*, *COL27A1*, *CTHRC1*, *CRTAP*), laminin synthesis (*LAMA1* and *LAMA4*), and fibronectin binding (*FLRT3*). Concomitantly, an upregulation of *SPOCK2*, *EFEMP1* and *FBLN5* genes, which code for proteins involved in glycosaminoglycans binding and proteoglycans (Bandtlow and Zimmermann 2000), was observed. Together these results suggested a significant remodeling of the ECM composition in the 3D environment of the differentiated neurospheres towards a higher similarity to the *in vivo* neural ECM composition (Dwyer and Matthews 2011).

3.3. Extended 3D differentiation enhances dopaminergic phenotype

Neuronal differentiation towards the dopaminergic lineage depends on specific developmental programs that rely on the sequential activation of specific transcription factors. At 21Diff, an increase in the expression levels of *NURR1*, a transcription factor critical for the development of the dopaminergic phenotype, *TH* (tyrosine hydroxylase), the rate-limiting enzyme in dopamine synthesis and *DRD2 (*dopamine receptor D2), indicated the activation of genetic pathways controlling the dopaminergic phenotype (Fig. 2.6 *A*-*C*). Extending the differentiation process for additional 18 days in presence of dbcAMP, a membrane-permeable analogue of cAMP, led to a significant upregulation of these markers (10-, 450- and 4-fold increase at 18Mat relatively to day 7, for *NURR1, TH*, and DRD2 respectively) (Fig. 2.6 *A*-*C*). Moreover, the increase in TH protein levels along differentiation (Fig. 2.6*E*) and detection of cells positive for TH (Fig. 2.6*F*), as well as dopaminergic transcription factor Pitx3 (Fig. 2.6*H*) at 18Mat, further suggested the establishment and maintenance of the dopaminergic phenotype.

Along with the expression of dopaminergic markers, a significant upregulation of the pre-synaptic vesicular GABA transporter (*vGAT*) was observed (Fig. 2.6*D*), suggesting the co-existence of dopaminergic and GABAergic neuronal populations.

Altogether, the presented data indicates that hmNPC neurospheres retained their midbrain developmental patterns by expressing key dopaminergic markers upon dif-

ferentiation, and revealed the importance of extending the differentiation process by 18 days to increase the neuronal differentiation efficiency.

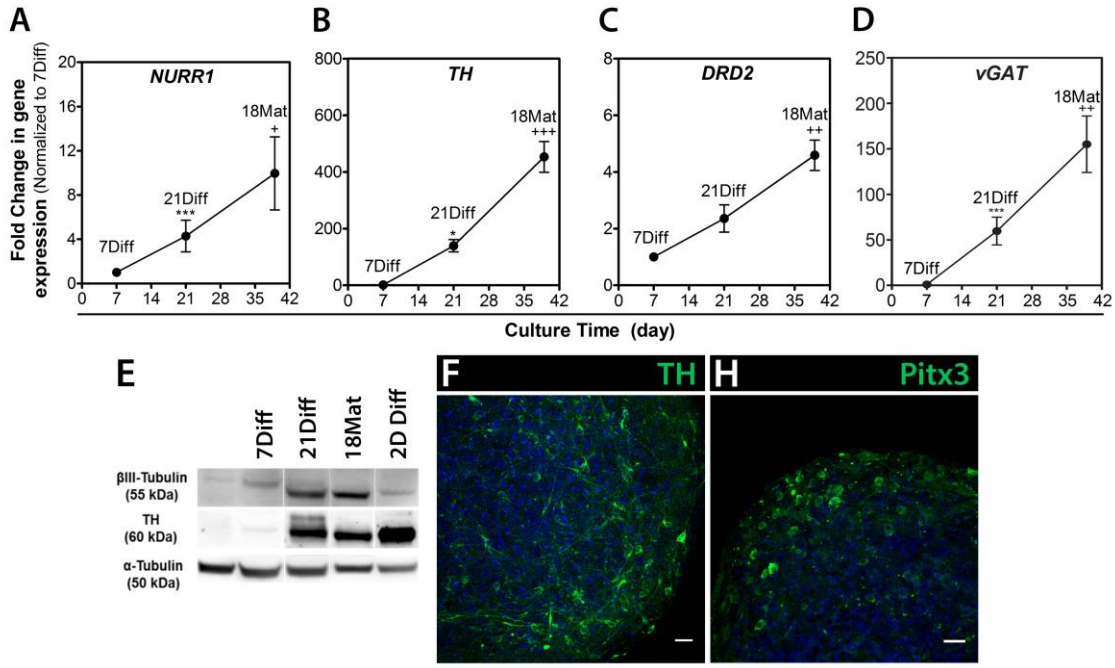

Figure 2.6 – Neuronal differentiation of hmNPC neurospheres. (A-C) RT-qPCR analysis of *NURR1* **(A)**, *TH* **(B)**, *DRD2* **(C)** and *vGAT* **(D)** gene expression. Fold changes in gene expression were normalized to 7Diff. Data are mean ± SEM of 3 independent cultures, asterisks indicate significant difference (*p<0.05, ***p<0.001 vs 7Diff; $^{+}$p<0.05, $^{++}$p<0.01, $^{+++}$p<0.001 vs 21Diff) by a one-way ANOVA analysis with a Tukey's post-hoc multiple comparison test. **(E)** Western blot analysis of undifferentiated hmNPC and neurospheres along differentiation. α-tubulin detection was used as loading control. Data from one representative experiment of 3 independent experiments. P0 – undifferentiated hmNPC expanded in 2D culture systems; 7Diff – 7 days in aggregation medium; 21Diff – 14 days in differentiation medium; 18Mat – 18 days in maturation medium. **(F-H)** Confocal immunofluorescence microscopy of whole neurospheres from 18Mat. Maximum intensity z-projections of 5 **(E)** and 56 **(F)** optical sections of 0.5 **(E)** and 0.33 µm **(F)**. Detection of TH and Pitx3, nuclei were labeled with TO-PRO-3. Scale bar, 20 µm.

3.4. Neuronal maturation and synaptic functionality

In addition to the increased expression of key lineage-specific markers, it was essential to demonstrate the functional properties of the differentiated cells derived from hmNPC neurospheres. To assess neuronal synaptic maturation, the expression of proteins involved in synaptic formation and homeostasis was analyzed. Expression of different pre-synaptic markers, such as synapsin II (*SYN2*), synaptophysin (*SYP*) and synaptotagmin I (*SYT1*), gradually increased during differentiation, reaching up to 5-, 2- and 6-fold greater levels by the end of the differentiation process (Fig. 2.7A). Addi-

tionally, synaptophysin, an integral pre-synaptic vesicle glycoprotein, was detected in a typical punctate pattern across the differentiated neurospheres (Fig. 2.7B). These results together with the ultrastructural evidence (Fig. 2.3) suggest that pre-synaptic components cluster in differentiated hmNPC neurospheres into synaptic vesicle-like organelles. The 1.5-fold increase in the *PSD95* gene, encoding for postsynaptic density protein 95 at 18Mat suggested the accumulation of post-synaptic markers in these cultures (Fig. 2.7A).

Synaptic activity was assessed using the fluorescent probe FM1-43 (Gaffield and Betz 2006; Hoopmann *et al.* 2012), by the ability of differentiated neurospheres to respond to depolarizing stimuli. Neurospheres at different stages of differentiation were loaded with FM1-43, and their destaining kinetics upon depolarization indicated that the same depolarizing stimuli led to a modest decrease in the fluorescence intensity of 7Diff and 21Diff neurospheres, when compared to neurospheres at the end of the differentiation process (18Mat), in which fluorescence dropped to less than half of its initial value (Fig. 2.7D). These results suggested that differentiated neurospheres showed a higher number of mature neurons with functional synaptic terminals, which were able to respond to depolarizing stimuli.

To further assess neuronal functionality, Fluo-4 based Ca^{2+} imaging studies were performed in 18Mat neurospheres (Fig. 2.7C). A variety of spontaneous firing patterns identified in individual cells may suggest the presence of both neurons and astrocytes, since the latter can also present spontaneous Ca^{2+} transients, although with significant lower frequencies compared to neurons (Ikegaya *et al.* 2005; Tashiro *et al.* 2002).

Moreover, an important physiological property of dopaminergic neurons is their ability to produce and release dopamine in response to a depolarizing stimulus. Differentiated neurospheres (18Mat) in presence of 100 mM KCl were able to respond, releasing 252 ng of dopamine per mg of total protein (Fig. 2.7E), further indicating a mature phenotype of the dopaminergic neurons in culture. In agreement with observation of upregulation of GABAergic marker *vGAT*, differentiated hmNPC neurospheres were also able to synthesize and release GABA (Fig 2.7E), in a KCl-dependent response, further suggesting the presence of mature GABAergic neurons.

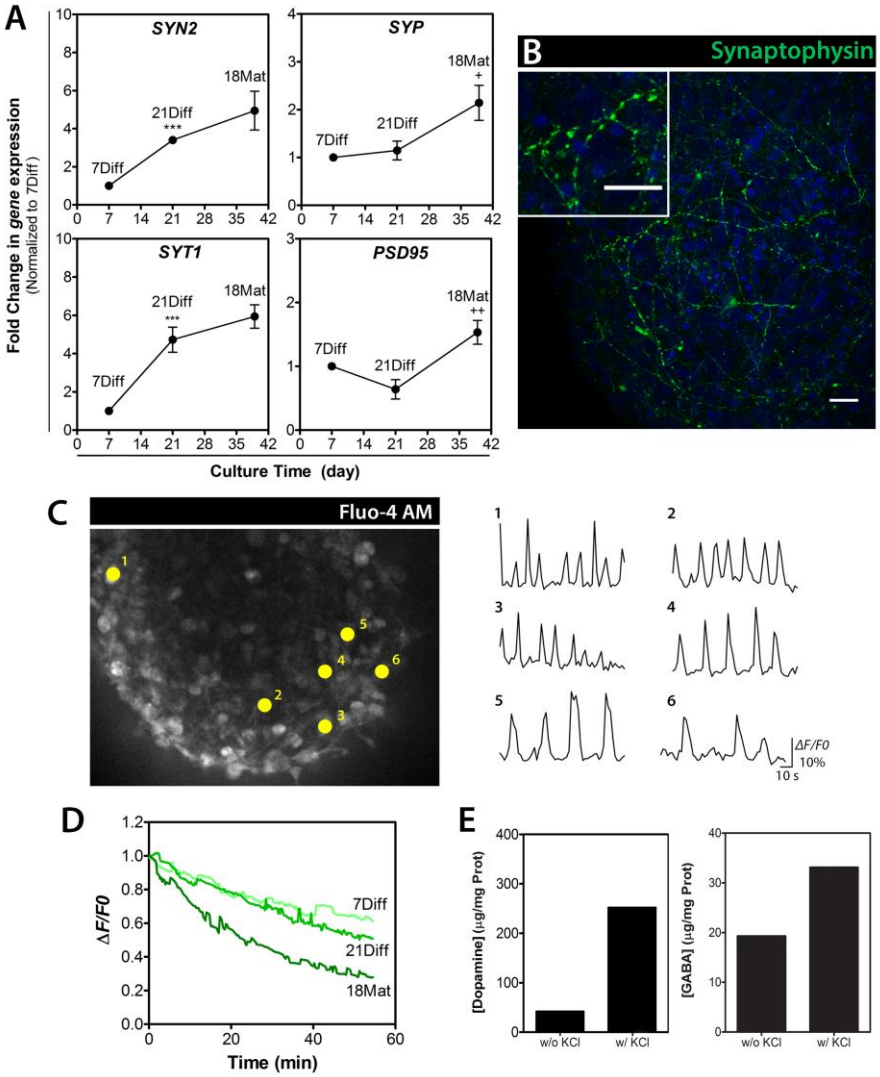

Figure 2.7 – Synaptic marker enrichment and synaptic vesicle trafficking in hmNPC neurospheres along differentiation. (A) RT-qPCR analysis of *SYN2*, *SYP*, *SYT1* and *PSD95* gene expression. Fold changes in gene expression were normalized to 7Diff. Data are mean ± SEM of 3 independent cultures, asterisks indicate significant difference (***$p<0.001$ vs 7Diff; $^{+}p<0.05$, $^{++}p<0.01$ vs 21Diff) by a one-way ANOVA analysis with a Tukey's post-hoc multiple comparison test. **(B)** Confocal immunofluorescence microscopy of whole neurospheres from 18Mat. Maximum intensity z-projections of 16 optical sections of 0.5 µm. Detection of synaptophysin, nuclei were labeled with TO-PRO-3. Scale bars, 20 µm. **(C)** Spontaneous Ca^{2+} oscillations in differentiated neurospheres at day 18Mat. Analysis of Ca^{2+} oscillations in individual neurons (numbers correspond to individual cells analyzed simultaneously); data are from one representative experiment of 3 independent experiments. **(D)** Fluorescence intensity analysis of FM 1-43 dye in exocytosis inducing conditions; data are from one representative experiment of 3 independent experiments. **(E)** Dopamine and GABA release quantification with and without KCl stimuli; data are from one representative experiment of 3 independent experiments. 7Diff – 7 days in aggregation medium; 21Diff – 14 days in differentiation medium; 18Mat – 18 days in maturation medium.

3.5. Voltage activated and glutamate evoked currents

Functionality of neurons within differentiated neurospheres was further accessed by whole-cell voltage-clamp recordings. Cells exhibited hyperpolarized membrane potential values (V_m= -70.1 ± 0.3 mV n= 9), indicating a high level of polarity. Voltage-activated potassium currents recorded at physiological K^+ concentrations generated typical neuronal outward currents (Fig. 2.8A). The outward current following the prepulse to -120 mV comprised two major components, I_{fast} and I_{slow}, which were fit with a sum of two exponentials to determine time constants of 25.9±0.9 ms (n=9) (τ_{fast}) and 234.4±5.4 ms (n=9) (τ_{slow}). In contrast, the outward current following a prepulse to -30 mV comprised only one slow component, as current decay was best fit by a single exponential with a time constant of 235.7±6.3 ms (n=7). The subtraction of the two current traces enabled to isolate A-type-like currents (I_{fast}), which were quickly activated (≤ 3 ms), indicating a strong dependency on voltage for inactivation. The current decay was best fit with a single exponential with time constant of 23.4 ± 1.1 ms (n=7), values of the same range as those reported as typical for A-type current (Coetzee *et al.* 1999). K^+ currents were also characterized in terms of voltage dependence of activation (Fig. 2.8B), where current records were converted to conductance, and steady-state inactivation (Fig. 2.8C). Data were fit with the Boltzmann equation (eq.1) obtaining for activation a $V_{1/2}$ value of -0.3 ± 0.4 mV (n=4) and 5.3 ± 0.5mV (n=4), for I_{fast} and I_{slow} respectively. As for inactivation a $V_{1/2}$ value of -81.3 ± 1.6mV (n=3) was obtained.

As midbrain mainly receives glutamatergic projections from other surrounding brain regions (Korotkova *et al.* 2004), glutamate-evoked ionic currents were evaluated to assess the functionality of glutamate receptors. Glutamate was added to clamped cells under different holding potentials, with increased responses observed at a more hyperpolarized potential (-70 mV) and reversed currents obtained under positive potentials (Fig. 2.9A). A linear current-voltage relationship was obtained with a reversing potential close to zero mV (Fig. 2.9 B). The observed glutamate-evoked currents were characterized by a dual phase response, which was more noticeable over a longer period of time (Fig. 2.9 C), with a faster response followed by a slower and more sustained current. In the presence of antagonists of AMPA/kainate and NMDA glutamate receptors (CNQX 10 μM and AP5 10 μM, respectively), no or small responses to glutamate were registered (Fig. 2.9 D). After 15 minutes washing, the same clamped cell (n=3) exhibited a robust response to glutamate, confirming the presence and specific activation of glutamate receptors during glutamate application.

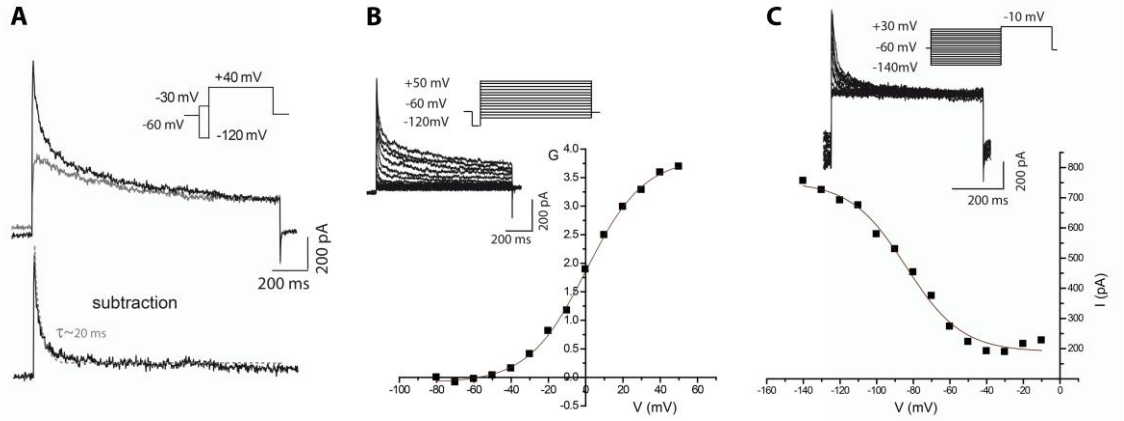

Figure 2.8 – Voltage-activated potassium (K_v) currents in hmNPC differentiated neurospheres. (A) Whole-cell voltage-activated K^+ current were evoked by a depolarizing step to +40 mV for 0.8 s (holding potential of -60 mV) preceded by a prepulse of 150 ms to -120 mV (black trace) or to -30 mV (grey trace). On the bottom the resultant subtraction of both currents is shown to isolate the fast current component (A-type), which was best fit by a single exponential (discontinuous line) with a time constant of 20.1 ms. **(B-C)** Voltage-dependence of steady-state activation **(B)** and inactivation **(C)**. **(B)** Currents evoked by depolarizing steps in increments of 10 mV (1040 ms in duration) following a -120 mV hyperpolarizing prepulse (150 ms in duration from holding potential of -60 mV). Consequent activation curve of peak current ($V_{1/2}$=-0.3 ± 0.4 mV; n=4). **(C)** Currents evoked by a command pulse to +40 mV (400 ms in duration) preceded by prepulses from -140 to +30 mV (600 ms in duration from -60 mV), in 10 mV increments. Consequent inactivation curve of peak current ($V_{1/2}$=-81.3 ± 1.6 mV; n=3).

4. Discussion

This study demonstrated that hmNPC can be efficiently differentiated within neurospheres into functional dopaminergic and GABAergic neurons, cells from the astrocytic and oligodendrocytic lineages and be maintained in long-term *in vitro* cultures. By providing homogeneous aggregation and efficient differentiation of hmNPC, with establishment of 3D cell-cell interactions, an efficient scalable culture system was attained, which is directly transferable to feeding of HTS platforms. These features are critical in basic research on the pathways responsible for the onset and progression of human neurological disorders, as well as for drug discovery.

The cell model presented herein can represent an alternative to organotypic cultures in which cytoarchitecture and cellular functionality of the original tissue (Bodea and Blaess 2012; Pampaloni *et al.* 2007) are preserved but fail in maintaining long-term cellular viability and phenotype and present limited availability.

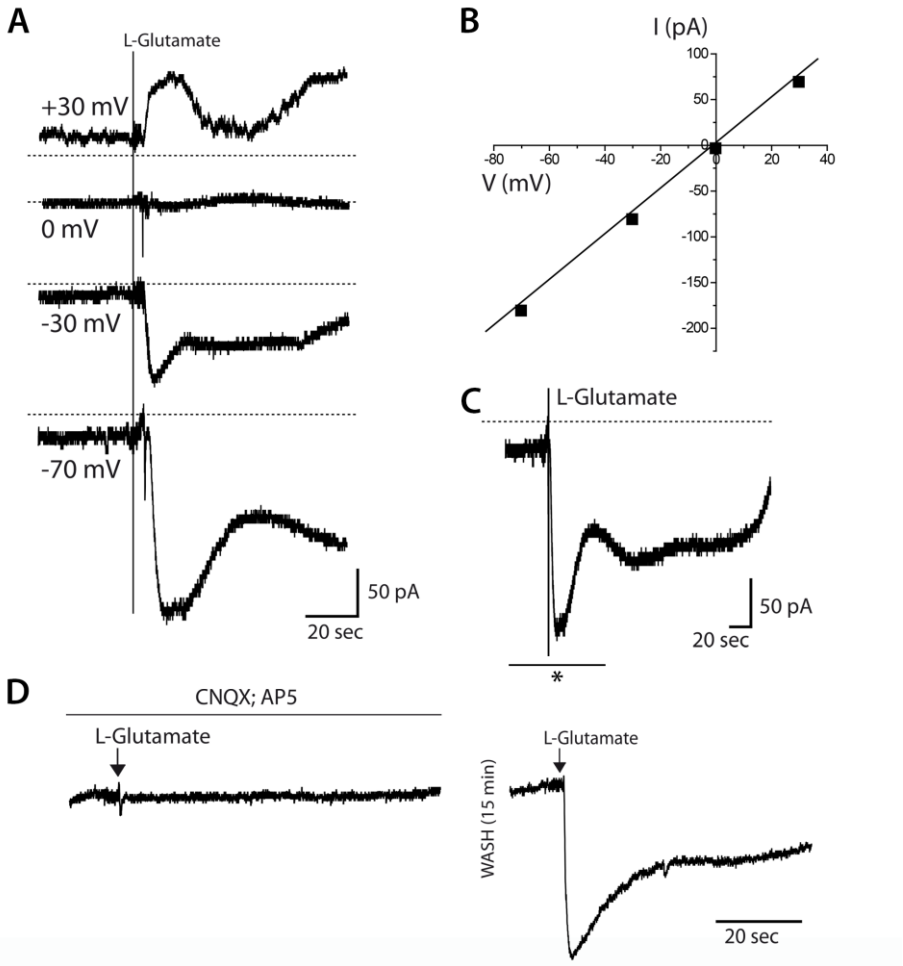

Figure 2.9 - Whole-cell voltage-clamp recordings of glutamate-gated currents in hmNPC differentiated neurospheres. (A) Glutamate-gated responses from holding potentials of +30, 0, -30 and -70 mV. **(B)** Peak current-voltage (I-V) relationship of glutamate evoked responses. **(C)** Glutamate-evoked response displayed with longer period to show typical dual response to glutamate (* represents time detail of recording at -70 mV in the bottom panel of **A**) **(D)** Glutamate-gated current inhibition by CNQX and AP5 (AMPA/kainate and NMDA antagonists, respectively), response recovered upon 15 min wash.

hmNPC have been initially established and extensively described in 2D culture systems, demonstrating an efficient differentiation into the dopaminergic lineage (Schwarz 2007; Schaarschmidt *et al.* 2009a; Storch *et al.* 2001). Nevertheless, these 2D culture systems recapitulate to a lower extent the three-dimensional cell-cell interactions of the brain. The ability of hmNPC to be efficiently differentiated as neurospheres was demonstrated, by the expression of several neuronal and dopaminergic-specific markers after 14 days of differentiation. The extension of culture time in 18 days further promoted the neuronal differentiation, successfully aiding the progression into later developmental stages. Increased neuronal maturation and synaptic functionality

was attained, mimicking the developmental stages that multipotent mesencephalic progenitors undergo to acquire a mature dopaminergic neuronal phenotype. Differentiation of hmNPC neurospheres activated the expression of *NURR1*, with significant upregulation of the mature dopaminergic markers, *Pitx3*, *TH*, and *DRD2*, suggesting the preservation of midbrain region identity and developmental programs. These depend on the integration of various external cues culminating in the activation of signaling pathways, such as the Wnt/β-catenin canonical pathway that mediates the proliferation and differentiation of $NURR1^+$ immature dopaminergic neurons (Joksimovic *et al.* 2009; Alves dos Santos and Smidt 2011). In later stages of differentiation, NURR1 is required for dopaminergic neuron specification and maturation, regulating the expression of mature markers, such as Pitx3 and TH (Ang 2006; Prakash and Wurst 2006; Abeliovich and Hammond 2007).

Moreover, the expression of vGAT and the ability of differentiated neurospheres to synthesize and release GABA upon stimuli suggested the presence of a GABAergic population, as previously demonstrated in 2D cultures of differentiated hmNPC (Wegner *et al.* 2008). These evidences further suggest that the developed 3D model can mimic the main midbrain developmental pathways, generating heterogeneous neurospheres with the two neuronal subpopulations found in the human midbrain, dopaminergic and GABAergic (Korotkova *et al.* 2004).

Extension of the differentiation process was performed in presence of dbcAMP, which has been described to promote the differentiation, maturation and survival of midbrain dopaminergic neurons (Goldberg and Barres 2000; Michel and Agid 1996). Moreover, cAMP has been reported to enhance neuronal differentiation in NPC derived from other brain regions, such as forebrain in murine NPC (Zahir *et al.* 2009), and also in other pluri/multipotent cells, as mesenchymal stem cells, inducing the expression of *NURR1* and *TH* (Tio *et al.* 2010).

The transition from multipotent neural progenitors towards a mixed culture of differentiated neural cells induced modulation of cellular metabolism. The maintenance of a highly glycolytic phenotype despite lower glucose consumption, together with increased pyruvate consumption, suggested the recapitulation of metabolic features of mature neural cells. Both neurons and astrocytes can utilize extracellular pyruvate (Zwingmann and Leibfritz 2003) and production of lactate from pyruvate has been reported for neurons cultured in glucose containing medium as a faster way to recycle NAD^+ produced in glycolysis (Cruz *et al.* 2001). Neural reliance on glycolytic metabolism has been linked to the high energy requirements of the brain, where glycolysis may act as a fast response pathway to accommodate high ATP demands, namely to enable the constant activity of Na^+/K^+ ATPases, essential for maintenance of neuronal

membrane ionic gradients (Fornazari *et al.* 2011; Magistretti and Allaman 2013) and/or provide local ATP supply to molecular motors (Zala *et al.* 2013).

Differentiated neurospheres presented significantly increased accumulation of pyroglutamate, which can derive from degradation of proteins containing modified N-terminal glutamic acid residues or from glutamate/glutamine cyclization (Schilling *et al.* 2008) and has been suggested to act as a reservoir of neural glutamate, the main excitatory neurotransmitter in the CNS (Kumar and Bachhawat 2012).

The accumulation of intermediates of BCAA catabolism (2-oxoisocaproate and methylsuccinate), points to recapitulation of important astrocyte-neuron nitrogen shuttling systems of human CNS (Bixel *et al.* 2004), complementing the extensively described glutamine–glutamate cycle between neurons and astrocytes (Magistretti and Allaman 2013). The obtained results suggest that establishment of some of these nitrogen shuttles may occur in an early stage of CNS development and maturation.

The developed cell model, in combination with NMR and/or mass spectrometry analysis of isotopic (^{13}C, ^{15}N) tracer studies, can be applied in depicting these neural metabolic shuttles and contribute to increase the mechanistic understanding on the correlation between cell metabolism and stemness/cell identity determination driven by genetic and epigenetic switches (Folmes *et al.* 2012).

Upon differentiation, neurospheres exhibited extensive ECM composition remodeling and morphological rearrangements. Gene expression results evidenced a closer resemblance to the *in vivo* neural ECM, which is mainly comprised of glycosaminoglycans, namely hyaluronan, heparan sulfate proteoglycans (HSPGs) and chondroitin sulfate proteoglycans (CSPGs) and displays low levels of fibrilliar proteins, such as collagens, fibronectin, and laminin (Ruoslahti 1996; Dwyer and Matthews 2011), regularly used as matrix in 2D cultures. This was accompanied by changes in the plasma membrane architecture, with a transition from highly prevalent lamellipodia found in undifferentiated neurospheres towards a dense filopodia network in differentiated neurospheres. Filopodia have been shown to be paramount in dendritic branching, axonal development and synapse formation (Zito *et al.* 2004). The formation of newborn synapses is concomitant with an increase in expression of synaptic markers (Valtorta *et al.* 2011). The expression levels of synaptic proteins, such as SYN2, SYP, SYT1 and PSD95, steadily increased during hmNPC neurosphere differentiation. Moreover, synaptophysin-positive organelles could be detected in puncta along neuronal processes, suggesting that these neurons are fully competent for the biogenesis and clustering of synaptic vesicles.

Neurons in differentiated neurospheres were able to elicit spontaneously Ca2+ oscillations at frequencies reminiscent of action potential firing, as well as to respond to depolarization stimuli leading to FM-1-43 and neurotransmitter release (dopamine and GABA). These results indicate that midbrain neurons generated in hmNPC neurospheres contain functional synapses, where the rapid influx of Ca2+ through voltage-dependent Ca^{2+} channels arriving in the nerve terminals triggers fusion of neurotransmitter-containing vesicles with the plasma membrane, leading to neurotransmitter release into the synaptic shaft (Evans and Cousin 2007). Furthermore, the electrophysiology recordings, which to our knowledge are the first recordings from single cells within the 3D structure of neurospheres, demonstrated that the generated neurons were fully polarized ($V_m \approx$ -70mV) at potentials modulated by functional voltage activated ion channels. The registered voltage-activated K^+ currents pointed out for the existence of at least two populations of voltage-gate K^+ channels (K_V), one underlying I_{fast} and other underlying I_{slow}. The conspicuous I_{fast} component showed typical patterns of an A-type current, which are perceived to have high relevance in numerous physiological and pathological contexts. From the K_V channels/subunits that are known to be responsible to trigger A-type currents, two emerge as probable candidates to underlie the I_{fast} component. Considering that this current showed (i) a voltage profile for activation with a $V_{1/2}$ of around -10 mV (considering a -9 mV junctional potential), which points out for high threshold activating channels, (ii) a hyperpolarized voltage dependence of inactivation and, most noticeably, (iii) a time constant for the inactivation time course in the order of 20 ms, the channels K_V1.4 and K_V4.2 are envisaged to be the most likely candidates to be present in neurons of hmNPC differentiated neurospheres. Indeed, extensive characterization on a predominant A-type current in hmNPC cells differentiated in 2D cultures was reported (Schaarschmidt *et al.* 2009b), which according to the authors is evoked by K_V4.2 channels. Nevertheless, one cannot exclude the possibility of K_V1.4 channels to be also present in the differentiated neurospheres.

Moreover, the excitability of differentiated hmNPC neurospheres was challenged by the addition of glutamate, with the generated neurons demonstrating to be able to elicit glutamate-gated currents with two clear components, one faster followed by a slower and more sustained current. The linear voltage current relationship reversing close to 0 mV corroborates the involvement of channels with unspecific cationic conductance. Furthermore, these currents were blocked by co-incubation of AMPA/kainate and NMDA antagonists (CNQX and AP5, respectively). Altogether, these results showed that hmNPC neurospheres contain mature neurons with functional glutamate receptors, which are most likely AMPA/kainate and NMDA receptor types, as well as the associated channels. These observations are in agreement to what

was described previously for hmNPC differentiated in 2D cultures (Wegner *et al.* 2009). The presence of functional post-synaptic glutamatergic molecular machinery further suggests that the developed 3D model recapitulate *in vivo* features, since the midbrain is known to receive and integrate multiple glutamatergic inputs from other brain regions (Korotkova *et al.* 2004).

This work established a novel culture system that yields a reproducible human 3D CNS cell model enriched in dopaminergic neurons. By combining scalable protocols with an extensive toolbox of characterization methods, a comprehensive set of developmental data on the *in vitro* differentiation of human midbrain neurons was generated. This approach can be extended to other sources of human neural stem cells (hNSC), such as patient-derived iPSC, based on recent reports on the generation of regionally-specified neural progenitors from hPSC under defined conditions (Kirkeby *et al.* 2012). The exploitation of these novel cellular models is likely to boost our mechanistic understanding of the pathogenesis of human disorders as well as accelerate the discovery of new therapeutics.

5. Acknowledgements

The authors gratefully acknowledge Dr. Johannes Schwarz for the supply of hmNPC within the scope of the EU project BrainCAV (FP7-222992), Pedro Almada and Dr. Emilio Gualda for support on confocal microscopy; Dr. Ana Amaral for support on hmNPC 3D cultures and Dr Rodolfo Negri and Dr Enrico Tagliafico for chip bioinformatics. IBET Analytical Services Unit, Portugal is acknowledged for HPLC analysis and Institute of Ophthalmology, UCL, UK is acknowledged for collection of SBF-SEM data. The NMR spectrometers are part of The National NMR Facility, supported by Fundação para a Ciência e a Tecnologia (RECI/BBB-BQB/0230/2012). This work was supported by BrainCAV (FP7-222992) and Brainvectors (FP7-286071), funded by the EU, PTDC/EBB-BIO/112786/2009 and PTDC/EBB-BIO/119243/2010, funded by Fundação para a Ciência e Tecnologia, Portugal and Cancer Research UK. Daniel Simão acknowledges the PhD fellowship from FCT, Portugal (SFRH/BD/78308/2011, FCT).

6. References

Abeliovich A., Hammond R. (2007) Midbrain dopamine neuron differentiation: factors and fates. *Dev. Biol.* **304**, 447–54.

Alves dos Santos M. T. M., Smidt M. P. (2011) En1 and Wnt signaling in midbrain dopaminergic neuronal development. *Neural Dev.* **6**, 1–15.

Ang S.-L. (2006) Transcriptional control of midbrain dopaminergic neuron development. *Development* **133**, 3499–3506.

Bandtlow C. E., Zimmermann D. R. (2000) Proteoglycans in the developing brain: new conceptual insights for old proteins. *Physiol. Rev.* **80**, 1267–90.

Benjamini Y., Hochberg Y. (1995) Controlling the False Discovery Rate: A Practical and Powerful Approach to Multiple Testing. *J. R. Stat. Soc. Ser. B* **57**, 289–300.

Bixel M. G., Engelmann J., Willker W., Hamprecht B., Leibfritz D. (2004) Metabolism of [U-(13)C]leucine in cultured astroglial cells. *Neurochem Res* **29**, 2057–67.

Bodea G. O., Blaess S. (2012) Organotypic slice cultures of embryonic ventral midbrain: a system to study dopaminergic neuronal development *in vitro*. *J. Vis. Exp.* 59, e3350.

Breslin S., O'Driscoll L. (2013) Three-dimensional cell culture: The missing link in drug discovery. *Drug Discov. Today* **18**, 240–249.

Carinhas N., Bernal V., Monteiro F., Carrondo M. J. T., Oliveira R., Alves P. M. (2010) Improving baculovirus production at high cell density through manipulation of energy metabolism. *Metab. Eng.* **12**, 39–52.

Coetzee W. A., Amarillo Y., Chiu J., Chow A., Lau D., McCormack T., Moreno H., *et al.* (1999) Molecular diversity of K+ channels. *Ann. N. Y. Acad. Sci.* **868**, 233–85.

Cruz F., Villalba M., García-Espinosa M. a, Ballesteros P., Bogónez E., Satrústegui J., Cerdán S. (2001) Intracellular compartmentation of pyruvate in primary cultures of cortical neurons as detected by (13)C NMR spectroscopy with multiple (13)C labels. *J. Neurosci. Res.* **66**, 771–81.

Deerinck T. J., Bushong E. A., Thor A., Ellisman M. H. (2010) NCMIR methods for 3D EM: a new protocol for preparation of biological specimens for serial block face scanning electron microscopy.

Duarte T. M., Carinhas N., Silva A. C., Alves P. M., Teixeira A. P. (2014) ^{1}H-NMR protocol for exometabolome analysis of cultured mammalian cells. *Methods Mol. Biol.* **1104**, 237–47.

Dwyer C., Matthews R. (2011) The Neural Extracellular Matrix, Cell Adhesion Molecules and Proteolysis in Glioma Invasion and Tumorigenicity, in *Mol. Targets CNS Tumors,* (Garami M., ed), pp. 239–264. InTech, Rijeka.

Evans G. J. O., Cousin M. A. (2007) Simultaneous monitoring of three key neuronal functions in primary neuronal cultures. *J. Neurosci. Methods* **160**, 197–205.

Fennema E., Rivron N., Rouwkema J., Blitterswijk C. van, Boer J. de (2013) Spheroid culture as a tool for creating 3D complex tissues. *Trends Biotechnol.* **31**, 108–15.

Folmes C. D. L., Nelson T. J., Dzeja P. P., Terzic A. (2012) Energy metabolism plasticity enables stemness programs. *Ann. N. Y. Acad. Sci.* **1254**, 82–9.

Fornazari M., Nascimento I. C., Nery A. A., Silva C. C. C. da, Kowaltowski A. J., Ulrich H. (2011) Neuronal differentiation involves a shift from glucose oxidation to fermentation. *J. Bioenerg. Biomembr.* **43**, 531–9.

Gaffield M. a, Betz W. J. (2006) Imaging synaptic vesicle exocytosis and endocytosis with FM dyes. *Nat. Protoc.* **1**, 2916–21.

Goldberg J. L., Barres B. A. (2000) The relationship between neuronal survival and regeneration. *Annu. Rev. Neurosci.* **23**, 579–612.

Griffith L. G., Swartz M. A. (2006) Capturing complex 3D tissue physiology *in vitro*. *Nat. Rev. Mol. Cell Biol.* **7**, 211–24.

Hoopmann P., Rizzoli S. O., Betz W. J. (2012) Imaging synaptic vesicle recycling by staining and destaining vesicles with FM dyes. *Cold Spring Harb. Protoc.* **2012**, 77–83.

Ikegaya Y., Bon-Jego M. Le, Yuste R. (2005) Large-scale imaging of cortical network activity with calcium indicators. *Neurosci. Res.* **52**, 132–8.

Iwama E., Tsuchimoto D., Iyama T., Sakumi K., Nakagawara A., Takayama K., Nakanishi Y., Nakabeppu Y. (2011) Cancer-related PRUNE2 protein is associated with nucleotides and is highly expressed in mature nerve tissues. *J. Mol. Neurosci.* **44**, 103–14.

Joksimovic M., Yun B. a, Kittappa R., Anderegg A. M., Chang W. W., Taketo M. M., McKay R. D. G., Awatramani R. B. (2009) Wnt antagonism of Shh facilitates midbrain floor plate neurogenesis. *Nat. Neurosci.* **12**, 125–31.

Jontes J. D., Smith S. J. (2000) Filopodia, spines, and the generation of synaptic diversity. *Neuron* **27**, 11–14.

Kirkeby A., Grealish S., Wolf D. a, Nelander J., Wood J., Lundblad M., Lindvall O., Parmar M. (2012) Generation of regionally specified neural progenitors and functional neurons from human embryonic stem cells under defined conditions. *Cell Rep.* **1**, 703–14.

Korotkova T. M., Ponomarenko A. A., Brown R. E., Haas H. L. (2004) Functional diversity of ventral midbrain dopamine and GABAergic neurons. *Mol. Neurobiol.* **29**, 243–59.

Kumar A., Bachhawat A. K. (2012) Pyroglutamic acid: throwing light on a lightly studied metabolite. *Curr Sci* **102**, 288–97.

Lakshmana M. K., Raju T. R. (1997) An isocratic assay for norepinephrine, dopamine, and 5-hydroxytryptamine using their native fluorescence by high-performance liquid chromatography with fluorescence detection in discrete brain areas of rat. *Anal. Biochem.* **246**, 166–70.

Lendvai B., Stern E. A., Chen B., Svoboda K. (2000) Experience-dependent plasticity of dendritic spines in the developing rat barrel cortex *in vivo*. *Nature* **404**, 876–81.

Lima P. A., Marrion N. V (2007) Mechanisms underlying activation of the slow AHP in rat hippocampal neurons. *Brain Res.* **1150**, 74–82.

Lin R.-Z., Lin R.-Z., Chang H.-Y. (2008) Recent advances in three-dimensional multicellular spheroid culture for biomedical research. *Biotechnol J* **3**, 1172–84.

Livak K. J., Schmittgen T. D. (2001) Analysis of relative gene expression data using real-time quantitative PCR and the 2(-Delta Delta C(T)) Method. *Methods* **25**, 402–8.

Maere S., Heymans K., Kuiper M. (2005) BiNGO: a Cytoscape plugin to assess overrepresentation of gene ontology categories in biological networks. *Bioinformatics* **21**, 3448–3449.

Magistretti P. J., Allaman I. (2013) Brain Energy Metabolism, in *Neurosci. 21st Century From Basic to Clin.,* (Pfaff D. W., ed), pp. 1591–1620. Springer, New York.

Michel P. P., Agid Y. (1996) Chronic activation of the cyclic AMP signaling pathway promotes development and long-term survival of mesencephalic dopaminergic neurons. *J. Neurochem.* **67**, 1633–1642.

Miller G. (2010) Is pharma running out of brainy ideas? *Science (80-.).* **329**, 502–504.

Moors M., Rockel T. D., Abel J., Cline J. E., Gassmann K., Schreiber T., Schuwald J., Weinmann N., Fritsche E. (2009) Human neurospheres as three-dimensional cellular systems for developmental neurotoxicity testing. *Env. Heal. Perspect* **117**, 1131–8.

Nishio T., Furukawa S., Akiguchi I., Sunohara N. (1998) Medial nigral dopamine neurons have rich neurotrophin support in humans. *Neuroreport* **9**, 2847–51.

Numan S., Gall C. M., Seroogy K. B. (2005) Developmental expression of neurotrophins and their receptors in postnatal rat ventral midbrain. *J. Mol. Neurosci.* **27**, 245–60.

Pampaloni F., Reynaud E. G., Stelzer E. H. K. (2007) The third dimension bridges the gap between cell culture and live tissue. *Nat. Rev. Mol. Cell Biol.* **8**, 839–845.

Potter W., Kalil R. E., Kao W. J. (2008) Biomimetic material systems for neural progenitor cell-based therapy. *Front Biosci* **13**, 806–21.

Prakash N., Wurst W. (2006) Genetic networks controlling the development of midbrain dopaminergic neurons. *J. Physiol.* **575**, 403–10.

Ruoslahti E. (1996) Brain extracellular matrix. *Glycobiology* **6**, 489–492.

Schaarschmidt G., Schewtschik S., Kraft R., Wegner F., Eilers J., Schwarz J., Schmidt H. (2009a) A new culturing strategy improves functional neuronal development of human neural progenitor cells. *J. Neurochem.* **109**, 238–47.

Schaarschmidt G., Wegner F., Schwarz S. C., Schmidt H., Schwarz J. (2009b) Characterization of voltage-gated potassium channels in human neural progenitor cells. *PLoS One* **4**, e6168.

Schilling S., Wasternack C., Demuth H.-U. (2008) Glutaminyl cyclases from animals and plants: a case of functionally convergent protein evolution. *Biol. Chem.* **389**, 983–91.

Schüle B., Pera R. a R., Langston J. W. (2009) *Can cellular models revolutionize drug discovery in Parkinson's disease?* Elsevier B.V.

Schwarz J. (2007) Developmental perspectives on human midbrain-derived neural stem cells. *Parkinsonism Relat. Disord.* **13**, S466–S468.

Serra M., Correia C., Malpique R., Brito C., Jensen J., Bjorquist P., Carrondo M. J. T., Alves P. M. (2011) Microencapsulation technology: a powerful tool for integrating expansion and cryopreservation of human embryonic stem cells. *PLoS One* **6**, e23212.

Smyth G. K. (2005) Limma: linear models for microarray data, in *Bioinforma. Comput. Biol. Solut. Using R Bioconductor,* (Gentleman R., Carey V., Huber W., Irizarry R., Dudoit S., eds), pp. 397–420. Springer New York.

Storch A., Paul G., Csete M., Boehm B. O., Carvey P. M., Kupsch A., Schwarz J. (2001) Long-term proliferation and dopaminergic differentiation of human mesencephalic neural precursor cells. *Exp Neurol* **170**, 317–325.

Tashiro A., Goldberg J., Yuste R. (2002) Calcium Oscillations in Neocortical Astrocytes under Epileptiform Conditions. *J. Neurobiol.* **50**, 45–55.

Tio M., Tan K. H., Lee W., Wang T. T., Udolph G. (2010) Roles of db-cAMP, IBMX and RA in aspects of neural differentiation of cord blood derived mesenchymal-like stem cells. *PLoS One* **5**, e9398.

Valtorta F., Pozzi D., Benfenati F., Fornasiero E. F. (2011) The synapsins: multitask modulators of neuronal development. *Semin. Cell Dev. Biol.* **22**, 378–86.

Vicente M. I., Costa P. F., Lima P. A. (2010) Galantamine inhibits slowly inactivating K+ currents with a dual dose-response relationship in differentiated N1E-115 cells and in CA1 neurones. *Eur. J. Pharmacol.* **634**, 16–25.

Wegner F., Kraft R., Busse K., Härtig W., Ahrens J., Leffler A., Dengler R., Schwarz J. (2012) Differentiated human midbrain-derived neural progenitor cells express excitatory strychnine-sensitive glycine receptors containing α2β subunits. *PLoS One* **7**, e36946.

Wegner F., Kraft R., Busse K., Härtig W., Schaarschmidt G., Schwarz S. C., Schwarz J., Hevers W. (2008) Functional and molecular analysis of GABA receptors in human midbrain-derived neural progenitor cells. *J. Neurochem.* **107**, 1056–1069.

Wegner F., Kraft R., Busse K., Schaarschmidt G., Härtig W., Schwarz S. C., Schwarz J. (2009) Glutamate receptor properties of human mesencephalic neural progenitor cells: NMDA enhances dopaminergic neurogenesis *in vitro*. *J. Neurochem.* **111**, 204–16.

Zahir T., Chen Y. F., MacDonald J. F., Leipzig N., Tator C. H., Shoichet M. S. (2009) Neural stem/progenitor cells differentiate *in vitro* to neurons by the combined action of dibutyryl cAMP and interferon-gamma. *Stem Cells Dev.* **18**, 1423–32.

Zala D., Hinckelmann M.-V., Yu H., Lyra da Cunha M. M., Liot G., Cordelières F. P., Marco S., Saudou F. (2013) Vesicular glycolysis provides on-board energy for fast axonal transport. *Cell* **152**, 479–91.

Zaman V., Nelson M. E., Gerhardt G. A., Rohrer B. (2004) Neurodegenerative alterations in the nigrostriatal system of trkB hypomorphic mice. *Exp. Neurol.* **190**, 337–46.

Zito K., Knott G., Shepherd G. M. G., Shenolikar S., Svoboda K. (2004) Induction of spine growth and synapse formation by regulation of the spine actin cytoskeleton. *Neuron* **44**, 321–34.

Zwingmann C., Leibfritz D. (2003) Regulation of glial metabolism studied by 13C-NMR. *NMR Biomed.* **16**, 370–99.

3

Imaging of human differentiated neurospheres using light sheet fluorescence microscopy

This chapter was adapted from:

Gualda E, Simão D, Pinto C, Alves PM, Brito C (2014) Imaging of human differentiated 3D neural aggregates using light sheet fluorescence microscopy. *Frontiers in Cellular Neuroscience 8:221*

Table of Contents

Abstract

The development of three dimensional (3D) cell cultures represents a big step for the better understanding of cell behavior and disease in a more natural like environment, providing not only single but multiple cell type interactions in a complex 3D matrix, highly resembling physiological conditions. Light sheet fluorescence microscopy (LSFM) is becoming an excellent tool for fast imaging of such 3D biological structures. In this work, the potential of this technique for the imaging of human differentiated 3D neural aggregates is demonstrated, both for fixed and live samples, namely calcium imaging and cell death processes. The obtained results show the power of this imaging modality compared with traditional microscopy. The combination of light sheet microscopy and 3D neural cultures will open the door to more challenging experiments involving drug testing at large scale as well as a better understanding of relevant biological processes in a more realistic environment.

1. Introduction

Human cellular models capable of mimicking the characteristics of living tissues are essential in both basic research and drug discovery. Cells within a tissue constantly integrate external cues that influence important cellular functions such as proliferation and differentiation, to which the interaction with neighboring cells and extracellular matrix is crucial. Thus, three-dimensional (3D) models present a more physiologically relevant approach that can increase the reliability and predictability of pre-clinical assays (Pampaloni *et al.* 2007; Breslin and O'Driscoll 2013), while decreasing the dependence on animal testing in pharmaceutical industry. Additionally, 3D cellular aggregates represent a simple and straightforward strategy even for fundamental studies on pathological pathways in human disorders. Such aggregates have been used for a broad spectrum of studies in cancer biology to study proliferation, cell death, differentiation, and metabolism of cells in tumors and the response of tumors to radiotherapy and chemotherapy (Hirschhaeuser *et al.* 2010; Vinci *et al.* 2012). Also, hepatocyte spheroids have been proposed as a cell model for a variety of diagnostic, discovery, and therapeutic applications, such as a bio-artificial liver (No *et al.* 2012; Yu *et al.* 2012). As for central nervous system (CNS) modeling, 3D neural aggregates have been reported to efficiently mimic basic processes of brain development (Moors *et al.* 2009). Recently, human induced pluripotent stem cell-derived (iPSC) neurons were reported to self-organize in 3D cortical structures, recapitulating the early dorsal telencephalic developmental program (Mariani *et al.* 2012).

Therefore, the establishment of 3D cultures as an increasingly used strategy by the scientific community is driving the field toward the development of standardized culturing protocols and more suitable characterization and imaging techniques (Pampaloni *et al.* 2007). On one hand, classically used techniques for culturing cells as aggregates, such as hanging drop techniques, rotating wall vessels, and agitation-based culture systems, are now being explored for their potential to support the generation of accessible human 3D models (Kim *et al.* 2004; Justice *et al.* 2009). On the other hand, advances in imaging techniques will be essential to fully take advantage of these complex cultures, which are typically several hundred microns thick and highly scattering (Pampaloni *et al.* 2007). The quantitative analysis of the spatio-temporal organization of the different cell types in an aggregate requires well-suited 3D imaging techniques with high resolution, high speed, and minimal photodamage. However, conventional visualization techniques like point scanning or spinning disk confocal microscopes are not optimal for thick samples, providing a short penetration depth into the aggregates. This can be partially solved by performing immunofluorescence microscopy of cryosections, although limited to fixed samples. Light sheet fluorescence microscopy

(LSFM) techniques have been proposed as an alternative approach, to overcome these limitations in cancer cell spheroids (Pampaloni *et al.* 2007; Lorenzo *et al.* 2011). LSFM is a fluorescence microscopy technique, where the illumination is done perpendicularly to the detection (Huisken and Stainier 2007; Verveer *et al.* 2007). The illumination laser beam is shaped into a rectangle and then focused into a thin "sheet of light" using a cylindrical lens (Selective Plane Illumination Microscopy-SPIM) or a fast moving laser scanner (Digital Scanned Light sheet Microscopy-DSLM) in the focal plane of the detection objective. As the sample moves through the focal plane, different planes of the sample are illuminated, creating a z stack of images that can be three-dimensionally reconstructed. As the light-sheet can be tailored to the micron range, it achieves good sectioning of the sample and out-of-focus light suppression. Since illumination and detection pathways are decoupled, the lateral resolution is given by the detection objective only. Images are acquired with CCD or sCMOS cameras, enabling higher sensitivity and faster acquisition rates than photomultiplier (PMT) based devices. Also, due to inherent setup that only illuminates a fraction on the sample, it is less phototoxic when compared with conventional florescence microscopy (Reynaud *et al.* 2008). Moreover LSF microscopes have a good penetration depth because the numerical aperture of the illumination system is much smaller than that of the detection system. Among the several advantages the current prototypes offer, is the possibility of obtaining multi-views of the sample by rotating it, so that hidden parts of the sample become visible. This feature is not typically offered in conventional multidimensional microscopy imaging systems, such as confocal or multi-photon microscopy, and leads to the possibility of obtaining detailed 3D volume reconstruction of the sample, not achieved with any other microscopic technique.

LSFM imaging strategies offer high speeds, large fields of view and long-term imaging capacity. Here, the implementation of a SPIM/DSLM system is decribed, as well as the assessment of its potentialities through a detailed characterization of differentiated human neural aggregates, derived from stem cells. A 3D strategy based on agitation-based culture systems was previously explored for its potential to support CNS differentiation, resulting in a 3D CNS cell model composed of cells from the three neural lineages (neurons, astrocytes, and oligodendrocytes) (Brito *et al.* 2012). This has important applications ranging from drug screening to disease modeling and its coupling with the LSFM microscope developed represents one step forward in conceding the neural model system developed its full potential.

2. Materials and Methods

2.1. Imaging set up Description

All the images shown in this paper were acquired with a home-made light sheet microscopy system, based on an open software and hardware approach, the OpenSpinMicroscopy project (Gualda *et al.* 2013). The set-up of the light-sheet microscope is shown in Figure 3.1D. Briefly, the illumination is performed with an Argon/Kryton laser (Melles Griot 35 LTL 835-230) providing excitation wavelengths of 488, 568, and 647 nm. Excitation laser lines are selected using a filter wheel with three different filters (D488/10, 568/10 and D647/10). The laser power is controlled using a shutter (Uniblitz electronics LS3T2) and a varying neutral density filter. The laser scanning is carried in the vertical axis using a galvanometric mirror (6210H Cambridge Technologies) which optical plane is conjugated with the back focal aperture of an objective lens (Plan Fluor 4× 0.13 WD17.4 mm) using a 3.5× telescope system consisting in a 50 mm and a 175 mm plano-convex lenses. For detection, a water immersion objective (Nikon LWD 16× 0.8NA WD 3 mm or Nikon Fluor 60× 1.0NA WD 2 mm), placed perpendicularly to the excitation plane, is used to collect fluorescence emission. Excitation light is rejected using emission filters placed in infinity space before the camera, with filters mounted in a second automatic filter wheel, consisting of the following: HQ 535/70m-2p, HQ 580/25m-2p, HQ 620/90m-2p, and ET 700/75. Finally a 200 mm tube lens creates the image on the chip of a CMOS camera (Hamamatsu Orca-Flash4) recording the entire illuminated plane at the same time. With the 16× objective the total field of view is of 819 × 819 µm with a final pixel size of 0.4 µm, which means that for this objective under-sampled images are acquired.

OpenSPINMicroscopy provides a Java plugin for Micromanager (open-source image acquisition software for microscopy) to fully control sample rotation, filter wheels, shutter, and image acquisition as well as galvo speed and deflection angle for DSLM mode, with a single window. It allows the capture of time lapse sequences, multicolor, z stacks and multi-view recordings. The innovative approach of this setup consists on the use of cheap open source hardware, i.e., Arduino microcontrollers, opening this technology to any lab with a minimum technical background. The system uses three Arduino boards with modified firmware to control a shutter, a galvo for DSLM and three stepper motors, one for sample rotation and others for filter wheels excitation and detection. All image processing is performed using free software ImageJ.

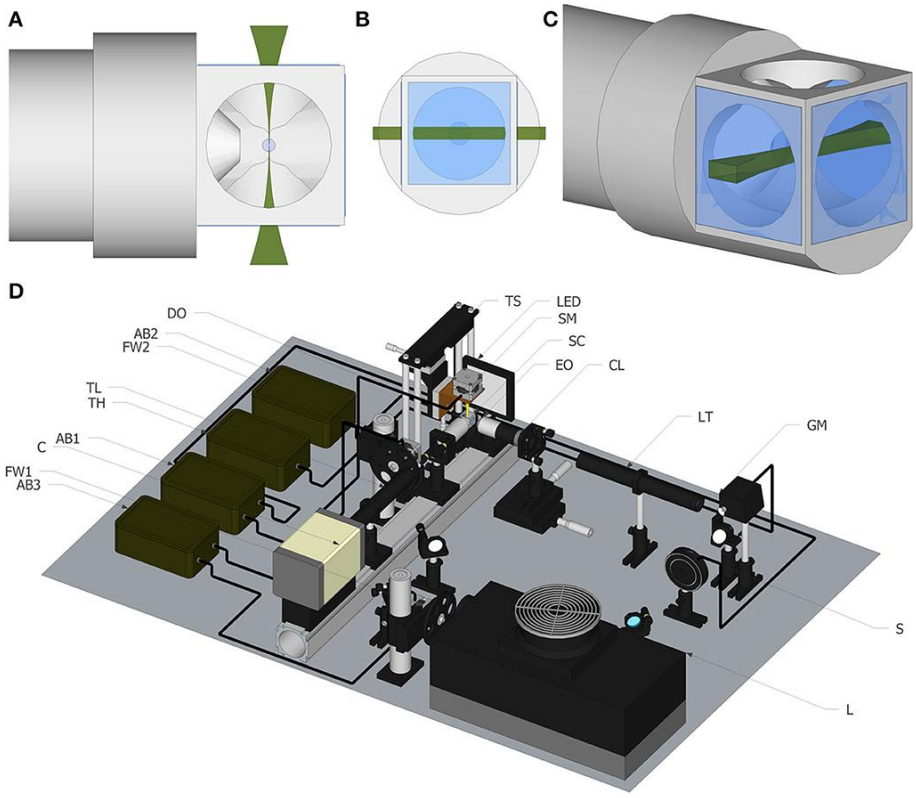

Figure 3.1 - Light sheet fluorescence microscopy. (A) Top view of the light sheet, including objective and newly developed chamber. **(B)** Front view of the light sheet. **(C)** Perspective view of the light sheet. **(D)** Schematic of the experimental setup. The list of elements are: Argon/Krypton laser (L), excitation filter wheel (FW1), shutter (S) galvanometric mirror (GM), excitation objective (EO), 3.5× lens telescope (LT), detection objective (DO), sCMOS camera (C), tube lens (TL), emission filter wheel (FW2), translational stage (TS), stepper motor to rotate the sample (SM), Arduino board (AB), sample chamber (SC) for water immersion objectives.

2.2. Sample Preparation

All Human midbrain-derived neural progenitor cells (hmNPC) were differentiated as neural aggregates using agitation-based culture systems with orbital shaking, in the presence of morphogens and under low oxygen conditions, as previously described (Brito *et al.* 2012).

Transduction of differentiated neural aggregates with CAVGFP vectors (an E1-deleted CAV-2 vector expressing GFP) (Bru *et al.* 2010) was performed as previously described (Brito *et al.* 2012). Briefly, CAVGFP vectors were added to the culture, with 50% reduction of the working volume, according to the intended Multiplicity of Infection (MOI). Four hours post-transduction (hpt) the initially working volume was restored by adding fresh medium and changed at 72 hpt.

NTERA-2/cl.D1 cells (NT2) were differentiated as aggregates in 125-mL spinner vessels (from Wheaton, Techne, NJ) equipped with a ball impeller and maintained at 37°C and 5% CO_2, as previously described (Serra *et al.* 2009). Briefly, neuronal differentiation was induced by addition of retinoic acid (RA, Sigma) to the culture media, at a final concentration of 10 µM. A 50% media exchange was performed three times a week for 3 weeks.

2.3. Immunofluorescence Protocol

Neural aggregates were fixed in 4% paraformaldehyde (PFA) + 4% Sucrose in PBS for 1 h at 4°C, permeabilized and blocked with 1% (w/v) Triton X-100 (TX-100) solution/0.2% fish skin gelatin (FSG) (Sigma) for 2 h at RT and subsequently incubated overnight at RT with primary antibodies (anti−βIII-tubulin, Millipore; anti-Tyrosine Hydroxylase, Santa Cruz Biotechnology) diluted in 0.1% TX-100/0.125% FSG. Aggregates were then washed three times with 0.08% Tween 20 and incubated with secondary antibodies (AlexaFluor 488 goat anti-rabbit IgG, AlexaFluor 549 goat anti-mouse IgG, Invitrogen), diluted in 0.125% FSG, for 5 h at RT. After three washes with 0.08% Tween 20 cell nuclei were counter stained with TO-PRO-3 (Invitrogen).

2.4. Live/Dead Assays

Viability of cells within differentiated neural aggregates was visualized with NucView 488 and MitoView 633 Apoptosis Kit according to the manufacturer's instructions (Biotium, Hayward, CA, USA). Briefly, neural aggregates were exposed to NucView™ 488 1× and MitoView™ 633 1× simultaneously in Hibernate (Invitogen), a media designed to maintain embryonic neural tissue in ambient CO_2, and imaged overnight. NucView™ 488 is a caspase-3 substrat that detects caspase-3 in live cells without interfering with the enzyme activity and MitoView™ 633 is a mitochondrial dye which only stains viable cells since its fluorescence is dependent on the mitochondria's membrane potential. Tert-butyl hydroperoxide (tBHP) (Sigma), an oxidative stress inducer, was used to trigger apoptosis at a concentration of 1 mM in Hibernate. Two full stacks of images, one for each color, were acquired every 10 min during a period of 16 h, using the 16× objective and the sample mounting described below.

2.5. Tracking of Ca^{2+} Transients

Neural aggregates were incubated with 1× Fluo4 Direct calcium reagent (Invitrogen) for 30 min at 37°C, 5% CO_2, and 3% O_2 followed by 15 min at RT. Fluorescence change over time was defined as $\Delta F/F_0 = (F-F_0)/F_0$, where F is the fluorescence at any

time point, and F0 the baseline fluorescence determined by baseline fitting across the whole movie for each cell using PeakFit Software (v4.12).

2.6. Sample Mounting

Fixed samples were embedded on 1% low melting temperature agarose and placed on the tip of a plastic pipette. The other end of the plastic pipette is inserted on the rotational stepper motor for sample rotation, which is attacked to a linear DC motor for sample scanning though the light sheet, as described in (Gualda *et al.* 2013). In order to perform multi-view fusion, fluorescence TetraSpeck 0.5 µm beads 1:10000 diluted (Invitrogen) are added to the agarose. The fusion is performed using the free plugin for Fiji, SPIMRegistration (Preibisch *et al.* 2010).

For the calcium imaging experiments, agarose was mixed with medium in order to maintain liability of the samples. Images were acquired for 30 min, and neuronal activity was still observed.

For the live/dead assay experiments samples were immersed inside Fluorinated Ethylene Propylene (FEP) tubes with a medium that ensures liability for long periods of time. FEP tubes (Kaufmann *et al.* 2012) are ideal for light sheet microscopy since it refractive index is close to water, reducing the optical aberrations, providing a better environment to the samples with high optical clarity. The medium, pumped with a motorized controlled syringe, can flow through the tube providing the nutrients needed by the samples to ensure liability. Samples are placed at the end of the tube, stopped by a filter that leaves the medium flow, while keeping the sample at that position. However, samples are not tidily hold so they are susceptible to move during long term experiments.

3. Results

3.1. Characterization of Neural Aggregates

The great potential of this 3D CNS cell model can be enhanced by imaging techniques that allow the study of the interaction between therapeutic viral vectors and human neural populations, within a more physiological 3D context. The model system here characterized has several applications ranging from drug screening to disease modeling (Brito *et al.* 2012). *In vivo* gene transfer using viral vectors is still the primary strategy for delivering novel genes to the CNS (Björklund and Kordower 2010), and previous work has proven the differentiated human neural aggregates' amenability to transduction by canine adenovirus derived vectors (CAV) (Brito *et al.* 2012). The implemented setup enabled the visualization of the 3D network of the transduced cells

inside the neural aggregates (Figure 3.2A). In order to determine the penetration depth, the same aggregate is also shown with a depth dependent lookup table. Sections on the surface are plotted in yellow, while the deepest layer is plotted in red, illustrating this network up to 270 µm deep (Figure 3.2B). In Figure 3.2C an aggregate was imaged with a 60× objective and the recorded image has been saturated to allow the visualization of neurites. Deep inside the sample, fluorescent spots are still detected, corresponding to neuronal somas, increasing the penetration depth up to 1.5-fold when compared to spinning-disk confocal microscopes (Brito *et al.* 2012).

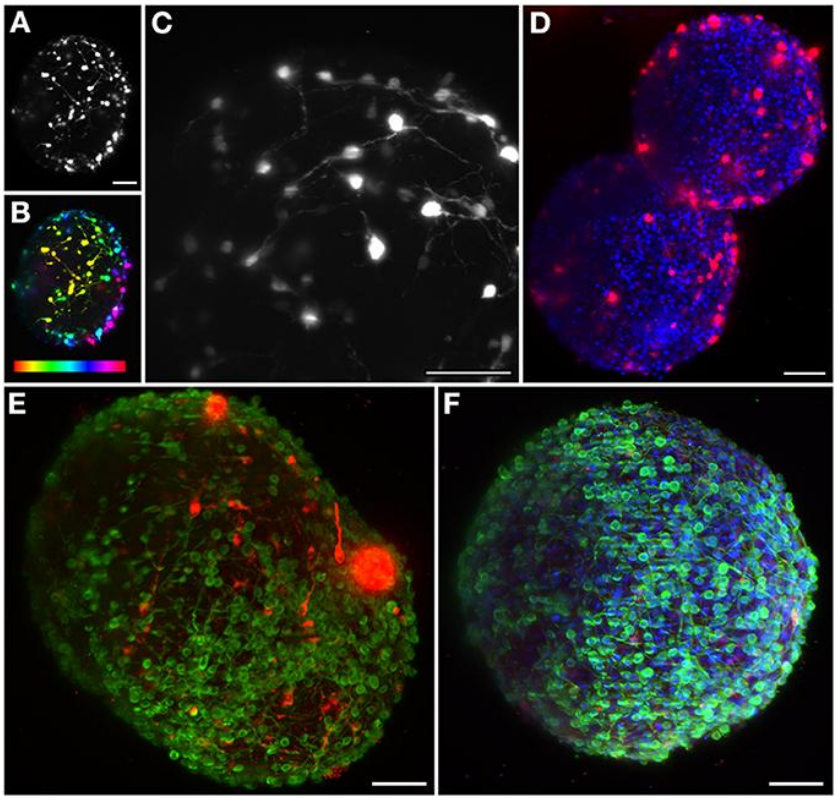

Figure 3.2 - Maximum intensity projection of different neural aggregates imaged using light sheet microscopy. (A) Transduced differentiated hmNPC neural aggregates expressing GFP transgene. **(B)** Same neural aggregate with depth lookup table. Red indicates 0 µm and purple 270 µm. **(C)** Transduced differentiated neural aggregate expressing GFP transgene; Objective: 60x. **(D)** Two differentiated neural aggregates with dopaminergic marker TH and TO-PRO-3 for the nuclei. **(E)** Differentiated neural aggregate with dopaminergic marker TH and βIII-tubulin was used as neuronal marker. **(F)** Differentiated neural aggregate with TH, TO-PRO-3 and βIII-tubulin. All images except **(C)** obtained with 16x objective. Scale bar: 50 µm.

The neural circuits present in the human brain are comprised of highly diverse and specialized cell types (Nelson *et al.* 2006). The ability to objectively classify a specific cellular lineage is still a matter of debate and research, resulting in a growing list of phenotypic markers (Nelson *et al.* 2006). Therefore, the ability to simultaneously visual-

ize different markers using multicolor staining approaches is essential when characterizing different cells in culture and studying multicellular heterotypic interactions. The light-sheet fluorescence microscope here implemented is equipped with three excitation wavelengths. In this way, optimally imaging of three different fluorescent channels was possible.

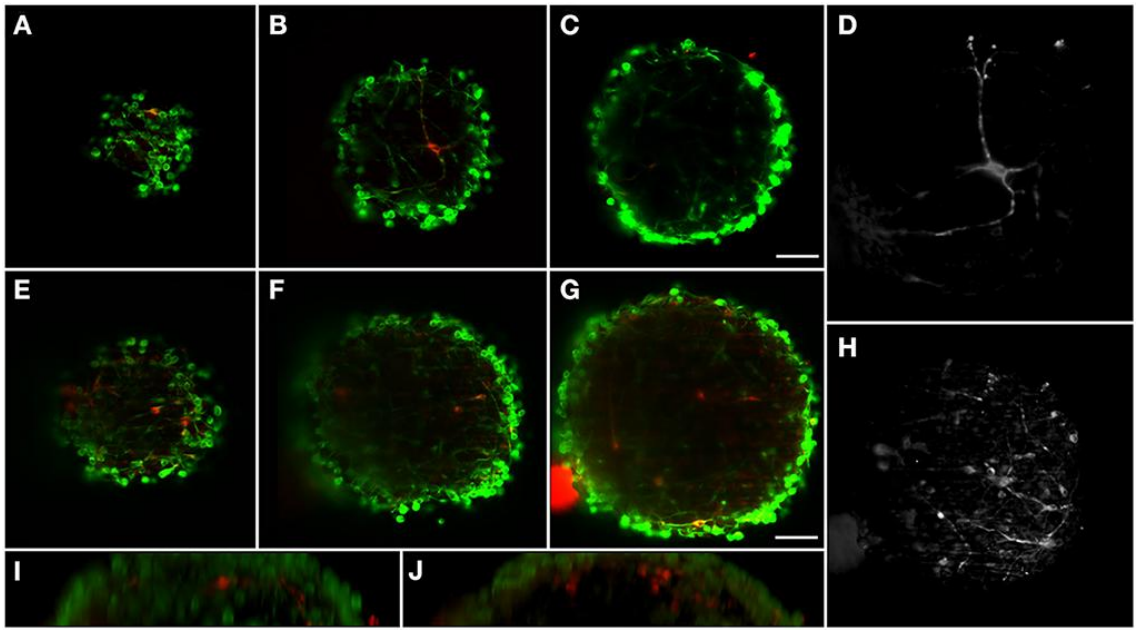

Figure 3.3 - Dopaminergic neurons distribution in two different differentiated neural aggregates with depth. (A-D) βIII-tubulin was used as neuronal marker (green) and TH as dopaminergic marker (red). Neural aggregate #1 showing mature dopaminergic neurons with long axonal connections at: **(A)** 17 µm from surface; **(B)** 43 µm and **(C)** 75 µm. **(D)** Maximum intensity projection of the dopaminergic neuron. **(E-H)** Neural aggregate #2 showing a complex dopaminergic neuron network at: **(E)** 29 µm from surface; **(F)** 59 µm and **(G)** 97 µm. **(H)** Maximum intensity projection of the dopaminergic neuronal network. Sagittal views of **(I)** Neural aggregate #1 and **(J)** Neural aggregate #2. Scale bar: 50 µm.

Immunodetection of βIII-tubulin evidenced the extensive neuronal network present in differentiated neural aggregates (Figure 3.2E). Further investigation of the specific neuronal lineages present in culture revealed intense staining of tyrosine hydroxylase (TH), a dopaminergic marker, throughout the aggregates (Figures 3.2D,E). Additionally, nuclei were stained with TO-PRO-3, which provided a bright signal (Figure 3.2F). Taking advantage of the abovementioned increased penetration power of the setup; the dopaminergic neuronal network present in the culture was analyzed in greater detail. TH+ cells were detected up to 100 µm deep within the aggregates on a single view (Figures 3.3A–C,E–G), indicating efficient differentiation throughout the entire neural aggregate. Figure 3.3H depicts the extensive dopaminergic network de-

veloped and Figure 3.3D highlights the long projections exhibited by these cells, suggesting their maturation and functionality. Figures 3.3I,J also shows that βIII-tubulin signal is lost in the deeper layers of the aggregate. Since TH-positive cells are still detected, this probably results from inefficient antibody penetration, which becomes exhausted in the first layers of cells, due to the dense neuronal network present.

3.2. Multi-View Imaging and Fusion

Sample rotation is one of the main characteristics of LSFM techniques and has been used to solve the problems caused by light scattering, shadowing, anisotropy, and sensitivity, inherent to the specific configuration of these microscopes (Edelstein *et al.* 2010). Successive z stacks can be acquired for different view angles, showing hidden features of the samples. In the case of neural aggregates, with a spherical shape and with diameters that can reach 400 µm, this feature allows imaging the center area of the sample from different angles, increasing the final penetration depth. Figures 3.4A–C show the maximum projection of the final fused image of TH-, βIII-Tubulin-positive neurons, and TO-PRO-3 in the nuclei, respectively. To obtain the resulting image, eight single-view images recorded every 45° were computationally fused into a single 3D dataset. However, fusion is an extremely demanding process in terms of computational resources and a powerful computer with several tens of RAM memory is needed. Nonetheless, the general goal of these algorithms is to extract the "most useful" information from all the datasets and to merge it into a single dataset, replacing the inferior information that may be present in some of the datasets. Due to the computational procedure, some sharpness is lost in the final image when compared with the original data. To solve that, a free deconvolution software for Fiji recently developed can be used to increase the final quality of the image (Preibisch *et al.* 2014).

In order to better appreciate the multi-view information, the data set is presented with depth-dependent lookup table (Figures 3.4A–C), as well as the 0° single view image (Figures 3.4D–F). When comparing the two set of images, the amount of information that is gained with the multi-view fusion becomes clear. Specifically, there is a considerable number of undetectable neurons within the single view (Figure 3.4; arrows), that become visible with the multi-view fusion. This shows the potential of the rotating feature, unique to this microscope, for extracting more information from the sample and for providing a more accurate analysis of the object in study.

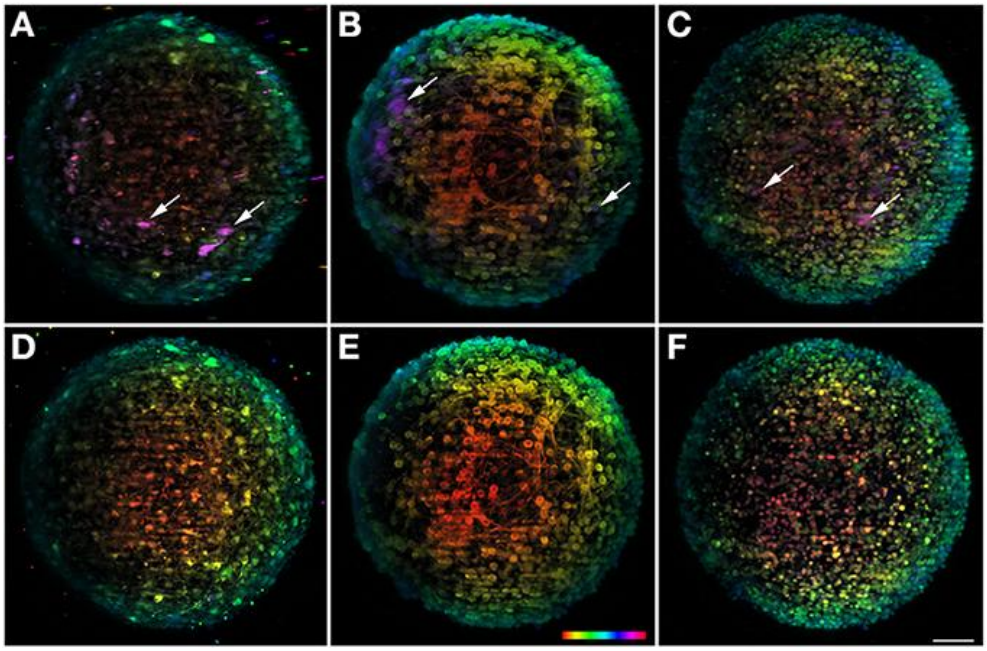

Figure 3.4 - Multi-view fusion on neuronal aggregates. In the upper row result of the fusion of 8 stacks recorded after rotation of the sample 45° is shown for the three different channels. For the sake of comparison the lower row shows the information obtained with a single view. All images are plotted using the same depth color map. **(A,D)** Shows dopaminergic neurons with TH and **(B,E)** βIII-tubulin as neuronal marker and **(C,F)** TO-PRO-3 in the nuclei. Some neurons visible after fusion but undetectable in a single view are highlighted with arrows. Scale bar: 50 µm.

3.3. Tracking of Ca^{2+} Transients

Having demonstrated the utility and advantages of this system for fixed samples, its potentialities for *in vivo* imaging were explored through a set of experiments on calcium imaging for assessment of neural cells' functionality. Differentiated neural aggregates were exposed to the Fluo4 live probe, an AM-ester calcium indicator. Loaded samples were embedded in agarose and imaged during 25 min at 6 frames per minute, in 5 optical sections with 2 µm of z-step. The monitoring of fluorescence intensity over time enabled the detection of spontaneous Ca^{2+} transients within the cells in culture, which differed in frequency, regularity, and duration (Figures 3.5A,B). After this time the activity ceases since at the time of acquisition the system did not have a proper incubation chamber with CO_2 control. Nevertheless, this technique allowed recording different planes in a fast way, enabling the reconstruction of the 3D map of spontaneously occurring transients in the intracellular Ca^{2+} concentration in neural cells.

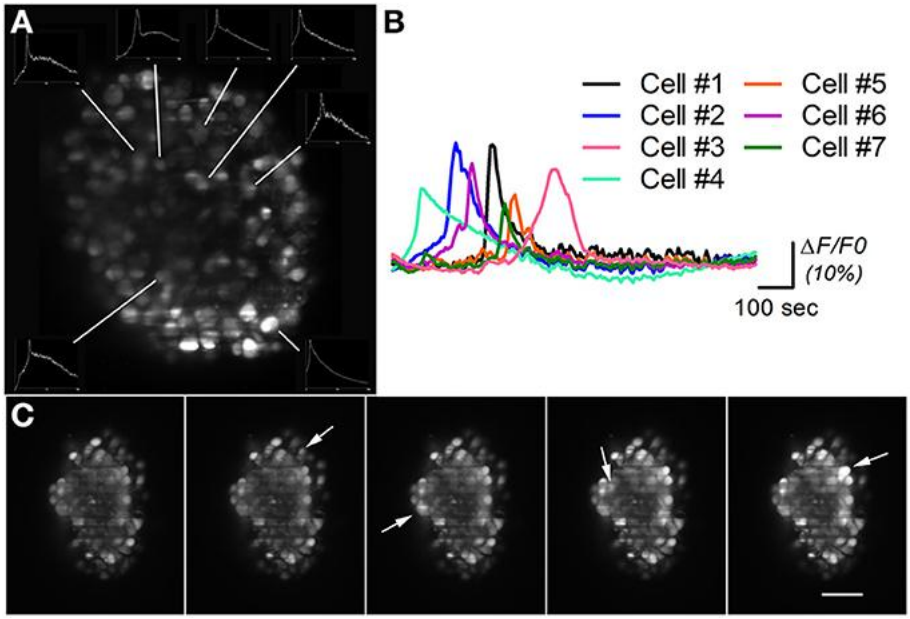

Figure 3.5 - Calcium imaging on differentiated neural aggregates stained with AM-ester calcium indicator. (A) Section of a neural aggregate with Ca^{2+} oscillations (insets) **(B)** Normalized intensity of the Ca^{2+} oscillations at seven different cells of neural aggregate in **(A)** imaged during 25 min. **(C)** Five time points of a neural aggregate showing Ca2+ oscillations in different cells (arrows). Scale bar: 50 µm.

Figure 3.5A shows a section of a neural aggregate stained with AM-ester calcium indicator. Ca^{2+} oscillations were observed in seven different cells during the 25 min of observation. The insets in Figure 3.5A show the total intensity over time, recorded on the area surrounding the analyzed cell. The normalized recorded signal is plotted in Figure 3.5B, as described in the experimental procedures. Different time points of a different neural aggregate where cells pointed by arrows shows an increase of fluorescent signal are displayed in Figure 3.5C. During the period of observation conformational changes in the structure were observed, as well as changes in the overall fluorescence. Same results have been obtained with a spinning disk confocal microscope (Simão *et al.* 2015). The advantage of a LSFM consist that same type of results can be obtained in a system more than one order of magnitude cheaper, with high speed, able to simultaneously record the activity of the cells in the surface, as well as the deeper layers of the neural aggregate. Although high speeds, up to 100 fps in this system, can be acquired on a single slice, 3D imaging of neural activity was limited to 4 fps by the slow movement of the translational stage for sample scanning.

3.4. Live/Dead Assays

The great potential for the 3D CNS cell model presented to increase the reliability of pre-clinical trials is dependent on the development of suitable characterization tech-

niques. To test the system's potential to address this question, a set of experiments on real-time analysis of apoptosis were performed. Differentiated neural aggregates were kept in the field of view in a medium, as described in the experimental procedure section, that allows proper maintenance of neuronal cells in ambient CO_2 and temperature conditions, exposed to NucView™ 488 Caspase-3 Substrate and MitoView™ 633 mitochondrial dye, and imaged for 16 h recording a two-color stack every 10 min. The samples remained viable for the duration of the assay (Figure 3.6A), with the majority of the cells viable, apart from the few initial apoptotic cells typically present in these cultures. These results indicate that the setup is suitable for performing toxicity experiments, as the phototoxicity resultant from long-term imaging is low enough to have no impact on apoptosis.

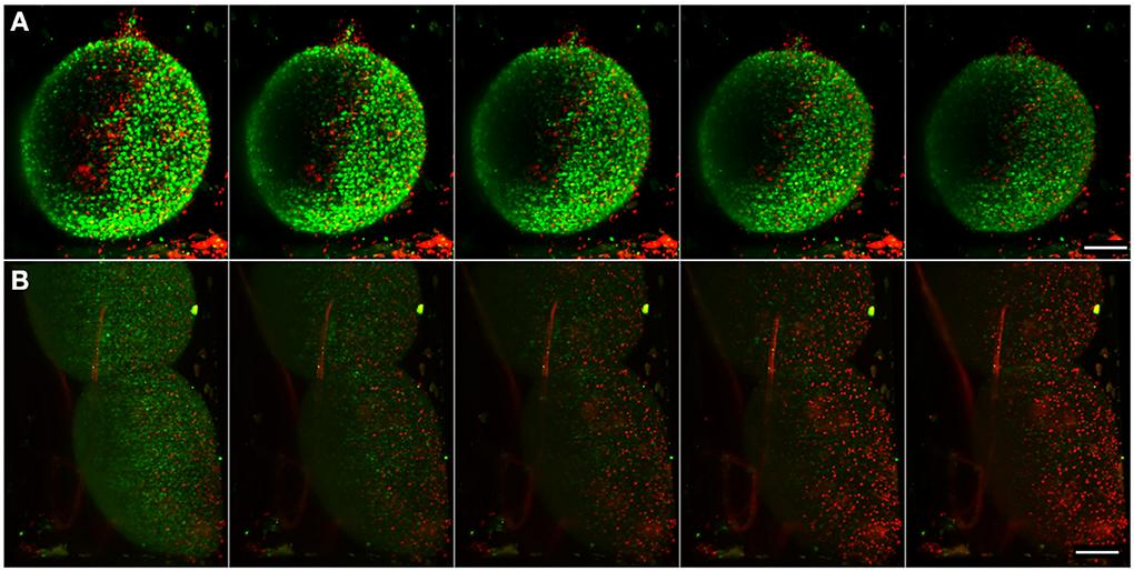

Figure 3.6 - Imaging of apoptosis in differentiated neural aggregates. Maximum intensity projection of five different time points, acquired every 150 min, of samples with NucView 488 (green) and MitoView 633 (red). **(A)** Control sample with culture medium. **(B)** Differentiated neural aggregates exposed to tBHP, which triggers apoptosis. Scale bar: 100 µm.

Using the setup described above, differentiated neural aggregates were exposed to tBHP, a potent oxidant, which triggers apoptosis (Peterson *et al.* 2007). Figure 3.6B shows the toxicant effect over time. Using apoptosis and mitochondrial activity as readouts, as opposed to the usually conducted end-point toxicological assays, this system enables a dynamic, real-time measuring of apoptosis. At the concentration of toxicant tested, cells remained viable for approximately 16 h. Apoptotic cell death occurs at time-point 40 (after 6 h of imaging) and is widespread through the neural aggregate, indicating equivalent sensitivity to the toxicant of the deeper layers of cells. As a proof of concept, these results show that the inherent low phototoxicity of the system here

developed, coupled with different fluorescent probes, allows the assessment of different levels of metabolic activity in cells in normal conditions and in response to a given compound, increasing the reliability of pre-clinical studies.

4. Discussion

LSFM imaging techniques are useful to image broad collection of fixed differentiated human neural aggregates, with different immunofluorescence labeling, as well as live imaging. The DSLM configuration is able to provide a complete view of the neuronal network of βIII-Tubulin-positive cells present in these samples. The possibility to rotate the object in different directions, shining light into otherwise inaccessible areas of the sample and increasing axial resolution gives us the overall picture and better insight into the structures in study.

Also, the multichannel sequential acquisition capabilities of this system comined with the higher penetration depth over widely used confocal microscopes, increase the obtained spatial resolution. This allowed to image the inner morphology of the dopaminergic networks and detection of GFP-positive cells, after CAVGFP transduction, even in the inner layers of the aggregate. Therefore, this work contributed for the development of a versatile SPIM/DSLM system based on open software (Micromanager) (Edelstein *et al.* 2010) and hardware (Arduino boards for device control), providing a specialized plugin for image acquisition control. This includes also sample rotation, a feature that is not available in standard systems. Open source platforms were made available (OpenSpinMicroscopy; Gualda *et al.* 2013), presenting a dedicated webpage for custom construction of light-sheet microscopes, making these systems available to the labs with minimum background. LSFM techniques provide a powerful tool for imaging thick complex samples, including long term *in vivo* imaging experiments, because their special configuration and advance capacities overcome the classical limitation shown by traditional single axis illumination microscopy techniques, increasing speed and penetration while reducing bleaching and phototoxicity. Previous works have already demonstrated the capabilities of LSFM in 3D cell cultures (Lorenzo *et al.* 2011; Bruns 2012). Madin-Darby canine kidney (MDCK) cysts grown in extracellular matrix hydrogels have been successfully imaged by SPIM microscopes (Reynaud *et al.* 2008; Swoger *et al.* 2014). Moreover, monitoring of live cell division dynamics in 3D large multicellular tumor spheroids (HCT116 colon carcinoma) expressing a histone H2B-HcRed fluorescent nuclear reporter protein has been recorded (Lorenzo *et al.* 2011).

Although those works have shown the great achievement on tumor cancer cells, to our knowledge, this was the first time that light-sheet microcopy techniques has been

applied for imaging of neural aggregates. The study of the human CNS is especially challenging due to its anatomical and functional complexity. Neuronal signal transduction and communication *in vivo* depends on highly complex and dynamic 3D networks among neurons. Studies of cell-cell and cell-matrix interactions, synaptogenesis, and neural network plasticity are pivotal in improving our understanding of neurodegenerative disorders, such as Parkinson's disease. 3D cell based models are thus becoming the widespread strategy used to address these issues. However, to fully take advantage of these models and study cells' phenotype, interaction, and spatial organization within the aggregates, there is a need for more powerful and informative tools that enable a characterization *in toto* of the culture with sufficient resolution in space and in time (Pampaloni *et al.* 2013). The large size and highly scattering nature of these samples constitutes a challenge when it comes to imaging and classical imaging techniques do not seem to be ideal in terms of penetration depth and rapid acquisition. The LSFM system here presented represents an important breakthrough in order to fully exploit the benefits of the third dimension in the life sciences, and particularly in neural cell biology. The major interest at this point is the improvement of the sample preparation protocol for efficient immune-staining of the inner part of the aggregates to further test the penetration depth of the setup. Nevertheless, with the use of cells expressing constitutive fluorescent markers, it is possible to bypass the limiting step of antibody penetration and fully exploit the potentialities of the system. The results presented in this study demonstrate the setup's ability to visualize the 3D network of cells transduced with viral vectors. This highlights the potential that arises from combining this powerful imaging technique with 3D cell models for future studies on the efficacy of viral vectors as gene delivery approach.

The development of new compounds targeting CNS disorders has struggled with toxicity and efficacy issues during clinical trials, with only an 8% approval rate in clinical trials (Miller 2010). Moreover, the failure of the drugs tends to happen in later stages of the clinical trials, resulting in huge investment losses (Miller 2010). Therefore, new approaches are needed to screen and characterize the neurotoxic potential of chemicals in pre-clinical stages.

LSFM specific configuration, with the use of fluorescence optical sectioning, exposes the samples up to 5000 times less energy than commonly used confocal microscopes, making it suitable for imaging live cultures over long periods of time, with reduced photobleaching and phototoxicity (Pampaloni *et al.* 2013). As proof-of-principle, dedicated incubation and feeding systems were developed based on FEP tubes, avoiding the use of agarose and maintaining live cells under conditions of higher physiological relevance to perform long-term toxicity studies with the use of fluorescent probes.

The obtained results demonstrate that this setup is able to maintain differentiated neural aggregates viable for the duration of the assay. The readily accessible feeding tube gives the possibility to add nutrients, pharmaceutical agents and fluorescent dyes without moving the samples, and enables real time acquisition and monitoring of the effects. In this study, a prototypical stress inducer drug was used—tBHP (Peterson *et al.* 2007)—and time-dependent cell death by apoptosis was monitored. This setup and the use of an apoptotic fluorescence marker surpasses the usually conducted endpoint assays, by enabling to visualize the effects of the toxic compound in real time, as well as to follow-up of each individual sample along time.

This work demonstrated that this setup is able to deliver a spatially resolved analysis of new therapeutics effects in 3D models. By combination with different fluorescent probes, this system has the potential to undercover a given compound's outcome at the morphological, biochemical and gene expression levels, highly improving the accuracy of toxicity screenings in pre-clinical trials.

Because of their high quality (especially good axial resolution, high dynamic range, and low noise), LSFM datasets generally do not require common preprocessing routines such as denoising, deconvolution, or unmixing. Rather, it is the complexity and quantity of the new information acquired that calls for new tools for data segmentation, visualization and navigation. As SPIM data are mostly not only 3D, multi-color and multi-view, but also represent a time sequence, it is especially challenging to extract and illustrate the dynamics that are hidden in these data. The capabilities of the multiview fusion in fixed samples was demonstrated, enabling to extract useful information that otherwise would be lost on traditional microscopy techniques lacking sample rotation. However there are still limitations inherent to the new way of seeding light into the sample can be easily overcome increasing the complexity of the system. One of the major limitations of LSFM is the creation of stripe patterns due to absorption of light at the surface of the samples on the light propagation path. Different approaches have been proposed to overcome those artifacts. On one hand image processing for variational stationary noise removal (Fehrenbach *et al.* 2012) or multi-view fusion (Preibisch *et al.* 2010), used in this work, allow to correct those artifacts up to some extent, but requires powerful workstations and long processing times. On the other hand double side illumination systems (Huisken and Stainier 2007) or systems that allow to pivot the light sheet (Greger *et al.* 2007) remove stripes of shadows generated by the light being scattered in the first layers during acquisition, reducing the image processing time. Another promising approach is by the used of self-regenerative Bessel laser beams (Olarte *et al.* 2012). Image acquisition frame rate is another issue that must be taken into account, depending on the processes under analysis. Nowadays,

sCMOS cameras allow to record at higher frame rates, so the limitation on the acquisition speed depends only on the fluorescent signal of the sample, and the sample scanning speed. The described system is actually limited, for 3D imaging, by the scanning method, where the sample is moved through the light sheet at relatively slow speeds, allowing a maximum of four frames per second at full resolution. Recently different approaches, where the sample is maintained at the same position, while the focal point of the detection objective is moved in coordination with the light sheet axial position, allowed increased imaging speeds. The position of the objective focal point can be modified either mechanically with a piezo-electric motor such the case of the iSPIM system (Wu *et al.* 2011) or optically using tunable lens (Fahrbach *et al.* 2013) providing from rates from 200 to 500 fps. However those systems do not include the sample rotation option. Moreover, configuration with two sided illumination and two cameras increase the speed of the system either by imaging two views simultaneously, so reducing the number of views needed for image fusion either acquiring two fluorescence channels simultaneously (Krzic *et al.* 2012). Finally, another limitation of this technique for experimental application is the fact that samples need to be mounted on agarose one by one in order to be imaged, limiting the number of samples analyzed. High throughput imaging could represent the last barrier, since sample mounting by embedding it in agarose limits the controlled delivery of drugs or an ideal environment for long term imaging, such as cell proliferation and differentiation. However new advances has been presented for combining light sheet imaging approaches to microfluidics (Bruns 2012), flow cytometry (Wu *et al.* 2013), and tissue culture experiments (Ansari *et al.* 2013), opening the door to increasingly complex experiments.

3D models are progressively becoming more relevant as research tools and consequent advances in optical microscopy are required to more accurately assess these thick and highly scattering samples. This 3D organization is especially important in the CNS, where the connections between cells actively contribute to their maturation and functionally (Momčilović *et al.* 2012). Therefore, light sheet-based fluorescence microscopy is here presented as a promising approach, not only to assess immunofluorescence staining of fixed samples, but also suitable to monitor functional properties of the different neural cells in live assays.

5. Acknowledgments

The authors gratefully acknowledge Dr Eric J. Kremer for the supply of CAVGFP vector and Dr. Johannes Schwarz for the supply of hmNPC. The authors acknowledge support from Fundação para a Ciência e Tecnologia, Portugal—grants SFRH/BD/80717/2011, EXPL/BBB-IMG/0363/2013, PTDC/EBB-BIO/119243/2010,

and PTDC/EBB-BIO/112786/2009; and from BrainCAV (FP7-222992), funded by the EU. Catarina Pinto and Daniel Simão were recipients of PhD fellowships from FCT, Portugal (SFRH/BD/52202/2013 and SFRH/BD/78308/2011, respectively).

6. References

Ansari N., Müller S., Stelzer E. H. K., Pampaloni F. (2013) Quantitative 3D Cell-Based Assay Performed with Cellular Spheroids and Fluorescence Microscopy. *Methods in Cell Biology*. **113**, 295-309

Björklund T., Kordower J. H. (2010) Gene therapy for Parkinson's disease. *Mov. Disord*. **25**, S161–S173.

Breslin S., O'Driscoll L. (2013) Three-dimensional cell culture: The missing link in drug discovery. *Drug Discov. Today* **18**, 240–249.

Brito C., Simão D., Costa I., Malpique R., Pereira C. I., Fernandes P., Serra M., *et al.* (2012) 3D cultures of human neural progenitor cells: dopaminergic differentiation and genetic modification. *Methods* **56**, 452–60.

Bru T., Salinas S., Kremer E. J. (2010) An Update on Canine Adenovirus Type 2 and Its Vectors. *Viruses* **2**, 2134–2153.

Bruns T. (2012) Preparation strategy and illumination of three-dimensional cell cultures in light sheet–based fluorescence microscopy. *J. Biomed. Opt.* **17**, 101518.

Edelstein A., Amodaj N., Hoover K., Vale R., Stuurman N. (2010) Computer control of microscopes using micromanager. *Curr. Protoc. Mol. Biol.* **92**:14.20, 14.20.1–14.20.17.

Fahrbach F. O., Voigt F. F., Schmid B., Helmchen F., Huisken J. (2013) Rapid 3D light-sheet microscopy with a tunable lens. *Opt. Express* **21**, 21010–21026.

Fehrenbach J., Weiss P., Lorenzo C. (2012) Variational algorithms to remove stationary noise: Applications to microscopy imaging. *IEEE Trans. Image Process.* **21**, 4420–4430.

Greger K., Swoger J., Stelzer E. H. K. (2007) Basic building units and properties of a fluorescence single plane illumination microscope. *Rev. Sci. Instrum*. **78**.

Gualda E. J., Vale T., Almada P., Feijó J. A., Martins G. G., Moreno N. (2013) OpenSpinMicroscopy: an open-source integrated microscopy platform. *Nat Methods* **10**, 599–600.

Hirschhaeuser F., Walenta S., Mueller-Klieser W. (2010) Efficacy of catumaxomab in tumor spheroid killing is mediated by its trifunctional mode of action. *Cancer Immunol. Immunother.* **59**, 1675–1684.

Huisken J., Stainier D. Y. R. (2007) Even fluorescence excitation by multidirectional selective plane illumination microscopy (mSPIM). *Opt. Lett.* **32**, 2608–2610.

Justice B. A., Badr N. A., Felder R. A. (2009) 3D cell culture opens new dimensions in cell-based assays. *Drug Discov. Today* **14**, 102–107.

Kaufmann A., Mickoleit M., Weber M., Huisken J. (2012) Multilayer mounting enables long-term imaging of zebrafish development in a light sheet microscope. *Development* **139**, 3242–3247.

Kim J. Bin, Stein R., O'Hare M. J. (2004) Three-dimensional *in vitro* tissue culture models of breast cancer - a review. *Breast Cancer Res. Treat.* **85**, 281–91.

Krzic U., Gunther S., Saunders T. E., Streichan S. J., Hufnagel L. (2012) Multiview light-sheet microscope for rapid *in toto* imaging. *Nat. Methods* **9**, 730–733.

Lorenzo C., Frongia C., Jorand R., Fehrenbach J., Weiss P., Maandhui A., Gay G., Ducommun B., Lobjois V. (2011) Live cell division dynamics monitoring in 3D large spheroid tumor models using light sheet microscopy. *Cell Div.* **6**, 22.

Mariani J., Simonini M. V., Palejev D., Tomasini L., Coppola G., Szekely A. M., Horvath T. L., Vaccarino F. M. (2012) Modeling human cortical development *in vitro* using induced pluripotent stem cells. *Proc. Natl. Acad. Sci.* **109:**31, 12770-5

Miller G. (2010) Is pharma running out of brainy ideas? *Science*. **329**, 502-504

Momčilović O., Montoya-Sack J., Zeng X. (2012) Dopaminergic differentiation using pluripotent stem cells. *J. Cell. Biochem.* **113**, 3610–3619.

Moors M., Rockel T. D., Abel J., Cline J. E., Gassmann K., Schreiber T., Schuwald J., Weinmann N., Fritsche E. (2009) Human neurospheres as three-dimensional cellular systems for developmental neurotoxicity testing. *Env. Heal. Perspect* **117**, 1131–8.

Nelson S. B., Sugino K., Hempel C. M. (2006) The problem of neuronal cell types: a physiological genomics approach. *Trends Neurosci.* **29**, 339–345.

No D. Y., Lee S. a., Choi Y. Y., Park D., Jang J. Y., Kim D. S., Lee S. H., Johnson R. (2012) Functional 3D Human Primary Hepatocyte Spheroids Made by Co-Culturing Hepatocytes from Partial Hepatectomy Specimens and Human Adipose-Derived Stem Cells. *PLoS One* **7**.

Olarte O. E., Licea-Rodriguez J., Palero J. a., Gualda E. J., Artigas D., Mayer J., Swoger J., *et al.* (2012) Image formation by linear and nonlinear digital scanned light-sheet fluorescence microscopy with Gaussian and Bessel beam profiles. *Biomed. Opt. Express* **3**, 1492.

Pampaloni F., Ansari N., Stelzer E. H. K. (2013) High-resolution deep imaging of live cellular spheroids with light-sheet-based fluorescence microscopy. *Cell Tissue Res.* **352**, 161–177.

Pampaloni F., Reynaud E. G., Stelzer E. H. K. (2007) The third dimension bridges the gap between cell culture and live tissue. *Nat. Rev. Mol. Cell Biol.* **8**, 839–845.

Peterson B., Knotts T., Cummings B. S. (2007) Involvement of Ca2+-independent phospholipase A2 isoforms in oxidant-induced neural cell death. *Neurotoxicology* **28**, 150–160.

Preibisch S., Amat F., Stamataki E., Sarov M., Singer R. H., Myers E., Tomancak P. (2014) Efficient Bayesian-based multiview deconvolution. *Nat. Methods* **11**, 645–8.

Preibisch S., Saalfeld S., Schindelin J., Tomancak P. (2010) Software for bead-based registration of selective plane illumination microscopy data. *Nat. Methods* **7**, 418–419.

Reynaud E. G., Krzic U., Greger K., Stelzer E. H. K. (2008) Light sheet-based fluorescence microscopy: more dimensions, more photons, and less photodamage. *HFSP J.* **2**, 266–275.

Serra M., Brito C., Costa E. M., Sousa M. F. Q., Alves P. M. (2009) Integrating human stem cell expansion and neuronal differentiation in bioreactors. *BMC Biotechnol.* **9**, 82.

Simão D, Pinto C, Piersanti S, Weston A, Peddie CJ, Bastos AEP, Licursi V, Schwarz SC, Collinson LM, Salinas S, Serra M, Teixeira AP, Saggio I, Lima PA, Kremer EJ, Schiavo G, Brito C, Alves PM (2015) Modeling human neural functionality *in vitro*: 3D culture for dopaminergic differentiation. *Tissue Eng. Part A* **21**:3-4, 654-68

Swoger J., Pampaloni F., Stelzer E. H. K. (2014) Imaging MDCK Cysts with a Single (Selective) Plane Illumination Microscope. *Cold Spring Harb Protoc.*

Verveer P. J., Swoger J., Pampaloni F., Greger K., Marcello M., Stelzer E. H. K. (2007) High-resolution three-dimensional imaging of large specimens with light sheet-based microscopy. *Nat. Methods* **4**, 311–313.

Vinci M., Gowan S., Boxall F., Patterson L., Zimmermann M., Court W., Lomas C., Mendiola M., Hardisson D., Eccles S. a (2012) Advances in establishment and analysis of three-dimensional tumor spheroid-based functional assays for target validation and drug evaluation. *BMC Biol.* **10**, 29.

Wu J., Li J., Chan R. K. Y. (2013) A light sheet based high throughput 3D-imaging flow cytometer for phytoplankton analysis. *Opt. Express* **21**, 14474–80.

Wu Y., Ghitani a., Christensen R., Santella a., Du Z., Rondeau G., Bao Z., Colon-Ramos D., Shroff H. (2011) Inverted selective plane illumination microscopy (iSPIM) enables coupled cell identity lineaging and neurodevelopmental imaging in Caenorhabditis elegans. *Proc. Natl. Acad. Sci.* **108**, 17708–17713.

Yu Y., Fisher J. E., Lillegard J. B., Rodysill B., Amiot B., Nyberg S. L. (2012) Cell therapies for liver diseases. *Liver Transplant.* **18**, 9–21.

4

Evaluation of helper-dependent canine adenovirus vectors in a 3D human CNS model

This chapter was adapted from:

Simão D, Pinto C, Fernandes P, Peddie CJ, Piersanti S, Collinson LM, Salinas S, Saggio I, Schiavo G, Kremer EJ, Brito C, Alves PM (2016) Evaluation of helper-dependent canine adenovirus vectors in a 3D human CNS model. *Gene Therapy* 23(1): 86-94

Table of Contents

Abstract

Gene therapy is a promising approach with enormous potential for treatment of neurodegenerative disorders. Viral vectors derived from canine adenovirus type 2 (CAV-2) present attractive features for gene delivery strategies in the human brain, by preferentially transducing neurons, are capable of efficient axonal transport to afferent brain structures, have a 30-kb cloning capacity and have low innate and induced immunogenicity in pre-clinical tests. For clinical translation, in-depth pre-clinical evaluation of efficacy and safety in a human setting is primordial. Stem cell-derived human neural cells have a great potential as complementary tools by bridging the gap between animal models, which often diverge considerably from human phenotype, and clinical trials.

Herein, helper-dependent CAV-2 (hd-CAV-2) efficacy and safety for gene delivery were explored in a human stem cell-derived 3D neural *in vitro* model. Assessment of hd-CAV-2 vector efficacy was performed at different multiplicities of infection, by evaluating transgene expression and impact on cell viability, ultrastructural cellular organization and neuronal gene expression. Under optimized conditions, hd-CAV-2 transduction led to stable long-term transgene expression with minimal toxicity. hd-CAV-2 preferentially transduced neurons, while human adenovirus type 5 (HAdV5) showed increased tropism towards glial cells.

This work demonstrates, in a physiologically relevant 3D model, that hd-CAV-2 vectors are efficient tools for gene delivery to human neurons, with stable long-term transgene expression and minimal cytotoxicity.

1. Introduction

Neurodegenerative diseases, typically characterized by a progressive nervous system dysfunction, represent a heavy burden both in terms of patient suffering and economic cost. The prevalence of neurologic disorders has dramatically increased over the last decades and continues to increase, mainly due to higher life expectancy of populations, which elicits the urgent need for effective therapeutics (Forman *et al.* 2004).

With the increasing knowledge on the etiology of these disorders, several genetic mutations have been linked with the sporadic and familial forms of neurodegenerative diseases. The identification of these mutations provides new insight on the molecular mechanisms involved in disease onset and progression, but also promising therapeutic targets for alternative approaches to traditional pharmacological treatments, such as gene therapy (Ulusoy and Kirik 2011). Briefly, most gene delivery approaches focus either on enzyme replacement, by restoring the enzymatic capacity of the affected brain regions, or on delivery of neurotrophic factors to prevent the progression of the neurodegeneration process (Björklund and Kirik 2009).

Over the last three decades multiple non-viral gene delivery vehicles have been explored, yet viral vectors are still the most efficient tools for *in vivo* gene transfer. Each viral vector system has unique strengths and specific drawbacks (Gan *et al.* 2013; Lentz *et al.* 2012). Therefore, thorough evaluation is required for selection of the optimal vector system for central nervous system (CNS) gene delivery. Most neurological disorders only affect a specific cell type, as is the case of the dopaminergic neurons of the nigrostriatal pathway in Parkinson's disease (PD) (Toulouse and Sullivan 2008). Thus, in addition to high transduction efficiency, vector tropism is paramount to achieve targeted gene delivery to the affected cells of a confined brain region, minimizing off-target transduction. To maximize the therapeutic effect and minimize repeated dosage, an ideal vector should be able to sustain long-term expression of the transgene with a single treatment. Most importantly, the vector must be safe and avoid host immune responses or cytotoxicity, which may also hinder the therapeutic effect. Finally, it is important to consider vector manufacturing methods, which should be scalable, allow high titers and high purity (Gray *et al.* 2010; Lentz *et al.* 2012; Feng and Maguire-zeiss 2010).

Recombinant adeno-associated viruses (AAV) have been the most widely used and studied vectors for gene delivery in the CNS and peripheral nervous system. The variety of AAV serotypes enables the mixing of viral genomes and capsids creating mosaic "pseudotype" which display a range of tropisms and efficacies, along with low pathogenicity and immunogenicity (Manfredsson and Mandel 2010; Lentz *et al.* 2012).

However, AAV vectors have a limited cloning capacity (≈4-6 kb), which limits their use in some applications. Recombinant adenovirus (AdV) vectors are an attractive alternative, due to a large cloning capacity (8-30 kb) and long-term transgene expression (Manfredsson and Mandel 2010; Lentz *et al.* 2012), being the most explored platform in clinical trials worldwide (http://www.wiley.com/legacy/wileychi/genmed/clinical). Nonetheless, the toxicity and immunogenicity of some AdV types have been widely described (Lentz *et al.* 2012; Gray *et al.* 2010; Manfredsson and Mandel 2010), limiting the therapeutic efficacy. Non-human AdV vectors, such as canine adenovirus type 2 (CAV-2) vectors emerged as an alternative to human AdV (HAdV), mainly due to lack of immunological memory (Perreau and Kremer 2006). CAV-2 vectors preferentially transduce neurons in the rodent brain and in human organotypic cultures, along with efficient biodistribution via axonal retrograde transport in neurons (Salinas *et al.* 2009; Soudais *et al.* 2001b). The development of helper-dependent CAV-2 vectors (hd-CAV-2) (Bru *et al.* 2010; Soudais *et al.* 2004) improved the efficiency and duration of transgene expression, minimizing the adaptive cell-mediated immune response (Bru *et al.* 2010). hd-CAV-2 vectors have a cloning capacity of 30 kb (Bru *et al.* 2010) and allow stable transgene levels over 1 year in immunocompetent rat brain without immunosuppression (Soudais *et al.* 2004).

During viral vector development, preclinical testing is crucial to evaluate both efficacy and safety, while understanding vector-cell interactions. Although the traditional primary cultures of rodent brain cells and animal models provide valuable data, these models too often diverge considerably from the human phenotype (Schüle *et al.* 2009), thus not accurately predicting the outcome of clinical trials. In this context, stem cell-derived human neural cells, along with three dimensional (3D) culture systems, have great potential as complementary tools in pre-clinical research, bridging the gap between human clinical studies and animal models (Schüle *et al.* 2009; Pampaloni *et al.* 2007). The development of a 3D neural cell model based on the differentiation of human midbrain-derived neural progenitor cells (hmNPC) as neurospheres, in a agitation-based culture system, was previously reported (Brito *et al.* 2012; Simão *et al.* 2015). Differentiated neurospheres contain glial cells, oligodendrocytes and functional neurons, with enrichment in the dopaminergic phenotype.

In this study, hd-CAV-2 vectors gene delivery efficiency and cytotoxicity were evaluated taking advantage of the 3D neural *in vitro* model (Brito *et al.* 2012; Simão *et al.* 2015). For this, a reporter eGFP-expressing hd-CAV-2 was used, which can be produced in a robust and scalable bioprocess (Fernandes *et al.* 2013a; Fernandes *et al.* 2015), compatible with pre-clinical and clinical applications. Assessment of hd-CAV-2 transduction was performed at different multiplicities of infection (MOI), by evaluating

transgene expression and cell viability, impact on neuronal gene expression and cell morphology. This study show that hd-CAV-2 transduction led to stable long-term transgene expression with low toxicity, demonstrating in a physiologically relevant human *in vitro* model, that hd-CAV-2 vectors are efficient vehicle for gene transfer to human neurons for treatment of neurodegenerative diseases.

2. Materials and Methods

2.1. hmNPC expansion and differentiation

Human midbrain-derived neural progenitor cells (hmNPC) derived from aborted fetal brain tissue 12 to 14 weeks post-fertilization (Brito *et al.* 2012; Storch *et al.* 2001) were kindly provided by Dr. Johannes Schwarz (Technical University of Munich, Germany), within the scope of the EU project BrainCAV (FP7-222992). Tissue was obtained with mother's consent and in accordance with the Ethics Committee of the University of Leipzig and the German state and federal laws. Expansion and differentiation of hmNPC was performed as previously described (Brito *et al.* 2012; Simão *et al.* 2015). Briefly, hmNPC were expanded on poly-L-ornithine-fibronectin (PLOF)-coated surfaces and serum-free medium (Brito *et al.* 2012). Differentiation was performed as neurospheres in shake flasks (Corning, New York, USA) under constant orbital shaking (Simão *et al.* 2015). Cells were maintained in a multi-gas cell incubator (Panasonic Biomedical, Leicestershire, UK) at 37°C, in a humidified atmosphere of 5% CO_2 and 3% O_2 in air. Cells were routinely screened to exclude mycoplasm contamination.

2.2. Viral stock production

hd-CAV-2 are vectors derived from CAV-2 strain Toronto A 26/61, GenBank J04368. HAdV5 vectors are E1-deleted adenovirus type 5, based on plasmid pGS66, containing viral genome sequences from nucleotide 1 to 440 and 3523 to 35935 (Schiedner *et al.* 2000). Both vectors contain an eGFP expression cassette consisting in a human cytomegalovirus immediate early promoter, cDNA coding for eGFP and the SV40 polyA signal. hd-CAV-2 stocks were produced by co-infection with JBΔ5 helper virus of E1-complementing dog kidney cells expressing Cre recombinase (DKCre) and purified by CsCl gradients, as previously described (Kremer *et al.* 2000; Fernandes *et al.* 2013b; Soudais *et al.* 2004). HAdV5 were produced using human embryonic kidney cells (HEK293) followed by CsCl purification, according to previous reports (Ferreira *et al.* 2009; Silva *et al.* 2015). Stocks titration were performed by infectivity assay for number of infectious particles/mL (ip/mL) (Ferreira *et al.* 2009; Fernandes *et al.* 2013a). The obtained preparations had a physical to infectious particles (pp/ip) unit ratio of 100:1 for hd-CAV-2 and 15:1 for HAdV5. hd-CAV-2 had a helper virus contamination level

of 1.8%. In this study, multiplicity of infection (MOI) was determined by the number of infectious viral particles per cell (ip/cell).

2.3. Transduction

Following hmNPC neurospheres differentiation, transduction was performed with 50% reduction of the working volume. Total cell number was determined by counting cell nuclei using a Fuchs-Rosenthal hemacytometer after digestion with lysis buffer (0.1 M citric acid, 1% Triton X-100 (w/w) and 0.1% crystal violet (w/v)) (Alves *et al.* 1996). At 4 h post-transduction a complete media exchange was performed. Neurospheres were maintained in culture up to 30 days post-transduction, with a 75% medium exchange performed every 3 days.

2.4. Cell viability

Cell viability was assessed using the metabolic indicator PrestoBlue™ (Life Technologies, Paisley, UK), according to the manufacture's recommendation. Briefly, neurospheres were plated on PLOF-coated multi-well plates and allowed to attach for 2 hours. Cells were incubated with fresh medium containing 10% (v/v) PrestoBlue, for 2 hours. Supernatant's fluorescence was measured in 96-well plates using a microwell plate fluorescence reader (FluoroMax-4, Horiba JobinYvon, Kyoto, Japan) and neurospheres were harvested for total protein quantification, using the Micro BCA Protein Assay Kit (Life Technologies). Fluorescence intensity was normalized for total protein and evaluated relatively to control (MOI 0).

2.5. Fluorescence microscopy

Neurospheres were plated on PLOF-coated glass coverslips and allowed to attach for 2 days, fixed in 4% (w/v) paraformaldehyde (PFA) + 4% (w/v) sucrose in PBS for 30 min and processed for immunostaining as previously described (Serra *et al.* 2011). Primary and secondary antibodies were used as follows: mouse anti-βIII-tubulin (1:200; Millipore Darmstadt, Germany, MAB1637); mouse anti-GFP (1:200; Sigma-Aldrich, St Louis, MO, USA, G6539); rabbit anti-TH (1:100; Santa Cruz Biotechnology, Dallas, TX, USA, sc-14007); rabbit anti-GFAP (1:200; Millipore, AB5804); rabbit anti-CAR (1:200; gift from Joseph Zabner), mouse anti-CAR (1:200; Millipore, 05-644); AlexaFluor® 488 goat anti-mouse IgG (1:500; Life Technologies, A11001) and AlexaFluor® 594 goat anti-rabbit IgG (1:500; Life Technologies, A11012). Cell nuclei were counterstained with DAPI or TO-PRO-3 (Life Technologies). Samples were visualized using point scan confocal microscopy (SP5, Leica, Wetzlar, Germany). Merge

between channels and maximum z-projections, as well as linear brightness and contrast adjustments of the images, were performed using the ImageJ software.

2.6. Electron microscopy

Neurospheres were fixed in 2.5% (w/v) glutaraldehyde and 4% (w/v) formaldehyde in 0.1 M phosphate buffer (pH 7.4) and then processed for serial blockface scanning electron microscopy (SBF-SEM). Samples were embedded in Durcupan resin following the method of NCMIR (Deerinck *et al.* 2010). Small groups of neurospheres were mounted on pins and trimmed for SBF-SEM. Images were acquired using a 3View2XP (Gatan Pleasanton, CA, USA) attached to a Sigma VP SEM (Zeiss, Cambridge, UK), at a resolution of 8,192 x 8,192 pixels (horizontal frame width of 64.29 µm; pixel size of 7.8 nm) with 2 µs dwell time and 35 nm slice thickness. SEM was operated in high vacuum, with high current mode active, at an indicated magnification of 4,000. The 20 µm aperture was used, at an accelerating voltage of 1.4 kV (hd-CAV-2 transduced) or 1.2 kV (control). Alignment of the image stack was accomplished using the 'Register virtual stack slices' plugin in Fiji (Schindelin *et al.* 2012), with translation based extraction and registration models to minimize distortion of the dataset. Aligned image stacks were then calibrated for pixel dimensions. Movies were generated using Amira (FEI Visualization Sciences Group, Merignac, France) and Quicktime Pro, showing 500 slices from the center of each dataset (total dataset for hd-CAV-2 transduced = 1,450 slices, representing a total volume of 209,760 μm^2; total dataset for control = 533 slices, representing a total volume of 77,105 μm^2).

2.7. RT-qPCR

Neurospheres were sedimented by centrifugation at 500 x*g* for 5 min, washed with PBS and the dry pellet snap-freezed by immersion in liquid nitrogen. Samples were stored at -80 °C until RNA extraction. Total RNA was extracted with High Pure RNA Isolation Kit (Roche Applied Science, Mannheim, Germany), according to the manufacturer's instructions. RNA was quantified in a NanoDrop 2000c (Life Technologies) and used for cDNA synthesis. Reverse transcription was performed with High Fidelity cDNA Synthesis Kit (Roche Applied Science), using Anchored-oligo(dT)18 Primer (Roche) or with the Super Script III First Strand synthesis system (Life Technologies), using random hexamers (Life Technologies). qPCRs were performed in triplicates using LightCycler 480 SYBR Green I Master Kit (Roche Applied Science) with the following primers: eGFP (GFP fwd 5'-CAACAGCCACAACGTCTATATCATG-3' and GFP rev 5'-ATGTTGTGGCGGATCTTGAAG-3'), tyrosine hydroxylase (TH fwd 5'-agccctaccaagaccagacg-3' and TH rev 5'-gcgtgtacgggtcgaactt-3'), synapsin II (SYN2 fwd

5′-tggaacaggcagaattttca-3′ and SYN2 rev 5′-ggacaacctttgtgccattc-3′) and ribosomal protein L22 (RPL22 fwd 5′-cacgaaggaggagtgactgg-3′ and RPL22 rev 5′-tgtggcacaccactgacatt-3′). As alternative TaqMan Universal PCR Master Mix (Life Technologies), and the following TaqMan® Gene Expression Assays (Life Technologies): *TRKA* (ID: Hs01021011_m1); *TRKB* (ID: Hs00178811_m1); *TRKC* (ID:Hs00176797_m1); *RET* (ID:Hs01120030_m1); *DDC* (ID: Hs01105048_m1); *QDPR* (ID: Hs00165610_m1), *GCH1* (ID: Hs00609198_m1); *DRD2* (ID: Hs00241436_m1); *SYT1* (ID: Hs00194572_m1); *SYP* (ID: Hs00300531_m1); *SYNPO* (ID: Hs00702468_s1); *PSD95* (ID: Hs00176354_m1); *vGAT* (ID: Dm01823909_g1). The reactions were performed with Applied Biosystems 7300 Real Time PCR system or LightCycler 480 Instrument II 96-well block (Roche Applied Science). Quantification cycle values (Cq's) and melting curves were determined using LightCycler 480 Software version 1.5 (Roche Applied Science). All data were analyzed using the $2^{-\Delta\Delta Ct}$ method for relative gene expression analysis (Livak and Schmittgen 2001). Changes in gene expression were normalized using the housekeeping gene *RPL22* (ribosomal protein L22) as internal control.

2.8. Statistical Analysis

All values are presented as means ± standard error of the mean (s.e.m.) of independent experiments as indicated in the figure captions. Sample size was chosen without accounting for a pre-specified effect size. Data were tested for normality of distribution with the D'Agostino & Pearson omnibus normality test. Statistical significance between groups was assessed using Student's t-tests. Before choosing the adequate type of t-test, Levene's test for equal variances was performed. $P<0.05$ was chosen as the level of significance. All comparisons were made using two-tailed statistical tests.

3. Results

3.1. hd-CAV-2 impact on cell viability and neuronal population

To determine the most suitable transduction parameters, three MOIs were tested on the human 3D neural model (Figure 4.1A). Gene delivery efficiency was assessed by evaluating transgene expression levels, and cytotoxic effects exerted by the vectors, measuring cell viability and expression levels of neuronal and synaptic markers. The MOIs (20, 50 and 100 infectious particles/cell) were selected based on data previously generated with an E1-deleted CAV-2 vector expressing GFP (Brito *et al.* 2012). Neurosphere transduction showed an increase in transgene mRNA levels according to the MOI increase, with a 3- and 4.5-fold increase relatively to MOI 20 for MOI 50 and 100, respectively, at 5 days post-transduction (dpt) (Figure 4.1B). In agreement with

these observations, the fraction of GFP-positive cells also increased with the MOI, as observed by confocal microscopy (Figure 4.1C).

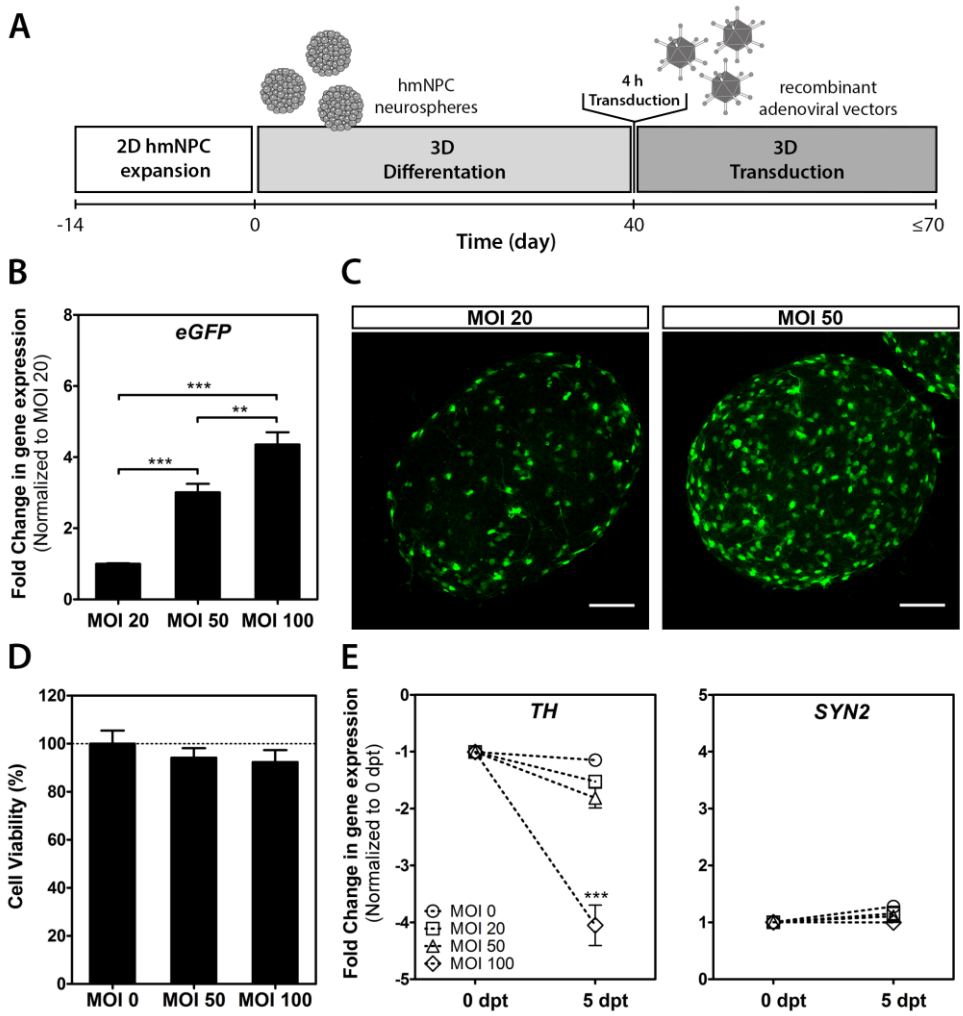

Figure 4.1 – hd-CAV-2 transduction of differentiated human midbrain-derived neural precursor cells (hmNPC) neurospheres. (A) Timeline of cell differentiation and transduction. **(B)** Fold changes of *eGFP* expression for multiplicities of infection (MOI) 20, 50 and 100 infectious particles per cell (normalized to MOI 20). **(C)** Confocal microscopy of whole neurospheres. Maximum intensity z-projections of 38 (MOI 20) and 33 (MOI 50) optical sections of 1 µm. Scale bars, 100 µm. **(D)** Cell viability assessment, normalized for control (MOI 0). **(E)** Fold changes in tyrosine hydroxylase (*TH*) and synapsin II (*SYN2*) gene expression at 0 and 5 days post-transduction (dpt) (normalized for 0 dpt). Each group was performed in triplicates. Data are mean ± s.e.m. of 3 independent experiments. Asterisks indicate significant difference (**P < 0.01, ***P < 0.001).

Cytotoxicity assessment showed no significant decrease in cell viability for MOI 50 and 100, relatively to control (Figure 4.1D). Moreover, no significant modulation in the pre-synaptic marker synapsin II (*SYN2*) gene expression was observed for the different

MOIs (Figure 4.1E). Still, a 4-fold decrease in the expression of the dopaminergic marker tyrosine hydroxylase (*TH)* was observed for MOI 100 at 5 dpt, relatively to the neurospheres before hd-CAV-2 transduction. These results suggest that higher hd-CAV-2 MOIs, although allowing higher gene delivery efficiency, can affect specific neuronal populations, such as dopaminergic neurons. These observations emphasize the need for a careful dose assessment in pre-clinical studies to identify toxic effects, while sustaining an efficient gene delivery to target cells. In this study, considering the level of transgene expression and the absence of modulation for the neuronal markers evaluated, MOI 20 and 50 were selected for further characterization of hd-CAV-2 transduction.

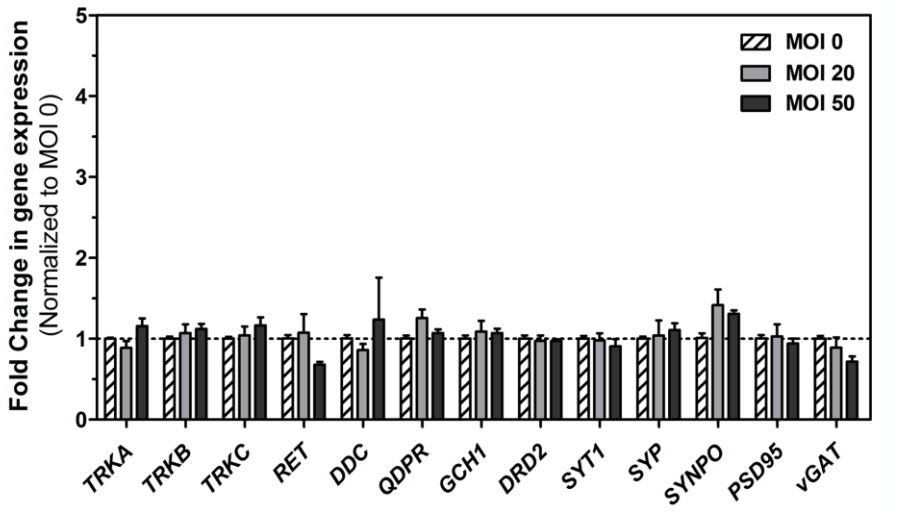

Figure 4.2 – Gene expression analysis of differentiated neurospheres transduced with hd-CAV-2. Gene expression fold changes (normalized to the MOI 0 control) of neurotrophic receptors (*TrkA*, *TrkB*, *TrkC* and *RET*), dopamine biosynthesis pathway enzymes (*DDC*, *QDPR*, *GCH1*), dopamine receptor (*DRD2*), pre-synaptic proteins (*SYT1*, *SYP*, *SYNPO* and *vGAT*) and post-synaptic protein (*PSD95*). Each group was performed in triplicates. Data are mean ± s.e.m. of 3 independent experiments.

The impact of hd-CAV-2 transduction on the neurospheres was further addressed by analyzing the expression of an enlarged set of neuronal markers (Figure 4.2), comprising neurotrophic receptors (*TrkA*, *TrkB*, *TrkC* and *RET*), dopamine biosynthesis pathway enzymes (*DDC*, *QDPR*, *GCH1*), dopamine receptor (*DRD2*), pre-synaptic (*SYT1*, *SYP*, *SYNPO* and *vGAT*) and post-synaptic (*PSD95*) proteins. Compared with the control (MOI 0), an MOI of 20 or 50 did not induce significant modulation on these markers. Thus, given the 3-fold increase in transgene expression with an MOI 50 (Figure 4.1B) and the comparable low cytotoxic effects, the MOI 50 was selected for more

comprehensive studies addressing the impact of hd-CAV-2 transduction on ultrastructural cell morphology, vector tropism and duration of transgene expression.

3.2. hd-CAV-2 impact on cell morphology

Cellular ultrastructure was analysed both for transduced (MOI 50) and non-transduced neurospheres by serial blockface scanning electron microscopy (SBF-SEM; Figure 4.3). The image stacks showed similar numbers and spatial distribution of cell bodies, as well as the complexity of the extending neuronal network. Moreover, comparable cellular ultrastructural details within non-transduced and transduced cells were observed, including clearly defined mitochondria, Golgi stacks, endoplasmic reticulum and other subcellular membrane structures. Altogether, these results suggest that hd-CAV-2 transduction did not induced noticeable structural alterations on human neural cells within the neurospheres.

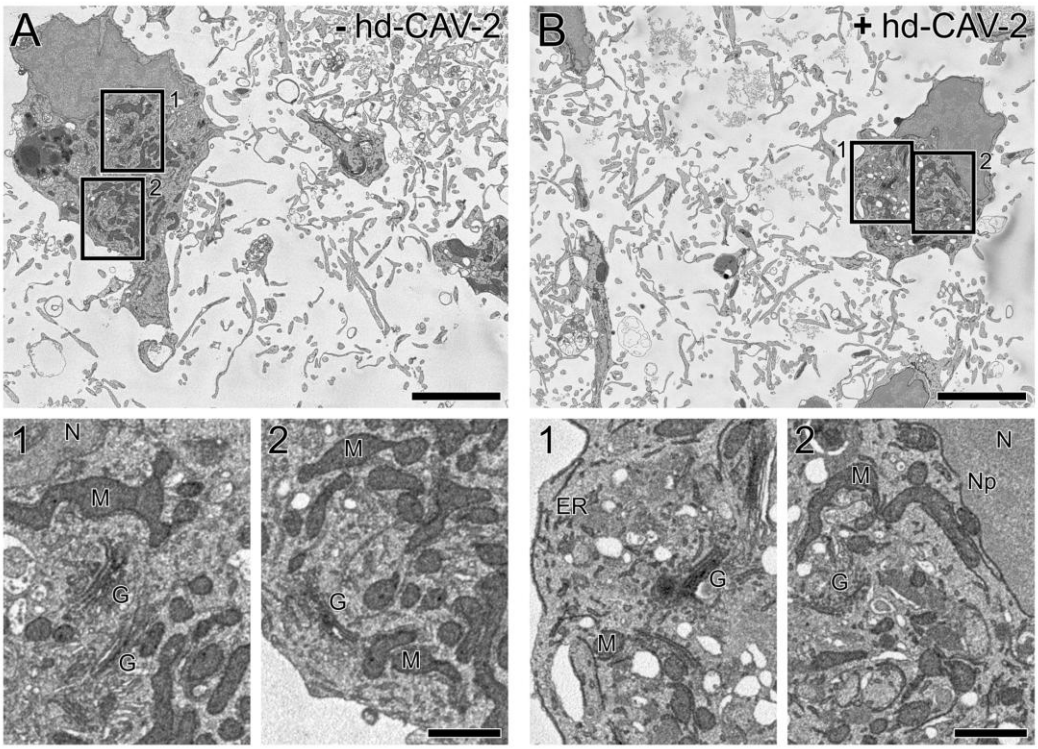

Figure 4.3 – Effects of hd-CAV-2 transduction on the ultrastructural cell organization of differentiated neurospheres. (A-B) Electron micrographs extracted from the SBF-SEM image stacks showing the internal structure of non-transduced **(A)** and hd-CAV-2 transduced (**B**; MOI 50) neurospheres at 5 days post-transduction. Boxed areas (1, 2) highlight details of ultrastructure within each cell, including mitochondria (M), Golgi stacks (G), endoplasmic reticulum (ER), and other subcellular structures (N: nucleus, Np: nuclear pore). Scale bars, 5 µm (a, b), 1 µm (1, 2).

3.3. hd-CAV-2 tropism and long-term transduction dynamics

hd-CAV-2 preferential transduction of neurons in rodent has been linked with the expression of coxsackievirus and adenovirus receptor (CAR) (Salinas *et al.* 2009; Soudais *et al.* 2001b; Soudais *et al.* 2000). Given this, the expression and distribution of CAR on human neurospheres was analyzed by confocal microscopy. As shown in Figure 4.4A, CAR is highly expressed in βIII-tubulin positive neurons, but not in glial cells labeled with GFAP. To further explore the interaction between CAV-2 vectors and human neurons, neurospheres were incubated with fluorescent CAV-2 (CAV-Cy3), followed by immunofluorescence labeling of neurons with βIII-tubulin. CAV-Cy3 particles were detected along neuronal cells (Figure 4.4B), indicating that CAV-2 vectors recognize these cells, both at the soma and branching processes, for attachment and internalization.

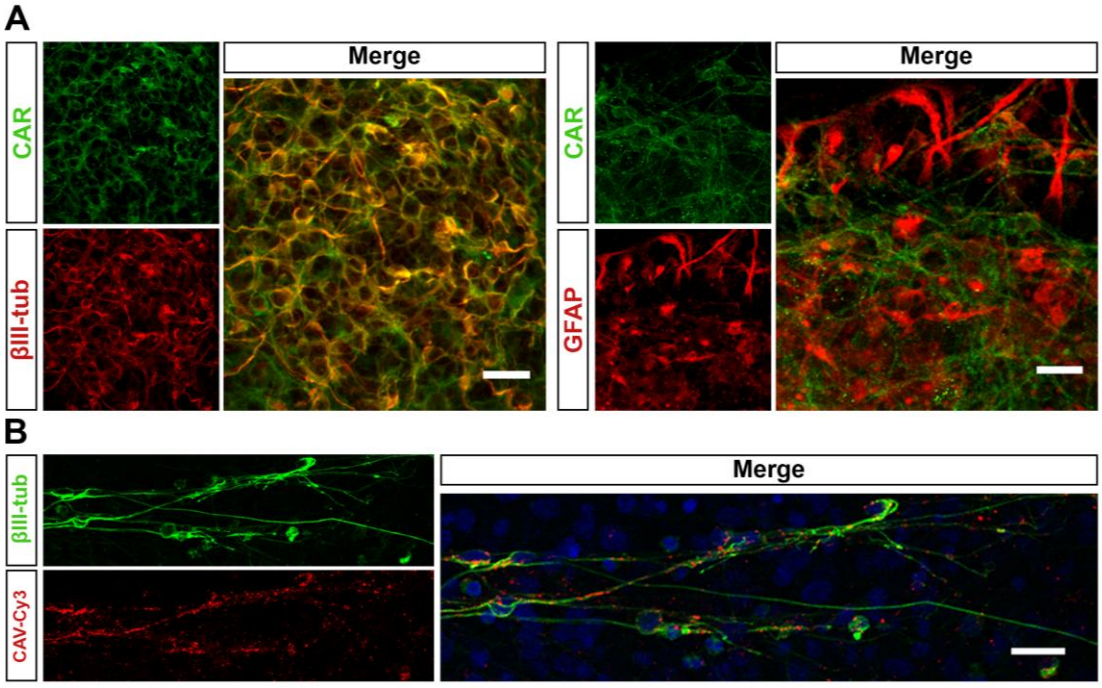

Figure 4.4 – CAR and CAV-2 distribution in differentiated neurospheres. (A) Immunofluorescence analysis of neurospheres stained for CAR, βIII-tubulin and GFAP. Maximum intensity z-projections of 33 (βIII-tubulin) and 14 (GFAP) optical sections of 0.38 µm. Scale bars, 20 µm. **(B)** Immunofluorescence of neurospheres incubated with CAV-Cy3 particles (red) stained for βIII-tubulin (green). Nuclei were labelled with TO-PRO3. Single optical section. Scale bar, 20 µm.

For a more detailed study on the tropism of hd-CAV-2 in human neural cells, the phenotype of hd-CAV-2 transduced cells was compared to a vector derived from human adenovirus type 5 (HAdV5), which has been widely explored in gene therapy (Ghosh *et al.* 2006; Räty *et al.* 2008). Differences both in terms of morphology and distri-

bution of transduced cells along the neurospheres' volume were observed (Figure 4.5A). The typical morphology of hd-CAV-2 transduced cells was neuronal-like, with long processes extending from the soma. In contrast, HAdV5-transduced cells presented glial-like morphology, with larger cytoplasmic volume and no neurites. Interestingly, upon hd-CAV-2 transduction, it was possible to identify multiple GFP-positive cells across different layers towards the inner core of the neurospheres (Figure 4.5A). Sections were plotted in blue progressing to green and red/pink across a 41-µm-volume depth. On the other hand, upon HAdV5 transduction, the presence of GFP-positive cells was restricted to the neurospheres' surface, presenting a radial pattern from blue cells in the center towards red/pink cells only in the periphery.

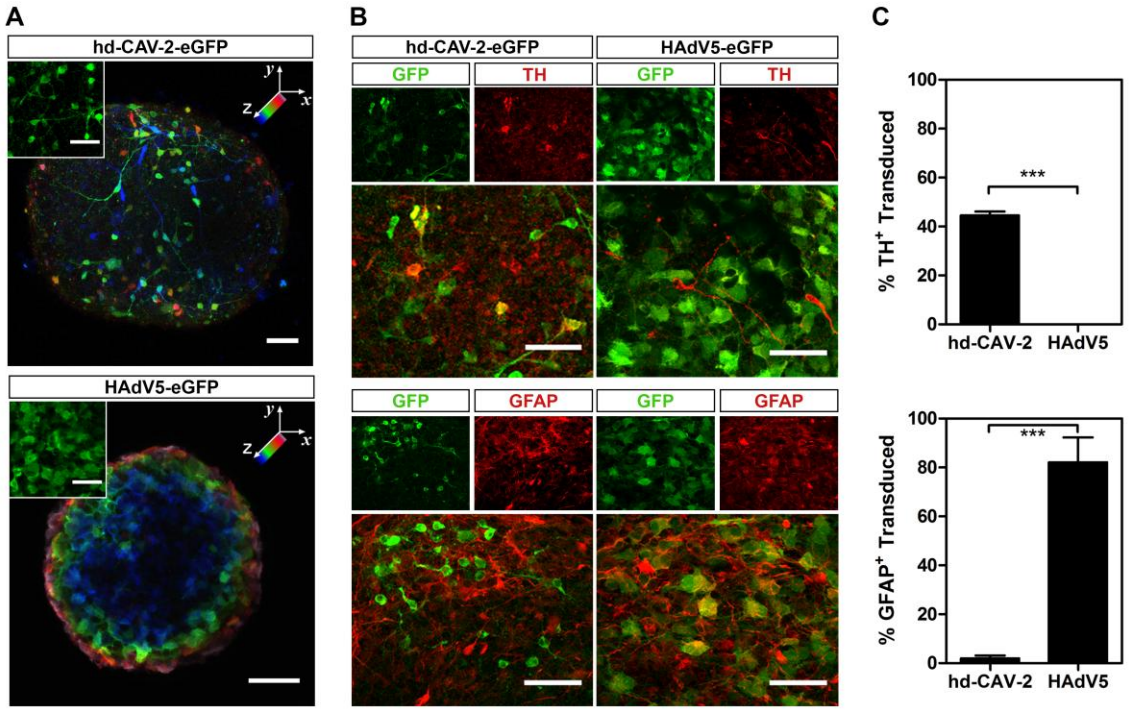

Figure 4.5 – Characterization of hd-CAV-2 and HAdV5 tropism. (A) Confocal microscopy of hd-CAV-2 and HAdV5 transduced neurospheres. Spatial distribution of transduced cells is highlighted by a depth lookup table. Maximum intensity z-projections of 41 optical sections of 1 µm, where blue indicates 0 µm and pink 41 µm. Inset depicts typical morphology of transduced cells. Scale bars, 50 µm. **(B)** Immunofluorescence analysis of neurospheres transduced with hd-CAV-2 and HAdV5, stained for TH and GFAP. Maximum intensity z-projections of 55 (TH – hd-CAV-2), 19 (TH – HAdV5), 42 (GFAP – hd-CAV-2) and 23 (GFAP – HAdV5) optical sections of 0.33 µm. Scale bars, 50 µm. **(C)** Quantification of TH+ and GFAP+ transduced cells for hd-CAV-2 and HAdV5, expressed as percentage of total TH+ or GFAP+ cells. Data are mean ± s.e.m. of 2 independent experiments.

To address the identity of hd-CAV-2 and HAdV5 transduced cells using another approach, the cell lineages were identified by immunodetection: TH staining for dopaminergic neurons and GFAP staining for glia (Figure 4.5 B and C). This assay revealed that hd-CAV-2 efficiently transduced dopaminergic neurons (TH-positive cells), with up to 50% of total TH-positive cells being GFP-positive (Figure 4.5C). Glial cells (GFAP-positive cells) were poorly transduced by hd-CAV-2. These data are consistent with CAR expression on neurons. By contrast, HAdV5 preferentially transduced glial cells, with more than 80% GFAP-positive cells also GFP-positive (Figure 4.5C), while poorly transducing TH-positive cells.

In addition to tropism, hd-CAV-2-driven transgene expression was also analyzed. Following incubation with hd-CAV-2 the neurospheres were maintained for at least 30 dpt. Compared to controls, no significant change in cell viability was detected. hd-CAV-2 transduction led to stable *eGFP* expression during this culture time (Figure 4.6). *TH* expression dynamics revealed no significant modulations over the 30 dpt, suggesting low long-term cytotoxic effects of hd-CAV-2 on dopaminergic neurons at the MOI used in this experiments. These analyses were performed in parallel for HAdV5 transduction, which resulted in slightly less stable transgene expression levels with a 2-fold increase during the first 21 dpt, followed by a decrease at 30 dpt to levels similar to those observed at 5 dpt. Similarly to hd-CAV-2, no significant modulation was observed for HAdV5 in terms of transduction impact on TH expression.

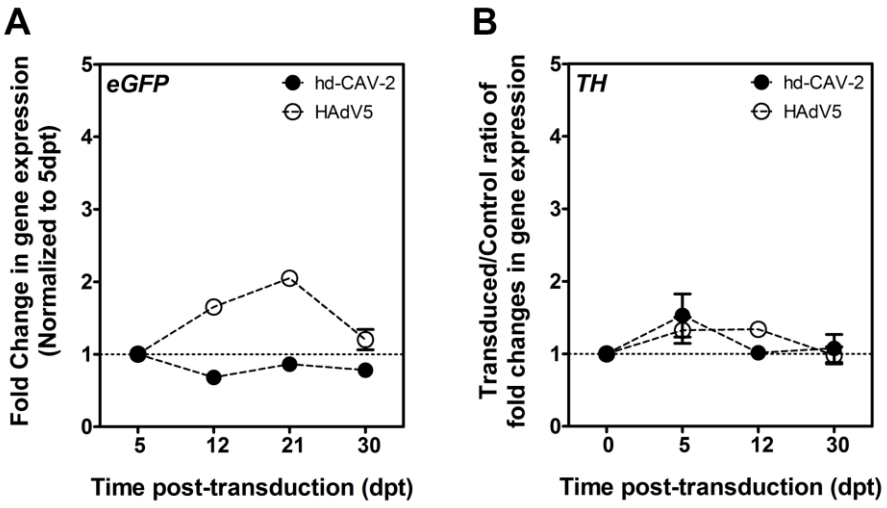

Figure 4.6 – hd-CAV-2 and HAdV5 transgene expression dynamics. Gene expression fold changes of eGFP **(A)** and TH **(B)** expression in hd-CAV-2 and HAdV5 transduced neurospheres, along 30 dpt. Each group was performed in triplicate. Data are mean ± s.e.m. of 2 independent experiments.

4. Discussion

In the rodent brain CAV-2 vectors efficiently and preferentially transduce neurons, undergoing fast retrograde axonal transport, allow long-term transgene expression and induce negligible levels of immunogenicity (Soudais *et al.* 2004; Soudais *et al.* 2001b). Given the fundamental differences between rodent and human cells, it is critical to demonstrate the efficacy and safety of such vectors in human cells at early stages of development. In this study, hd-CAV-2 vectors efficacy was assayed in a human 3D *in vitro* CNS model based on differentiation of hmNPC. During differentiation, these cells recapitulate the specific midbrain developmental program, resulting in a human cell model enriched in functional dopaminergic neurons (Simão *et al.* 2015).

This work demonstrated that hd-CAV-2 vectors efficiently transduce human neural cells. The performed screening detected cytotoxic effects at high MOIs (100 ip/cell). These effects were more evident on the dopaminergic population, as determined by a significant decrease in *TH* expression levels and no modulation on the synaptic gene *SYN2*. Notably, differential hd-CAV-2 transduction efficacy has also been observed in the rodent brain, where the higher efficiency was observed for dopaminergic neurons, followed by noradrenergic neurons and serotonergic neurons (Schwarz *et al.* 2015). Dopaminergic neurons are more susceptible to GFP toxicity, relative to other neuronal populations (Klein *et al.* 2006). In this study, transduction of rodent brain with high doses of an AAV8-GFP vector induced a significant loss in TH^+ neurons compared to an empty vector. By contrast, no loss of pyramidal or granular neurons was observed in the hippocampus. Together, these data indicate different transduction efficiencies or transgene related effects in different neuronal subtypes, which can lead to differential survival.

To confirm the absence of cytotoxicity for MOIs of 20 and 50 ip/cell, expression of a panel of neuronal genes, including neurotrophic receptors, dopamine biosynthesis pathway enzymes, dopamine receptors and synaptic proteins was evaluated at 5 dpt. No significant changes were observed for both MOIs in comparison with the control. These results are in agreement with data on the toxicogenomic profile of hd-CAV-2 transduction of 2D hmNPC cultures, showing no significant vector-induced modulation of the neuron morphogenesis pathways and an activation of pro-survival genes (Piersanti *et al.* 2013). Moreover, hd-CAV-2 transduction of neurospheres (MOI 50) did not induce overt ultrastructural alterations, either in terms of the spatial distribution within neurospheres or at intracellular level.

These results show the importance of MOI screening and optimization to attain efficient levels of gene delivery, while maintaining cytotoxic effects to a minimum. Nev-

ertheless, when considering an *in vivo* setting, one must not exclude possible immunological complications often associated with a diseased brain and gene transfer vectors, which in case of AdV are related with innate and memory immunity to the wild-type pathogen. This can lead to adverse effects upon administration, such as acute inflammatory reactions, posing a safety risk for the patient. Previous reports have shown negligible levels of neutralizing CAV-2 antibodies in healthy humans (Kremer *et al.* 2000), as well as lower immunogenicity than HAdV in immunologically naïve rodents (Soudais *et al.* 2004; Keriel *et al.* 2006). As with all vectors, this should be a matter of careful scrutiny in potential clinical trials to ensure patient safety and the success of therapy. Moreover, data obtained from rodents may not accurately reflect the human setting. A recent study showed that HAdV5 and murine coagulation factor X (FX) complexes stimulated an innate inflammatory response via Toll-like receptor 4 in murine macrophages (Doronin *et al.* 2012). However, HAdV5 and human FX complexes do not stimulate an innate response in human mononuclear phagocytes (Eichholz *et al.* 2015).

This works demonstrated in a 3D human cell model that hd-CAV-2 vectors preferentially transduce neurons rather than glial cells, in agreement with previous reports on animal models and *ex vivo* human brain slices (Soudais *et al.* 2001b; Soudais *et al.* 2004). In contrast, transduction with HAdV5 resulted in preferential glial transduction, further confirming the distinct vector tropism of CAV-2 and HAdV5 in spite of sharing many characteristics, such as a very similar capsid structure and genomic organization (Soudais *et al.* 2001a). The molecular basis for CAV-2 neuronal tropism relies on the exclusive binding of CAR and CAR-mediated internalization. Notably, the CAV-2 capsid does not contain a readily identifiable integrin-interacting motif (e.g. RGD motif) (Soudais *et al.* 2000). Hence, CAR expression is essential for CAV-2 transduction, which in this human model was restricted to the neuronal population, in agreement with previous reports in rodent models (Soudais *et al.* 2001b). Thus, these results obtained in a human context further support the CAR-dependent CAV-2 binding and internalization hypothesis, which leads to increased neuronal tropism of CAV-2 and poor glia transduction. Although HAdV5 is also a "CAR-tropic" virus and can transduce neurons, these vectors preferentially transduce glia (Soudais *et al.* 2001b). One can only speculate as to why HAdV5 does not efficiently use neuronal CAR. The different CAR binding efficiencies reported for the two vectors, where HAdV5 presents lower CAR affinity than CAV-2 (K_d values of 7.9 and 1.1 nM, respectively) (Seiradake *et al.* 2006) could explain the lower neuronal transduction efficiency of HAdV5. Also, it is conceivable that integrin-associate internalization of HAdV5 is poorly functional in CAR-rich lipid rafts of the neuron membrane, or that intracellular transport of HAdV5 is ineffi-

cient because it is released from CAR-positive vesicles prematurely during axonal transport, precluding its delivery to the soma. Clearly, CAV-Cy3 particles were shown to accumulate along neuronal processes, which indicates that CAV-2 vectors can bind and be internalized along neurites and not only in the soma. This observation, in addition to the presence of transduced neurons in the inner layers of the neurospheres, is consistent with the trafficking mechanism reported for murine primary neurons (Salinas *et al.* 2009; Salinas *et al.* 2014). These studies demonstrate that after CAR binding and subsequent internalization, CAV-2 vectors are transported in axons via a CAR-associated mechanism. Retrograde axonal transport of CAV-2 in murine neurons is 10-fold greater compared to HAdV5 (Soudais *et al.* 2001b), allowing long distance targeting that provides means of targeting cells or brain regions that are typically difficult to reach. In addition to CAV-2 tropism, one can further explore strategies for neuronal specific transgene expression, such as neuronal specific promoters (Huang *et al.* 2005; Namikawa *et al.* 2006) that can reduce potential off-target transduction and/or restrict transgene expression to a neuronal subpopulation (e.g. dopaminergic neurons).

This work demonstrates, in a physiologically relevant 3D model, that hd-CAV-2 vectors are efficient vehicles for gene transfer to human neurons, with stable transgene expression and minimal cytotoxicity. In the long term, this study addresses the potential of hd-CAV-2 vectors for gene therapy of human neurodegenerative diseases, such as PD, further supporting the valuable data previously obtained from pre-clinical animal models.

5. Acknowledgements

The autjors gratefully acknowledge Dr. Johannes Schwarz for the supply of hmNPC within the scope of the EU project BrainCAV (FP7-222992). This work was supported by BrainCAV (FP7-222992) and Brainvectors (FP7-286071), funded by the EU, PTDC/EBB-BIO/112786/2009 and PTDC/EBB-BIO/119243/2010, funded by Fundação para a Ciência e Tecnologia, Portugal and Cancer Research UK. Daniel Simão, Catarina Pinto and Paulo Fernandes acknowledge the PhD fellowships from FCT, Portugal (SFRH/BD/78308/2011, PD/BD/52202/2013 and SFRH/BD/70810/2010, respectively).

6. References

Alves P., Moreira J., Rodrigues J., Aunins J., Carrondo M. (1996) Two-dimensional versus three-dimensional culture systems: Effects on growth and productivity of BHK cells. *Biotechnol. Bioeng.* **52**, 429–432.

Björklund T., Kirik D. (2009) *Scientific rationale for the development of gene therapy strategies for Parkinson's disease*. Elsevier B.V.

Brito C., Simão D., Costa I., Malpique R., Pereira C. I., Fernandes P., Serra M., *et al.* (2012) 3D cultures of human neural progenitor cells: dopaminergic differentiation and genetic modification. *Methods* **56**, 452–60.

Bru T., Salinas S., Kremer E. J. (2010) An Update on Canine Adenovirus Type 2 and Its Vectors. *Viruses* **2**, 2134–2153.

Deerinck T. J., Bushong E. A., Thor A., Ellisman M. H. (2010) NCMIR methods for 3D EM: a new protocol for preparation of biological specimens for serial block face scanning electron microscopy.

Doronin K., Flatt J. W., Paolo N. C. Di, Khare R., Kalyuzhniy O., Acchione M., Sumida J. P., *et al.* (2012) Coagulation factor X activates innate immunity to human species C adenovirus. *Science (80-.).* **338**, 795–8.

Eichholz K., Mennechet F. J. D., Kremer E. J. (2015) Human Coagulation Factor X-Adenovirus Type 5 Complexes Poorly Stimulate an Innate Immune Response in Human Mononuclear Phagocytes. *J. Virol.* **89**, 2884–2891.

Feng L. R., Maguire-zeiss K. A. (2010) Gene Therapy in Parkinson's Disease: Rationale and Current Status. *CNS Drugs* **24**, 177–192.

Fernandes P., Peixoto C., Santiago V. M., Kremer E. J., Coroadinha A. S., Alves P. M. (2013a) Bioprocess development for canine adenovirus type 2 vectors. *Gene Ther.* **20**, 353–60.

Fernandes P., Santiago V. M., Rodrigues A. F., Tomás H., Kremer E. J., Alves P. M., Coroadinha A. S. (2013b) Impact of E1 and Cre on adenovirus vector amplification: developing MDCK CAV-2-E1 and E1-Cre transcomplementing cell lines. *PLoS One* **8**, e60342.

Fernandes P., Simão D., Guerreiro M. R., Kremer E. J., Coroadinha a S., Alves P. M. (2015) Impact of adenovirus life cycle progression on the generation of canine helper-dependent vectors. *Gene Ther.* **22**, 40–49.

Ferreira T. B., Perdigão R., Silva A. C., Zhang C., Aunins J. G., Carrondo M. J. T., Alves P. M. (2009) 293 cell cycle synchronisation adenovirus vector production. *Biotechnol. Prog.* **25**, 235–43.

Forman M. S., Trojanowski J. Q., Lee V. M. (2004) Neurodegenerative diseases: a decade of discoveries paves the way for therapeutic breakthroughs. *Nat. Med.* **10**, 1055–63.

Gan Y., Jing Z., Stetler R. A., Cao G. (2013) Gene delivery with viral vectors for cerebrovascular diseases. *Front. Biosci. (Elite Ed).* **5**, 188–203.

Ghosh S. S., Gopinath P., Ramesh A. (2006) Adenoviral vectors: a promising tool for gene therapy. *Appl. Biochem. Biotechnol.* **133**, 9–29.

Gray S. J., Woodard K. T., Samulski R. J. (2010) Viral vectors and delivery strategies for CNS gene therapy. *Ther. Deliv.* **1**, 517–34.

Huang D., Desbois A., Hou S. T. (2005) A novel adenoviral vector which mediates hypoxia-inducible gene expression selectively in neurons. *Gene Ther.* **12**, 1369–1376.

Keriel A., René C., Galer C., Zabner J., Kremer E. J. (2006) Canine Adenovirus Vectors for Lung-Directed Gene Transfer : Efficacy , Immune Response , and Duration of Transgene Expression Using Helper-Dependent Vectors Canine Adenovirus Vectors for Lung-Directed Gene Transfer : Efficacy , Immune Response , and Durat. *J. Virol.* **80**, 1487–1496.

Klein R. L., Dayton R. D., Leidenheimer N. J., Jansen K., Golde T. E., Zweig R. M. (2006) Efficient neuronal gene transfer with AAV8 leads to neurotoxic levels of tau or green fluorescent proteins. *Mol. Ther.* **13**, 517–27.

Kremer E. J., Boutin S., Chillon M., Danos O. (2000) Canine Adenovirus Vectors : an Alternative for Adenovirus-Mediated Gene Transfer. *J. Virol.* **74**, 505–512.

Lentz T. B., Gray S. J., Samulski R. J. (2012) Viral vectors for gene delivery to the central nervous system. *Neurobiol. Dis.* **48**, 179–88.

Livak K. J., Schmittgen T. D. (2001) Analysis of relative gene expression data using real-time quantitative PCR and the 2(-Delta Delta C(T)) Method. *Methods* **25**, 402–8.

Manfredsson F. P., Mandel R. J. (2010) Development of gene therapy for neurological disorders. *Discov. Med.* **9**, 204–211.

Namikawa K., Murakami K., Okamoto T., Okado H., Kiyama H. (2006) A newly modified SCG10 promoter and Cre/loxP-mediated gene amplification system achieve highly specific neuronal expression in animal brains. *Gene Ther.* **13**, 1244–1250.

Pampaloni F., Reynaud E. G., Stelzer E. H. K. (2007) The third dimension bridges the gap between cell culture and live tissue. *Nat. Rev. Mol. Cell Biol.* **8**, 839–845.

Perreau M., Kremer E. J. (2006) The conundrum between immunological memory to adenovirus and their use as vectors in clinical gene therapy. *Mol. Biotechnol.* **34**, 247–256.

Piersanti S., Astrologo L., Licursi V., Costa R., Roncaglia E., Gennetier A., Ibanes S., *et al.* (2013) Differentiated neuroprogenitor cells incubated with human or canine adenovirus, or lentiviral vectors have distinct transcriptome profiles. *PLoS One* **8**, e69808.

Räty J. K., Pikkarainen J. T., Wirth T., Ylä-Herttuala S. (2008) Gene therapy: the first approved gene-based medicines, molecular mechanisms and clinical indications. *Curr. Mol. Pharmacol.* **1**, 13–23.

Salinas S., Bilsland L. G., Henaff D., Weston A. E., Keriel A., Schiavo G., Kremer E. J. (2009) CAR-associated vesicular transport of an adenovirus in motor neuron axons. *PLoS Pathog.* **5**, e1000442.

Salinas S., Zussy C., Loustalot F., Henaff D., Menendez G., Morton P. E., Parsons M., Schiavo G., Kremer E. J. (2014) Disruption of the coxsackievirus and adenovirus receptor-homodimeric

interaction triggers lipid microdomain- and dynamin-dependent endocytosis and lysosomal targeting. *J. Biol. Chem.* **289**, 680–95.

Schiedner G., Hertel S., Kochanek S. (2000) Efficient transformation of primary human amniocytes by E1 functions of Ad5: generation of new cell lines for adenoviral vector production. *Hum. Gene Ther.* **11**, 2105–2116.

Schindelin J., Arganda-Carreras I., Frise E., Kaynig V., Longair M., Pietzsch T., Preibisch S., *et al.* (2012) Fiji: an open-source platform for biological-image analysis. *Nat. Methods* **9**, 676–82.

Schüle B., Pera R. a R., Langston J. W. (2009) *Can cellular models revolutionize drug discovery in Parkinson's disease?* Biochim. Biophys. Acta 1792, 1043–51.

Schwarz L. a., Miyamichi K., Gao X. J., Beier K. T., Weissbourd B., DeLoach K. E., Ren J., et al. (2015) Viral-genetic tracing of the input–output organization of a central noradrenaline circuit. *Nature.*

Seiradake E., Lortat-Jacob H., Billet O., Kremer E. J., Cusack S. (2006) Structural and mutational analysis of human Ad37 and canine adenovirus 2 fiber heads in complex with the D1 domain of coxsackie and adenovirus receptor. *J. Biol. Chem.* **281**, 33704–33716.

Serra M., Correia C., Malpique R., Brito C., Jensen J., Bjorquist P., Carrondo M. J. T., Alves P. M. (2011) Microencapsulation technology: a powerful tool for integrating expansion and cryopreservation of human embryonic stem cells. *PLoS One* **6**, e23212.

Silva A. C., Simão D., Küppers C., Lucas T., Sousa M. F. Q., Cruz P., Carrondo M. J. T., Kochanek S., Alves P. M. (2015) Human amniocyte-derived cells are a promising cell host for adenoviral vector production under serum-free conditions. *Biotechnol. J.* **10**, 760–771.

Simão D., Pinto C., Piersanti S., Weston A., Peddie C. J., Bastos A. E. P., Licursi V., *et al.* (2015) Modeling Human Neural Functionality *In vitro* : Three-Dimensional Culture for Dopaminergic Differentiation. *Tissue Eng. Part A* **21**, 654–668.

Soudais C., Boutin S., Hong S. S., Chillon M., Danos O., Bergelson J. M., Boulanger P., Kremer E. J. (2000) Canine Adenovirus Type 2 Attachment and Internalization : Coxsackievirus-Adenovirus Receptor, Alternative Receptors, and an RGD-Independent Pathway. *J. Virol.* **74**, 10639–10649.

Soudais C., Boutin S., Kremer E. J. (2001a) Characterization of cis-acting sequences involved in canine adenovirus packaging. *Mol. Ther.* **3**, 631–40.

Soudais C., Laplace-Builhe C., Kissa K., Kremer E. J. (2001b) Preferential transduction of neurons by canine adenovirus vectors and their efficient retrograde transport *in vivo*. *FASEB J.* **15**, 2283–2285.

Soudais C., Skander N., Kremer E. J. (2004) Long-term *in vivo* transduction of neurons throughout the rat CNS using novel helper-dependent CAV-2 vectors. *FASEB J.* **18**, 391–393.

Storch A., Paul G., Csete M., Boehm B. O., Carvey P. M., Kupsch A., Schwarz J. (2001) Long-term proliferation and dopaminergic differentiation of human mesencephalic neural precursor cells. *Exp Neurol* **170**, 317–325.

Toulouse A., Sullivan A. M. (2008) Progress in Parkinson's disease-where do we stand? *Prog. Neurobiol.* **85**, 376–92.

Ulusoy A., Kirik D. (2011) Development of advanced therapies based on viral vector-mediated overexpression of therapeutic molecules and knockdown of disease-related genes for Parkinson's disease. *Ther. Deliv.* **2**, 37–50.

5

Functional metabolic interactions of neuron-astrocyte 3D networks derived from human stem cells

This chapter was adapted from:

Simão D, Terrasso AP, Teixeira AP, Brito C, Sonnewald U, Alves PM (2016) Functional metabolic interactions of neuron-astrocyte 3D networks derived from human stem cells. Submitted

Table of Contents

Abstract

Generation of functional human neural cells by directed differentiation of stem cells in 3D culture systems holds great promise for disease modeling, drug discovery and toxicology. This work demonstrates the establishment of neuronal and astrocytic specific metabolic signatures and shuttles in human stem cell-derived neuron-astrocyte 3D networks, namely the glutamine-GABA shuttle. This was indicated by the labeling of neuronal GABA following incubation with the glia-specific substrate [2-^{13}C]acetate, which decreased with the inhibition of glial enzyme glutamine synthetase by methionine sulfoximine (MSO). Pyruvate carboxylase-derived labeling was higher in glutamine than in glutamate, indicating the exclusive activity of this enzyme in astrocytes and further highlighting the metabolic specialization of the generated cells. Labeling patterns resulting from [1-^{13}C]glucose incubation indicated the presence of two neuronal populations, glutamatergic and GABAergic. Exposure of these cells to neurotoxic acrylamide resulted in intracellular accumulation of glutamate and decreased GABA synthesis. These suggested an acrylamide-induced impairment of neuronal synaptic vesicle trafficking and imbalanced glutamine-GABA cycle due to loss of cell-cell contacts at synaptic site. This work demonstrates that the neural differentiation of human stem cells in a 3D setting allows the recapitulation of neuron-astrocyte metabolic interactions, highlighting the relevance of these models to better understand the metabolic interactions occurring in human neural cells and for preclinical research.

1. Introduction

Over the last years, the drug discovery and development pipelines have registered low success rates both during preclinical and clinical phases, with only 23 small molecules and 2 biologics being approved by the Food and Drug Administration (FDA) in 2013 (Paul *et al.* 2010; Mullard 2014). These is even more dramatic for neurological disorders, such as Alzheimer's disease for which there is an estimated overall success rate of only 0.5% (Calcoen *et al.* 2015). Although several factors have been described to contribute for this, the current lack of adequate and predictive preclinical models play an important role. Most of the available preclinical models are based on animals or immortalized cell lines, which do not recapitulate accurately key events of human pathologies (Jucker 2010; Begley and Ellis 2012; Mak *et al.* 2014). Therefore, there has been an increasing demand for a paradigm shift towards more robust human cell models of higher physiological relevance (Giri and Bader 2014).

In this context, the generation of human neural cells by directed differentiation of stem cells holds great promise for disease modeling, drug discovery and toxicology. Multiple human stem cell sources have become available, including immortalized cell lines, embryonic or adult stem cells and induced pluripotent stem cells (iPSC) (Schüle *et al.* 2009). Traditional cell culture systems based on cell monolayers do not reflect the *in vivo* architecture complexity, mechanical and biochemical cues, failing to mimic important features of the target tissue/organ. Conversely, 3D culture systems allow to recapitulate the *in vivo* cell-cell and cell-extracellular matrix interactions (ECM), while presenting an intermediate degree of complexity between traditional 2D cultures and the organ (Pampaloni *et al.* 2007). Different strategies can be explored for 3D cell culture, including embedding cells in artificial matrices/scaffolds (Potter *et al.* 2008) or as cell aggregates (Moors *et al.* 2009). Neural differentiation of human stem cells in these 3D systems results in a heterogeneous culture, composed of the different neural cell lineages present in the brain: neurons, astrocytes and oligodendrocytes (Paşca *et al.* 2015; Simão *et al.* 2015; Terrasso *et al.* 2015). Complex cell-cell interactions and networks can be established within these cell aggregates, or neurospheres, making it possible to mimic key brain features, such as synaptic activity or electrophysiological properties. Recently, Choi *et al.* have been able to recapitulate amyloid-β and tau pathological events of Alzheimer's disease in a human stem cell-derived 3D model, which was not possible to model in rodent cultures (Choi *et al.* 2014). Human neural 3D cell models can thus be valuable tools to study human neural metabolism (Ramirez *et al.* 2013), as this field has traditionally relied on rodent models, using both *in vivo* studies and primary cultures, which can diverge considerably from the human phenotype and make it impossible to develop appropriate treatment approaches.

The brain's homeostasis depends on multiple metabolic cycles between the different cell populations that represent major hallmarks of neural metabolism. For instance, as neurons are continually loosing tricarboxylic acid (TCA) cycle intermediates, mainly for the synthesis of neurotransmitters (α-ketoglutarate is metabolized into glutamate and subsequently GABA), compensatory mechanisms have to act in order to replenish the carbon skeleton for maintaining TCA cycle activity (Hertz *et al.* 1999). Some metabolic neural features have been showed to be present in 2D cultures of stem cell-derived neural cells, as glycogen synthesis in astrocytes or the ability to modulate glucose consumption in response to glutamate addition (Tarczyluk *et al.* 2013). Still, other important neural metabolic hallmarks, including the glutamate/GABA-glutamine cycle between neurons and astrocytes (Bak *et al.* 2006) has not been previously reported for these cultures. This specific neuron-astrocyte shuttle in one of the major metabolic specialization and compartimentalization in brain tissue, where astrocytes are able to take up glutamate or GABA released by neurons into the synaptic cleft and convert glutamate to glutamine or GABA to Succinyl CoA, entering the TCA cycle via the GABA shunt. Astrocyte derived-glutamine is then transported back to neurons, acting as precursor for neurotransmitter synthesis. These cycles are critical in order to control the excitotoxic effects of glutamate as well as to feed neurons with a neurotransmitter precursor.

The use of ^{13}C-labeled substrates and nuclear magnetic resonance (NMR) spectroscopy are powerful tools for the study of neural metabolic networks, having provided important insights into the biochemical mechanisms and compartmentation of neural metabolism (Rodrigues *et al.* 2013; Rothman *et al.* 2011; Sonnewald and Kondziella 2003). Different ^{13}C-labeled substrates have been used to study neuronal-glial metabolic interactions, taking advantage of cell specific metabolic features. An example of this metabolic specialization is the fact that glucose is taken up mostly by neurons (Lundgaard *et al.* 2015), while astrocytes have been shown to metabolize acetate (Sonnewald *et al.* 1993; Rae *et al.* 2012). Thus, the combination of these two substrates provides the possibility to study in detail the metabolic pathways and interaction between both cell types (Badar-Goffer *et al.* 1990; Taylor *et al.* 1996).

In this work, the use of a human 3D *in vitro* neural model was combined with ^{13}C-NMR spectroscopy to study the metabolic features of stem cell-derived human neuron-astrocyte networks. Furthermore, to study in detail neuronal-glial metabolic interactions the cells were challenged with compounds targeting specifically astrocytic or neuronal populations, using methionine sulfoximine (MSO) and acrylamide, respectively. This study demonstrates that some of the main metabolic features and speciali-

zations found in brain tissue are recapitulated in human stem cell-derived neuron-astrocyte 3D networks.

2. Materials and Methods

2.1. Cell culture and 3D neural differentiation

Undifferentiated Ntera-2 (NT2) cells were routinely cultivated in standard tissue culture flasks (Sarstedt) and maintained in DMEM (Life Technologies) supplemented with 10% (v/v) fetal bovine serum (FBS; Hyclone) and 1% (v/v) penicillin-streptomycin (P/S; Life Technologies), as previously described (Brito *et al.* 2007). NT2 neural differentiation was performed as previously described (Terrasso *et al.* 2015). Briefly, 125 mL silanized spinner flasks (Wheaton) equipped with ball impeller were inoculated with a single cell suspension at 6.7 x 10^5 cell/mL in 75 mL of DMEM with 10% FBS and 1% P/S. On the day after, 50 mL of fresh medium were added. At day 3, neural differentiation was induced adding 20 µM retinoic acid (RA; Sigma-Aldrich), by performing a 50% medium exchange. RA treatments were performed every 2-3 days, during 3 weeks. After this period, cells were posteriorly maintained in DMEM with 5% (v/v) FBS, 1% (v/v) P/S and absence of RA during 2 weeks, for neuronal maturation. Spinner flasks stirring speed was gradually increased from 40 to 100 rpm throughout culture time. Cells were maintained in a humidified atmosphere of 5% CO_2 in air at 37ºC.

2.2. Incubation with ^{13}C labeled substrates

After neural differentiation process (day 38), two 50% media exchanges were performed in the following two days of culture with a low glucose DMEM medium (5.5 mM glucose), 5% FBS and 1% P/S. At day 3 the medium was completely removed and replaced by 100 mL of: (i) DMEM with 5.5 mM [1-^{13}C]glucose, 3 mM acetate and 5% FBS or (ii) DMEM with 5.5 mM glucose, 3 mM [2-^{13}C]acetate and 5% FBS. After 12 hours incubation, neurospheres were harvested, centrifuged at 300 x*g* for 2 minutes and washed 2 times in ice-cold PBS followed by centrifugation. The obtained cell pellets were the immersed in liquid nitrogen and 2 mL of 70% (v/v) ethanol was added. Complete cell lysis was achieved by ultrasound sonication (Sonifier 250D, Branson). The cell extracts were centrifuged two times at 20,000 x*g* for 15 minutes. Cell pellets were stored at -80ºC for total protein quantification.

2.3. Fate of [1-^{13}C]glucose and [2-^{13}C]acetate

A simplified representation of the main neuronal and astrocytic metabolic networks, as well as the labeling patterns resulting from the metabolism of [1-^{13}C]glucose

and [2-^{13}C]acetate, is shown in Figure 1. Through glycolysis, [1-^{13}C]glucose can be metabolized into [3-^{13}C]pyruvate, which can then be reduced to [3-^{13}C]lactate or transaminated to [3-^{13}C]alanine. The labeled pyruvate molecules can enter the tricaboxylic acid (TCA) cycle in the mitochondria via pyruvate dehydrogenase (PDH) with formation of [2-^{13}C]acetyl-CoA, which is converted to [2-^{13}C]citrate. With the progression of the TCA cycle, α-[4-^{13}C]ketoglutarate is formed and can exit the cycle for the synthesis of [4-^{13}C]glutamate. This can act as neurotransmitter, in case of glutamatergic neurons, or be used to fuel the synthesis of [4-^{13}C]glutamine in astrocytes or [2-^{13}C]GABA in GABAergic neurons. In case α-[4-^{13}C]ketoglutarate remains in the TCA cycle, the label will be scrambled by the formation of succinate that is a symmetric molecule, resulting in equal amounts of [2-^{13}C]- and [3-^{13}C]succinate that gives rise to fumarate, malate and oxaloacetate labeled in the same positions. [2-^{13}C]- and [3-^{13}C]oxaloacetate can also exit the cycle by being converted into aspartate, which will have the same carbon positions labeled. If the cycle continues with the labeled oxaloacetate, this will be condensed with an acetyl-CoA molecule, which can be unlabeled or labeled. In presence of unlabeled acetyl-CoA, [3-^{13}C]- or [2-^{13}C]glutamate/glutamine and [3-^{13}C]- or [4-^{13}C]GABA will be generated from the second turn of TCA cycle. In case the of labeled acetyl-CoA, the generated molecules will also present labeling in the positions described previously for the first turn, resulting in [3,4-^{13}C]- or [2,4-^{13}C]glutamate/glutamine and [2,3-^{13}C]- or [2,4-^{13}C]GABA.

Alternatively, [3-^{13}C]pyruvate can enter the TCA cycle through the anaplerotic pathway, which in neural cells is achieved via pyruvate carboxylase (PC), leading to the formation of [3-^{13}C]oxaloacetate. This can exit the cycle by transamination generating [3-^{13}C]aspartate or proceed in the cycle forming α-[2-^{13}C]ketoglutarate, which can act as precursor for the synthesis of [2-^{13}C]glutamate/glutamine and [4-^{13}C]GABA. In case the label remains in the cycle for a second turn, [1-^{13}C]glutamate/glutamine will be formed and the decarboxylation of glutamate into GABA will result in the loss of the labeled carbon. It should be noted that backflux of labelled oxaloacetate after carboxylation of pyruvate will lead to scrambling of the label from the C3 position in oxaloacetate to the C2 position and make it indistinguishable from oxaloacetate obtained from cycling. Thus, pyruvate carboxylation assessment using [1-^{13}C]glucose can be underestimated, since backflux is not taken into account (Brekke *et al.* 2012).

Incubation with [2-^{13}C]acetate results in its conversion into [2-^{13}C]acetyl-CoA, which will then enter the TCA cycle and lead to a labeling pattern similar to what was described above for glucose.

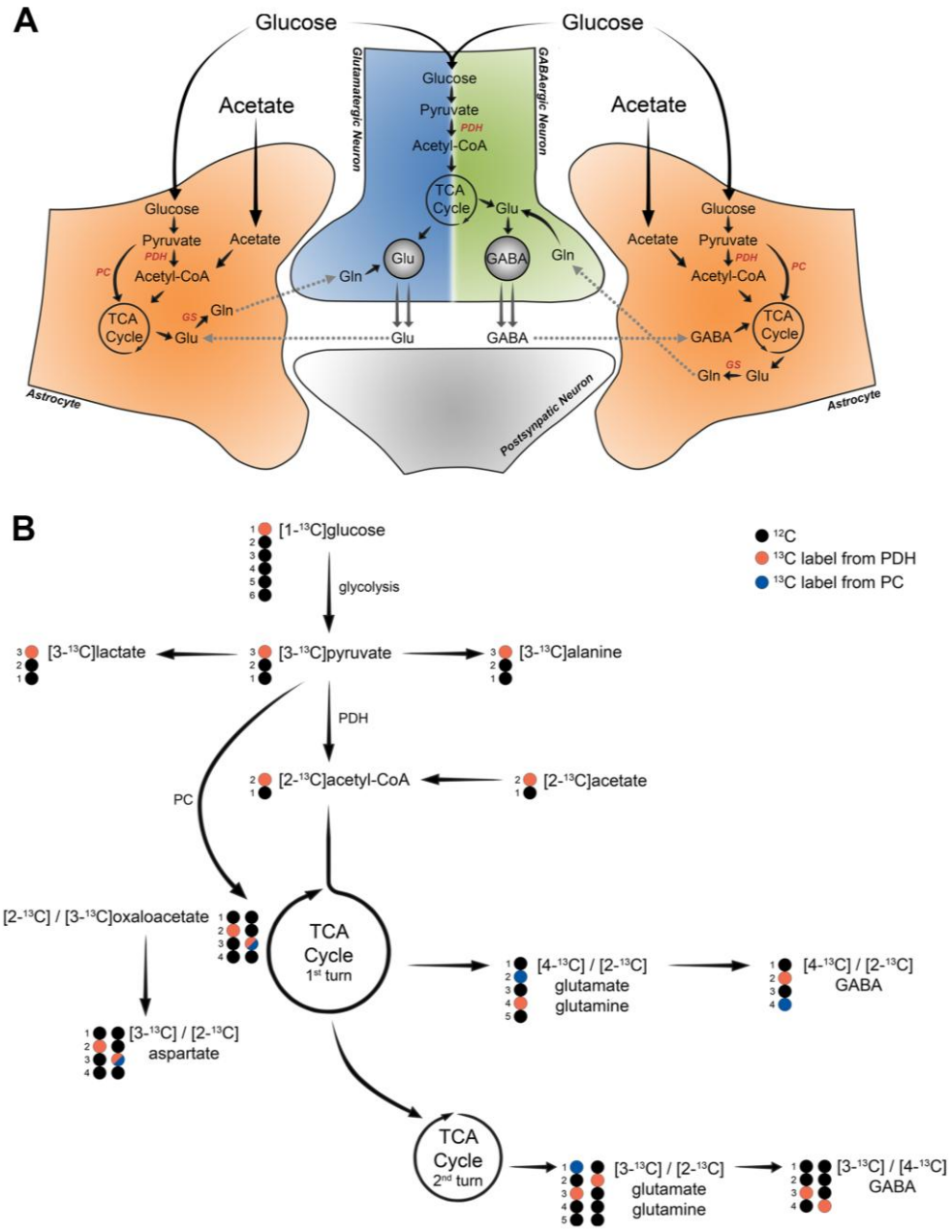

Figure 5.1 - Schematic representation outlining the main neural metabolic networks and ^{13}C-labelling patterns (A) Neuron-astrocyte metabolic networks and glutamine-glutamate/GABA cycle. **(B)** ^{13}C-labeling patterns of metabolites derived from [1-^{13}C]glucose and [2-^{13}C]acetate. ^{13}C-label can enter the TCA clycle via pyruvate dehydrogenase (PDH; orange circle) or via pyruvate carboxylase (PC; blue circle).

2.4. Incubation with toxic compounds

For the experiments with toxic compounds, two 50% media exchanges with low glucose medium were also performed in two consecutive days after neural differentiation (day 38). For acrylamide incubation experiments, at day 3 after differentiation, the

medium was completely removed and replaced by DMEM with 5.5 mM glucose, 3 mM acetate, 2.5 mM acrylamide and 5% FBS. After 36 hours of incubation, the medium was completely exchanged with a medium of similar composition but with [1-^{13}C]glucose and maintained for further 6 hours. For methionine sulphoximine (MSO) experiments, at day 3 after differentiation, the medium was completely removed and maintained for 12 hours with DMEM containing 5.5 mM glucose, 3 mM [2-^{13}C]acetate, 20 μM MSO and 5% FBS. Following incubation with labeled substrates, cells were harvested as described above. Control experiments were performed in parallel under the same experimental conditions except for the absence of the toxic compounds.

2.5. NMR sample preparation and analysis

Lyophilized samples were prepared as previously decribed (Brekke *et al.* 2014), by dissolving in 120 mL D_2O containing 0.25% ethylene glycol and 0.002% TSP. Samples were then transferred to SampleJet tubes (3.0±103.5 mm). All samples were analyzed on a 14.1T Ultra shielded Plus Avance III magnet (Bruker BioSpin GmbH, Rheinstetten, Germany) operating at 600 MHz (for ^{1}H) using QCI CryoProbe (Bruker BioSpin GmbH) and equipped with SampleJet auto sampler (Bruker BioSpin GmbH). ^{1}H-NMR spectra were accumulated with a pulse angle of 90°, 2.7 s acquisition time, and 10 s relaxation delay. The number of scans was 128. Proton decoupled ^{13}C-NMR spectra were obtained using an acquisition time of 1.7 s, 0.5 s relaxation delay, and a 30˚ flip angle. Scans were accumulated at 30 kHz spectral width with 98 K data points. The number of scans was typically 2000. Relevant peaks in the spectra were identified and integrated using MNova software (Mestrelab Research, Santiago de Compostela, Spain). Concentrations of metabolites were calculated from the integrals of the peaks using TSP (^{1}H-NMR spectra) or ethylene glycol (^{13}C-NMR spectra) as internal quantification standards. Concentrations from the ^{1}H-NMR spectra were corrected for the numbers of protons that constituted the peak. Correction factors for incomplete relaxation and nuclear Overhauser effects in the ^{13}C spectra were obtained by acquiring scans with completely relaxed nuclei (relaxation delay of 20 s) and only a brief proton decoupling during the radiofrequency pulse shortly before the signal was recorded to avoid heteronuclear splitting of signals, but no proton decoupling for the remainder of the acquisition to avoid nuclear Overhauser effects. The singlets in the ^{13}C-nuclear magnetic resonance spectroscopy (^{13}C-NMRS) data were corrected for naturally abundant ^{13}C by subtracting 1.1% of the total cellular contents obtained from ^{1}H spectra or HPLC data. All amounts were corrected for total protein weight. Percent excess enrichment was calculated after subtracting natural abundance where appropriate, and is in the following referred to as percent enrichment.

2.6. HPLC analysis

Amino acids were quantified by high performance liquid chromatography (HPLC) using a pre-column derivatization method based on the Waters AccQ.Tag Amino Acid Analysis (Waters, USA) as previously described (Carinhas *et al.* 2010). Briefly, sample proteins were precipitated by adding an equal volume of acetonitrile and removed by centrifugation at 13,000 x*g* for 15 minutes. The obtained supernatants were used for primary and secondary aminoacid derivatization by mixing with 6-aminoquinolyl N-hydroxysuccinimidyl-carbamate, which allows their separation in a reversed phase column (Waters, USA) and the detection of fluorescence at 395 nm. As internal standard, α-aminobutyric acid was added to ensure consistency between runs. Mobile phases were prepared following the manufacturer's instructions, filtered and degassed in an ultrasound bath before usage.

2.7. Total protein quantification

Total cell biomass was evaluated by quantification of total protein using the bicinchoninic acid (BCA) protein assay kit (Pierce), after dissolving the cell pellet in Tris buffer (50 mM Tris, 5 mM EDTA, 150 mM NaCl, pH 7.4).

2.8. Immunofluorescence microscopy

Neurospheres were fixed in 4% (w/v) paraformaldehyde (PFA) + 4% (w/v) sucrose in PBS for 20 min and processed for immunostaining as previously described (Serra *et al.* 2009). Primary and secondary antibodies were used as follows: mouse anti-βIII-tubulin (1:200; Millipore Darmstadt, Germany, MAB1637); rabbit anti-GFAP (1:200; Millipore, AB5804); AlexaFluor® 488 goat anti-mouse IgG (1:500; Life Technologies, A11001) and AlexaFluor® 594 goat anti-rabbit IgG (1:500; Life Technologies, A11012). Cell nuclei were counterstained with TO-PRO-3 (Life Technologies). Samples were visualized using point-scan confocal microscopy (SP5, Leica, Wetzlar, Germany). Merge between channels and maximum z-projections, as well as linear brightness and contrast adjustments of the images, were performed using the open source FIJI software (Schindelin *et al.* 2012).

2.9. RT-qPCR

Total RNA was extracted with High Pure RNA Isolation Kit (Roche), according to the manufacturer's instructions. RNA was quantified in a NanoDrop 2000c (Thermo Scientific) and used for cDNA synthesis. Reverse transcription was performed with High Fidelity cDNA Synthesis Kit (Roche), using Anchored-oligo(dT)18 Primer (Roche) or with the Super Script III First Strand synthesis system (Invitrogen), using

random hexamers (Invitrogen). qPCRs were performed in triplicates using LightCycler 480 SYBR Green I Master Kit (Roche) with the following primers: βIII-tubulin (*TUBB3;* fwd 5′-gggcctttggacatctcttc-3′ and rev 5′- cctccgtgtagtgacccttg-3′), glial fibrillary acidic protein (*GFAP*; fwd 5′-agagaggtcaagcccaggag-3′ and rev 5′-ggtcacccacaacccctact-3′) and ribosomal protein L22 (*RPL22*; fwd 5′-CACGAAGGAGGAGTGACTGG-3′ and rev 5′-TGTGGCACACCACTGACATT-3′). The reactions were performed with LightCycler 480 Instrument II 96-well block (Roche). Quantification cycle values (C_q′s) and melting curves were determined using LightCycler 480 Software version 1.5 (Roche). All data were analyzed using the 2-ΔΔCt method for relative gene expression analysis (Livak and Schmittgen 2001). Changes in gene expression were normalized using the housekeeping gene *RPL22* as internal control.

2.10. Statistical Analysis

All values are presented as means ± standard error of the mean (s.e.m.). All analyticals were performed as triplicates from samples of two independent experiments. Student's t-tests were used to compare means. Before choosing the adequate type of t-test, Levene's test for equal variances was performed. $P < 0.05$ was chosen as the level of significance. All comparisons were made using two-tailed statistical tests.

3. Results

3.1. Neuronal and glial metabolic signatures and trafficking

NT2 aggregates differentiation towards the neural lineage can be achieved upon RA induction and subsequent maturation (Figure 2A), resulting in highly viable differentiated neurospheres (Figure 5.2B) composed mainly of βIII-tubulin-positive neurons and GFAP-positive astrocytes (Figure 5.2C), as previously reported (Terrasso *et al.* 2015). Moreover, neuronal differentiation drives the generation of two major neuronal subtypes, glutamatergic (vGluT1-positive cells; Figure 5.2D) and GABAergic (GAD65/67-positive cells; Figure 5.2 E). In this study, differentiated NT2 neurospheres were incubated with [1-^{13}C]glucose or [2-^{13}C]acetate, and the fate of the ^{13}C label was observed by ^{13}C-NMR spectroscopy for the identification of major neural metabolic signatures.

Typical ^{13}C-NMR spectra after incubation with each ^{13}C labeled substrate are presented in Figure 5.3. Incubation with [1-^{13}C]glucose resulted in detectable levels of labeled glutamine, glutamate, lactate, alanine, aspartate and GABA (Figure 5.4A and Table 5.1). After 12 hours of incubation, glutamate and glutamine were mainly labeled at C4, which results from one turn in the TCA cycle (Figure 5.1). Additionally, the pres-

ence of labeling in C2 and C3 positions indicates label cycling in the TCA cycle. The amounts of [2-^{13}C]glutamine were higher relative to [2-^{13}C]glutamate, while the labeling in C3 was similar for both. This reflects the different contributions of the anaplerotic (via PC) and oxidative (via PDH) pathways for the synthesis of these two metabolites. These contributions can be expressed as the ratio PC/PDH, which can be estimated by dividing the difference between C2 and C3 by C4 ((C2-C3)/C4) (Hassel *et al.* 1995). This was found to be 2.3-fold higher for glutamine in comparison with glutamate (Figure 5.4B), revealing an increased contribution of PC over PDH for glutamine synthesis. GABA labeling was only observed in the C2 position, which derives from the decarboxylation of the most abundant glutamate isotopomer (C4). Aspartate was labeled in the C2 and C3 positions with no significant differences between the two. Labeling of alanine and lactate in the C3 position was also observed, which derive from [3-^{13}C]pyruvate molecules generated from glycolysis.

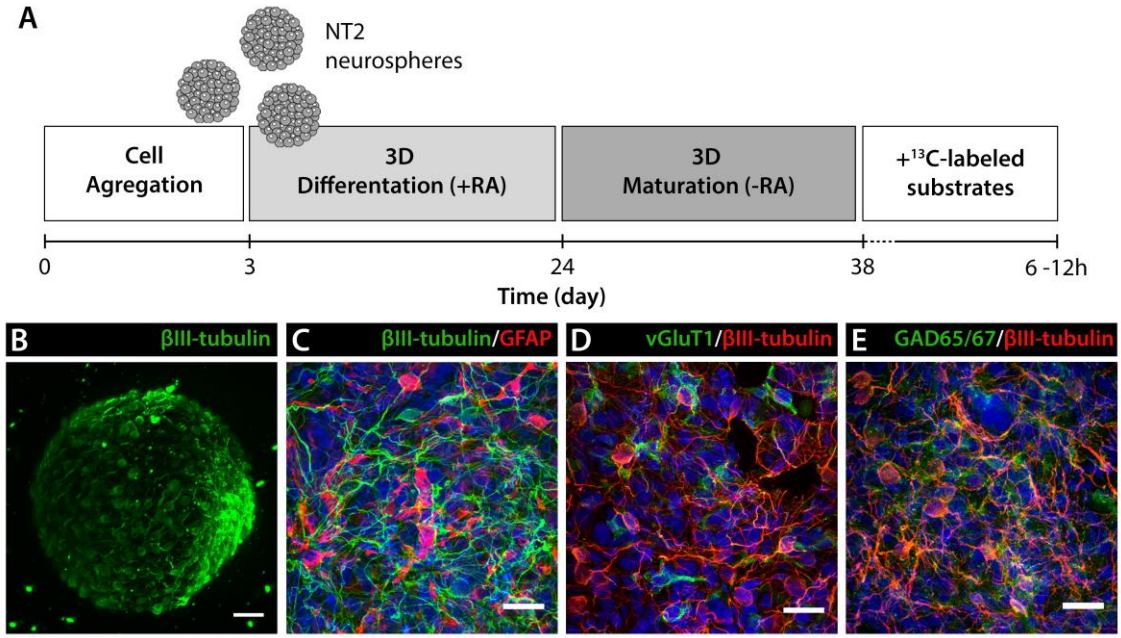

Figure 5.2 – Differentiation of NT2 cells as neurospheres (A) Schematic experimental workflow for NT2 3D differentiation. Cells were inoculated in a stirred suspension culture system and aggregated for 3 days. Neural differentiation was induced by exposure to retinoic acid (RA) for 3 weeks, followed by 2 weeks without RA. Differentiated neurospheres were further cultured in presence of ^{13}C-labeled substrates for 6-12 hours. **(B)** Immunofluorescence light-sheet microscopy of neurospheres stained for βIII-tubulin. Scale bar, 50 µm. **(C-E)** Immunofluorescence confocal microscopy of neurospheres stained for βIII-tubulin and GFAP **(C)**, βIII-tubulin and vGluT1 **(D)**, βIII-tubulin and GAD65/67 **(E)**. Scale bars, 20 µm.

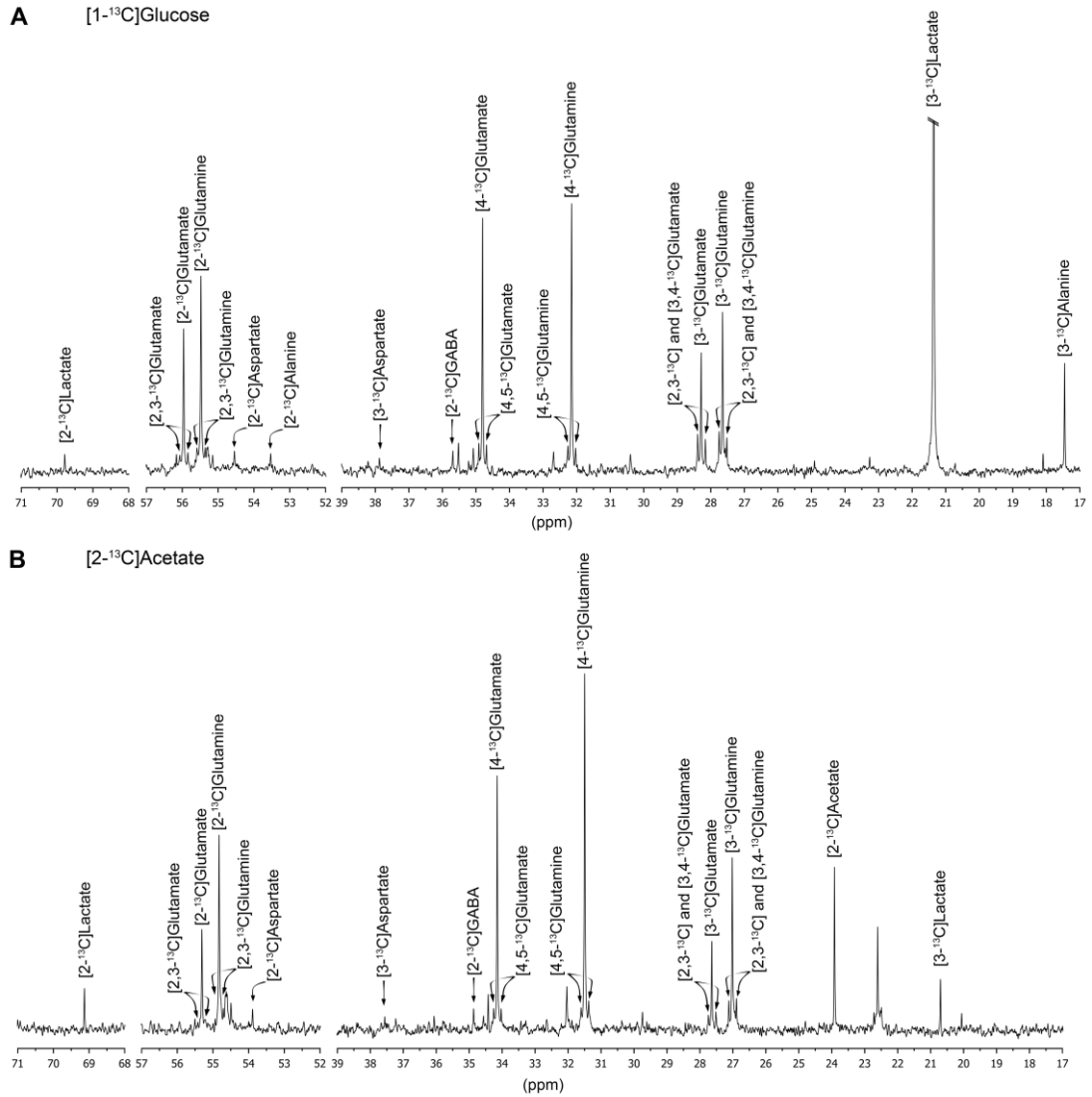

Figure 5.3 - Typical 13C-NMR spectra of cellular extracts from neurospheres incubated with [1-^{13}C]glucose **(A)** or [2-^{13}C]acetate **(B)**. Relevant metabolites are identified concerning each carbon position.

Incubation with [2-^{13}C]acetate during 12 hours resulted also in significant labeling of glutamate, glutamine, aspartate and GABA (Figure 5.4A and Table 5.1). The percentage of ^{13}C enrichment was similar or slightly lower than that from [1-^{13}C]glucose in all metabolites, except in glutamine, where a higher ^{13}C incorporation from [2-^{13}C]acetate is in accordance with acetate being a major carbon source for glutamine synthesis in astrocytes. As observed with [1-^{13}C]glucose, labeling in C4 was the most common in glutamate and glutamine. Moreover, significant differences were not observed for the PC/PDH ratio for glutamine and glutamate, as in this case there is not contribution from the PC pathway for the labeling pattern, since [2-^{13}C]acetate is con-

verted into [2-^{13}C]acetyl-CoA that enters directly the TCA cycle. Finally, labeling of GABA in the C2 position was observed (Figure 5.3 and 5.4A), suggesting the trafficking of labeled glutamine from astrocytes to neurons that acts as precursor for GABA synthesis.

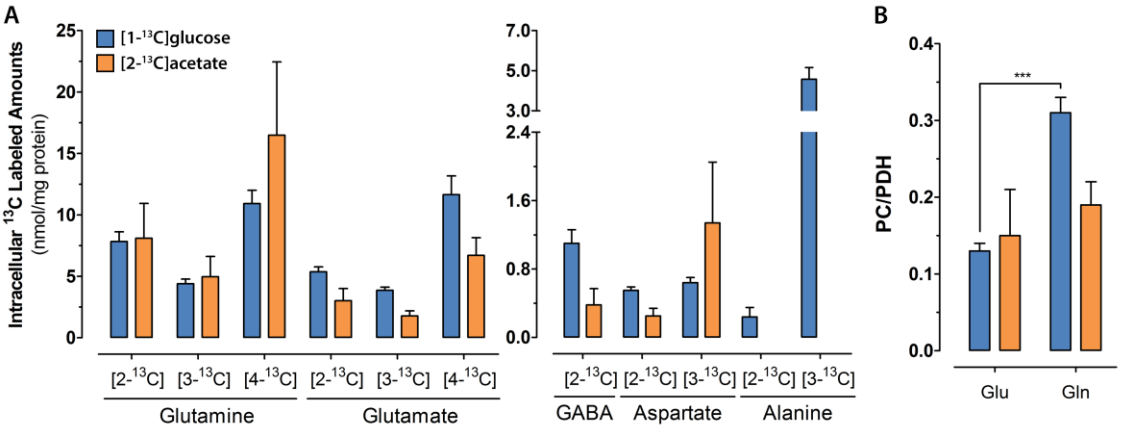

Figure 5.4 – Analysis of ^{13}C labeling derived from [1-^{13}C]glucose and [2-^{13}C]acetate. (A) Intracellular ^{13}C labeled amounts of metabolites in cultures incubated with [1-^{13}C]glucose (blue bars) or [2-^{13}C]acetate (orange bars). **(B)** Metabolic ratios for PC/PDH for glutamate (Glu) and glutamine (Gln) in cultures incubated with [1-^{13}C]glucose (blue bars) or [2-^{13}C]acetate (orange bars). Data are mean ± s.e.m. P values are given for PC/PDH ratio (analysis of glutamate versus glutamine): ***P<0.001. PC, pyruvate carboxylase; PDH, pyruvate dehydrogenase.

Table 5.1 - Percentage of ^{13}C enrichment for metabolites in cultures incubated with [1-^{13}C]glucose or [2-^{13}C]acetate. Results are presented as mean ± s.e.m.

		[1-^{13}C]glucose	[2-^{13}C]acetate
Glutamine	**C2**	2.87 ± 0.64	3.98 ± 0.57
	C3	1.66 ± 0.39	2.52 ± 0.44
	C4	3.83 ± 0.72	7.98 ± 1.42
Glutamate	**C2**	5.18 ± 1.35	3.29 ± 0.55
	C3	3.74 ± 0.98	2.07 ± 0.13
	C4	9.85 ± 1.90	7.91 ± 0.36
Alanine	**C2**	1.59 ± 0.71	n.d.
	C3	15.88 ± 4.21	n.d.
Aspartate	**C2**	4.09 ± 1.24	2.83 ± 1.13
	C3	4.49 ± 1.34	3.88 ± 1.06
GABA	**C2**	11.08 ± 1.79	2.89 ± 0.59

3.2. Inhibition of astrocytic glutamine synthesis

To isolate the contribution of astrocytic-derived glutamine as precursor for neuronal neurotransmitter synthesis, following the glutamine-glutamate/GABA shuttles between neurons and astrocytes, differentiated neurospheres were incubated with MSO, a specific glutamine synthase (GS) inhibitor.

The presence of MSO in the culture medium resulted in an almost complete absence of ^{13}C incorporation in glutamine coming from [2-^{13}C]acetate (Figure 5.5A) and a 2.8-fold decrease in the intracellular glutamine pool (Figure 5.5B). In accordance with the role of astrocytic glutamine as a key precursor for GABA synthesis in neurons, decreased [2-^{13}C]GABA labeling (Figure 5.5A) and a 50% reduction in intracellular GABA content was also observed (Figure 5.5B). As for glutamate, its total intracellular pool was not affected in MSO-treated cultures. Nevertheless, a modest increase in ^{13}C labeled glutamate was observed, mostly visible in the amount of [3-^{13}C]glutamate, suggesting a slower degradation or accumulation, as its condensation with ammonia to generate glutamine is impaired by MSO. The catabolism of branched chain amino acids (BCAA), comprising valine, isoleucine and leucine, was decreased in cultures exposed to MSO, as shown by the significantly higher intracellular pools detected (Figure 5.5B).

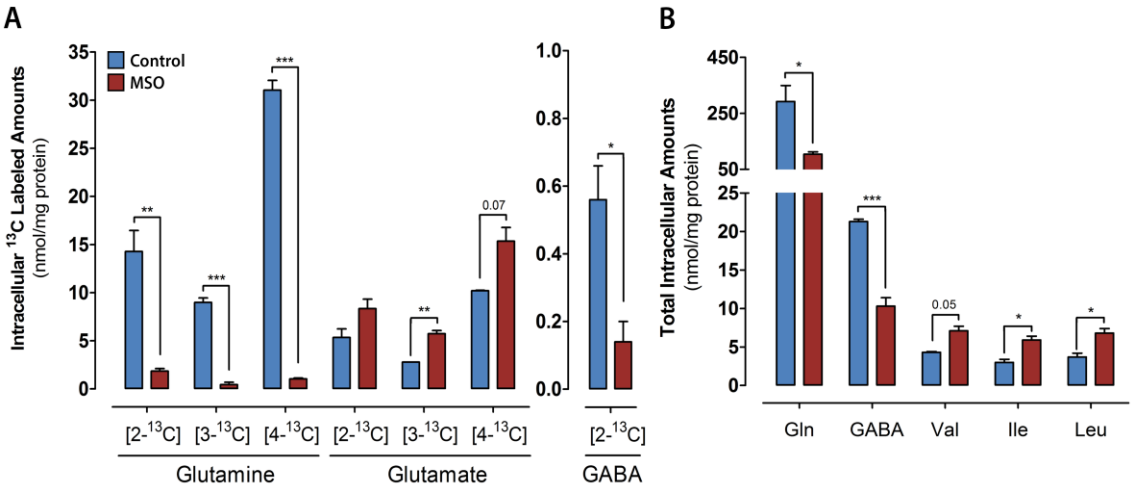

Figure 5.5 – Effect of MSO on ^{13}C labeling and concentration of intracellular metabolites. (A) Intracellular ^{13}C labeled amounts of metabolites in control (blue bars) and MSO-treated cultures (red bars). **(B)** Total concentration of intracellular metabolites in control (blue bars) and MSO-treated cultures (red bars). Data are mean ± s.e.m. Asterisks indicate significant difference: **P*<0.05; ***P*<0.01; ****P*<0.001; near significant *P* values (<0.1) are given in numbers. Gln, glutamine; Val, valine; Ile, isoleucine; Leu, Leucine.

3.3. Impairment of neuronal metabolism

The NT2 neural cells were further challenged by incubating the neurospheres with [1-^{13}C]glucose in the presence of acrylamide, a toxic compound that specifically targets the neuronal population.

The specificity of acrylamide toxicity towards neurons was confirmed by gene expression analysis of neuronal (*TUBB3* and *SYP*) and glial (*GFAP*) specific transcripts. After incubation with acrylamide, *TUBB3* and *SYP* expression levels were significantly lower in comparison with control, with a 4- and 5.3-fold decrease respectively, while no modulation on *GFAP* expression was observed (Figure 5.6B).

^{13}C-NMRS analysis revealed significant changes in the amounts of labeled glutamate and GABA after incubation with acrylamide (Figure 5.6A). While the amounts of labeled glutamate in the C2, C3 and C4 positions were significantly higher in comparison with the control, [2-^{13}C]GABA amounts significantly decreased in the presence of acrylamide. Additionally, a significant increase of [2-^{13}C]glutamine was observed, suggesting an increased contribution of the anaplerotic pathway for glutamine synthesis upon acrylamide exposure. As for the total intracellular metabolite pools, no significant differences were detected between acrylamide exposed neurospheres and control (data not shown).

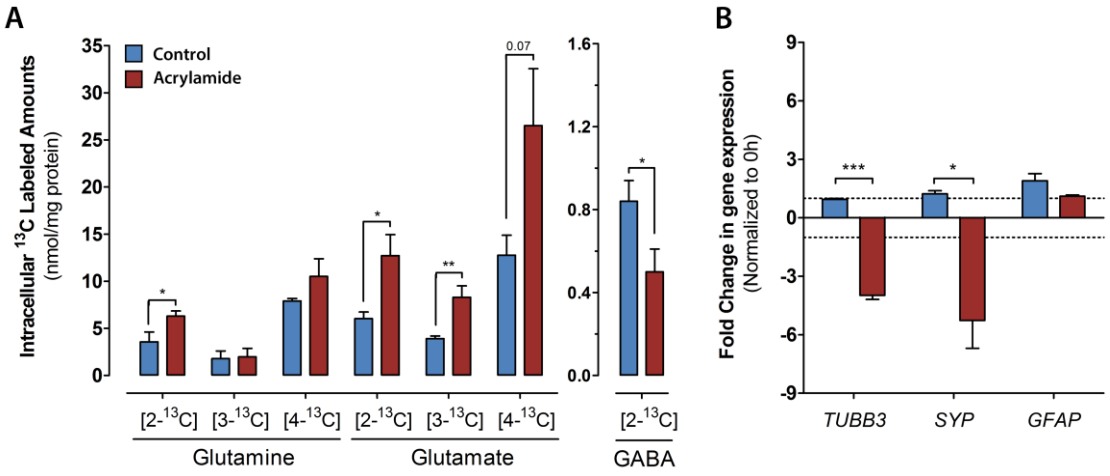

Figure 5.6 - Effect of MSO on ^{13}C labeling of intracellular metabolites and neural gene expression. (A) Intracellular ^{13}C labeled amounts of metabolites in control (blue bars) and acrylamide-treated cultures (red bars). **(B)** Gene expression analysis of differentiated neurospheres in control (blue bars) and acrylamide-treated cultures (red bars). Gene expression fold changes (normalized to expression levels previous to incubation) of neuronal markers (*TUBB3*, *SYP*) and glial marker (*GFAP*). Data are mean ± s.e.m. Asterisks indicate significant difference: **P*<0.05; ***P*<0.01; ****P*<0.001; near significant *P* values (<0.1) are given in numbers.

4. Discussion

Previous work have demonstrated that 3D cultures of human mature neurons and functional astrocytes can be derived from NT2 cells (Terrasso *et al.* 2015). Metabolic data from such neural cell models can provide valuable insights, by offering the possibility to better understand the biochemical changes induced by the compounds of interest in a controlled setting (Ramirez *et al.* 2013). In this context, the metabolic specialization and establishment of functional metabolic shuttles between the different cell compartments are major hallmarks of brain functionality. Thus, the main goal of this work was to investigate whether human neural cells differentiated from a stem cell line in 3D cultures were able to acquire the main metabolic features and interactions found in the *in vivo* human brain.

To analyze the metabolic profile of the differentiated NT2 neurospheres, the fate of two different ^{13}C-labelled substrates, [1-^{13}C]glucose and [2-^{13}C]acetate, was followed. While glucose acts as carbon source mainly for neurons, acetate is only taken up and metabolized by astrocytes (Sonnewald *et al.* 1993; Rae *et al.* 2012). Using both substrates it is possible to assess the presence of the two different cellular compartments by following the incorporation of the label by ^{13}C NMR spectroscopy. This approach had previously been explored for deciphering the main neural metabolic pathways in mono- and co-cultures of primary rodent neural cells in 3D culture systems (Santos *et al.* 2007; Sá Santos *et al.* 2011; Amaral *et al.* 2010).

Incubation with [1-^{13}C]glucose revealed the presence of cell-specific metabolic features, in agreement with phenotypic data that showed heterogeneous differentiated neurospheres composed of neurons and astrocytes (Terrasso *et al.* 2015). The obtained amounts of labeled glutamate and glutamine, namely the differences in C2 labeling, indicated differential contributions of anaplerotic and oxidative pathways for pyruvate incorporation into the TCA cycle for the synthesis of these two metabolites. The contribution of these two pathways was expressed as the ratio PC/PDH (Hassel *et al.* 1995), which was found to be 2.3-fold higher for glutamine synthesis, in comparison with glutamate, in agreement with PC activity restricted to astrocytes (Yu *et al.* 1983; Shank *et al.* 1985), the cellular compartment responsible for glutamine synthesis. Analyzing the labeling in C4, similar amounts of [4-^{13}C]glutamine and [4-^{13}C]glutamate were observed, suggesting that astrocytes are present in higher numbers than neurons in these 3D cultures. Moreover, the higher contribution of the oxidative pathway for glutamate synthesis, relative to glutamine, and the presence of labeled GABA strongly suggest the presence of mature neuronal populations comprising the glutamatergic and GABAergic lineages.

Incubation with [2-^{13}C]acetate resulted in labeling patterns reflecting glial specific metabolism, in agreement with previous reports describing that acetate is mostly metabolized by astrocytes, in murine primary cultures (Sonnewald *et al.* 1993; Rae *et al.* 2012). The overall percent enrichment in ^{13}C labeling with [2-^{13}C]acetate was similar to [1-^{13}C]glucose incubation, demonstrating the importance of oxidative pathways for the astrocytic metabolism. The data presented herein, demonstrated the presence of C2 labeled GABA, for which astrocyte-derived [4-^{13}C]glutamine would act as precursor (Sonnewald *et al.* 1993). This indicates the establishment of such an important neuron-glia interaction as the glutamine-GABA shuttle (Bak *et al.* 2006).

The presence of neuron-astrocyte metabolic trafficking was further investigated by specifically challenging both astrocytic and neuronal populations with well described compounds, such as the GS inhibitor MSO and the neurotoxin acrylamide. MSO has been widely described to act as an irreversible inhibitor of GS activity (Ronzio *et al.* 1969), and has been linked to debilitating neurological disorders when administered to animals or humans (Shaw and Bains 1998). The presence of 20 µM MSO in differentiated neurospheres led to an almost complete inhibition of glutamine synthesis, as observed by the extensive reduction in ^{13}C labeled glutamine. Also the intracellular pools of BCAAs were found to be higher in MSO exposed cultures, suggesting a decreased catabolism of these amino acids. BCAAs have been described to have an important role in nitrogen turnover, contributing with its amino group for *de novo* glutamate biosynthesis, mainly through the activity of brached-chain aminotransferase (BCAT) (Kanamori *et al.* 1998; Lieth *et al.* 2001; Hutson *et al.* 2001). Still, in the adult human brain and contrary to rodent neural cells, this enzyme is absent in astrocytes and is only expressed as a cytosolic isoform in neuronal cells, mostly glutamatergic and GABAergic, and as a mitochondrial isoform in endothelial cells of the vasculature (Hull *et al.* 2012). Therefore, the obtained results suggest that MSO exposure can modulate BCAA metabolism in human neurons, where MSO can induce a less potent BCAT inhibition, as opposed to GS, as this molecule has been previously shown to be able to modulate this enzyme's activity in rodent brain (Jessy and Murthy 1988). More importantly, a significant decrease (50%) in the intracellular pool of GABA was observed after 12 hours of incubation with MSO, which is in agreement with previous reports arguing that GABAergic neurons are highly dependent on astrocyte-derived glutamine for neurotransmitter synthesis (Sonnewald *et al.* 1993).

To specifically target the neuronal population, neurospheres were incubated for 48h with acrylamide, adding [1-^{13}C]glucose during the last 6 hours. Acrylamide, an water-soluble alkene, causes cumulative neurotoxicity and neurodegeneration in adult humans and animals (LoPachin and Gavin 2012). The mechanisms of acrylamide tox-

icity have been described to involve interference with kinesin-related motor proteins in neurofilaments, impairing axonal transport and ultimately leading to axonal degeneration and cell death (LoPachin 2004). Gene expression analysis on differentiated neurospheres exposed to 2.5 mM acrylamide confirmed the cell specificity of this compound, leading to significant negative modulation on expression levels of neuronal markers, while glial markers did not show any significant modulation. ^{13}C-NMR spectroscopy data revealed significant alterations in the intracellular pools of glutamate and GABA neurotransmitters, demonstrating the detrimental effects of acrylamide exposure on the neuronal populations. On one hand, the amounts of labeled glutamate increased upon acrylamide exposure and on the other hand, labeling in GABA decreased. Although, a decrease in GABA synthesis was likely to occur as outcome of the acrylamide-induced neurodegenerative processes, the increase in glutamate was unexpected. One possible mechanism underlying the accumulation of glutamate would be the impairment of synaptic vesicle trafficking and cycling (LoPachin 2004). Acrylamide has been suggested to affect nerve terminals at structural and functional levels, with reports showing reduction in number of synaptic vesicles in the active zone as well as decreased neurotransmitter release (DeGrandchamp *et al.* 1990; LoPachin *et al.* 2004). This is also in agreement with previous observations on the effects of acrylamide on this NT2 cell model, where exposure to toxic concentrations of acrylamide induced a significant decrease of synaptic activity (Terrasso *et al.* 2015). Moreover, synaptic terminal degeneration occurring in acrylamide-exposed neurons has also been described to include many structural abnormalities (DeGrandchamp *et al.* 1990). This is likely to impact also on the delicate neuron-astrocyte contacts at synaptic sites, impairing to some extend the metabolic interactions between both cell types. Thus, this imbalance may also contribute to lower GABA synthesis upon acrylamide exposure, due to the higher dependence of this neuronal sub-type on astrocyte-derived glutamine for GABA synthesis (Sonnewald *et al.* 1993). For astrocytes, the decrease in neurotransmitter release represents a significant loss of carbon skeletons influx. This is particularly important for glutamate, since GABA uptake is mainly done in the presynaptic nerve endings of the GABAergic neurons (Gram *et al.* 1988). Consequently, astrocytes will undergo a continuous loss of TCA cycle intermediates to feed biosynthesis processes, as for instance glutamine synthesis. In neural cells, the main enzyme responsible to replenish carbon skeletons loss due to exit of TCA cycle intermediates is PC, and cells modulate its activity to supply the needs of *de novo* synthesis of these intermediates, as oxaloacetate (Shank *et al.* 1985; Sibson *et al.* 2001). This would support the observation of an increase in [2-^{13}C]glutamine, which derives from PC activity, in acrylamide-exposed neurospheres.

This work demonstrates that human stem cell-derived neural cells in a tissue-like 3D setting achieve the metabolic specialization and establish functional neuron-astrocyte shuttles, such as the glutamine-GABA shuttle, found in the *in vivo* brain. Moreover, this human 3D neural *in vitro* model can contribute to a better understanding of human neural metabolism, namely neuron-astrocyte metabolic coupling, both for healthy and pathological phenotypes.

5. Acknowledgements

This work was supported by PTDC/EBB-BIO/112786/2009 and PTDC/EBB-BIO/119243/2010, FCT, Portugal. D. Simão and A.P. Terrasso were recipients of PhD fellowships from FCT, Portugal (SFRH/BD/78308/2011 and SFRH/BD/ 52473/2014, FCT).

6. References

Amaral A. I., Teixeira A. P., Martens S., Bernal V., Sousa M. F. Q., Alves P. M. (2010) Metabolic alterations induced by ischemia in primary cultures of astrocytes: Merging 13C NMR spectroscopy and metabolic flux analysis. *J. Neurochem.* **113**, 735–748.

Badar-Goffer R. S., Bachelard H. S., Morris P. G. (1990) Cerebral metabolism of acetate and glucose studied by 13C-n.m.r. spectroscopy. A technique for investigating metabolic compartmentation in the brain. *Biochem. J.* **266**, 133–139.

Bak L. K., Schousboe A., Waagepetersen H. S. (2006) The glutamate/GABA-glutamine cycle: Aspects of transport, neurotransmitter homeostasis and ammonia transfer. *J. Neurochem.* **98**, 641–653.

Begley C. G., Ellis L. M. (2012) Drug development: Raise standards for preclinical cancer research. *Nature* **483**, 531–533.

Brekke E. M. F., Morken T. S., Widerøe M., Håberg A. K., Brubakk A.-M., Sonnewald U. (2014) The pentose phosphate pathway and pyruvate carboxylation after neonatal hypoxic-ischemic brain injury. *J. Cereb. blood flow Metab.* **34**, 724–34.

Brekke E., Walls A. B., Nørfeldt L., Schousboe A., Waagepetersen H. S., Sonnewald U. (2012) Direct measurement of backflux between oxaloacetate and fumarate following pyruvate carboxylation. *Glia* **60**, 147–158.

Brito C., Escrevente C., Reis C. A., Lee V. M.-Y., Trojanowski J. Q., Costa J. (2007) Increased levels of fucosyltransferase IX and carbohydrate Lewis(x) adhesion determinant in human NT2N neurons. *J. Neurosci. Res.* **85**, 1260–70.

Calcoen D., Elias L., Yu X. (2015) What does it take to produce a breakthrough drug? *Nat. Rev. Drug Discov.* **14**, 161–162.

Carinhas N., Bernal V., Monteiro F., Carrondo M. J. T., Oliveira R., Alves P. M. (2010) Improving baculovirus production at high cell density through manipulation of energy metabolism. *Metab. Eng.* **12**, 39–52.

Choi S., Kim Y., Hebisch M., Sliwinski C., Lee S., D'Avanzo C., Chen H., et al. (2014) A three-dimensional human neural cell culture model of Alzheimer's disease. *Nature* **515**, 274–278.

DeGrandchamp R. L., Reuhl K. R., Lowndes H. E. (1990) Synaptic terminal degeneration and remodeling at the rat neuromuscular junction resulting from a single exposure to acrylamide. *Toxicol. Appl. Pharmacol.* **105**, 422–433.

Giri S., Bader A. (2014) A low-cost, high-quality new drug discovery process using patient-derived induced pluripotent stem cells. *Drug Discov. Today* **20**, 37–49.

Gram L., Larsson O. M., Johnsen a H., Schousboe a (1988) Effects of valproate, vigabatrin and aminooxyacetic acid on release of endogenous and exogenous GABA from cultured neurons. *Epilepsy Res.* **2**, 87–95.

Hassel B., Sonnewald U., Fonnum F. (1995) Glial-neuronal interactions as studied by cerebral metabolism of [2-13C]acetate and [1-13C]glucose: an ex vivo 13C NMR spectroscopic study. *J. Neurochem.* **64**, 2773–2782.

Hertz L., Dringen R., Schousboe A., Robinson S. R. (1999) Astrocytes: Glutamate producers for neurons. *J. Neurosci. Res.* **57**, 417–428.

Hull J., Hindy M. El, Kehoe P. G., Chalmers K., Love S., Conway M. E. (2012) Distribution of the branched chain aminotransferase proteins in the human brain and their role in glutamate regulation. *J. Neurochem.* **123**, 997–1009.

Hutson S. M., Lieth E., LaNoue K. F. (2001) Function of leucine in excitatory neurotransmitter metabolism in the central nervous system. *J. Nutr.* **131**, 846S–850S.

Jessy J., Murthy C. R. (1988) Branched chain amino acid transaminases in brain in methionine sulphoximine (MSI) toxicity. *Biochem. Int.* **16**, 245–251.

Jucker M. (2010) The benefits and limitations of animal models for translational research in neurodegenerative diseases. *Nat. Med.* **16**, 1210–1214.

Kanamori K., Ross B. D., Kondrat R. W. (1998) Rate of glutamate synthesis from leucine in rat brain measured in vivo by 15N NMR. *J. Neurochem.* **70**, 1304–1315.

Lieth E., LaNoue K. F., Berkich D. a., Xu B., Ratz M., Taylor C., Hutson S. M. (2001) Nitrogen shuttling between neurons and glial cells during glutamate synthesis. *J. Neurochem.* **76**, 1712–1723.

Livak K. J., Schmittgen T. D. (2001) Analysis of relative gene expression data using real-time quantitative PCR and the 2(-Delta Delta C(T)) Method. *Methods* **25**, 402–8.

LoPachin R. M. (2004) The changing view of acrylamide neurotoxicity. *Neurotoxicology* **25**, 617–630.

LoPachin R. M., Gavin T. (2012) Molecular mechanism of acrylamide neurotoxicity: Lessons learned from organic chemistry. *Environ. Health Perspect.* **120**, 1650–1657.

LoPachin R. M., Schwarcz A. I., Gaughan C. L., Mansukhani S., Das S. (2004) In vivo and in vitro effects of acrylamide on synaptosomal neurotransmitter uptake and release. *Neurotoxicology* **25**, 349–363.

Lundgaard I., Li B., Xie L., Kang H., Sanggaard S., Haswell J. D. R., Sun W., et al. (2015) Direct neuronal glucose uptake heralds activity-dependent increases in cerebral metabolism. *Nat. Commun.* **6**, 6807.

Mak I. W., Evaniew N., Ghert M. (2014) Lost in translation: animal models and clinical trials in cancer treatment. *Am. J. Transl. Res.* **6**, 114–8.

Moors M., Rockel T. D., Abel J., Cline J. E., Gassmann K., Schreiber T., Schuwald J., Weinmann N., Fritsche E. (2009) Human neurospheres as three-dimensional cellular systems for developmental neurotoxicity testing. *Env. Heal. Perspect* **117**, 1131–8.

Mullard A. (2014) 2013 FDA drug approvals. *Nat. Rev. Drug Discov.* **13**, 85–9.

Pampaloni F., Reynaud E. G., Stelzer E. H. K. (2007) The third dimension bridges the gap between cell culture and live tissue. *Nat. Rev. Mol. Cell Biol.* **8**, 839–845.

Paşca A. M., Sloan S. a, Clarke L. E., Tian Y., Makinson C. D., Huber N., Kim C. H., et al. (2015) Functional cortical neurons and astrocytes from human pluripotent stem cells in 3D culture. *Nat. Methods* April.

Paul S. M., Mytelka D. S., Dunwiddie C. T., Persinger C. C., Munos B. H., Lindborg S. R., Schacht A. L. (2010) How to improve R&D productivity: the pharmaceutical industry's grand challenge. *Nat. Rev. Drug Discov.* **9**, 203–14.

Potter W., Kalil R. E., Kao W. J. (2008) Biomimetic material systems for neural progenitor cell-based therapy. *Front Biosci* **13**, 806–21.

Rae C., Fekete A. D., Kashem M. a., Nasrallah F. a., Bröer S. (2012) Metabolism, compartmentation, transport and production of acetate in the cortical brain tissue slice. *Neurochem. Res.* **37**, 2541–2553.

Ramirez T., Daneshian M., Kamp H., Bois F. Y., Clench M. R., Coen M., Donley B., et al. (2013) Metabolomics in toxicology and preclinical research. *ALTEX* **30**, 209–25.

Rodrigues T. B., Valette J., Bouzier-Sore A.-K. (2013) 13C NMR spectroscopy applications to brain energy metabolism. *Front. Neuroenergetics* **5**, 9.

Ronzio R. a, Rowe W. B., Meister a (1969) Studies on the mechanism of inhibition of glutamine synthetase by methionine sulfoximine. *Biochemistry* **8**, 1066–1075.

Rothman D. L., Feyter H. M. de, Graaf R. a. de, Mason G. F., Behar K. L. (2011) 13C MRS studies of neuroenergetics and neurotransmitter cycling in humans. *NMR Biomed.* **24**, 943–957.

Sá Santos S., Sonnewald U., Carrondo M. J. T., Alves P. M. (2011) The role of glia in neuronal recovery following anoxia: In vitro evidence of neuronal adaptation. *Neurochem. Int.* **58**, 665–75.

Santos S. S., Leite S. B., Sonnewald U., Carrondo M. J. T., Alves P. M. (2007) Stirred vessel cultures of rat brain cells aggregates: characterization of major metabolic pathways and cell population dynamics. *J. Neurosci. Res.* **85**, 3386–3397.

Schindelin J., Arganda-Carreras I., Frise E., Kaynig V., Longair M., Pietzsch T., Preibisch S., et al. (2012) Fiji: an open-source platform for biological-image analysis. *Nat. Methods* **9**, 676–82.

Schüle B., Pera R. a R., Langston J. W. (2009) *Can cellular models revolutionize drug discovery in Parkinson's disease?* Elsevier B.V.

Serra M., Brito C., Costa E. M., Sousa M. F. Q., Alves P. M. (2009) Integrating human stem cell expansion and neuronal differentiation in bioreactors. *BMC Biotechnol.* **9**, 82.

Shank R. P., Bennett G. S., Freytag S. O., Campbell G. L. (1985) Pyruvate carboxylase: an astrocyte-specific enzyme implicated in the replenishment of amino acid neurotransmitter pools. *Brain Res.* **329**, 364–367.

Shaw C. A., Bains J. S. (1998) Did consumption of flour bleached by the agene process contribute to the incidence of neurological disease? *Med. Hypotheses* **51**, 477–481.

Sibson N. R., Mason G. F., Shen J., Cline G. W., Zara Herskovits a., Wall J. E. M., Behar K. L., Rothman D. L., Shulman R. G. (2001) In vivo 13C NMR measurement of neurotransmitter glutamate cycling, anaplerosis and TCA cycle flux in rat brain during [2-13C]glucose infusion. *J. Neurochem.* **76**, 975–989.

Simão D., Pinto C., Piersanti S., Weston A., Peddie C. J., Bastos A. E. P., Licursi V., et al. (2015) Modeling Human Neural Functionality In Vitro : Three-Dimensional Culture for Dopaminergic Differentiation. *Tissue Eng. Part A* **21**, 654–668.

Sonnewald U., Kondziella D. (2003) Neuronal glial interaction in different neurological diseases studied by ex vivo 13C NMR spectroscopy. *NMR Biomed.* **16**, 424–429.

Sonnewald U., Westergaard N., Schousboe A., Svendsen J. S., Unsgård G., Petersen S. B. (1993) Direct demonstration by [13C]NMR spectroscopy that glutamine from astrocytes is a precursor for GABA synthesis in neurons. *Neurochem. Int.* **22**, 19–29.

Tarczyluk M. A., Nagel D. A., O'Neil J. D., Parri H. R., Tse E. H., Coleman M. D., Hill E. J. (2013) Functional astrocyte-neuron lactate shuttle in a human stem cell-derived neuronal network. *J. Cereb. Blood Flow Metab.* **33**, 1386–93.

Taylor A., McLean M., Morris P., Bachelard H. (1996) Approaches to Studies on Neuronal/Glial Relationships by 13C-MRS Analysis. *Dev. Neurosci.* **18**, 434–442.

Terrasso A. P., Pinto C., Serra M., Filipe A., Almeida S., Ferreira A. L., Pedroso P., Brito C., Alves P. M. (2015) Novel scalable 3D cell based model for in vitro neurotoxicity testing: Combining human differentiated neurospheres with gene expression and functional endpoints. *J. Biotechnol.*

Yu a C., Drejer J., Hertz L., Schousboe a (1983) Pyruvate carboxylase activity in primary cultures of astrocytes and neurons. *J. Neurochem.* **41**, 1484–1487.

6

Perfusion Stirred-tank Bioreactors for 3D differentiation of Human Induced Pluripotent Stem Cells-derived Neural Stem Cells

Table of Contents

Abstract

The limited access to primary human neurons has hindered the development of accurate models to mimic human central nervous system (CNS), as well as the development of efficient therapies for neuropathologies. Current available models rely on animal testing or on monolayer *in vitro* cell cultures that often fail in mimicking human phenotype or the target tissue features. The emergence of human induced pluripotent cells (hiPSC) enabled an unlimited source of neural stem cells (NSC) with the ability to differentiate into the neural lineage, including neurons and glia. Three-dimensional (3D) *in vitro* models allow a closer recapitulation, over traditional monolayer cultures, of the microenvironment complexity and interactions, such as cell-cell and cell-extracellular matrix (ECM) interactions.

The development of robust and scalable processes for the 3D differentiation of hiPSC-derived NSC (hiPSC-NSC) can improve the accuracy of early stage development in preclinical research. In this context, the use of software-controlled stirred-tank bioreactors (STB) provides an efficient technological platform for hiPSC-NSC aggregation and differentiation. This system enables to monitor and control important physico-chemical parameters, such as pH, dissolved oxygen and temperature. Importantly, the adoption of a perfusion operation mode allows a stable flow of nutrients and small molecules, while clearing the toxic by-products. This contributes to a more physiologically relevant setting by mimicking the *in vivo* microenvironment. In this work, the technical requirements and procedures for the implementation of 3D differentiation strategies of hiPSC-NSC are addressed.

This culture system is likely to contribute for the development of human 3D neural *in vitro* models, with an approach amenable to feed high-throughput screening platforms, contributing to expand the available in vitro tools for drug screening and toxicological studies.

1. Introduction

Human cell-based central nervous system *in vitro* models enable the study of healthy and pathophysiological features of neural cells in a human genome-based system, contributing to increased accuracy in preclinical research (Casarosa *et al.* 2013). Although primary human neurons present limited availability, a diversity of human neural cell sources have been made available, including immortalized cell lines or neural stem cells (NSC) from embryonic or adult origin or derived from human induced pluripotent stem cells (hiPSC) (Schüle *et al.* 2009). hiPSC can be generated from somatic cells from any individual at any time point which enables the generation of pluripotent cells carrying the genetic background from healthy donors or patients with specific mutations (Zeng *et al.* 2014). These cells can be committed towards the neural phenotype, giving rise to multipotent NSC with self-renewal capacity and ability to differentiate into the three neural lineages – neurons, astrocytes and oligodendrocytes (Gage 2000). Therefore the use of hiPSC-derived NSC (hiPSC-NSC) enables the study of how specific sets of mutations lead to the respective neurological disease across a lifetime, which was not possible with non-iPSC models (Zeng *et al.* 2014).

To date, many studies using healthy and patient-derived hiPSCs have already been developed (Zeng *et al.* 2014) demonstrating that some common challenges remain. These challenges include a resulting heterogeneous population, low reproducibility between lines from the same and between patients (Dolmetsch and Geschwind 2011) and the lack of a mature disease phenotype. Also, the development of some pathophysiological features may require at least a partial recapitulation of CNS architecture which is not achieved in traditional monolayer cultures (Choi *et al.* 2014; Hungsberg *et al.* 2013; Saporta *et al.* 2011). Three dimensional (3D) culture systems are able to more closely mimic tissue architecture and complexity, namely in terms of cell-cell and cell-extracellular matrix interactions (ECM) (Breslin and O'Driscoll 2013).

3D cultures systems include scaffold-based and scaffold-free systems. In scaffold-based systems cells are embedded within or on the top of scaffolds, either from natural origin or synthetic, providing an initial support to seeded cells while allowing cellular migration and organization into a 3D architecture (Drury and Mooney 2003). Scaffold-free systems enable to recapitulate a tissue-like architecture without the aid of any exogenous ECM. These culture systems take advantage of the potential of many cell types to self-organize into 3D structures named cell spheroids, or neurospheres if composed of neural cells (Pampaloni *et al.* 2007; Hopkins *et al.* 2015). Cellular aggregation can be attained through several strategies, such as the use of non-adherent surfaces, restricting cells to a small volume in a hanging drop or by culturing single cells under

constant agitation. In the latter, agitation promotes cell-cell collisions and interactions that consequently lead to aggregation (Breslin and O'Driscoll 2013). Thus, an important advantage of scaffold-free 3D culture approaches is the possibility to efficiently generate differentiated neural cells with no addition of exogenous ECM components, inducing cells to recreate their own microenvironment. As previously demonstrated, this enables to efficiently drive human NSC differentiation as neuroshperes into mature and functional neurons, astrocytes and oligodendrocytes (Terrasso *et al.* 2015; Simão *et al.* 2015; Paşca *et al.* 2015; Mariani *et al.* 2012). Some limitations of static aggregate cultures include the low control over neurosphere size, which can be overcome by optimizing the number of cells seeded in multi-well plates for single neurosphere generation per well (Valamehr *et al.* 2008; Zhang *et al.* 2012; Ng *et al.* 2005). Agitation-based cultures systems allow higher degree of control over neurosphere size by modulating the agitation rate. These systems present also increased mass transfer coefficients over static cultures, which minimize the formation of necrotic centers due to shortage of oxygen and nutrients in the inner layers (Kinney *et al.* 2011).

Among the agitation-based culture systems, the use of stirred-tank bioreactors (STB) to culture cell spheroids have been reported to improved cell survival, proliferation and differentiation efficiency, relatively to 2D culture systems (Serra *et al.* 2009; Rodrigues *et al.* 2011). Software-controlled STB are dynamic systems that allow monitoring and controlling important physico-chemical culture parameters, as pH, dissolved oxygen and temperature. Importantly, the possibility to operate STB cultures under perfusion mode, allows more stable culture conditions in terms of nutrient and small molecules availability. This continuous flow condition sustains also a clearing of cell debris and metabolic by-products, which resemble the in vivo blood flow, improving cell viability/functionality and providing a more physiological environment (Serra *et al.* 2010; Li and Cui 2014). Together, these features offer a highly controlled culture system, which greatly contributes to improve the robustness and reproducibility of differentiation processes.

Cell aggregation in STB is highly dependent on cell type and the hydrodynamics of the system. There are several parameters that modulate the hydrodynamics, including the geometry of the vessel, the type and size of the impeller and stirring rate. Optimization of these parameters is crucial to sustain neurosphere formation, while minimizing detrimental effects of shear stress and allowing efficient gas/nutrient diffusion within the neurospheres (Kinney *et al.* 2011). Accurate hydrodynamic characterization of the systems provides data for process scale-up, providing the production of large cell numbers required in industrial and clinical settings. STB design is compatible with non destructive sampling, enabling the characterization of long-term cultures through-

out culture time (Serra *et al.* 2012). Importantly, these features enable the use of STB cultures as feeding system of cell-based assays in high-throughput platforms.

This chapter will address the aggregation and differentiation of hiPSC-NSC in perfusion-operated STB cultures. These cultures can play a relevant role in preclinical research, by providing a physiological relevant system that recapitulates closely the chemical, mechanical and biochemical *in vivo* microenvironment.

2. Materials and Methods

2.1. Cell Expansion

hiPSC-derived NSC (hiPSC-NSC) were kindly supplied by Dr. Tomo Saric from University of Cologne, Germany. Expansion of hiPSC-NSC was performed on poly-L-ornithine-laminin (PLOL)-coated surfaces. PLOL coating was prepared by performing a 3 hour incubation at 37°C with 0.16 mg/mL solution of poly-L-ornithine in PBS (with Ca^{2+} and Mg^{2+}), followed by a washing step and a 3 hour incubation at 37°C with 1 µg/mL solution of laminin in PBS (with Ca^{2+} and Mg^{2+}). hiPSC-NSC were cultured in expansion medium (EM), composed of DMEM/F12 media with Glutamax (Life Technologies) supplemented with 1% N2 supplement (Life Technologies), 0.1% B27 supplement (Invitrogen), 1.6 µg/mL glucose (Sigma-Aldrich), 20 µg/mL insulin (Sigma-Aldrich), 20 ng/mL rhu-bFGF (Peprotech), 20 ng/mL rhu-EGF (Sigma-Aldrich). Cells were split typically every 4-5 days at 90-100% confluence. Cells were dislodged through incubation with 0.05% Trypsin-EDTA for 1-2 minutes. Cells were ressuspended in DMEM supplemented with 10% FBS (Life Technologies), sedimented by centrifugation and the resultant pellet ressuspended in EM. Cell concentration and viability were determined by the trypan blue exclusion method in a Fuchs-Rusenthal hemocytometer. The cell suspension was used to inoculate PLOL-coated T-flasks, at a cell density of 3×10^4 cell/cm^2. A 50 % media exchange was performed at day 2 of culture. Cells were maintained under humidified atmosphere, in a multi-gas cell incubator (Sanyo), with 5 % CO_2 and 3 % O_2, at 37 °C.

2.2. hiPSC-NSC differentiation in 3D culture system

hiPSC-NSC were expanded and dislodged with trypsin into a cell suspension, as described above. This cell suspension was passed through a 70 µm nylon strainer (Millipore) prior to bioreactor inoculation, in order to eliminate cell clumps. The obtained single cell suspension was diluted for a cell density of 4×10^5 cell/mL in aggregation medium (AM), with the same composition as EM, except for reduced EGF/FGF concentration (5 ng/mL) and the addition of 5 µM Y-27632. Cells were then inoculated in-

to software-controlled stirred-tank DASGIP® Bioblock bioreactor system (Eppendorf) in a setup as depicted in Figure 6.1. Culture conditions were set to maintain cells under 3 % dissolved oxygen (15 % of air with 21 % of oxygen), pH 7.4, 37 ºC and a stirring rate of 70 rpm. In order to control the aggregate size and avoid aggregate fusion, the stirring rate was gradually increased up to 90 rpm with 10 rpm steps, based on visual inspection of the culture. After 48 hours of culture, perfusion operation mode was activated, with a dilution rate of 0.33 day^{-1} (i.e., 33 % working volume exchange *per* day) under gravimetric control. To prevent the loss of aggregates through the outlet perfusion line, a metallic filter of 20 µm pore size was adopted as cell retention device. After a 7 day aggregation period with AM, differentiation was induced by replacing the perfusion medium with differentiation medium (DM). DM was prepared by supplementing DMEM/F12 with Glutamax with 2 % B27 supplement, 1.6 µg/mL glucose, 10 µg/mL insulin, 10 µg/mL putrescin, 63 ng/mL progesterone, 50 µg/mL apotransferrin, 50 ng/mL sodium selenium (all from Sigma-Aldrich) and 200 mM ascorbic acid (Wako).

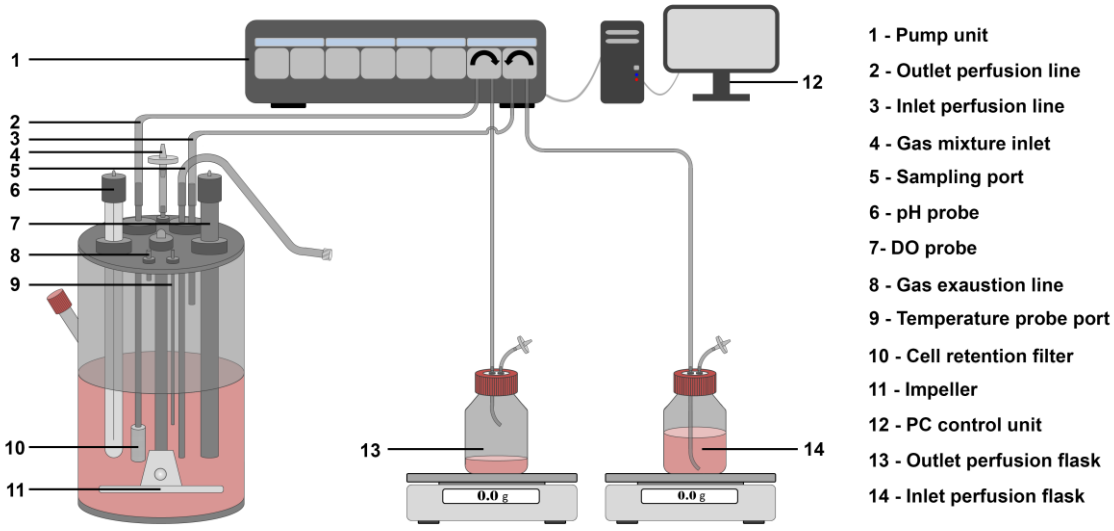

Figure 6.1 - Schematic representation of STB system used for hiPSC-NSC differentiation, operating under perfusion mode.

2.3. Viability assay

For cell viability assessment, neurospheres were incubated with 20 mg/mL fluorescein diacetate, which stains viable cells, and 10mg/mL propidium iodide, a membrane-impermeable DNA dye that stains nonviable cells, in phosphate-buffered saline (PBS) for 5min, washed with PBS, and observed using fluorescence microscopy (DMI6000, Leica).

2.4. DNA quantification-based cell concentration determination

For cell density determination, 0.5 mL samples were collected, sedimented by centrifugation at 1000 x g, 5 min and ressuspended in ultrapure distilled water. Complete cell lysis was achieved through a freeze-thaw cycle in liquid nitrogen coupled to 15 min sonication into an ultrasound bath at 35 kHz. DNA quantification was performed using the Quant-iT™ PicoGreen® dsDNA Assay Kit (Life Technologies), according to the manufacturer's instructions. Fluorescence intensity was measured in spectrofluorometer at 480 nm excitation and 520 nm emission wavelengths. The obtained values were correlated with calibration curves performed by serial dilutions of standard DNA solutions and cell lysates from samples with known cell concentrations.

2.5. Extracellular metabolite quantification

The determination of glutamate and glutamine concentration was performed using automated YSI 7100 Multi-parameter Bioanalytical System (YSI Life Sciences).

2.6. Aggregate Size Determination

Neurosphere size determination was performed by imaging analysis of phase contrast images, using ImageJ software (version 1.49g). Briefly, the aggregate boundaries were defined by manual threshold adjustment and the Feret's diameter was automatically determined for each one of the neurospheres.

2.7. Cell proliferation

The percentage of proliferative cells within neurospheres was determined through the EdU (5-ethynyl-2´-deoxyuridine) incorporation assay, using the Click-iT® EdU Alexa Fluor® 488 Assay Kit (Life Technologies). Briefly, neurospheres were allowed to adhere to PLOL-coated glass coverslips and incubated with 10 μM EdU in culture media for 20 h. After incubation, cells were fixed with 4 % paraformaldehyde (PFA) and 4 % sucrose in PBS for 20 min, washed twice with PBS with 1 % bovine serum albumin (BSA) and permeabilized with saponin-based working reagent for 20 to 30 min, depending on neurosphere size. Cells were incubated with AlexaFluor488 anti-EdU antibody, according to manufacturer's instructions, for 45 min to 1 h 15 min, depending on neurosphere size. Coverslips were mounted in ProLong Gold antifade reagent with DAPI (Life Technologies). Preparations were visualized in spinning disk microscope (Nikon Eclipse Ti-E, confocal scanner: Yokogawa CSUx1) and resultant images processed in ImageJ software (version 1.49g). For quantitative analysis, Edu-positive cells and total DAPI-labeled nuclei were determined using cell counter plug-in in ImageJ.

2.8. Immunofluorescence microscopy

Neurospheres were allowed to adhere to PLOL-coated glass coverslips or µ-Slide 4 Well (Ibidi), fixed in 4%paraformaldehyde +4% sucrose in PBS for 40min, and processed for immunostaining as described previously (Serra *et al.* 2011) Primary and secondary antibodies were used as follows: rabbit anti-nestin, rabbit anti-Sox2, mouse anti-βIII-tubulin, mouse anti-synaptophysin (1:200; all from Millipore), chicken anti-MAP2 (1:10 000, Abcam), AlexaFluor 488 goat anti-mouse IgG, AlexaFluor 594 goat anti-chicken IgY or AlexaFluor 594 goat anti-rabbit IgG, AlexaFluor 488 goat anti-rabbit IgG (1:500; all from Life Technologies). Cell nuclei were counterstained with DAPI or TO-PRO-3 (Life Technologies). Coverslips were mounted in ProLong Gold antifade reagent with DAPI (Life Technologies). Preparations were visualized in point scan confocal microscope (SP5, Leica). The obtained images were processed using ImageJ software (version 1.49g) and only linear manipulations were performed. For cell quantifications, the number of positively labeled cells was quantified by counting 4 to 5 randomly selected fields of approximately 100 cells or 4 to 5 neurospheres of at least two independent experiments.

2.9. RT-qPCR

Total RNA was extracted with High Pure RNA Isolation Kit (Roche), according to the manufacturer's instructions. RNA was quantified in a NanoDrop 2000c (Thermo Scientific) and used for cDNA synthesis. Reverse transcription was performed with High Fidelity cDNA Synthesis Kit (Roche), using Anchored- oligo(dT)18 Primer (Roche). Real-time quantitative polymerase chain reaction (qRT-PCR) were performed in triplicates using LightCycler 480 SYBR Green I Master Kit (Roche) and primers were listed in Table 6.1. Reactions were performed with LightCycler 480 Instrument II 96-well block (Roche). Quantification of cycle values (Ct) and melting curves was determined using LightCycler 480 Software version 1.5 (Roche). All data was analyzed using the $2^{-\Delta\Delta Ct}$ method for relative gene expression analysis (Livak and Schmittgen 2001). Changes in gene expression were normalized using the Ct geometric mean of housekeeping genes *RPL22* (encoding for ribosomal protein L22) and *GAPDH* (encoding for glyceraldehyde 3-phosphate dehydrogenase) as internal controls.

Table 6.1 - List of primers and discrimination of its sequences used for RT-qPCR analysis.

Gene	Primer forward (Top) and reverse (Bottom)
RPL22	CACGAAGGAGGAGTGACTGG TGTGGCACACCACTGACATT
GAPDH	AATGAAGGGGTCATTGATGG AAGGTGAAGGTCGGAGTCAA
PCNA	CGGAGTGAAATTTTCTGCAAG TTCAGGTACCTCAGTGCAAAAG
NES	TAAGGTGAAAAGGGGTGTGG GCAAGAGATTCCCTTTGCAG
TUBB3	GGGCCTTTGGACATCTCTTC CCTCCGTGTAGTGACCCTTG
NURR1	CGACCAAGACCTGCTTTTTG ATTGCAACCTGTGCAAGACC
TH	AGCCCTACCAAGACCAGACG GCGTGTACGGGTCGAACTT
GAD 67	ACCAGAAAACTGGGGCTCA GCAGGTTCTTGGAGGATTG
GLAST	TACCATCCATGGAGCACGAG ACCTGGTGACCACCACACAC
S100B	GGAGACGGCGAATGTGACTT GAACTCGTGGCAGGCAGTAGTAA

2.10. Synaptic vesicle trafficking

Neurospheres were allowed to adhere to PLOL-coated glass coverslips, washed with PBS and exposed to a high-potassium depolarizing solution (100mM KCl buffer; 5 mM Hepes-NaOH, 10 mM Glucose, 2.5 mM $CaCl_2$, 1 mM $MgCl_2$, 100 mM KCl, 37 mM NaCl), for 5 min. Afterward, neurospheres were incubated with 10mM FM 1–43 dye (Life Technologies) dissolved in normal saline (5mM KCl buffer: 5 mM Hepes-NaOH, 10 mM Glucose, 2.2 mM $CaCl_2$, 1 mM $MgCl_2$, 5 mM KCl, 137 mM NaCl) for 15 min and washed with ADVASEP-7 (Sigma-Aldrich) dissolved in 5mM KCl buffer for 1 min. This was followed by three washes of 1 min with 5mM KCl buffer prior to imaging. Exocytosis was stimulated with 100mM KCl buffer and samples were imaged live in a fluorescence microscope (DMI6000; Leica) to monitor synaptic vesicle release. Fluorescence intensity was measured using ImageJ Software.

2.11. Calcium transients assay

Neurospheres were incubated with 1X Fluo-4 Direct calcium reagent (Life Technologies) for 30 min at 37 ^{o}C, 5 % CO_2 and 3 % O_2, followed by 15 min at room temperature. Fluo-4 is a cell permeant with high affinity to Ca^{2+} and its fluorescence is 100-fold increased at 488nm upon Ca^{2+} binding. Samples were imaged live in a spinning disk microscope (Nikon Eclipse Ti-E, confocal scanner: Yokogawa CSUx1). Fluores-

cence intensity change over time was defined as $\Delta F/F0 = (F - F0)/F0$, where F represented the fluorescence at any time point, and F0 the baseline fluorescence determined by baseline fitting across the whole movie for each cell using PeakFit Software (v4.12).

3. Results

For the development of a scalable and reproducible process for 3D differentiation of hiPSC-NSC, a software-controlled STB was adopted as culture system. The culture strategy was based on previously successfully implemented protocols for the generation of mature and functional neurons and astrocytes from other pluripotent and neural progenitor cells using agitation-based culture systems (Brito *et al.* 2012; Simão *et al.* 2015; Terrasso *et al.* 2015). This included a first aggregation step, were cells inoculated as a single cell suspension were allowed to aggregate into neurospheres during 7 days in a reduced concentration of growth factors (Figure 6.2A). After stabilization of the aggregation process during the first 7 days of culture, neural differentiation was induced by exposing cells to cocktail of antioxidants, neurotrophic factors and in absence of growth factors.

3.1. Cell aggregation and proliferation dynamics

During the first days of culture, agitation rate was adjusted stepwise between 70 rpm and 90 rpm in order to control the aggregation process by maintaining a homogeneous aggregate size. For this, three main morphological features were tightly monitored during the first 8-10 h after inoculation, namely neurosphere size, the presence of single cells and fusion between aggregates.

During the first week of culture, a 3-fold decrease was observed in terms of neurosphere density (Figure 6.2B). This is is mostly related to a process of neurosphere fusion, as indicated by an increase in the mean diameter from 52.1 ± 10.7 μm at day 1 to 90.9 ± 13.6 μm by day 7 (Figure 6.2C). Neurospheres at day 7 presented homogeneous size, with compact structure and high cell viability (Figure 6.2F).

As stated above, hiPSC-NSC neurospheres were cultured in AM during the aggregation stage, in presence of EGF and bFGF. The exposure to these growth factors allowed cells to maintain a proliferative phenotype, as demonstrated by the incorporation of EdU in approximately 65 % of cells (Figure 6.2E). Still, the cell density remained almost constant around $5x10^5$ cell/mL (Figure 6.2D), indicating that although cells retained their proliferative phenotype the proliferation rate was considerably decreased in the 3D cultures, which is supported by the 4-fold reduction in the concentration of growth factors over the 2D expansion process.

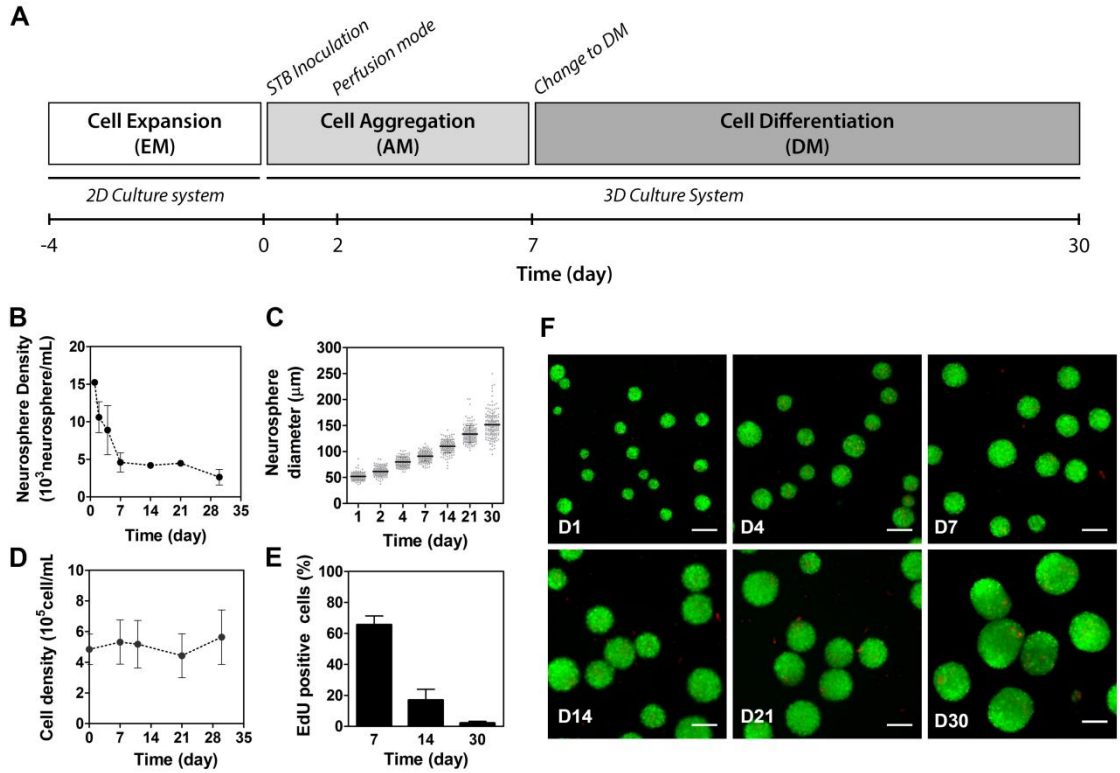

Figure 6.2 – hiPSC-NSC aggregation dynamics during 3D differentiation. (A) Workflow for hiPSC-NSC expansion and 3D differentiation. EM – Expansion medium; AM – Aggregation medium; DM – Differentiation medium. **(B-C)** Neurosphere density **(B)** and diameter **(C)** as a function of time. **(D)** Cell density along culture time, evaluated by DNA quantification. **(E)** Percentage of actively proliferating cells in culture along culture time, as expressed by the percentage of cells positive for EdU incorporation. Data are mean ± s.e.m. from two independent experiments. **(F)** hiPSC-NSC neurosphere viability assay (fluorescein diacetate (FDA) - green; propidium iodide (PI) – red) along culture time. Scale bars, 100 µm.

Neural differentiation induced from day 7 onward, sustained a continuous increase in the neurosphere size, attaining a mean diameter of 151.7 ± 38.2 µm by day 30 (Figure 6.2C). Along differentiation, a considerable decrease in the percentage of actively proliferating cells was observed, with only 2 % of cells staining positively for EdU at day 30 (Figure 6.2E). Cell density was maintained at approximately $5x10^5$ cell/mL (Figure 6.2D) despite the reduction in cell proliferation, further supporting the observation of high cell viability observed along culture time (Figure 6.2F).

3.2. Phenotypic characterization

Cellular identity was evaluated during aggregation period, enabling to identify the maintenance of typical neural precursor markers. After 7 days in culture hiPSC-NSC were mostly composed by nestin- and Sox-2-positive cells (Figure 6.3 B-C). The

induction of differentiation led to a decrease in the expression levels of these neural precursor markers, as shown by a 3- and 5-fold decrease in *NES* and *PCNA* expression, respectively (Figure 6.3A), and few Sox-2-positive cells at day 30 of culture (data not shown). Concomitantly, the activation of neuronal markers, as βIII-tubulin was observed from day 7 onward, with a 6.1-fold increase attained by day 30 of culture in comparison with day 0 (Figure 6.3D). This is agreement with the early detection of few βIII-tubulin-positive neurons at day 7 (Figure 6.3C), whereas by day 30 of culture a dense network was readily observable (Figure 6.3E).

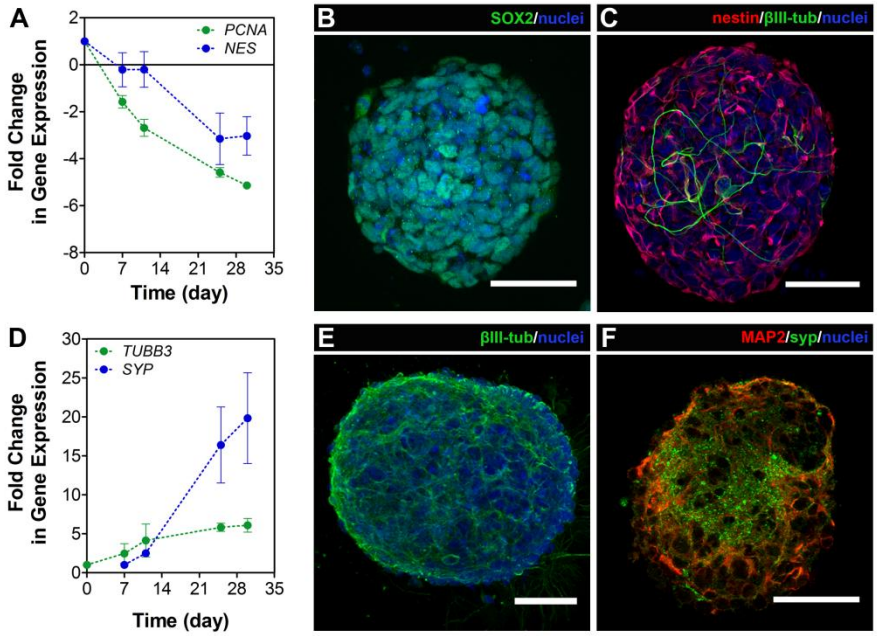

Figure 6.3 – hiPSC-NSC 3D differentiation dynamics. (A) RT-qPCR analysis of PCNA and NES expression. Fold changes in gene expression normalized to day 0 of culture. **(B-C)** Detection of Sox-2 **(B)**, nestin and βIII-tubulin **(C)** at day 7 of culture. Nuclei were counterstained with DAPI (blue). Scale bars: 50 µm. **(D)** RT-qPCR analysis of TUBB3 and SYP expression. Fold changes in gene expression normalized to day 0 of culture (for TUBB3) or to day 7 (for SYP). **(E-F)** Detection of βIII-tubulin **(E)**, MAP2 and synaptophysin (syp) **(F)** at day 30 of culture. Nuclei were counterstained with DAPI (blue). Scale bars: 50 µm. Data are mean ± s.e.m. (for gene expression data) or representative (immunofluorescence microscopy) of two independent experiments.

The obtained data showed that the 3D differentiation process was also able to support neuronal maturation, as indicated by the increased detection of proteins typical of mature neurons, such as MAP-2 and synaptophysin (syp) (Figure 6.3F). MAP-2 was already present in the majority of cells by day 14 (data not shown) and was distributed throughout the neurosphere, presenting an extensive network by day 30 (Fig-

ure 6.3F). The expression of syp was observed to be upregulated during differentiation, being only detect at low levels by day 7 and revealing a 20-fold increase in expression levels relatively to day 7 of culture (Figure 6.3D). These observations at gene expression level were consistent with the detection of syp protein in the differentiated neurospheres. After 14 days of culture syp was already observable in a punctated pattern (data not shown). By day 30, syp detection in a vesicular pattern was extensive and evident throughout the entire neurosphere (Figure 6.3F), indicating the progression in the synaptogenic process.

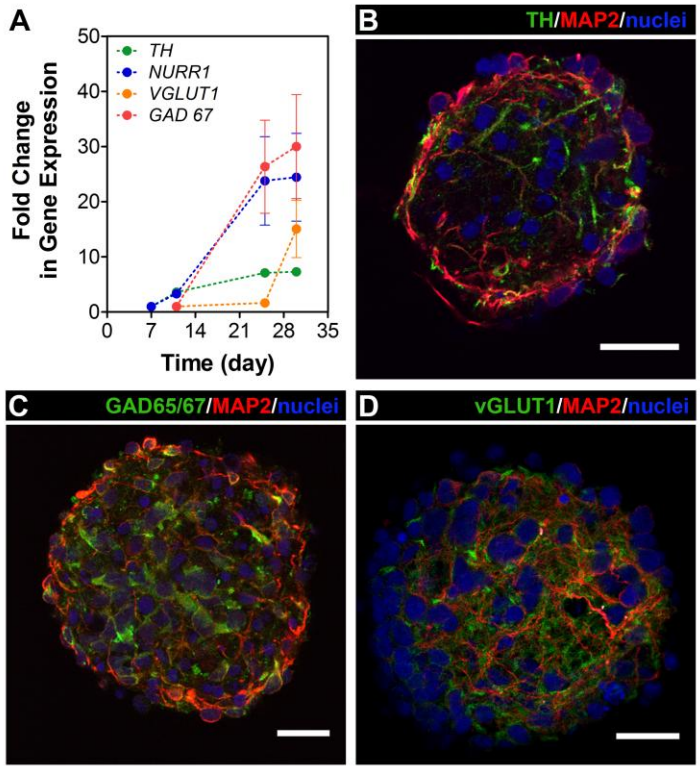

Figure 6.4 - hiPSC-NSC neuronal differentiation. (A) RT-qPCR analysis of TH, NURR1, VGLUT1 and GAD 67 expression. Fold changes in gene expression normalized to day 7 (for TH and NURR1) or to day 11 (for GAD 67 and VGLUT1). **(B-D)** Detection of TH and MAP2 **(B)**, GAD65/67 and MAP-2 **(C)** and vGLUT1 and MAP2 **(D)** at day 30 of culture. Nuclei were counterstained with DAPI. Scale bars: 25 µm. Data are mean ± s.e.m. (for gene expression data) or representative (immunofluorescence microscopy) of two independent experiments.

The neuronal population was further characterized by analyzing the expression of neuronal subtype specific markers (Figure 6.4). Expression of the dopaminergic-related gene encoding for the nuclear receptor related 1 (*NURR1*) was detected by day 7 of culture, being up-regulated with a 24-fold increase by day 30 of culture (Figure 6.4A). Accordingly, the gene encoding for tyrosine hydroxylase (*TH*) was also up-regulated along differentiation, attaining a 7-fold increase from day 7 to day 30 (Figure 6.4A).

Concordant with gene expression analysis, TH protein was detected throughout the neurosphere (Figure 6.4B), indicating the presence of fully committed dopaminergic neurons.

GABAergic phenotype was identified by the expression of glutamate decarboxylase 67 isozyme gene (*GAD67*) from day 11 onwards. *GAD67* expression attained a 30-fold increase by day 30 comparatively to day 11 of culture (Figure 6.4A). Concomitantly, GAD65/67-positive cells could be also detected in differentiated neurospheres by day 30 (Figure 6.4C). The presence of cells from the glutamatergic lineage was evaluated by analyzing the expression of the vesicular glutamate transporter 1 ecoding gene (*VGLUT1*). This gene was detectable from day 7 onwards, reaching a 15-fold increase at day 30 (Figure 6.4A). vGLUT1 protein was also detected along neurites in a punctuated pattern (Figure 6.4D).

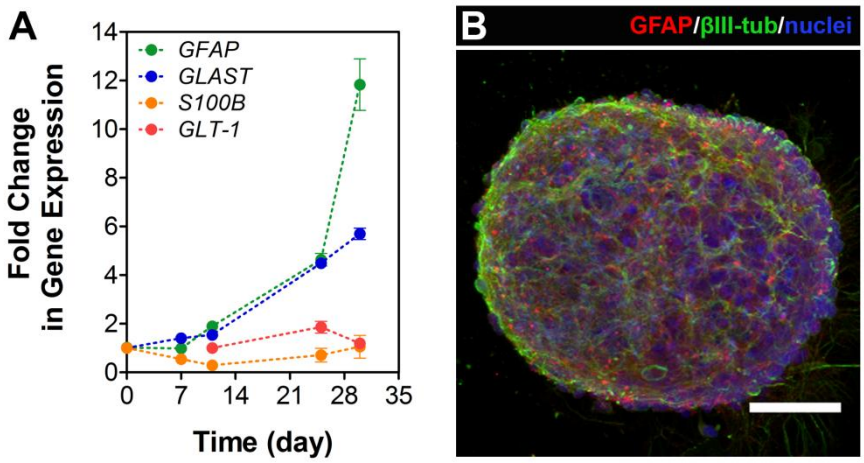

Figure 6.5 - hiPSC-NSC astrocytic differentiation. (A) RT-qPCR analysis of GFAP, GLAST, S100B and GLT-1 expression. Fold changes in gene expression normalized to day 0 of culture, with the exception for GLT-1 (normalized to day 11). **(B)** Detection of GFAP and βIII-tubulin. Nuclei were counterstained with DAPI (blue). Scale bar: 50 µm. Data are mean ± s.e.m. (for gene expression data) or representative (immunofluorescence microscopy) of two independent experiments.

Astroglia differentiation in these 3D cultures was also evaluated. The expression of glial fibrillary acidic protein (*GFAP*) encoding gene was detected by day 7 of culture and up-regulated during differentiation, reaching a 12-fold increase at day 30 (Figure 6.5A) and being widely detected in the differentiated neurospheres (Figure 6.5B). Astrocytic maturation was interrogated by analyzing the expression of cell markers associated with latter stages of astrocyte development, such as *S100B*, *GLAST* and *GLT-1*. The expression of *S100B* and *GLAST* was already detectable in undifferentiated cells

at day 0, where *S100B* showed no significant modulation during differentiation and *GLAST* presented a 5.7-fold increase by day 30 (Figure 6.5A). *GLT-1* expression was activated by day 7, although this was not followed by a significant up-regulation (Figure 6.5A).

3.3. Cell Functionality assessment

Considering the presence of differentiated neurons and astrocytes in the hiPSC-NSC neurospheres, some of the functional features of these cells were assessed providing data on the maturation stage of the generated cells. For neuronal functionality, both spontaneous and induced neuronal activity was assessed. Imaging of spontaneous Ca^{2+} transients was performed in neurospheres at day 7 and 30 of culture. At day 7, the presence of Ca^{2+} transients was only observed in 8 % of cells, whereas by day 30 almost 40 % of cells were shown to be able to spontaneously elicit these Ca^{2+} transients (Figure 6.6A). A variety of patterns in these transients were observed showing different amplitudes.

Synaptic activity was interrogated by analyzing the release of vesicles loaded with fluorescent probe FM 1-43 after induction of a depolarizing stimulus, by exposing cells to a high KCl concentration. Neurospheres at day 7 presented 30 % decrease in fluorescence intensity, while the fluorescent signal showed 50 % decay in neurospheres at day 30 (Figure 6.6B).

Extracellular glutamate clearance and the ability to metabolize this into glutamine represent a major hallmark of astrocytic metabolic features and specialization (Bélanger *et al.* 2011). These properties were evaluated in differentiated neurospheres at day 30 of culture, by exposing cells to culture media supplemented with 5 mM of glutamate and devoid of glutamine for 72 hours (Figure 6.6C). The time profile of glutamate extracellular concentration revealed a reduction of around 2 mM after 72 hours, representing an uptake rate of $6.4 \pm 0.7 \times 10^{-3}$ μmol.mg protein.h^{-1}. Concomitantly, an accumulation of glutamine was observed during the same period with build-up of 1 mM, which corresponds to a secretion rate of $2.9 \pm 0.1 \times 10^{-3}$ μmol.mg protein.h^{-1}.

4. Discussion

The work presented in this chapter, demonstrated that software-controlled STB can provide an efficient technological platform to sustain the differentiation of hiPSC-NSC in a 3D setting. The features of this system offer a scalable and robust approach for the generation of large amounts of differentiated neurospheres, which may be then used to feed high-throughput or high-content screening platforms. This may contribute and sustain studies for understanding neurological disease-related mechanism, as well

as to study the interactions between the different cell types and therapeutics or compounds of interest.

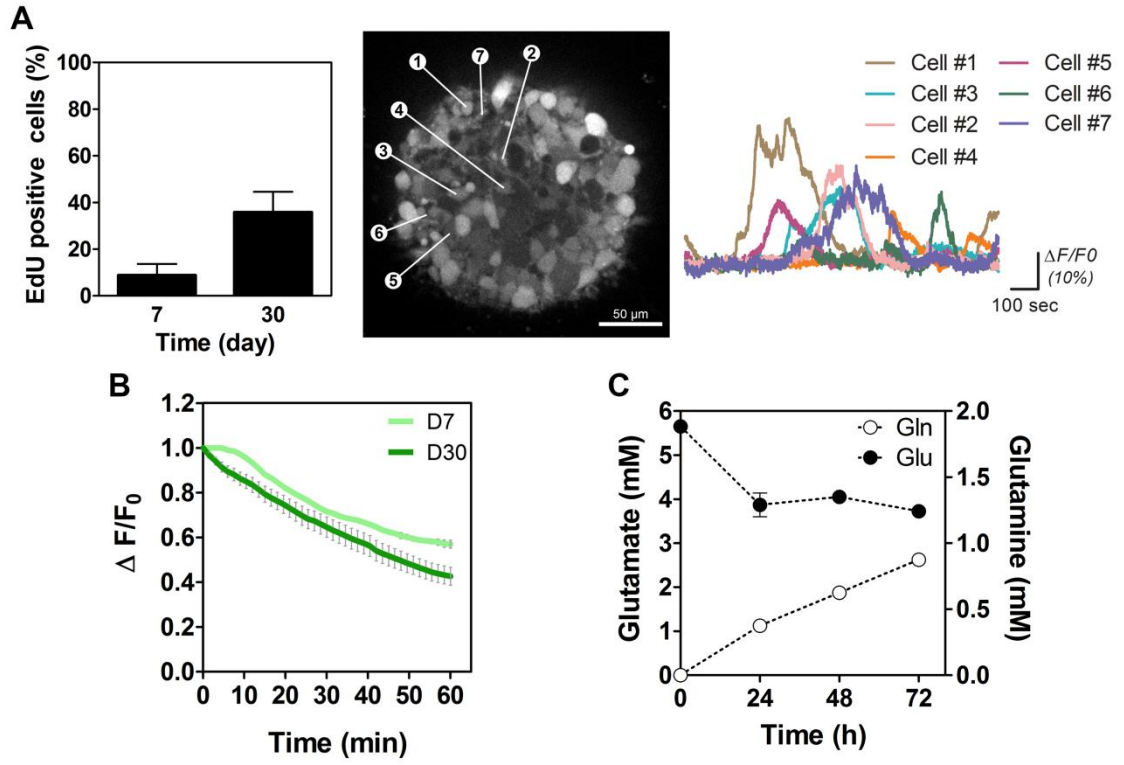

Figure 6.6 - Functional characterization of differentiated hiPSC-NSC neurospheres. (A) Quantification of spontaneous Ca2+ transients, showing the percentage of responsive cells at day 7 and 30 of culture; and normalized intensity of Ca2+ transients from seven different cells of one differentiated neurosphere at day 30 of culture, imaged during approximately 5 minutes. **(B)** Fluorescence intensity of FM 1-43 dye in exocytosis-inducing conditions in neurospheres at day 7 (light green) and at day 30 (dark green) of culture. **(C)** Extracellular concentration of glutamate (Glu, black) and glutamine (Gln, white) during 72 h in medium containing 5 mM of glutamate. Data are mean ± SD of one experiment with two technical replicates.

Cell aggregation dynamics in the STB system showed an efficient and homogeneous aggregation process with the generation of neurospheres of up to 200 µm in diameter. Previous studies using static culture systems, described 200 µm to be the maximal aggregate diameter to allow and efficient diffusion of nutrients and oxygen to the cells in the inner layers (Wu *et al.* 2014). Still, in agitation-based culture systems diameters of 300-400 µm were obtained without formation of necrotic centers (Simão *et al.* 2015; Terrasso *et al.* 2015). This suggests that the factors driving the formation of a necrotic core are strongly cell source- and culture system-dependent. Moreover, agitation-based culture systems by providing increased mass transfer coefficients in comparison with static cultures, promote higher diffusion efficiencies, which contribute to minimize the

necrotic center formation in larger cell aggregates (Kinney *et al.* 2011; Li and Cui 2014; Serra *et al.* 2010). The presence of few non-viable cells identified within neurospheres and as single cells, has been reported as a common feature during NSC neurosphere differentiation being related with apoptotic cell death (Watanabe *et al.* 2007). This programmed cell death processes have been also proposed to play an important role in the development and morphogenesis of the nervous system (Kuan *et al.* 2000).

For this process, a perfusion strategy was implemented to enable continuous and controlled media exchange along long-term cultures. Different strategies were initially tested that continuously resulted in a loss of neurospheres through the outlet perfusion line (data not shown). This indicated the need for the implementation of a cell retention device. However, the commercially available devices, such as alternating tangential flow system (ATF)-based devices or spin filters systems, are still not compatible with small scale bioreactors (Pollock *et al.* 2013). To overcome this limitation, in this work a microsparger unit (20 μm of pore size) was adapted into the outlet line. This strategy was efficient in retaining neurospheres in culture, while still being able to remove non-viable single cells and cell debris. Furthermore, the perfusion operation mode provides a constant removal of toxic metabolic by-products accumulated during culture along with the addition of fresh essential metabolites and small molecules, contributing to the maintenance of high viability in culture. The challenges faced for the application of an efficient cell retention device compatible with small scale bioreactors, as the one used in this work, demonstrates a current need in the biotechnology engineering field that needs to be further addressed.

After 7 days in culture the generated neurospheres comprised mostly Sox-2 and nestin-positive neural precursor cells with a proliferative phenotype, indicated by the detection of Ki-67 and EdU incorportation. These results indicated that the presence of reduced concentration of bFGF and EGF during this first aggregation stage, promoted the maintenance of hiPSC-NSC undifferentiated phenotype, although decreasing proliferation rate as no considerable increase in cell density was observed. These results are in agreement with previous reports, where the removal of growth factors prior to differentiation induction was demonstrated to slow the proliferation rate of hNSC in neurospheres, while increasing the differentiation efficiency after induction (Schwindt et al., 2009). In this work, differentiation induction was achieved by the complete removal of growth factors and addition of antioxidants and neurotrophic factors that have been described to sustain and promote differentiation of neural stem cells (Thier *et al.* 2012; Koch *et al.* 2009; Androutsellis-Theotokis *et al.* 2008). As result, the expression of neural precursor markers, including nestin, PCNA and Sox-2, decreased along culture time, which is in agreement with reported data for 3D cultures of human NSC

of fetal origin upon withdrawal of growth factors (Schwindt *et al.* 2009; Simão *et al.* 2015). Together with the observed reduction in proliferative cells, these results suggest that removal of EGF and bFGF was sufficient for activation of the neurogenic developmental pathways, which in case of neuronal cells leads to a cell cycle exit.

The loss of neural precursor cell identity was followed by the activation of neuronal and astrocytic markers. Progression in neurogenic development was shown by the earlier expression of βIII-tubulin, typical cytoskeletal component of newly generated neurons, followed by the presence of MAP-2- and syp-positive cells, which are expressed after neuronal commitment (Dehmelt and Halpain 2005; Marazzi and Buckley 1993). MAP-2 is a cytoskeleton integrant protein that plays an important role in dendritic development by stabilizating microtubules and F-actin fibers (Dehmelt and Halpain 2005). The detection of syp in a punctuated pattern indicates also the development of the synaptogenic processes, as this protein is integrated in membranes of pre-synaptic vesicle with important functions during vesicle recycling at the synaptic terminal (Kwon and Chapman 2011).

In this work, the adopted differentiation protocol did not aim to target specific neuronal lineages, which enabled to evaluate the neuronal differentiation potential of hiPSC-NSC. The obtained results demonstrated that the 3D differentiation resulted in the presence of dopaminergic, glutamatergic and GABAergic neurons. Dopaminergic differentiation was demonstrated by the expression NURR1 transcription factor, which plays important roles in dopaminergic specification, inducing the expression of lineage-specific genes as *TH* that was also observed (Lee *et al.* 2010). GABAergic phenotype was identified by the expression of GAD enzyme. This enzyme, with two isoforms GAD65 and GAD67, is essential for neurotransmitter synthesis by catalyzing the decarboxylation of glutamate to GABA and being reported to couple its activity with vesicular GABA transporter (vGAT) for synaptic vesicle packing of newly synthesized GABA (Jin *et al.* 2003). vGLUT1 was detection indicated the presence of glutamatergic neurons, being detected in vesicular pattern. This is in accordance with its role in mature glutamatergic neurons, as glutamate transporter into synaptic vesicles (Melo *et al.* 2013). The considerable increase in the percentage of cells able to elicit spontaneous Ca^{2+} transients after differentiation, demonstrated functional improvement of the generated neurons. Ca^{2+} transients are implicated in nerve impulse transmission along neuronal axon, acting as second messenger in the neuronal activation mechanisms, where its intracellular concentration increases during action potentials propagation until reaching the synaptic terminals (Maggio and Vlachos 2014; Grienberger and Konnerth 2012). Synaptic activity, evaluated by the decay in fluorescence upon depolarizing stimulus-evoked vesicle release, was also shown to increase after differentia-

tion, although with more a more modest improvement (20 %). This could be improved by establishing an additional maturation step, as previously demonstrated for human NSC from fetal origin (Simão *et al.* 2015).

In astrocytic differentiation, the up-regulation of GFAP along culture time is consistent with reports of GFAP accumulation in later stages of development, despite being expressed also in radial glia neural precursors (Middeldorp and Hol 2011). The later activation in *GLT-1* expression as compared with *GLAST*, was also in agreement with previous studies describing *GLAST* to be already expressed in radial glia cells and other neural progenitor cells (Hartfuss *et al.* 2001), while *GLT-1* expression is activated and increased during astrocytic differentiation (Minelli *et al.* 2001). Together, the expression of GFAP, GLAST and GLT-1 and the ability to uptake extracellular glutamate and synthesize glutamine clearly indicates the commitment of these cells towards the astrocytic lineage. Still, the observed glutamate uptake and glutamine secretion rates are lower in comparison with previous studies on 3D neural differentiation of NT2 cells (Terrasso *et al.* 2015), suggesting the presence in lower numbers of mature astrocytes. No relevant modulation was observed for the expression of S100β encoding gene, which also supports the need to promote and increase the astrocytic maturation in this culture. This is in accordance with reports exploring neural differentiation approaches for hESC, where neuronal cells can be generated in the first month and astrocytes only after 2-3 months of culture (Hu *et al.* 2010). The astrocytic population can be also better described by the assessment of markers typical of later developmental stages, such as aquaporin-4, the most abundant water channel in astrocytic processes (Patel *et al.* 2014).

The 3D differentiation platform established herein demonstrated to be able to sustain both neuronal and astrocytic differentiation of hiPSC-NSC. Moreover, the detection of different neuronal subtypes indicated that this hiPSC-NSC are in an early developmental stage, presenting the potential to be directed to specific neuronal lineages by adopting targeted differentiation protocols. Combined with the possibility to use patient-derived cells, this approach can contribute to the development of relevant human models for disease modeling, such as Parkinson's disease following dopaminergic differentiation or schizophrenia and bipolar disorders that have been related with GAD67 dysfunctions in GABAergic neurons (Subburaju and Benes 2012).

5. Acknowledgements

Dr Tomo Saric is gratefully acknowledged for the supply of hiPSC-NSC. This work was supported by: Brainvectors (FP7-286071) funded by the EU. Daniel Simão and Ana

Paula Terrasso were recipients of a PhD fellowship from FCT, Portugal (SFRH/BD/78308/2011 and PD/BD/52473/2014, respectively).

6. References

Androutsellis-Theotokis A., Murase S., Boyd J. D., Park D. M., Hoeppner D. J., Ravin R., McKay R. D. G. (2008) Generating neurons from stem cells, in *Neural Stem Cells,* (Weiner L. P., ed), Vol. 438, pp. 31–38. Humana Press.

Bélanger M., Allaman I., Magistretti P. J. (2011) Brain energy metabolism: focus on astrocyte-neuron metabolic cooperation. *Cell Metab.* **14**, 724–38.

Breslin S., O'Driscoll L. (2013) Three-dimensional cell culture: the missing link in drug discovery. *Drug Discov. Today* **18**, 240–9.

Brito C., Simão D., Costa I., Malpique R., Pereira C. I., Fernandes P., Serra M., et al. (2012) 3D cultures of human neural progenitor cells: dopaminergic differentiation and genetic modification. *Methods* **56**, 452–60.

Casarosa S., Zasso J., Conti L. (2013) Systems for ex-vivo Isolation and Culturing of Neural Stem Cells, in *Neural Stem Cells - New Perspect.,* (Bonfanti L., ed), pp. 3–28. InTech.

Choi S. H., Kim Y. H., Hebisch M., Sliwinski C., Lee S., D'Avanzo C., Chen H., et al. (2014) A three-dimensional human neural cell culture model of Alzheimer's disease. *Nature.*

Dehmelt L., Halpain S. (2005) The MAP2/Tau family of microtubule-associated proteins. *Genome Biol.* **6**, 204.

Dolmetsch R., Geschwind D. H. (2011) The human brain in a dish: the promise of iPSC-derived neurons. *Cell* **145**, 831–4.

Drury J. L., Mooney D. J. (2003) Hydrogels for tissue engineering: scaffold design variables and applications. *Biomaterials* **24**, 4337–4351.

Falk A., Koch P., Kesavan J., Takashima Y., Ladewig J., Alexander M., Wiskow O., et al. (2012) Capture of neuroepithelial-like stem cells from pluripotent stem cells provides a versatile system for in vitro production of human neurons. *PLoS One* **7**, 1–13.

Gage F. H. (2000) Mammalian neural stem cells. *Science* **287**, 1433–1438.

Grienberger C., Konnerth A. (2012) Imaging Calcium in Neurons. *Neuron* **73**, 862–885.

Hartfuss E., Galli R., Heins N., Götz M. (2001) Characterization of CNS precursor subtypes and radial glia. *Dev. Biol.* **229**, 15–30.

Hopkins A. M., DeSimone E., Chwalek K., Kaplan D. L. (2015) 3D in vitro modeling of the central nervous system. *Prog. Neurobiol.* **125**, 1–25.

Hu B.-Y., Weick J. P., Yu J., Ma L.-X., Zhang X.-Q., Thomson J. a, Zhang S.-C. (2010) Neural differentiation of human induced pluripotent stem cells follows developmental principles but with variable potency. *Proc. Natl. Acad. Sci. U. S. A.* **107**, 4335–40.

Hungsberg J. G., Efthymiou A. G., Malik N., Behl M., Mead I. L., Zeng X., Simenov A., Rao M.

D. (2013) nduced pluripotent stem cell models to enable in vitro models for screening in CNS. 336, 1–39.

Jin H., Wu H., Osterhaus G., Wei J., Davis K., Sha D., Floor E., Hsu C.-C., Kopke R. D., Wu J.-Y. (2003) Demonstration of functional coupling between gamma -aminobutyric acid (GABA) synthesis and vesicular GABA transport into synaptic vesicles. *Proc. Natl. Acad. Sci. U. S. A.* **100**, 4293–8.

Kinney M. a, Sargent C. Y., McDevitt T. C. (2011) The multiparametric effects of hydrodynamic environments on stem cell culture. *Tissue Eng. Part B. Rev.* **17**, 249–262.

Koch P., Opitz T., Steinbeck J. A., Ladewig J., Brüstle O. (2009) A rosette-type, self-renewing human ES cell-derived neural stem cell with potential for in vitro instruction and synaptic integration. *Proc. Natl. Acad. Sci. U. S. A.* **106**, 3225–30.

Kuan C. Y., Roth K. a, Flavell R. a, Rakic P. (2000) Mechanisms of programmed cell death in the developing brain. *Trends Neurosci.* **23**, 291–297.

Kwon S. E., Chapman E. R. (2011) Synaptophysin Regulates the Kinetics of Synaptic Vesicle Endocytosis in Central Neurons. *Neuron* **70**, 847–854.

Lee H. S., Bae E. J., Yi S. H., Shim J. W., Jo a. Y., Kang J. S., Yoon E. H., et al. (2010) Foxa2 and Nurr1 synergistically yield A9 nigral dopamine neurons exhibiting improved differentiation, function, and cell survival. *Stem Cells* **28**, 501–512.

Li Z., Cui Z. (2014) Three-dimensional perfused cell culture. *Biotechnol. Adv.* **32**, 243–254.

Livak K. J., Schmittgen T. D. (2001) Analysis of relative gene expression data using real-time quantitative PCR and the 2(-Delta Delta C(T)) Method. *Methods* **25**, 402–8.

Maggio N., Vlachos A. (2014) Synaptic plasticity at the interface of health and disease: new insights on the role of endoplasmic reticulum intracellular calcium stores. *Neuroscience.*

Marazzi G., Buckley K. M. (1993) Accumulation of mRNAs encoding synaptic vesicle-specific proteins precedes neurite extension during early neuronal development. *Dev. Dyn.* **197**, 115–24.

Mariani J., Simonini M. V., Palejev D., Tomasini L., Coppola G., Szekely A. M., Horvath T. L., Vaccarino F. M. (2012) Modeling human cortical development in vitro using induced pluripotent stem cells. *Proc. Natl. Acad. Sci. U. S. A.* **109**, 12770–5.

Melo C. V., Mele M., Curcio M., Comprido D., Silva C. G., Duarte C. B. (2013) BDNF Regulates the Expression and Distribution of Vesicular Glutamate Transporters in Cultured Hippocampal Neurons. *PLoS One* **8**, 1–17.

Middeldorp J., Hol E. M. (2011) GFAP in health and disease. *Prog. Neurobiol.* **93**, 421–443.

Minelli a., Barbaresi P., Reimer R. J., Edwards R. H., Conti F. (2001) The glial glutamate transporter GLT-1 is localized both in the vicinity of and at distance from axon terminals in the rat cerebral cortex. *Neuroscience* **108**, 51–59.

Pampaloni F., Reynaud E. G., Stelzer E. H. K. (2007) The third dimension bridges the gap between cell culture and live tissue. *Nat. Rev. Mol. Cell Biol.* **8**, 839–845.

Paşca A. M., Sloan S. a, Clarke L. E., Tian Y., Makinson C. D., Huber N., Kim C. H., et al. (2015) Functional cortical neurons and astrocytes from human pluripotent stem cells in 3D culture. *Nat. Methods* April.

Patel A. B., Lai J. C. K., Chowdhury G. M. I., Hyder F., Rothman D. L., Shulman R. G., Behar K. L. (2014) Direct evidence for activity-dependent glucose phosphorylation in neurons with implications for the astrocyte-to-neuron lactate shuttle. *Proc. Natl. Acad. Sci. U. S. A.* **111**, 5385–90.

Pollock J., Ho S. V., Farid S. S. (2013) Fed-batch and perfusion culture processes: Economic, environmental, and operational feasibility under uncertainty. *Biotechnol. Bioeng.* **110**, 206–219.

Rodrigues C. a V, Fernandes T. G., Diogo M. M., Silva C. L. da, Cabral J. M. S. (2011) Stem cell cultivation in bioreactors. *Biotechnol. Adv.* **29**, 815–829.

Saporta M. a, Grskovic M., Dimos J. T. (2011) Induced pluripotent stem cells in the study of neurological diseases. *Stem Cell Res. Ther.* **2**, 37.

Schüle B., Pera R. a R., Langston J. W. (2009) Can cellular models revolutionize drug discovery in Parkinson's disease? *Biochim. Biophys. Acta* **1792**, 1043–51.

Schwindt T. T., Motta F. L., Barnabé G. F., Massant C. G., Guimarães A. D. O., Calcagnotto M. E., Conceição F. S., Pesquero J. B., Rehen S., Mello L. E. (2009) Short-term withdrawal of mitogens prior to plating increases neuronal differentiation of human neural precursor cells. *PLoS One* **4**, e4642.

Serra M., Brito C., Correia C., Alves P. M. (2012) Process engineering of human pluripotent stem cells for clinical application. *Trends Biotechnol* **30**, 350–359.

Serra M., Brito C., Costa E. M., Sousa M. F., Alves P. M. (2009) Integrating human stem cell expansion and neuronal differentiation in bioreactors. *BMC Biotechnol* **9**, 82.

Serra M., Brito C., Sousa M. F. Q., Jensen J., Tostões R., Clemente J., Strehl R., Hyllner J., Carrondo M. J. T., Alves P. M. (2010) Improving expansion of pluripotent human embryonic stem cells in perfused bioreactors through oxygen control. *J. Biotechnol.* **148**, 208–15.

Serra M., Correia C., Malpique R., Brito C., Jensen J., Bjorquist P., Carrondo M. J. T., Alves P. M. (2011) Microencapsulation technology: a powerful tool for integrating expansion and cryopreservation of human embryonic stem cells. *PLoS One* **6**, e23212.

Simão D., Pinto C., Piersanti S., Weston A., Peddie C. J., Bastos A. E. P. P., Licursi V., et al. (2015) Modeling human neural functionality in vitro: three-dimensional culture for dopaminergic differentiation. *Tissue Eng. Part A* **21**, 654–68.

Subburaju S., Benes F. M. (2012) Induction of the GABA cell phenotype: An in vitro model for studying neurodevelopmental disorders. *PLoS One* **7**, 1–10.

Terrasso A. P., Pinto C., Serra M., Filipe A., Almeida S., Ferreira A. L., Pedroso P., Brito C., Alves P. M. (2015) Novel scalable 3D cell based model for in vitro neurotoxicity testing: Combining human differentiated neurospheres with gene expression and functional endpoints. *J. Biotechnol.* **205**, 82–92.

Thier M., Wörsdörfer P., Lakes Y. B., Gorris R., Herms S., Opitz T., Seiferling D., et al. (2012) Direct conversion of fibroblasts into stably expandable neural stem cells. *Cell Stem Cell* **10**, 473–479.

Watanabe K., Ueno M., Kamiya D., Nishiyama A., Matsumura M., Wataya T., Takahashi J. B., et al. (2007) A ROCK inhibitor permits survival of dissociated human embryonic stem cells. *Nat. Biotechnol.* **25**, 681–686.

Wu J., Rostami M. R., Cadavid Olaya D. P., Tzanakakis E. S. (2014) Oxygen transport and stem cell aggregation in stirred-suspension bioreactor cultures. *PLoS One* **9**, e102486.

Zeng X., Hunsberger J. G., Simenov A., Malik N., Pei Y., Rao M. (2014) Concise Review: Modeling Central Nervous System Diseases Using Induced Pluripotent Stem Cells. 10–14.

7

Discussion and perspectives

Table of Contents

1. Discussion

The development of reliable and predictive human central nervous system (CNS) models still remains as an unmet need for preclinical pharmaceutical development, namely in drug discovery and toxicology fields. This is mainly related with the intrinsic human brain cellular heterogeneity and network complexity, which makes its *in vitro* recapitulation a tremendous challenge. In this context, the synergy between different fields as neurobiology, tissue engineering and biotechnology can decisively contribute to leverage the development of *in vitro* neural cell models.

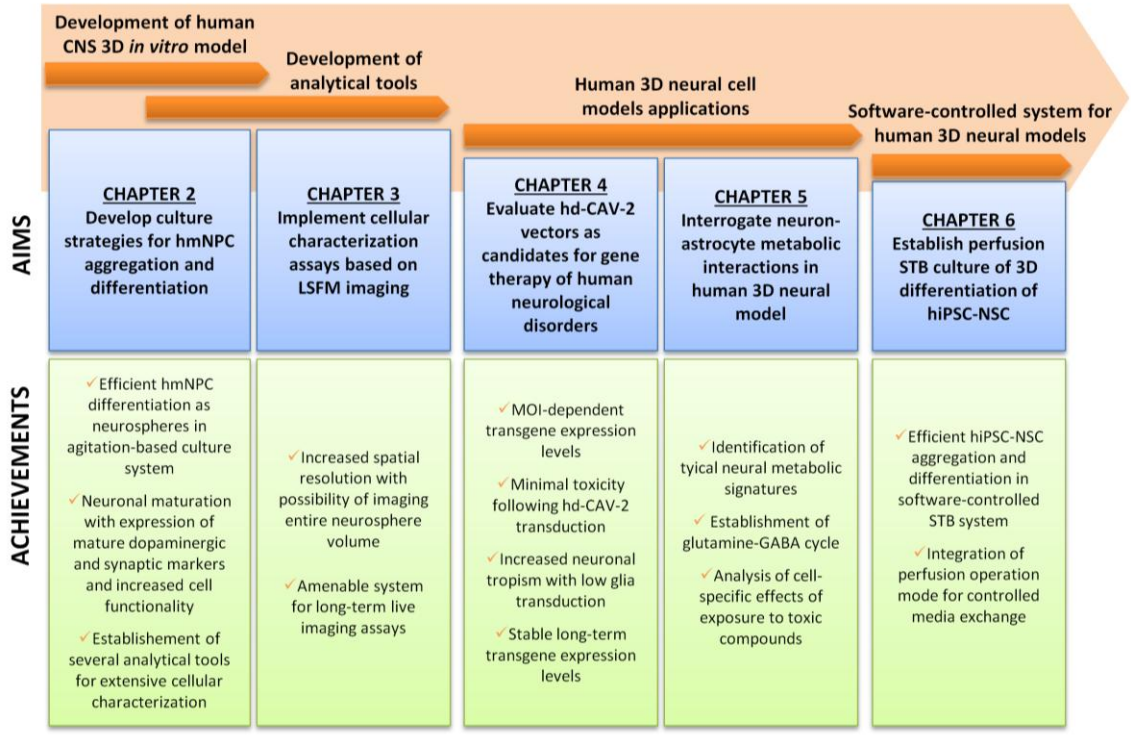

Figure 7.1 – Schematic representation of the major aims of this thesis and the achievements of each chapter (2-6). CNS – central nervous system; hmNPC – human midbrain-derived neural precursor cells; LSFM – light-sheet fluorescence microscopy; hd-CAV-2 – helper-dependent canine adenovirus vectors type 2; STB – stirred-tank bioreactors; hiPSC-NSC – neural stem cells derived from human induced pluripotent stem cells.

The work developed in this thesis aimed at developing novel 3D CNS *in vitro* models, which could mimic phenotypic and functional features of human brain tissue. For this, a strategy for aggregation and differentiation of human neural stem cells (hNSC) was developed by exploring agitation-based culture systems. This strategy was developed for human midbrain-derived neural progenitor cells (hmNPC) in **Chapter 2** and later extended to NSC derived from human pluripotent stem cells (hiPSC-NSC) in

Chapter 6. Moreover, different analytical methods were established and/or adapted for the characterization of 3D cell models, including tools for phenotypic, metabolic and functional interrogation. The generation of functional human neural cells in a 3D context of increased physiological relevance, combined with a scalable culture system that can be easily transferred to different sources of human neural cells, makes this a promising system for preclinical research. The application of human 3D neural models was also explored, namely the possibility to evaluate a promising gene therapy vector and as platform for toxicological studies.

1.1. Development of human 3D CNS *in vitro* models

For long researchers have bypassed the challenges of studying such a highly complex system such as the human brain, by developing models that can fuel the neuroscience research field. As referred in the introduction, this has traditionally relied on animal models, mostly genetically engineered mouse models (GEMM), or primary cultures of rodent neural cells (Jucker 2010; Mak *et al.* 2014). Animal models, despite presenting key neural features can diverge considerably from the human phenotype. Many neurodegenerative disorders are human specific with no parallel in rodents (Jucker 2010), which makes these models unable to fully recapitulate human disease mechanisms. Therefore, the existing interspecies differences have contributed to hamper relevant findings on human disease onset and progression.

Human cell-based models represent a compelling alternative, enabling to study neurological disorders and evaluate novel therapeutics in a human setting (Schüle *et al.* 2009; Ben-Nun and Benvenisty 2006). In this context, human stem cells are a relevant cell source, given the limited and scarce availability of human primary brain tissue. However, the tissue-specific architecture and cellular crosstalk interactions are not recapitulated in traditional monolayer culture systems. 3D culture systems emerged as promising approach for tissue modeling, by promoting more physiological cell-cell and cell-ECM interactions (Griffith and Swartz 2006).

In **Chapter 2**, the main focus was the establishment of a robust and reproducible methodology for the 3D differentiation of human neural stem cells (hNSC). For this, human fetal midbrain-derived neural progenitor cells (hmNPC) were used as cell source, which were described to retain its midbrain region commitment towards the dopaminergic phenotype (Storch *et al.* 2001). The specific properties of hmNPC make this an attractive cell source for studying the development and degeneration of human dopaminergic neurons, as well as for cell replacement therapies in patients with Parkinson's disease (Storch *et al.* 2004). hmNPC cultures were maintained in low oxygen tensions (3% O_2 in air), as previous reports demonstrated the beneficial effects in cell

proliferation yields and reducing the frequency of spontaneous cell differentiation and senescence events (Milosevic *et al.* 2005; Storch *et al.* 2001). For 3D differentiation, an agitation-based culture system was adopted, enabling to efficiently induce cell aggregation into neurospheres. This culture system presents important advantages over static culture systems, such as enhanced mass transfer coefficients that increase as a power function of agitation speed. This enables a higher degree of control over the cellular aggregation process, as this depends on the frequency of cell collisions, which in its turn is modulated by the mass transfer coefficient (Kinney *et al.* 2011).

hmNPC differentiation was induced by mitogen (bFGF/EGF) removal and exposure to neurogenic morphogens, including dibutyryl cyclic adenosine monophosphate (dbcAMP), forskolin and fusaric acid. dbcAMP is a membrane-permeable analogue of cAMP, while forskolin promotes adenylate cyclase activity contributing also to increase the intracellular levels of cAMP (Palmer *et al.* 1997). These morphogens were used for driving hmNPC differentiation, as it was previously reported that prolonged intracellular elevation of cAMP could induce the expression of several transcription factors involved in neuronal cell fate determination, while promoting neuronal survival during neurogenesis (Dworkin and Mantamadiotis 2010; Fujioka 2004; Lepski *et al.* 2013; Nakao 1998; Jagasia *et al.* 2009). hmNPC were shown to respond to these cAMP signaling-activating morphogens, which were also used in combinatorial treatments with other small molecules to increase the efficiency of dopaminergic differentiation, including fusaric acid (Milosevic *et al.* 2009; Milosevic *et al.* 2006; Wegner *et al.* 2012). In **Chapter 2,** the exposure of hmNPC neurospheres to these morphogens during 14 days resulted in a dense network of βIII-tubulin-positive neurons and GFAP-positive glia cells. Importantly, gene expression data showed a significant upregulation of dopaminergic marker *TH,* demonstrating the differentiation of these cells towards the dopaminergic lineage.

The developed strategy was further refined, aiming at improved cell maturation with increased functional features. A maturation step was added by extending the culture time in more 18 days, removing the morphogens from the culture media except for dbcAMP, which was shown to be important for survival and maturation of dopaminergic neurons in culture (Michel and Agid 1996). This protocol drove the progression of multipotent progenitors into later developmental stages, generating neurons with a more mature phenotype. Cells from the three neural lineages, neurons, astrocytes and oligodendrocytes were identified in the differentiated neurospheres generating a complex tissue-like structure. The differentiation process induced a significant modulation on ECM-associated genes, with downregulation of several collagen, laminin and fibronectin synthesis- and binding-related genes and concomitant

upregulation of glycosaminoglycans and proteoglycans binding-related genes. Also, morphological changes were observed, including cytoplasmic volume reduction and a transition from lamellipodia towards abundant filopodia membrane protrusions. Together, these observations indicated cellular remodeling during differentiation, with development of features resembling more mature neural tissue, such as proteoglycan-rich ECM composition (Dwyer and Matthews 2011) and dendritic spine development associated with increased filopodia outgrowth (Zito *et al.* 2004).

Neuronal differentiation was significantly improved after the 18 days maturation period, as compared with 7+14 days differentiation stage. Significant upregulation was observed in the expression of dopaminergic and GABAergic lineage-specific markers, which are the two neuronal subtypes present in the human midbrain (Korotkova *et al.* 2004). Neuronal maturation was also enhanced, with the correct development of synaptic machinery that resulted in improved neuronal functional features, such as the ability to synthesize and release dopamine/GABA in a stimuli-dependent manner and also displaying typical neuronal electrophysiological features, including polarized cell membranes (V_m = -70mV) and voltage- and ligand-gated currents.

The applicability of the developed 3D differentiation strategy to other human neural stem cells sources was addressed in **Chapter 6**, exploring the use of neural stem cells derived from human induced pluripotent stem cells (hiPSC-NSC) and software-controlled stirred-tank bioreactors (STB). hiPSC-NSC allow to overcome the major limitations of fetal-origin hNSC, being widely available from multiple donors and enabling its expansion *in vitro* for longer periods of time (Hunsberger *et al.* 2015). Promising results have also demonstrated that hiPSC-NSC based models can recapitulate key pathological mechanisms *in vitro*, such as amyloid-β and tau pathology in Alzheimer's disease that are not fully recapitulated in rodent models (Choi *et al.* 2014).

For hiPSC-NSC aggregation and differentiation, a commercially available software-controlled STB system was adopted. This enabled to monitor and control important culture parameters in real-time, including dissolved oxygen that was kept at 3 % (15 % of air with 21 % of oxygen) given its importance for neuronal differentiation and survival, as discussed above. The implementation of a gravimetric-controlled automatic perfusion system provided a stable setting for media feeding, avoiding more invasive media exchange regimes. Manual media exchanges regimes introduce more batch-to-batch variations and often result in loss of neurospheres with significant perturbation in working culture conditions. Consequently, perfusion systems have been shown to significantly contribute to an increase in the expansion yields of human embryonic stem cells (Fong *et al.* 2005; Serra *et al.* 2010), as well as enhancing the efficiency in cardiomyocyte differentiation (Bauwens *et al.* 2005; Niebruegge *et al.* 2008). The de-

gree of control offered by this operation mode over the culture physico-chemical environment favors the development of more robust and reproducible differentiation processes (Serra *et al.* 2012). More importantly, such agitation-based culture systems provide a scalable platform, enabling its scale-up in order to feed high throughput testing platforms, indispensable in preclinical research (Astashkina and Grainger 2014; Astashkina *et al.* 2012; Eglen and Randle 2015).

The 3D differentiation of hiPSC-NSC in STB resulted in the generation of neurospheres composed of astrocytic and neuronal cells. The ability to clear exogenously added glutamate while synthesizing/secreting glutamine, demonstrated the presence of a functional astrocytic population. The increase of MAP2- and synaptophysin-positive cells confirmed the neuronal and synaptic development along culture time. After 30 days, neuronal cells were shown to induce synaptic vesicle exocytosis upon a depolarizing stimulus, while eliciting spontaneous Ca^{2+} transients. The non-targeted differentiation strategy implemented here aimed to promote the differentiation of multiple neuronal lineages, which resulted in the detection of dopaminergic, glutamatergic and GABAergic neuronal cells within the differentiated neurospheres. This was achieved by removing the growth factors from the culture media, while adding neurogenic and neurotrophic factors, including ascorbic acid, progesterone, apo-transferrin and sodium selenium. Ascorbic acid can promote neuronal differentiation, inducing the expression of genes involved in neurogenesis, maturation, and neurotransmission (Shin *et al.* 2004) and was reported to increase the yield in dopaminergic neurons from rat mNPC by 10-fold (Yu *et al.* 2004; Yan *et al.* 2001). Progesterone has also been shown to efficiently drive the differentiation of embryonic stem cells towards the neuronal lineages (López-González *et al.* 2011). Other components are essential for the maintenance of homeostasis and viability, as the apo-transferrin antioxidant properties and sodium selenium that can inhibit oxidative stress-mediated apoptosis (Yeo and Kang 2007).

Targeted hiPSC-NSC differentiation protocols could be implemented for the enrichment in lineages of interest, either to study the developmental pathways or disease-related mechanisms. Several strategies have been explored and reported in the literature, such as the temporal-defined exposure to purmorphamine, CHIR99021, FGF-8 and SHH for dopaminergic differentiation (Kriks *et al.* 2011) or purmorphanime, cAMP, BDNF, GDNF and IGF for the generation of GABAergic neurons (Liu *et al.* 2013).

1.2. Cellular Characterization Toolbox for 3D *in vitro* models

The development of 3D cell models raises several technical challenges, mostly related with the lack of reliable available analytical tools. This is due to the fact that many of the existing methodologies are readily applicable and optimized for 2D cultures, but often fail in providing accurate readouts in 3D settings. Most importantly, the majority of these tools do not capture the spatial information provided by the 3D structures, lacking cellular and regional discrimination. The integration and interpretation of multilevel *in vitro* data sets has been proposed to be decisive for improvement of accuracy and predictive power of the preclinical screenings in early stage pharmaceutical development (McKim 2010). With the aim of obtaining highly characterized systems capable of providing a comprehensive output, an extensive toolbox of methods for characterization of 3D neural cultures was implemented during this thesis. These enabled a wide range of readouts, including phenotypic and morphological features, gene expression data, metabolic profiling and functional properties.

1.2.1. Morphological Analysis

Ultrastructural analysis provides detailed cellular and subcellular information, as it was demonstrated in **Chapter 2** by exploring different electron microscopy modalities. Neurosphere surface topology was imaged by scanning electron microcopy (SEM), which allowed the observation of a transition from more abundant lamellipodia structures in early differentiation stages, towards filopodia structures in late differentiation. Filopodia protrusions are prominent structures during synaptogenesis, giving rise to the highly motile dendritic spines. These spines can sample large numbers of potential presynaptic partners until the synaptic connection is finally stabilized (Jontes and Smith 2000; Petrak *et al.* 2005; Zito *et al.* 2004).

Neurite network development and increase in arborization was observed with transmission electron microscopy (TEM), which could also provide indirect data on cell viability by the morphological analysis of mitochondria and Golgi apparatus. Serial block-face sectioning electron microscopy (SBF-SEM) could complement TEM data and increase the spatial resolution by the analysis of a large volume of the neurospheres (up to 100-200 µm), rendering a 3D volume from thousands of aligned images. This provided data on morphological changes during differentiation and maturation, such as a reduction in cytoplasmic volume and increase in cell arborization and cell-cell interactions. The obtained data demonstrated the great potential of SBF-SEM technology to study the neural differentiation of human cells *in vitro* by generating precise 3D reconstructions, which can be used to map neuronal circuits and synaptogenic events with high spatial resolution (Blumer *et al.* 2015).

SBF-SEM analysis confirmed also the absence of necrotic centers signs within the differentiated neurospheres. This is a major a concern when working with cellular aggregates, as oxygen and nutrient transport is limited in large aggregates, leading to necrosis of cells located in the aggregate core (Sutherland and Durand 1984). Still, as mentioned above, the use of agitation-based culture systems improves mass transfer when compared to static conditions, enabling to minimize the formation of necrotic centers even in larger aggregates with 200-300 µm in diameter (Sen *et al.* 2002; Sen *et al.* 2001).

1.2.2. Gene Expression Analysis

Global or targeted gene expression analysis offers a powerful tool to monitor the differentiation process over time, as it enables to assess the activation and modulation in the expression levels of lineage-specific markers. Moreover it allows the study of the developmental pathways of stem cell *in vitro* differentiation. Gene expression data on differentiating hmNPC neurospheres in **Chapter 2** demonstrated the activation of neurogenic pathways, with dowregulation of genes involved in cell cycle progression and upregulation of dopaminergic and synaptic genes. This data suggested the preservation of midbrain region identity and developmental programs, which depend on the integration of external cues for the activation of differentiation signaling pathways. Among these, Wnt/β-catenin signaling plays a major role, mediating the proliferation and differentiation of NURR1$^+$ immature dopaminergic neurons (Joksimovic *et al.* 2009; Alves dos Santos and Smidt 2011). The expression of NURR1 transcription factor is mandatory for the terminal differentiation of midbrain dopaminergic neurons, controlling the progenitor commitment by regulating the expression of proteins involved in dopamine synthesis (e.g. TH and AADC) and transport (e.g. DAT and VMAT2) (Jankovic *et al.* 2005).

The lack of spatial resolution to discriminate between different cell compartments is the main drawback of most current transcriptomic technologies. This makes data interpretation challenging for complex and heterogeneous systems, such as hmNPC differentiated neurospheres composed by different cell populations. These issues are being targeted and tackled by the development of more powerful tools, including the use of spatially resolved single-cell gene expression technologies that have been explored for studying neural development of simple organisms as a marine annelid (Pettit *et al.* 2014) and also mouse embryos (Huang *et al.* 2015). Still, these methodologies were limited to targeted analyses provided by RNA *in situ* hybridization methodologies to create spatially resolved expression maps. Recent breakthroughs have shown however that that these maps can be used as reference for the correlation with single cell RNA-

sequencing data, enabling to computationally map the transcriptome-wide data (Satija *et al.* 2015).

1.2.3. Image-based Phenotypic Analysis

Optical imaging analysis enables the characterization of 3D *in vitro* models at a cellular level, while maintaining spatial and temporal resolution. Nevertheless, cell spheroids are highly scattering structures and typically in the hundred microns thick range, which poses significant challenges for optical imaging (Pampaloni *et al.* 2013). Confocal microscopy technologies are among the most widely used imaging modalities for spheroid analysis, despite its short penetration depth.

Light sheet fluorescence microscopy (LSFM) has emerged as promising alternative for overcoming the limitations of confocal imaging (Pampaloni *et al.* 2007; Lorenzo *et al.* 2011). In **Chapter 3**, the capabilities of this technology were explored for the imaging analysis of neural 3D models. By illuminating the sample through a single plane with a light sheet, LSFM can achieve good penetration depths, enabling the imaging of millimeter-sized samples. This allowed imaging whole neurospheres, detecting different cell markers by immunofluorescence labeling or GFP-expressing cells with increased tissue penetration and spatial resolution, as compared with conventional confocal microscopy. Moreover, the ability to rotate the sample enabled the acquisition of optical sections from different angles, which could be later processed and fused into a multiview stack, increasing even more the spatial resolution of the system.

The developed LSFM system proved also suitable for long-term live imaging assays, as samples are exposed to around 5000 times less energy than conventional confocal microscopes, minimizing photoxicity and photobleaching issues (Keller *et al.* 2008). To explore the full potential of LSFM for long-term live imaging, a dedicated incubation and feeding system was developed, avoiding the use of agarose for sample immobilization and maintaining cells in culture media. This setting allowed addition of fresh media, pharmaceutical agents or other compounds of interest during live acquisition, monitoring its effects without moving the samples. As a proof-of-concept, the toxicity of the prototypical oxidative agent Tert-butyl hydroperoxide (tBHP) was analyzed during 16 hours. Oxidative stress induced by tBHP led to extensive cellular apoptosis within the neurospheres, which was monitored in real-time using a caspase-3 substrate that becomes fluorescent upon enzymatic cleavage (NucView™488). The combination of LSFM with these fluorescent probes demonstrated its potential to increase the temporal and spatial resolution of image-based toxicological screening assays.

1.2.4. Cellular Functionality Analysis

For the evaluation of specific functional features of the generated neural cells, multiple methodologies were also applied. Evaluation of metabolic activity provides data on the physiological state and differentiation stage of the cellular system. Non-targeted approaches for studying cell metabolism, such as NMR spectroscopy, offer a snapshot of a wide range of metabolites and pathways. In **Chapter 2**, ^{1}H-NMR spectroscopy was explored for a metabolic profiling of the extracellular metabolome, which provided cues on the remodeling of cellular activity towards more specialized neural metabolic features. These methodologies were further explored on **Chapter 5**, where the intracellular metabolome was analyzed tracking the fate of ^{13}C-labeled substrates by ^{13}C-NMR. This enabled to study the establishment of neuronal and astrocytic features, in addition to indentifying important metabolic shuttles between both cell types, as the glutamine-glutamate/GABA cycle.

Methods for direct assessment of neuronal functionality were explored in **Chapter 2**, namely image-based assays and electrophysiology recording. Image-based assays enable to spatially map cellular activity by using fluorescent probes to study features such as (i) the generation of spontaneous intracellular calcium transients, essential in neuronal signal transduction (Gu *et al.* 1994); and (ii) synaptic activity, by loading synaptic vesicles with a fluorescent dye and recording the signal loss in response to depolarizing stimuli. Still, electrophysiology recording is the gold standard in neuronal functionality, measuring properties as voltage- and ligand-gated currents. These recordings were not currently applied to 3D cultures, due to the technical difficulty of touching the membrane of a single cell with the microelectrode in neurospheres. The recordings performed on hmNPC differentiated neurospheres were achieved by following approaches based on the visual contact of the cells on the outer layers or more blind strategies for the deeper layers.

The combination of the different analytical tools implemented in this thesis, many of which were applied for the first time for neurosphere analysis, enable cellular interrogation at different levels. The obtained data provides increased information on cellular processes occurring during neural differentiation and in response to alterations in culture conditions. This enabled an extensive characterization for hmNPC 3D differentiation, providing a comprehensive data set on developmental data of human neural cells *in vitro*. Furthermore, these tools can also contribute to better understand the cellular changes induced by novel therapeutics or toxicants, as described in **Chapters 4 and 5**.

1.3. Applications of human 3D CNS *in vitro* models

1.3.1. Evaluation of gene therapy vectors

The applicability of the 3D CNS model developed in **Chapter 2** was explored in **Chapter 4** for a proof-of-concept preclinical evaluation of a vector candidate for gene delivery into human neurons. Helper-dependent canine adenovirus vector type 2 (hd-CAV-2) was selected given its attractive features for gene therapy of CNS disorders. These vectors, in previous data on animal studies, were reported to preferentially transduce neurons, being efficiently transported to afferent brain regions by retrograde axonal transport and presenting low innate and induced immunogenicity (Soudais *et al.* 2001; Soudais *et al.* 2004). Still, further data on the efficacy and toxicity of these vectors in a human setting would be required to support its clinical translation.

In **Chapter 4**, the efficacy of hd-CAV-2 transduction in human neural cells was assessed in differentiated hmNPC neurospheres by testing different multiplicities of infection (MOI). The resulting transgene expression levels were determined, as well as its impact on cell viability, ultrastructural cellular organization and neuronal gene expression. From these, only the higher MOI tested (100 infectious particle/cell) demonstrated to affect the cellular dynamics, namely on dopaminergic neurons where a decrease in the expression levels of *TH* was observed. hd-CAV-2 transduction with an MOI of 50 infectious particles per cell resulted in efficient transduction of neuronal cells, with no significant alterations on neuronal gene expression and ultrastructural morphological features.

hd-CAV-2 neuronal tropism, being one of the main features indentified in rodent studies, was also evaluated in this work by direct comparison with human adenovirus vectors type 5 (HAdV5). This highlighted the hd-CAV-2 neuronal tropism as a specific feature also in human neural cells, as human adenovirus vectors type 5 (HAdV5) showed an opposite tropism by preferentially transducing glia cells and presenting poor neuronal transduction. The molecular basis for CAV-2 neuronal tropism have been proposed to be mediated by the Coxsackie virus and adenovirus receptor (CAR), as its capsid does not present integrin-interacting domains and therefore rely exclusively on CAR for internalization (Soudais *et al.* 2000). This study also demonstrated that CAR expression is restricted to neurons in the human 3D neural model, suggesting similar mechanisms driving CAV-2 tropism towards human and rodent neurons (Soudais *et al.* 2001; Soudais *et al.* 2004).

This work showed that hd-CAV-2 vectors can efficiently deliver a gene of interest to human neurons, with stable long-term expression, minimal cytotoxic effects and low

off-target glia transduction. Together these features make hd-CAV-2 an attractive vector for gene therapy strategies in human patients. Clinical translation of hd-CAV-2 vectors has been hampered by the negative reputation of adenoviral vectors, mainly due to the extensive reports on the *in vivo* immunogenicity and toxicity issues of HAdV5 (Muruve *et al.* 1999; Lieber *et al.* 1997; Yang *et al.* 1995), and the challenges for the manufacturing of helper-dependent vectors (Alba *et al.* 2005). The data presented in this thesis and in other reports (Soudais *et al.* 2004; Soudais *et al.* 2001; Piersanti *et al.* 2015) describing hd-CAV-2 features and lack of immunogenicity in humans, support the claim of an effective and safe vector for neuronal gene delivery. Together, these data motivated also efforts on the improvement of the production process of clinical-grade hd-CAV-2 batches, with the development of GMP-compliant bioprocess using stirred-tank bioreactors and serum-free culture medium (Fernandes *et al.* 2013). Productivity, purity and quality of these batches have also been shown to meet the specifications required by the regulatory authorities for HAdV5.

1.3.2. Metabolomic studies for toxicology applications

Human stem-cell derived 3D neural models have been proposed to provide interesting platforms for toxicological studies (Mazzoleni *et al.* 2009). The study of the main human neural metabolic pathways contributes to better understand the biochemical changes induced by the compounds of interest, enabling the identification of potential targets and mechanisms-of-action of toxic compounds (Ramirez *et al.* 2013). This was explored in **Chapter 5** by following the fate of ^{13}C labeled substrates ([1-^{13}C]glucose or [2-^{13}C]acetate) through the central carbon metabolic pathways, which provided also insights on functional neuron-astrocyte *in vitro* cross-talk interactions. A human NT2 cell line-based 3D neural model developed for neurotoxicity testing applications (Terrasso *et al.* 2015) was used here, due to its renewable cell source that allows the generation of large amounts of biological material for the supply screening platforms.

^{13}C-NMR analysis demonstrated that NT2 differentiated neurospheres were able to generate functional 3D neuron-astrocytes networks, namely through the establishment of the glutamine-GABA shuttle. This shuttle is of utmost importance in neural homeostasis, providing neurons with glutamine that will act as substrate for neurotransmitter synthesis, compensating the continuous neuronal loss of carbon skeletons (Bak *et al.* 2006). Exposure of NT2 differentiated neurospheres to methionine sulfoximine (MSO) a potent glutamine synthase inhibitor, resulted in an almost complete impairment of astrocytic glutamine synthesis. This was accompanied by a decrease in GABA synthesis, further demonstrating the importance of the glutamine-GABA shuttle in this human 3D model. Neuronal metabolism was challenged by exposing cells to the known

neurotoxic compound acrylamide, which affects the synaptic vesicle trafficking while inducing axonal degeneration (LoPachin 2004). In the 3D model, acrylamide exposure resulted in intracellular accumulation of glutamate, suggesting the impairment of synaptic vesicle release machinery in glutamatergic neurons. As for GABAergic neurons, results showed a decrease in GABA synthesis, suggesting an acrylamide-induced imbalance in the glutamine-GABA shuttle associated with a loss of neuron-astrocyte contacts at synaptic terminal due to axonal degeneration.

Overall, these results support the potential of human stem cell-derived 3D neural models and metabolomic tools for toxicological studies and preclinical research. Moreover, this data is likely to contribute to increase our knowledge on human neural metabolism and on the importance of neuron-astrocyte interactions in pathological conditions.

2. Conclusions and perspectives

This thesis describes the development of novel human stem cell-derived 3D CNS models for preclinical research. Agitation-based culture strategies were explored for cell aggregation and differentiation, providing a scalable system with non-destructive sampling. The use of multiple analytical tools resulted in an extensive cellular characterization, including phenotypic, metabolic and functional interrogation. The applicability of human 3D neural cell models in preclinical research was explored in a proof-of-concept study, evaluating the efficacy and safety of a gene therapy vector candidate for human neuronal gene delivery. Moreover, human 3D neural models were shown to support studies on the mechanisms underlying metabolism and toxicity of specific compounds, as well as contribute to increase our knowledge on human neural metabolic pathways, namely neuron-glia interactions. These two studies demonstrated that relevant preclinical data can be extracted from human 3D CNS models, being complementary with animal studies and likely to contribute to more predictable clinical translation.

The strategies presented herein contributed to the progress of the state-of-the-art on human neural cell models, although further improvements can be pursued aiming at increased predictability in preclinical studies. Capturing the heterotypic complexity of the human brain can leverage the current cell models, namely introducing endothelial and microglia cells that play pivotal roles in disease and inflammation processes (Hanisch and Kettenmann 2007; Stanimirovic and Satoh 2000). Therefore the presence of these cells may enable to more closely recapitulate key pathological events *in vitro*, allowing to better understanding and possibly targeting human neurological diseases with more effective therapies. Given the importance of oligodendrocytes for neuronal

functionality and tissue homeostasis, it will be fundamental also to characterize and promote oligodendrocytic maturation and neuronal myelination. Moreover, the differential response of patients to the therapeutics is often associated with the natural variability of human populations, and therefore is typically challenging to accurately predict during preclinical development. The use of human iPSC from multiple donors, namely patient-derived cells, can aid in addressing this issue. Exploring cells from multiple donors will allow to partially cover the inherent patient variability. Also, by carrying the disease genetic background, patient-derived cells can be decisive for the disease modeling field, enabling to study *in vitro* the onset and progression mechanisms of human neural pathologies.

Technological and analytical developments will also play central role for the widespread implementation of 3D cultures for screening applications by the pharmaceutical industry. Traditional monolayer cultures are easier to manipulate, making it more amenable for screening platforms implementation. Still, the higher biological relevance provided by 3D cultures has pushed the development of automation technologies for high-throughput/high-content screening of cell spheroid-based assays (Eglen and Randle 2015). Therefore, the improvement and automation of the available tools for spheroid handling, sorting and analysis will reveal to be critical for its overall adoption over 2D cultures, with consequent increase of assay predictability. Using low throughput systems, as agitation-based culture systems, these tools can allow automated homogeneous sampling systems to feed higher throughput culture formats (e.g. multiwell microplates), reducing the inherent well-to-well variability.

In conclusion, this thesis showed that human neural stem cells can be successfully cultured and differentiated in agitation-based culture systems, sustaining the development of novel human neural *in vitro* models able to recapitulate key brain features. Therefore, its application in preclinical research can contribute to leverage early stage pharmaceutical development, namely for target identification and validation or for toxicological studies.

3. References

Alba R., Bosch A., Chillon M. (2005) Gutless adenovirus: last-generation adenovirus for gene therapy. *Gene Ther.* **12**, S18–S27.

Alves dos Santos M. T. M., Smidt M. P. (2011) En1 and Wnt signaling in midbrain dopaminergic neuronal development. *Neural Dev.* **6**, 1–15.

Astashkina A., Grainger D. W. (2014) Critical analysis of 3-D organoid in vitro cell culture models for high-throughput drug candidate toxicity assessments. *Adv. Drug Deliv. Rev.* **69-70**, 1–18.

Astashkina A., Mann B., Grainger D. W. (2012) A critical evaluation of in vitro cell culture models for high-throughput drug screening and toxicity. *Pharmacol. Ther.* **134**, 82–106.

Bak L. K., Schousboe A., Waagepetersen H. S. (2006) The glutamate/GABA-glutamine cycle: Aspects of transport, neurotransmitter homeostasis and ammonia transfer. *J. Neurochem.* **98**, 641–653.

Ben-Nun I. F., Benvenisty N. (2006) Human embryonic stem cells as a cellular model for human disorders. *Mol Cell Endocrinol* **252**, 154–159.

Blumer C., Vivien C., Genoud C., Perez-Alvarez A., Wiegert J. S., Vetter T., Oertner T. G. (2015) Automated analysis of spine dynamics on live CA1 pyramidal cells. *Med. Image Anal.* **19**, 87–97.

Choi S., Kim Y., Hebisch M., Sliwinski C., Lee S., D'Avanzo C., Chen H., et al. (2014) A three-dimensional human neural cell culture model of Alzheimer's disease. *Nature* **515**, 274–278.

Conti L., Pollard S. M., Gorba T., Reitano E., Toselli M., Biella G., Sun Y., et al. (2005) Niche-independent symmetrical self-renewal of a mammalian tissue stem cell. *PLoS Biol.* **3**, 1594–1606.

Dworkin S., Mantamadiotis T. (2010) Targeting CREB signalling in neurogenesis. *Expert Opin. Ther. Targets* **14**, 869–879.

Dwyer C., Matthews R. (2011) The Neural Extracellular Matrix, Cell Adhesion Molecules and Proteolysis in Glioma Invasion and Tumorigenicity, in *Mol. Targets CNS Tumors,* (Garami M., ed), pp. 239–264. InTech, Rijeka.

Eglen R. M., Randle D. H. (2015) Drug Discovery Goes Three-Dimensional: Goodbye to Flat High-Throughput Screening? *Assay Drug Dev. Technol.* **13**, 262–265.

Fernandes P., Peixoto C., Santiago V. M., Kremer E. J., Coroadinha A. S., Alves P. M. (2013) Bioprocess development for canine adenovirus type 2 vectors. *Gene Ther.* **20**, 353–360.

Fujioka T. (2004) Activation of cAMP Signaling Facilitates the Morphological Maturation of Newborn Neurons in Adult Hippocampus. *J. Neurosci.* **24**, 319–328.

Griffith L., Swartz M. (2006) Capturing complex 3D tissue physiology *in vitro*. *Nat Rev Mol Cell Biol.* **7**, 211-224.

Gu X., Olson E. C., Spitzer N. C. (1994) Spontaneous neuronal calcium spikes and waves during early differentiation. *J. Neurosci.* **14**, 6325–6335.

Hanisch U.-K., Kettenmann H. (2007) Microglia: active sensor and versatile effector cells in the normal and pathologic brain. *Nat. Neurosci.* **10**, 1387–1394.

Huang Y., Yu X., Sun N., Qiao N., Cao Y., Boyd-Kirkup J. D., Shen Q., Han J.-D. J. (2015) Single-cell-level spatial gene expression in the embryonic neural differentiation niche. *Genome Res.* **25**, 570–581.

Jagasia R., Steib K., Englberger E., Herold S., Faus-Kessler T., Saxe M., Gage F. H., Song H., Lie D. C. (2009) GABA-cAMP Response Element-Binding Protein Signaling Regulates Maturation and Survival of Newly Generated Neurons in the Adult Hippocampus. *J. Neurosci.* **29**, 7966–7977.

Jankovic J., Chen S., Le W. D. (2005) The role of Nurr1 in the development of dopaminergic neurons and Parkinson's disease. *Prog. Neurobiol.* **77**, 128–138.

Joksimovic M., Yun B. a, Kittappa R., Anderegg A. M., Chang W. W., Taketo M. M., McKay R. D. G., Awatramani R. B. (2009) Wnt antagonism of Shh facilitates midbrain floor plate neurogenesis. *Nat. Neurosci.* **12**, 125–31.

Jontes J. D., Smith S. J. (2000) Filopodia, spines, and the generation of synaptic diversity. *Neuron* **27**, 11–14.

Jucker M. (2010) The benefits and limitations of animal models for translational research in neurodegenerative diseases. *Nat. Med.* **16**, 1210–1214.

Keller P. J., Schmidt A. D., Wittbrodt J., Stelzer E. H. K. (2008) Reconstruction of zebrafish early embryonic development by scanned light sheet microscopy. *Science (80-.).* **322**, 1065–1069.

Kinney M. a, Sargent C. Y., McDevitt T. C. (2011) The multiparametric effects of hydrodynamic environments on stem cell culture. *Tissue Eng. Part B. Rev.* **17**, 249–262.

Korotkova T. M., Ponomarenko A. A., Brown R. E., Haas H. L. (2004) Functional diversity of ventral midbrain dopamine and GABAergic neurons. *Mol. Neurobiol.* **29**, 243–59.

Lepski G., Jannes C. E., Nikkhah G., Bischofberger J. (2013) cAMP promotes the differentiation of neural progenitor cells in vitro via modulation of voltage-gated calcium channels. *Front. Cell. Neurosci.* **7**, 1–11.

Lieber a, He C. Y., Meuse L., Schowalter D., Kirillova I., Winther B., Kay M. a (1997) The role of Kupffer cell activation and viral gene expression in early liver toxicity after infusion of recombinant adenovirus vectors. *J. Virol.* **71**, 8798–8807.

LoPachin R. M. (2004) The changing view of acrylamide neurotoxicity. *Neurotoxicology* **25**, 617–630.

Lorenzo C., Frongia C., Jorand R., Fehrenbach J., Weiss P., Maandhui A., Gay G., Ducommun B., Lobjois V. (2011) Live cell division dynamics monitoring in 3D large spheroid tumor models using light sheet microscopy. *Cell Div.* **6**, 22.

Mak I. W., Evaniew N., Ghert M. (2014) Lost in translation: animal models and clinical trials in cancer treatment. *Am. J. Transl. Res.* **6**, 114–8.

Mazzoleni G., Lorenzo D. Di, Steimberg N. (2009) Modelling tissues in 3D: The next future of pharmaco-toxicology and food research? *Genes Nutr.* **4**, 13–22.

McKim J. M. (2010) Building a tiered approach to in vitro predictive toxicity screening: a focus on assays with in vivo relevance. *Comb. Chem. High Throughput Screen.* **13**, 188–206.

Michel P. P., Agid Y. (1996) Chronic activation of the cyclic AMP signaling pathway promotes development and long-term survival of mesencephalic dopaminergic neurons. *J. Neurochem.* **67**, 1633–1642.

Milosevic J., Adler I., Manaenko A., Schwarz S. C., Walkinshaw G., Arend M., Flippin L. A., Storch A., Schwarz J. (2009) Non-hypoxic stabilization of hypoxia-inducible factor alpha (HIF-alpha): relevance in neural progenitor/stem cells. *Neurotox. Res.* **15**, 367–380.

Milosevic J., Brandt A., Roemuss U., Arnold A., Wegner F., Schwarz S. C., Storch A., Zimmermann H., Schwarz J. (2006) Uracil nucleotides stimulate human neural precursor cell proliferation and dopaminergic differentiation: Involvement of MEK/ERK signalling. *J. Neurochem.* **99**, 913–923.

Milosevic J., Schwarz S. C., Krohn K., Poppe M., Storch A., Schwarz J. (2005) Low atmospheric oxygen avoids maturation, senescence and cell death of murine mesencephalic neural precursors. *J. Neurochem.* **92**, 718–729.

Muruve D. a, Barnes M. J., Stillman I. E., Libermann T. a (1999) Adenoviral gene therapy leads to rapid induction of multiple chemokines and acute neutrophil-dependent hepatic injury in vivo. *Hum. Gene Ther.* **10**, 965–76.

Nakao N. (1998) An increase in intracellular levels of cyclic AMP produces trophic effects on striatal neurons developing in culture. *Neuroscience* **82**, 1009–1020.

Palmer T. D., Takahashi J., Gage F. H. (1997) The Adult Rat Hippocampus Contains Primordial Neural Stem Cells. *Mol. Cell. Neurosci.* **8**, 389–404.

Pampaloni F., Ansari N., Stelzer E. H. K. (2013) High-resolution deep imaging of live cellular spheroids with light-sheet-based fluorescence microscopy. *Cell Tissue Res.*, 161–177.

Pampaloni F., Reynaud E. G., Stelzer E. H. K. (2007) The third dimension bridges the gap between cell culture and live tissue. *Nat. Rev. Mol. Cell Biol.* **8**, 839–845.

Petrak L. J., Harris K. M., Kirov S. a (2005) Synaptogenesis on mature hippocampal dendrites occurs via filopodia and immature spines during blocked synaptic transmission. *J. Comp. Neurol.* **484**, 183–190.

Pettit J.-B., Tomer R., Achim K., Richardson S., Azizi L., Marioni J. (2014) Identifying Cell Types from Spatially Referenced Single-Cell Expression Datasets. *PLoS Comput. Biol.* **10**, e1003824.

Piersanti S., Burla R., Licursi V., Brito C., Torre M. La, Alves P. M., Simao D., et al. (2015) Transcriptional Response of Human Neurospheres to Helper-Dependent CAV-2 Vectors Involves the Modulation of DNA Damage Response, Microtubule and Centromere Gene Groups. *PLoS One* **10**, e0133607.

Pollard S. M., Conti L., Sun Y., Goffredo D., Smith A. (2006) Adherent neural stem (NS) cells from fetal and adult forebrain. *Cereb. Cortex* **16**.

Ramirez T., Daneshian M., Kamp H., Bois F. Y., Clench M. R., Coen M., Donley B., et al. (2013) Metabolomics in toxicology and preclinical research. *ALTEX* **30**, 209–25.

Satija R., Farrell J. a, Gennert D., Schier A. F., Regev A. (2015) Spatial reconstruction of single-cell gene expression data. *Nat. Biotechnol.* April.

Schüle B., Pera R. a R., Langston J. W. (2009) *Can cellular models revolutionize drug discovery in Parkinson's disease?* Elsevier B.V.

Sen A., Kallos M. S., Behie L. a (2001) Effects of Hydrodynamics on Cultures of Mammalian Neural Stem Cell Aggregates in Suspension Bioreactors. *Ind. Eng. Chem. Res.* **40**, 5350–5357.

Sen A., Kallos M. S., Behie L. a. (2002) Expansion of mammalian neural stem cells in bioreactors: Effect of power input and medium viscosity, in *Dev. Brain Res.,* Vol. 134, pp. 103–113.

Soudais C., Boutin S., Hong S. S., Chillon M., Danos O., Bergelson J. M., Boulanger P., Kremer E. J. (2000) Canine Adenovirus Type 2 Attachment and Internalization : Coxsackievirus-Adenovirus Receptor, Alternative Receptors, and an RGD-Independent Pathway. *J. Virol.* **74**, 10639–10649.

Soudais C., Laplace-Builhe C., Kissa K., Kremer E. J. (2001) Preferential transduction of neurons by canine adenovirus vectors and their efficient retrograde transport in vivo. *FASEB J.* **15**, 2283–2285.

Soudais C., Skander N., Kremer E. J. (2004) Long-term in vivo transduction of neurons throughout the rat CNS using novel helper-dependent CAV-2 vectors. *FASEB J.* **18**, 391–393.

Stanimirovic D., Satoh K. (2000) Inflammatory mediators of cerebral endothelium: a role in ischemic brain inflammation. *Brain Pathol.* **10**, 113–26.

Storch A., Paul G., Csete M., Boehm B. O., Carvey P. M., Kupsch A., Schwarz J. (2001) Long-term proliferation and dopaminergic differentiation of human mesencephalic neural precursor cells. *Exp Neurol* **170**, 317–325.

Storch A., Sabolek M., Milosevic J., Schwarz S. C., Schwarz J. (2004) Midbrain-derived neural stem cells: from basic science to therapeutic approaches. *Cell Tissue Res* **318**, 15-22.

Sun Y., Pollard S., Conti L., Toselli M., Biella G., Parkin G., Willatt L., Falk A., Cattaneo E., Smith A. (2008) Long-term tripotent differentiation capacity of human neural stem (NS) cells in adherent culture. *Mol. Cell. Neurosci.* **38**, 245–258.

Sutherland R. M., Durand R. E. (1984) Growth and Cellular Characteristics of Multicell Spheroids, in *Spheroids Cancer Res.,* (Acker H., Carlsson J., Durand R., Sutherland R. M., eds), Vol. 95, pp. 24–49. Springer Berlin Heidelberg.

Terrasso A. P., Pinto C., Serra M., Filipe A., Almeida S., Ferreira A. L., Pedroso P., Brito C., Alves P. M. (2015) Novel scalable 3D cell based model for in vitro neurotoxicity testing: Combining human differentiated neurospheres with gene expression and functional endpoints. *J. Biotechnol.* **205**, 82-92.

Wegner F., Kraft R., Busse K., Härtig W., Ahrens J., Leffler A., Dengler R., Schwarz J. (2012) Differentiated Human Midbrain-derived neural progenitor cells express excitatory strychnine-sensitive glycine receptors containing α2β subunits. PLOS One **7**, e36946.

Yang Y., Li Q., Ertl H. C., Wilson J. M. (1995) Cellular and humoral immune responses to viral antigens create barriers to lung-directed gene therapy with recombinant adenoviruses. *J. Virol.* **69**, 2004–15.

Zito K., Knott G., Shepherd G. M. G., Shenolikar S., Svoboda K. (2004) Induction of spine growth and synapse formation by regulation of the spine actin cytoskeleton. *Neuron* **44**, 321–34.